UNIVERSITÀ DEGLI STUDI DI PAVIA

DOTTORATO IN SCIENZE CHIMICHE E FARMACEUTICHE E INNOVAZIONE INDUSTRIALE
(XXXV Ciclo)
Coordinatore: Chiar.mo Prof. Giorgio Colombo

SUPRAMOLECULAR SYSTEMS FOR APPLICATION IN RECOGNITION AND SEPARATION PROCESSES

Tesi di Dottorato di
Riccardo Mobili

AA 2021/2022

Tutor
Chiar.ma Prof.ssa Valeria Amendola

INDEX

1. INTRODUCTION

This PhD project was focused on the development of organic cage-like molecules for applications in the recognition and sensing of anionic guests, and in gas adsorption/separation processes. According to the IUPAC definition, a cage molecule is a "polycyclic compound with the shape of a cage" [1]. The term "organic" narrows it down to species formed only by carbon-carbon bonds and/or other functional groups typically found in organic molecules. This excludes, for example, coordination compounds and fully inorganic systems [2]. Since 1969, when J. M. Lehn reported the first cryptands (synthetic organic macrobicyclic receptors) for the selective recognition of cations [3], organic cages have raised increasing interest in the scientific community for their structural aesthetics and, more importantly, for the possibility to be employed in recognition, sensing, catalysis, separation and transport processes [4]. The first synthetic approaches in the synthesis of cage-like molecules were based on the formation irreversible covalent bonds through *e.g.* cross-coupling or amidation reactions, that unfortunately produced a number of undesired side-products (*e.g.* oligomeric compounds) and required tedious purification steps, that generally resulted in daunting yields. More recently, the implementation of the dynamic covalent chemistry approach (DCC) gave a boost to the development of organic cage-like molecules. The DCC approach consists in the reversible reaction of molecular building blocks under thermodynamic control. This "self-correcting" process can lead to the construction of large molecular systems, starting from small building blocks, in very high yields. Even if various types of reversible reactions have been explored over the years (*e.g.* boronic ester or disulfide formation, alkene metathesis, Michael addition, ecc…), imine formation is still the most utilised in this field [5]. In particular, the three main reactions involving imine bonds are: i) the condensation between a carbonyl and an amine with the loss of a water molecule (and the reverse hydrolysis); ii) the imine exchange reaction between an already formed imine and a different amine; iii) the imine metathesis between two distinct imines (Figure 1.1) [6].
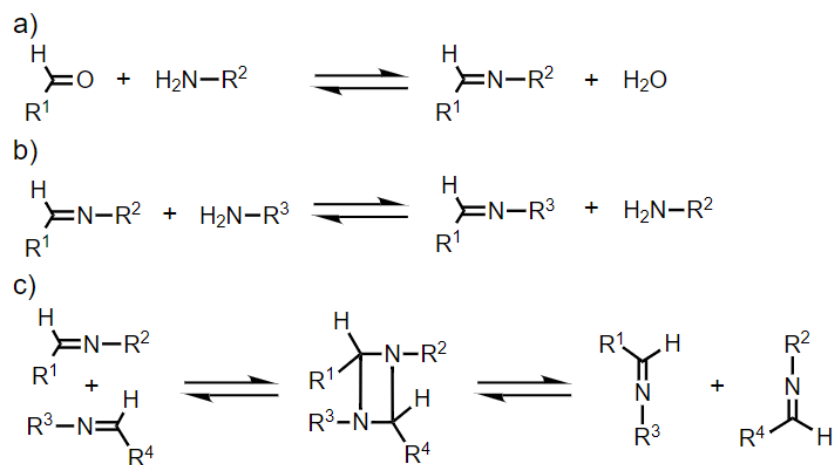
Figure 1.1 Three reversible reactions involving the imine bond: a) imine formation/hydrolysis; b) imine exchange; c) imine metathesis. From ref. [5].

The reversible nature of these reactions favours the removal of undesired intermediates (*e.g.* open oligomeric and polymeric species) and finally lead to the most thermodynamically stable structures. Moreover, DCC promotes self-sorting processes in multicomponent libraries of building blocks, and can also provide a pathway for cage-to-cage transformation in solution [7]. For example, a four-component narcissistic self-sorting process has been demonstrated by Mukherjee *et al*. In particular, when a solution of two amines (*i.e.* X and Y) was mixed with a solution of two aldehydes (*i.e.* A and B), in the right molar ratio, only two [2+3] imine cages (*i.e.* Y_2A_3 and X_2B_3) were formed out of the four possible architectures. Furthermore, when a non-preferred cage (like Y_2B_3) was treated with the required amount of amine (X) and aldehyde (A), the spontaneous re-assembling to give the most stable products (X_2B_3 and Y_2A_3) took place (Figure 1.2) [8].
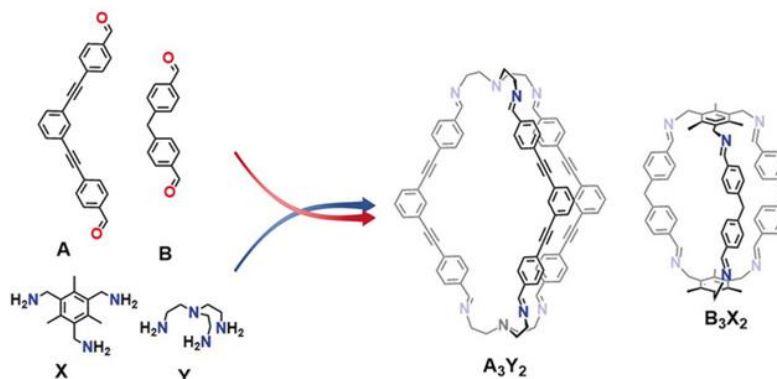
Figure 1.2 Example of a) self-sorting and b) cage-to-cage transformation in imine organic cages. From ref. [6]

However, the reversible nature of the imine bond reduces the stability of polyimine cages in water-containing environments. The easiest approach to stabilize these unsaturated species consists in the reduction of imines to the corresponding amines. A typical example of this type of cages is represented by the so-called bis-tren azacryptands [9]. The synthesis of bis-tren cages is rather simple, and consists in the [2+3] imine condensation between the commercial tris(2-aminoethyl)amine (*i.e.* tren) and a chosen dialdehyde, generally without metal templates. The reduction of the obtained imine-based cryptand leads to the saturated polyamine cage, that can be used in a variety of different applications such as anion recognition and separation (Figure 1.3) [10]. The spacers between the tren subunits have a crucial role in the binding of analytes within the cavity. They determine the shape and size of the cavity, thus controlling the selectivity and even the reactivity of the cage.
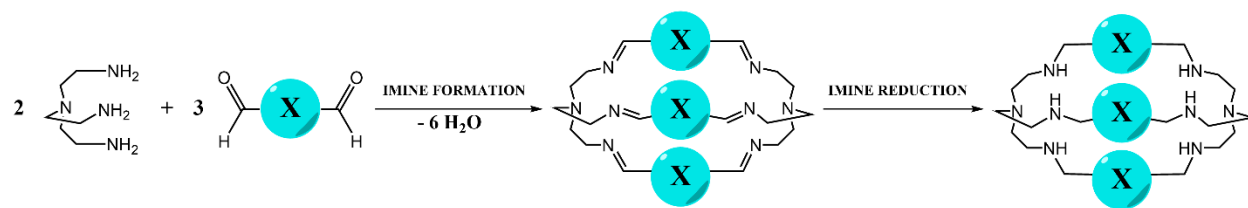
Figure 1.3 Scheme of a typical bis-tren cage synthesis.

The first work presented in this thesis deals with an asymmetric bis-tren cage developed as a selective chemosensor for perrhenate (ReO_4^-). The presence of the chiral binaphthol moiety made it possible to perform chiroptical sensing of the target anion in both acidic water and aqueous complex matrices, such as fruit juice and artificial urine medium.

In the second reported work, four different hexaimine bis-tren cages were prepared and tested as potential N-rich fillers in the construction of mixed matrix membranes for gas separation applications.

In the last study, two novel imine/imide organic cages were synthesized and studied as materials for the selective adsorption of CO_2 for potential application in post-combustion carbon capture and biogas upgrading processes. The novel cages were also tested as fillers in mixed matrix membranes for gas separation applications.

The results described in the next chapters have been published in scientific journals:

1) R. Mobili, G. Preda, S. La Cognata, L. Toma, D. Pasini, V. Amendola, "Chiroptical sensing of perrhenate in aqueous media by a chiral organic cage", *Chem. Commun.*, **2022**, 58, 3897.

2) M. Monteleone, R. Mobili, C. Milanese, E. Esposito, A. Fuoco, S. La Cognata, V. Amendola, J.C. Jansen, "PEEK-WC-Based Mixed Matrix Membranes Containing Polyimine Cages for Gas Separation", *Molecules*, **2021**, 26, 5557.

3) S. La Cognata, R. Mobili, C. Milanese, M. Boiocchi, M. Gaboardi, D. Armentano, J.C. Jansen, M. Monteleone, A.R. Antonangelo, M. Carta, V. Amendola, "CO_2 Separation by Imide/Imine Organic Cages", *Chem. Eur. J.*, **2022**, 28, e202201631.

1.1 REFERENCES

[1] P. Muller, *Pure Appl. Chem.*, **1994**, 66, 1077.

[2] G. Zhang, M. Mastalerz, *Chem. Soc. Rev.,* **2014**, 43, 1934.

[3] B. Dietrich, J.M. Lehn, J.P. Sauvage, *Tetrahedron Lett.*, **1969**, 10, 2885.

[4] J.M. Lehn, *Science*, **1985**, 227, 849.

[5] S.J. Rowan, S.J. Cantrill, G. R. Cousins, J.K. Sanders, J.F. Stoddart, *Angew. Chem. Int. Ed.*, **2002**, 41, 898.

[6] K. Acharyya, P.S. Mukherjee, *Angew. Chem. Int. Ed*., **2019**, 58, 8640.

[7] M. Kołodziejski, A.R. Stefankiewicz, J.M. Lehn, *Chem. Sci*., **2019**, 10, 1836.

[8] K. Acharyya, S. Mukherjee, P.S. Mukherjee, *J. Am. Chem. Soc*., **2013**, 135, 554.

[9] B. Dietrich, J. Guilhem, J.M. Lehn, C. Pascard, E. Souveaux, *Helv. Chim. Acta,* **1984**, *67*, 91.

[10] a) V. Amendola, L. Fabbrizzi, C. Mangano, P. Pallavicini, A. Poggi, A. Taglietti, *Coordination Chemistry Reviews,* **2001**, 219–221, 821. b) S. La Cognata, R. Mobili, F. Merlo, A. Speltini, M. Boiocchi, T. Recca, L.J. Maher III, V. Amendola, *ACS Omega*, **2020**, 5, 26573.

2. CHIROPTICAL SENSING IN AQUEOUS MEDIA BY CHIRAL ORGANIC CAGES

2.1 INTRODUCTION

The work reported in this chapter focuses on a chiral cage (*i.e.* **GB1**) used as an effective chiroptical sensor for perrhenate (surrogate for $^{99}TcO_4^-$) in water and in complex aqueous matrices such as fruit juice and artificial urine media. The key mechanism for the chiroptical sensing resides in the change of dihedral angle of the binaphthyl unit and in the formation of H-bonds with the guest, resulting in ample changes of the CD signal, as a result of the binding event.

2.1.1 Protonated Cryptands as Receptors for $^{99}TcO_4^-$

The synthesis of selective molecular receptors and sensors for hazardous materials is of great and actual interest. Among polluting harmful chemicals, radioactive species pose significant threat to human and environmental health. Nuclear fission has represented an important energy source for many countries, but the problems related to the management of radioactive wastes is still unsolved. Among radioactive pollutants, Technetium-99 (^{99}Tc), which is a weak β-emitter, with its high total fission product yield (6%) and long half-life (2.13 x 10^5 years), is a significant element in spent fuels. Environmental contamination from ^{99}Tc due to nuclear accidents, weapons testing, and spent nuclear fuel reprocessing, makes it one of the most problematic radionuclides in nuclear wastes [1]. In aqueous solution, ^{99}Tc is principally present in the +VII oxidation state as the pertechnetate anion, TcO_4^-, which is a kinetically stable and highly water-soluble species (up to 11.3 M for the sodium salt) [2]. The dangerous nature of TcO_4^- limits its use in standard laboratories thus making it necessary the use of non-radioactive substitutes. For this purpose, the perrhenate anion (ReO_4^-), which has identical geometry, similar size and hydration energy, is commonly used as a structural surrogate even if the chemical analogy is not perfect (Tab 2.1) [3,4].

Table 2.1 Properties of perrhenate and pertechnetate. From ref. [3].

$^{99}TcO_4^-$	ReO_4^-
r = 252 pm	r = 260 pm
pKa (HTcO$_4$) = 0.033	pKa (HReO$_4$) = −0.28
E° TcO$_4^-$/TcO$_2$ = 0.74 V	E° ReO$_4^-$/ReO$_2$ = 0.51 V
ΔG_{hydr} = −251 kJ/mol	ΔG_{hydr} = −330 kJ/mol

The sensing of ReO_4^- in aqueous matrices is also important because rhenium-based compounds are used as industrial catalysts and, moreover, Re radioisotopes (^{186}Re and ^{188}Re) are employed in a variety of therapeutic applications (*e.g.* in oncology, nuclear medicine and interventional cardiology) [5]. The relatively large size, the low charge/surface ratio and enthalpic contribution to complexation of perrhenate and pertechnenate make the design of effective receptors very challenging. It has to be noted that most studies on TcO_4^- recognition have been performed in pure organic solvents or aqueous mixtures [4,6-8]. In this context, water-soluble cage compounds like protonated azacryptands are good candidates for the inclusion of oxoanions of various size and geometry, through multiple H-bonding and electrostatic interactions involving the protonated amino groups [9,10]. Selectivity is connected to the geometric complementarity between the anion and the receptor cavity and, by consequence, it depends on the receptor protonation state [11]. The best condition for high selectivity is at low pH, where the cages are fully protonated and the cavities are expanded as a result of electrostatic repulsion [10a]. On the contrary, at higher pH values, when the azacryptands are only partially protonated, the anion access to the receptor cavities may be hampered by unfavourable cage conformations due to intramolecular H-bonding interactions involving the protonated and non-protonated amino groups [12]. In the literature, a large number of crystal structures of anions bound to protonated azacryptands are reported [11]. The most surprising aspect is that, depending on the crystallisation conditions (*e.g.* the amount of water, the presence of excess anion, the protonation degree of the receptor, etc.), the same anion-receptor couple may give rise to inclusion complexes, with the anionic guest bound into the receptor cavity, or other different structures, in which the anion is excluded from the cavity by water molecules and interacts with the protonated amines from the outside. Besides structural studies, many authors have studied anion encapsulation by polyammonium cages in solution [4]. In 2003 Nelson *et al.* investigated the affinity of azacryptands towards perrhenate with the goal of developing new

extractants from aqueous solutions [10b]. To enhance extraction efficiency, receptors need to be lipophilic enough to transport the bound anion into the organic phase, that is why liquid-liquid extraction studies have been performed at pH 7.4. In these conditions, the cages are only partially protonated and their anion binding capabilities are much lower than in the fully protonated forms [12]. Ten years later, Amendola *et al*. demonstrated that the hexaprotonated *p*-xylyl azacryptand **1** can effectively trap $^{99}TcO_4^-$ in aqueous solution. The encapsulation of the anion was proven by NMR and ITC studies in acidic water and by X-ray diffraction studies on a single crystal of the 1:1 inclusion complex [13]. Some years later, the same authors reported a fluorescent chemosensor for $^{99}TcO_4^-$ (**2**), obtained by replacing one of the p-xylyl spacers of **1** with an 9,10-anthracenyl unit [14]. This structural modification allowed to preserve the selectivity of the hexaprotonated ligand for pertechnetate and, at the same time, produced a fluorescent signal that could be modulated upon binding. In fact, the hexaprotonated cage $[2H_6]^{6+}$ displayed the typical emission band of anthracene centred at 425 nm; this emission was switched off by $^{99}TcO_4^-$, when the anion is trapped into the receptor cavity and forms a stable 1:1 inclusion complex.
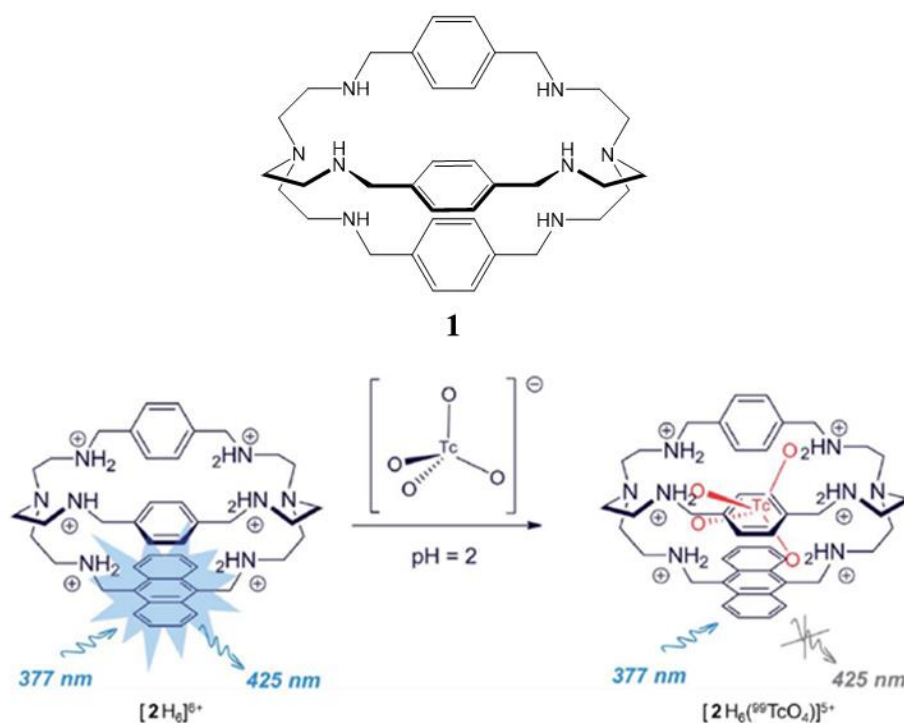

Figure 2.1 Bis-tren cage **1** and the mono-anthracenyl derivative **2** in a scheme showing the binding of pertechnetate and the consequent quenching of fluorescent signal. From ref. [14].

2.1.2 Chiroptical Sensing

As already mentioned, only a few examples of optical molecular sensors for ReO_4^- detection in water are known and they are mainly based on a fluorescent response [15]. However, self-absorption and the heavy-atom effect, which can be very significant in complex matrices, may hamper the application of fluorescence-based devices. In fact, in the analysis of real samples, the interference caused by other chromo- or fluorophores can drastically alter or hide the sensing of the target species. For this reason, the use of a single channel for the detection of the target analyte can lack a specific operational window, thereby making it necessary the use of another technique that can be defined as orthogonal to the former. In this context circular dichroism (CD) spectroscopy can offer better levels of detection compared with optical absorption and emission spectroscopies, and electrochemistry-based methods; in fact, it is frequently used in biosensing, where high sensitivities are required [16]. Moreover, it can be selective and free of interference from non-chiral species absorbing in the same region of the UV-Vis spectrum. Chiroptical sensors are an emerging class of molecular or nanoscale composites for the selective detection of a wide range of chemical and biological analytes. The appearance or the modulation of the CD spectroscopy signal resulting from the formation of a host-guest adduct represents the key channel of chiroptical readout [17]. We can divide chiroptical sensors in two different categories (Figure 2.2): i) CD silent chromophores that can interact with nonracemic chiral analytes thus resulting in a strong CD response; ii) CD active chiral chromophores that can sense achiral analytes upon modulation of the circular dichroism signal [18].
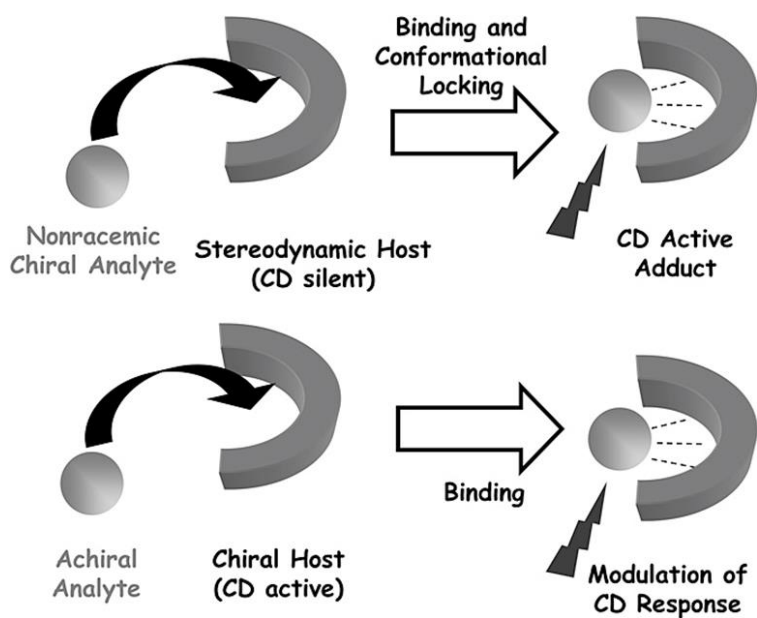
Figure 2.2 Main approaches of chiroptical sensors. From ref. [18].

The first class is applied, for instance, when the chiral guest does not possess any chromophore or fluorophore unit, and thus it cannot be monitored using UV-Vis. or fluorimetric spectroscopies. Since this kind of hosts can show different optical signals for the enantiomeric pairs of analytes, they became quite successful in the determination of absolute configuration, *ee* values and even reaction yields [19]. The second class of chiroptical sensors is instead particularly useful, as in our case, when an optical technique different from UV-Vis and fluorescence is needed to detect the target molecule. Axially-chiral π-extended compounds are particularly suitable for application in chiroptical sensing, since the expression of chirality is embedded into the chromophore, thus inducing ample CD activity.

There are several organic molecules that show atropoisomerism (*i.e.* the insurgence of chirality from limited rotation around an axis) but the most common ones are BINOL (1,1'-binaphthyl-2,2'-diol)-based compounds. BINOL-derivative probes exhibit a ''spring-like'' behaviour, with an intense CD signal modulation upon subtle changes in their conformation upon binding [20]. For example, in 2012 Pasini *et al*. reported a click-based macrocyclic receptor for chiroptical sensing of anions (**3**) with a methylated BINOL moiety embedded in the macrocycle skeleton as chiral probe (Figure 2.3). The Host-Guest complex was stabilized by hydrogen bonds between C-H triazole protons and spherical anions such as I⁻, Br⁻ and Cl⁻. Upon halide binding inside the receptor cavity in organic media, the BINOL group underwent conformational changes, generating a

modulation of its exciton-coupled initial signal. Even if the receptor selectivity was quite low, this example proved that when the receptor is properly designed, the binding of guests can promote a strong modulation of the CD signal and thus a chiroptical response [20b].
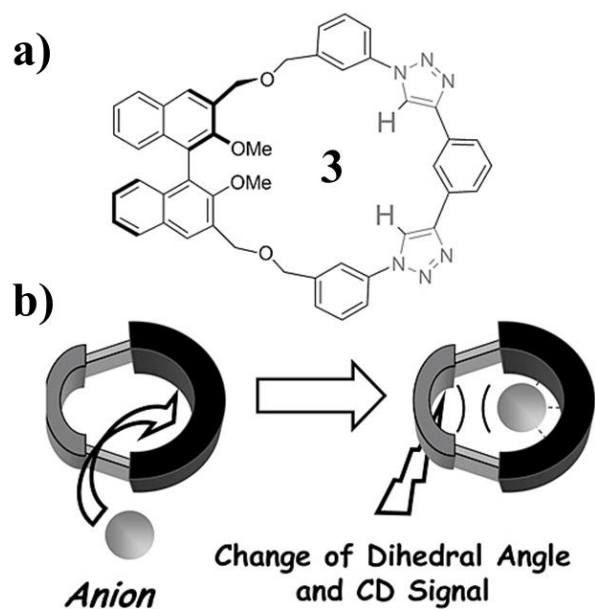

Figure 2.3 a) Structure of the macrocycle **3**. b) Induction of modulation of CD activity through secondary repulsive interaction. From ref. [18].

2.2 EXPERIMENTAL

2.2.1 Chemicals and Methods

All reagents for synthesis were purchased from Sigma-Aldrich and used without further purification. All reactions were performed under nitrogen. High-resolution mass spectra were recorded on a Sciex X500B QTOF System (Framingham, U.S.A.) operated in the ESI mode. ^{1}H- and ^{13}C-NMR spectra were recorded on a Bruker AVANCEIII 400 MHz (operating at 9.37 T, 400 MHz), equipped with a 5 mm BBO probe head with Z-gradient (Bruker BioSpin) or Bruker AMX 300 MHz. UV-Vis spectra were collected using a Varian Cary 50 SCAN spectrophotometer, with quartz cuvettes of the appropriate path length at 25.0 ± 0.1 °C. Emission spectra were collected using a Perkin Elmer LS50B fluorimeter, with a quartz cuvette of 1 cm path length. CD spectra were collected on a JASCO J1500 spectropolarimeter with quartz cuvettes of the appropriate path length at 25.0 ± 0.1 °C.

2.2.2 Synthesis of cages GB1 and GB2

The macrocyclic intermediate **4**, and the bisaldehydes (R)-3,3'-diformyl-1,1'-binaphthyl-2,2'-diol **5** and (R)-3,3'-diformyl-1,1'-binaphthyl-2,2'-dimethylether **6** were prepared following previously reported synthesis [14,21,22].

4

5: R = -H
6: R = -Me

1) MeOH, r.t., 12h
2) NaBH$_4$, MeOH, reflux, 12h

GB1: R = -H
GB2: R = -Me
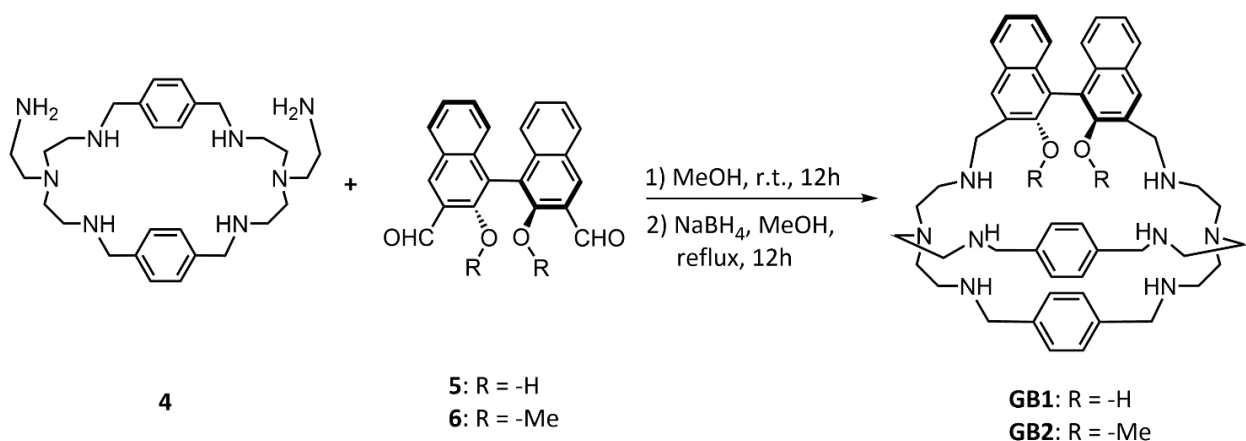
GB1. A solution of (*R*)-2,2′-dihydroxy-1,1′-binaphthyl-3,3′-dicarbaldehyde **5** (0.070 g; 0.205 mmol; 1.0 equiv) in MeOH (50 mL) was slowly added dropwise under N_2 to a solution of the macrocyclic intermediate **4** (0.102 g; 0.205 mmol; 1.0 equiv) dissolved in MeOH (100 mL), with continuous magnetic stirring at room temperature. The reaction mixture was stirred at room temperature under N_2 overnight. The solution was filtered to remove insoluble byproducts and then heated to reflux. $NaBH_4$ (0.155 g; 4.1 mmol; 20 equiv) was added in small portions in order to reduce imine bonds. After 12 h the mixture was cooled to room temperature and the solvent was evaporated under vacuum to give a white solid that was dissolved with brine (50 mL) and extracted with DCM (5 × 30 mL). The collected organic phases were then dried (Na_2SO_4), filtered and the solvent was evaporated under vacuum to obtain a dense brown oil (0.19 g) that was purified by precipitation as the nitrate salt. The free cage was dissolved in the minimum amount of EtOH and treated with conc. HNO_3 until precipitation of a solid. The solid was filtered and washed with EtOH and Et_2O. The free cage was then reobtained by dissolving the nitrate salt in basic water and extracting the aqueous mixture with DCM (6 × 25 mL). The collected organic phases were then dried (Na_2SO_4), filtered and evaporated under vacuum to yield **GB1** as a red solid (0.10 g, 60%). ^{1}H-NMR (400 MHz, D_2O + excess CF_3SO_3H) δ: 8.22 (s, 2H, *H₄*), 7.95 (d, 2H, *H₅*), 7.24-7.37 (m, 4H, *H₆₊₇*), 7.00-7.07 (m, 6H, *H₈₊ₚₕ*), 6.86 (d, 4H, *Hₚₕ*), 4.40+4.71 (m, 4H, *H₉*), 3.74-4.21 (m, 8H, *H₁₀₊₁₁*), 2.66-3.43 (m, 24H, N-(C*H₂*-C*H₂*-N)₃); ^{13}C-NMR (100 MHz, D_2O + excess CF_3SO_3H) δ: 43.93, 44.26, 44.73, 47.93, 48.90, 49.62, 50.00, 50.34, 50.62, 114.09, 120.18, 123.99, 124.96, 128.51, 128.74, 130.07, 130.20, 131.09, 131.21, 133.88, 134.44, 151.77; HRMS-ESI (CH_3CN) *m/z*: $[M + H]^+$ calculated for $C_{50}H_{62}N_8O_2$, 807.5068, found 807.5055.

GB2. A solution of (*R*)-2,2′-dimethoxy-1,1′-binaphthyl-3,3′-dicarbaldehyde **6** (0.060 g; 0.162 mmol; 1.0 equiv) in MeOH (50 mL) was slowly added dropwise under N_2 to a solution of the macrocyclic intermediate **4** (0.081 g; 0.162 mmol; 1.0 equiv) dissolved in MeOH (70 mL) with continuous magnetic stirring. The reaction mixture was stirred under N_2 at room temperature overnight. The MeOH solution was filtered to remove insoluble byproduct and then heated to reflux. $NaBH_4$ (0.130 g; 3.24 mmol; 20 equiv) was added in small portions in order to reduce imine bonds. After 12 h, the mixture was cooled to room temperature and the solvent was evaporated under vacuum to give a white solid that was dissolved with brine (30 mL) and extracted with DCM (5 × 20 mL). The collected organic phases were dried (Na_2SO_4), filtered and the solvent was

evaporated under vacuum to obtain a dense brown oil (0.15 g) that was purified by precipitation of the nitrate salt. The free cage was dissolved in the minimal amount of EtOH and treated with conc. HNO_3 until precipitation of a solid. The solid was filtered and washed with EtOH and Et_2O. The free cage was then reobtained by dissolving the nitrate salt in basic water and extracting the aqueous mixture with DCM (6×25 mL). The collected organic phases were then dried (Na_2SO_4), filtered and evaporated under vacuum to yield **GB2** as a yellow solid (0.07 g, 52%). ^{1}H-NMR (300 MHz, D_2O + excess CF_3SO_3H) δ: 8.16 (s, 2H, H_4), 7.92 (d, 2H, H_5), 6.91-7.45 (m, 10H, $H_{6+7+8+ph}$), 6.83 (d, 4H, H_{ph}), 4.29-4.59 (m, 4H, H_9), 3.75-4.16 (m, 8H, H_{10+11}), 3.13 (s, 6H, H_{12}), 2.47-3.03(m, 24H, N-(CH_2-CH_2-N)$_3$); ^{13}C-NMR (100 MHz, D_2O + excess CF_3SO_3H) δ: 44.16, 44.36, 44.54, 44.74, 47.93, 49.34, 49.71, 50.52, 50.64, 60.94, 123.46, 123.54, 123.67, 125.58, 126.38, 128.50, 129.98, 130.24, 131.22, 131.77, 133.17, 135.04, 154.32; HRMS-ESI (CH_3CN) *m/z*: [M + H]$^+$ calculated for $C_{52}H_{66}N_8O_2$, 835.5381, found 835.5382.

2.2.3 Potentiometric Titrations

Potentiometric titrations were performed in water-methanol mixtures (35% v/v and 70% v/v for **GB1** and **GB2**, respectively) because of the low solubility of both cages in pure aqueous solution. Either $NaNO_3$ or tetrabutylammonium nitrate ($TBANO_3$) were employed as supporting electrolytes at 0.025 M concentration. In a typical experiment, 15 mL of the receptor solution (5×10^{-4} M) was treated with excess HNO_3 (1.0 M). Titrations were performed by addition of 10 μL aliquots of carbonate-free standard 0.1 M NaOH, recording 80-100 points for each titration. Prior to each potentiometric titration, the standard electrochemical potential (E°) of the glass electrode was determined in the proper solvent mixture by a titration experiment according to the Gran method. Protonation titration data (emf vs mL of NaOH) were processed with the HyperQuad package to estimate the equilibrium constants [23].

2.2.4 Spectrophotometric, Spectrofluorimetric and CD Titrations

All titrations were performed in aqueous solution (0.05 M CF_3SO_3Na) at 25 °C and the pH of the solution was set to 2 by addition of concentrated CF_3SO_3H. For the determination of binding constants, receptor solutions were titrated with 1000-fold more concentrated solutions of the anions as sodium salts. After each addition of sub-stoichiometric amount of the anion, spectra were recorded using quartz cuvettes (UV-Vis. and CD, path length: 0.1 cm; fluorimetry, path length: 1 cm). Titration data were processed with the Hyperquad package to determine the equilibrium constants [23].

2.2.5 ^{1}H-NMR Titrations

All measurements were performed at 25 °C in a solution of D_2O (0.05 M CF_3SO_3Na), the pH of the solution was set to 2 by addition of concentrated CF_3SO_3H in D_2O. For the determination of binding constants, receptor was titrated with a 15-fold more concentrate solution of the anion. After each addition of sub-stoichiometric amount of the anion in the NMR tube containing 0.75 mL of receptor solution, ^{1}H-NMR spectra were recorded. Titration data were processed with HypNMR (Hyperquad package) to determine the equilibrium constants [23].

2.2.6 Computational Studies

All the calculations were carried out with the Gaussian 09 program package within the density functional approach at the B3LYP level with the 6-31G(d) basis set for all atoms except the effective core potential LanL2DZ basis set used for rhenium [24]. The free cages were modeled as hexavalent cations whereas for the perrhenate complexes an overall +5 charge was considered. The solvent effect was considered by using a self-consistent reaction field (SCRF) method, based on the polarizable continuum model (PCM), choosing water as the solvent.

2.2.7 Preparation of Complex Matrices

Commercial pineapple-lime juice was diluted (10×) and acidified with aqueous CF_3SO_3H until pH 2. The obtained solution was employed as solvent mixture for the preparation of standard solutions of both the receptor and sodium perrhenate. On the other hand, artificial urine medium (AUM) was prepared by dissolving the components reported in Table 2.2 in demineralized water [25]. The obtained solution was diluted (30×) and acidified with aqueous CF_3SO_3H until pH 2. The final mixture was employed in the preparation of the samples for CD titrations experiments. The pH value was checked before and after titrations.

Table 2.2 Components of AUM dissolved in demineralized water.

Component	Concentration	After dilution 30×
Citric acid	2 mM	$6.7 \; 10^{-5}$ M
Sodium chloride	90 mM	3 mM
L-glutamine	2 mM	$6.7 \; 10^{-5}$ M
Urea	170 mM	5.7 mM
Creatinine	7 mM	$2.3 \; 10^{-4}$ M
Calcium chloride · $2H_2O$	0.25 mM	$8.3 \; 10^{-6}$ M
Magnesium sulphate · $7H_2O$	2 mM	$6.7 \; 10^{-5}$ M
Sodium sulphate · $10H_2O$	10 mM	$3.3 \; 10^{-4}$ M
Sodium nitrate	6 mM	$2 \; 10^{-4}$ M
Potassium dihydrogen phosphate	1.8 mM	$6 \; 10^{-5}$ M

2.3 RESULTS AND DISCUSSION

2.3.1 Design of the Cages

With respect to macrocyclic receptors, organic cages can virtually increase the selectivity for target guests providing a more preorganized and complementary cavity, but chiral cages are quite rare and their applications in sensing of anions are limited to organic solvents [26]. To overcome these problems we designed an asymmetric bis-tren cage (**GB1**) with a BINOL unit embedded in the structure. This macrobicyclic molecule is soluble in acidic aqueous media when all the secondary amines are protonated and can thus act as chiroptical anion sensor. Cages **GB1** and **GB2** (Figure 2.4) have been synthesized in high yields using a reductive amination protocol from an ''open-shell'' bis-tren precursor and enantiopure (R)-3,3'-diformyl-1,1'-binaphthyl-2,2'- diol or (R)-3,3'-diformyl-1,1'-binaphthyl-2,2'-dimethylether, respectively.
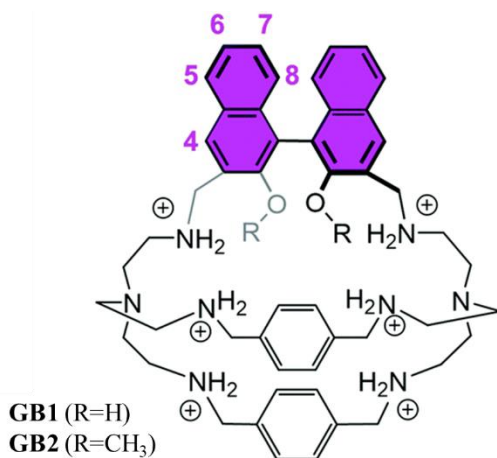

Figure 2.4 Structures of **GB1** and **GB2** in their hexaprotonated form (relevant protons are labelled in pink).

The greater distance between the two reactive aldehyde groups in the 3,3' positions of the binaphthyl spacers (ca. 8 Å) respect to that of 1,4-substituted phenyl spacers (6 Å) does not suppress the possibility of efficient macrocyclization, and results in only a slight distortion of the molecular system, with accessible cavities for both cages and an overall C2 symmetry imparted by the chiral element. The (R)-BINOL moiety has a double role: on the one hand, it can serve as the

signalling unit, due to both the strong variation of CD spectra and the modulation of its fluorescent emission in response to a binding event. On the other hand, the BINOL unit has H-bonding groups directed toward the cavity, and can cooperate with the positively charged NH_2^+ donors in the binding process. The active role of the BINOL OH groups as H-bonding donors is unravelled by comparing the binding properties of **GB1** with those of the methylated analogue system **GB2**.

2.3.2 Theoretical Calculations

A theoretical approach was used to give useful suggestions into the conformational preferences of the receptors **GB1** and **GB2**, and their complexes with perrhenate anion, $[\textbf{GB1}H_6(ReO_4)]^{5+}$ and $[\textbf{GB2}H_6(ReO_4)]^{5+}$. For the free cages, due to their high flexibility, several different conformers were found. The two most stable conformers of each compound are reported in figure 2.5. The global minima of the two hexaprotonated cages (*i.e.* $[\textbf{GB1}H_6]^{6+}$ and $[\textbf{GB2}H_6]^{6+}$) are quite different: **GB1a** has a rounder shape, while **GB2a** is more elongated with the binaphthyl moiety positioned apart from the remaining portion of the structure. Moreover, the dihedral angle between the planes of the naphthyls is about 30 degrees larger, in the case of **GB1a,** than for **GB2a**. It is worthy pointing out the similarity between conformer **GB2b** and conformer **GB1a** as well as that of **GB1b** with **GB2a**. Though the two most stable conformer of each cage show a similar geometry, the stability order is reversed.
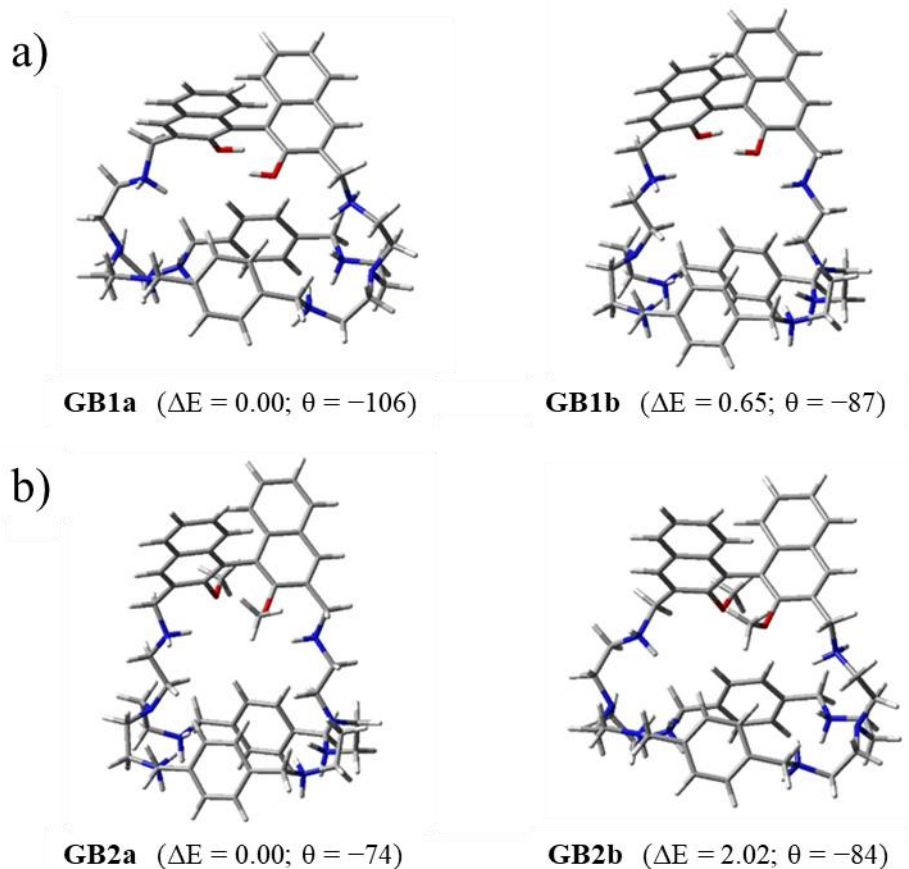
a)

GB1a ($\Delta E = 0.00$; $\theta = -106$)   **GB1b** ($\Delta E = 0.65$; $\theta = -87$)

b)

GB2a ($\Delta E = 0.00$; $\theta = -74$)   **GB2b** ($\Delta E = 2.02$; $\theta = -84$)

Figure 2.5 a) Three-dimensional plots of the preferred conformers of **GB1** in its hexaprotonated form. b) Three-dimensional plots of the preferred conformers of **GB2** in its hexaprotonated form. In parentheses the relative energy ΔE (kcal/mol) and the dihedral angle $\theta_{2\text{-}1\text{-}1'\text{-}2'}$ (°).

As for the perrhenate complexes $[\textbf{GB1}H_6(ReO_4)]^{5+}$ and $[\textbf{GB2}H_6(ReO_4)]^{5+}$, a large numbers of possible conformers were found: the three most stable ones are reported in figure 2.6. In the stable conformer $[\textbf{GB1a}H_6(ReO_4)]^{5+}$, the two naphthylic hydroxyl groups are hydrogen-bonded to two different oxygen atoms of the included anion. Several H-bonds with the protonated amines are also involved in the stabilization of the adduct. In this conformer, the cage geometry is quite similar to that of the free cage, **GB1a**, with some variation in the dihedral angle of the binaphthyl unit. Conversely, in the case of receptor **GB2,** the binaphthyl moiety does not give any contribution to the complexation of perrhenate, which, in the preferred conformer $[\textbf{GB2a}H_6(ReO_4)]^{5+}$, lies on the lower side of the cage.

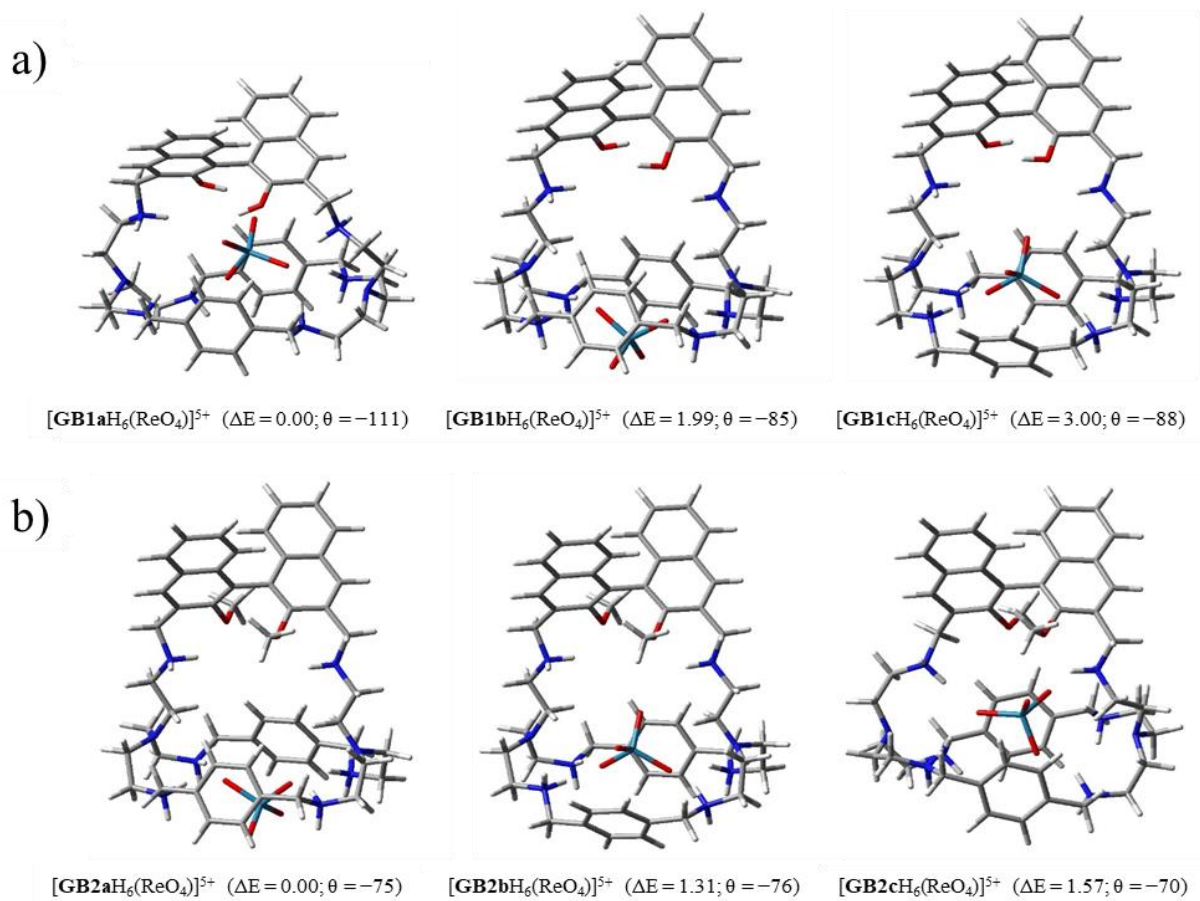**Figure 2.6** a) Three-dimensional plots of the preferred conformers of $[\mathbf{GB1}H_6(ReO_4)]^{5+}$. b) Three-dimensional plots of the preferred conformers of $[\mathbf{GB2}H_6(ReO_4)]^{5+}$. In parentheses the relative energy ΔE (kcal/mol) and the dihedral angle $\theta_{2\text{-}1\text{-}1'\text{-}2'}$ (°).

These calculations showed significant differences in the preferred geometry of $[\mathbf{GB1}H_6(ReO_4)]^{5+}$ and $[\mathbf{GB2}H_6(ReO_4)]^{5+}$, in which the BINOL moiety does not participate in the binding process. These results are in line with the CD titration results with $NaReO_4$, which showed that the anion inclusion by $[\mathbf{GB2}H_6]^{6+}$ does not cause any modification in the exciton couplet of the binaphthyl unit (see chapter 2.3.5).

2.3.3 Potentiometric Titrations

Because of the scarce solubility in pure water, the determination of the acid/base properties of **GB1** and **GB2** through potentiometric titrations were performed in aqueous mixtures, containing 35% and 70% (v/v) MeOH, respectively. In accordance with previous studies, the most suitable form for ReO_4^- binding is the one presenting all the secondary amino groups protonated: $[\mathbf{GB1}H_6]^{6+}$ and $[\mathbf{GB2}H_6]^{6+}$ [13,21]. For both cages, six protonation equilibria were found, and the $[H_6\mathbf{L}]^{6+}$ form prevails at pH 2. The corresponding protonation constants and distribution diagrams of the species for **GB1** and **GB2** are reported in table 2.3, and figures 2.7 and 2.8, respectively. We can consider that $[H_6\mathbf{L}]^{6+}$ is the main species at pH 2 also in 100% H_2O (*i.e.* the medium used for investigations with anions), as already observed in previous studies on bis-tren azacryptands [14,27]. In these pH conditions, the solubility of the cages was high enough (> 1 mM) to allow anion binding studies to be performed in pure aqueous media.

Table 2.3 Protonation constants obtained through potentiometric titrations at 25 °C in H_2O:MeOH mixtures (65:35 v/v, 0.025 M $NaNO_3$ for **GB1** and 30:70 v/v, 0.025 M $TBANO_3$ for **GB2**).

CAGE GB1	Logβ
$\mathbf{L} + \mathbf{H}^+ = \mathbf{HL}^+$	10.57(1)
$\mathbf{L} + 2\ \mathbf{H}^+ = \mathbf{H_2L}^{2+}$	20.58(2)
$\mathbf{L} + 3\ \mathbf{H}^+ = \mathbf{H_3L}^{3+}$	29.17(2)
$\mathbf{L} + 4\ \mathbf{H}^+ = \mathbf{H_4L}^{4+}$	35.60(3)
$\mathbf{L} + 5\ \mathbf{H}^+ = \mathbf{H_5L}^{5+}$	41.73(4)
$\mathbf{L} + 6\ \mathbf{H}^+ = \mathbf{H_6L}^{6+}$	47.95(4)

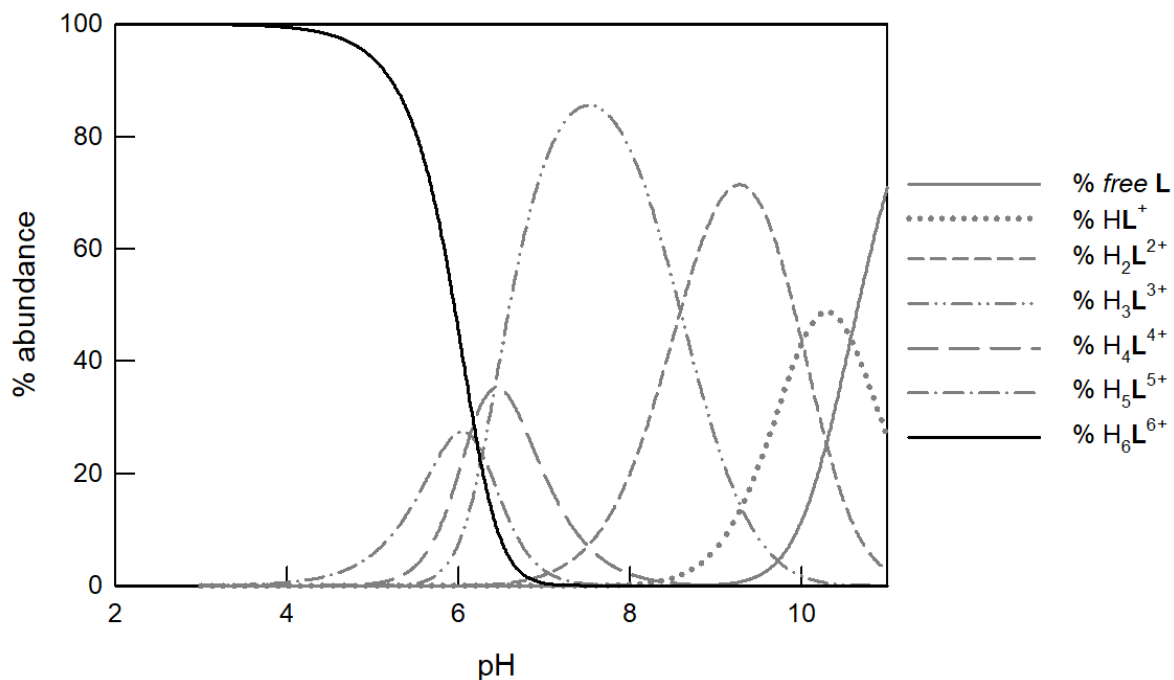| CAGE GB2	Logβ
$\mathbf{L} + \mathbf{H}^+ = \mathbf{HL}^+$	9.77(2)
$\mathbf{L} + 2\ \mathbf{H}^+ = \mathbf{H_2L}^{2+}$	18.01(3)
$\mathbf{L} + 3\ \mathbf{H}^+ = \mathbf{H_3L}^{3+}$	25.36(3)
$\mathbf{L} + 4\ \mathbf{H}^+ = \mathbf{H_4L}^{4+}$	31.43(4)
$\mathbf{L} + 5\ \mathbf{H}^+ = \mathbf{H_5L}^{5+}$	37.14(4)
$\mathbf{L} + 6\ \mathbf{H}^+ = \mathbf{H_6L}^{6+}$	40.47(3)

Figure 2.7 Distribution diagram of the species (% abundance *vs*. pH) of **GB1** in H_2O:MeOH (65:35 v/v), 0.025 M $NaNO_3$; T = 25 °C.
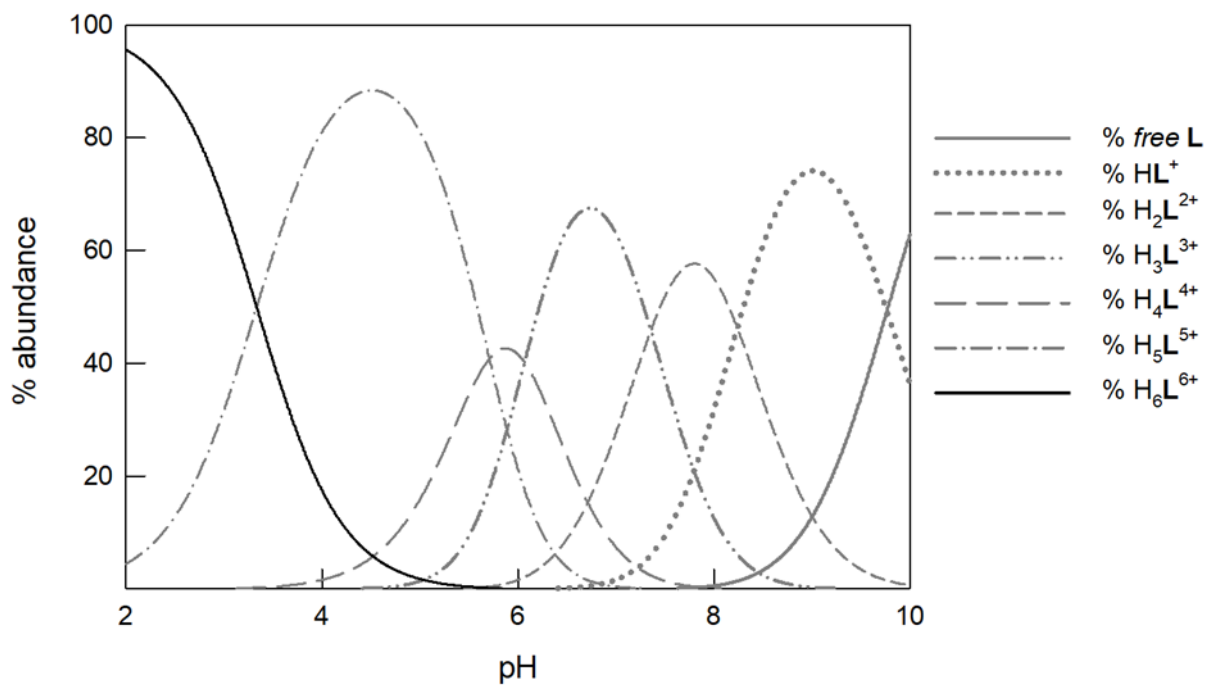

Figure 2.8 Distribution diagram of the species (% abundance *vs*. pH) of **GB2** in H_2O:MeOH (30:70 v/v), 0.025 M $TBANO_3$; T = 25 °C.

2.3.4 UV-Vis Titrations

Anion binding was found to have very little effect on the UV-Vis spectrum of $[\mathbf{GB1}H_6]^{6+}$. The receptor showed the typical absorption band of the binaphthyl chromophore (λ_{max} = 229 nm), attributable to the π-π* transition, and a less intense band around 320 nm. As it can be seen in figures 2.9 and 2.10, changes were negligible or attributable to the residual absorbance of the added analyte so that reliable binding constants for the studied anions (ReO_4^-, SO_4^{2-}, ClO_4^-, NO_3^- and Cl^- as their sodium salts) could not be calculated. For example, in the case of ReO_4^- (Figure 2.10) a linear increase of the absorbance around 215 nm was observed during titration, due to the absorption of the anion itself.
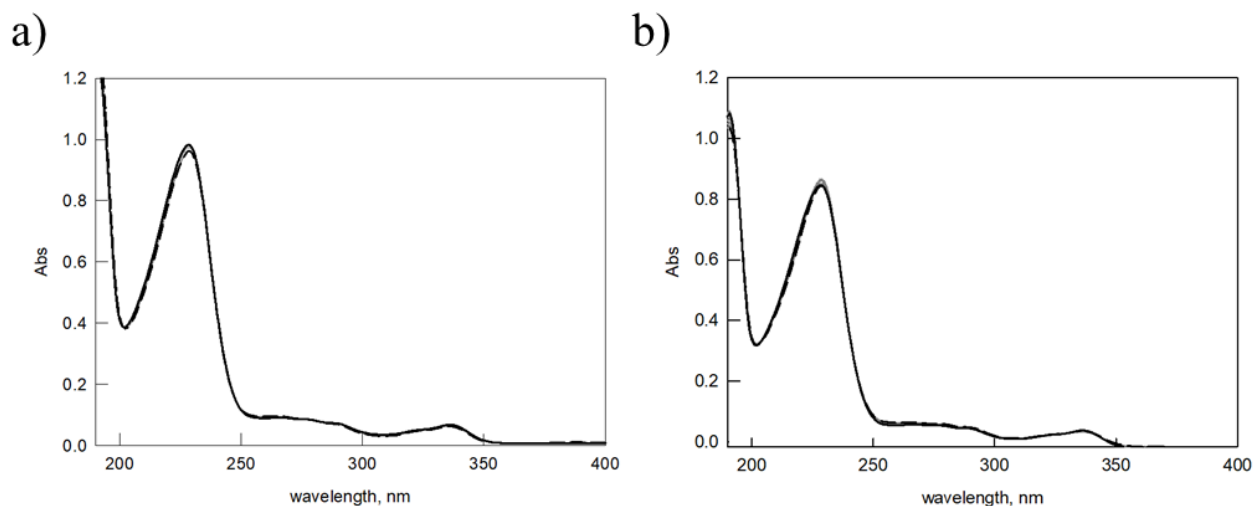

Figure 2.9 a) UV-Vis. spectra recorded over the titration of an aqueous solution of $[\mathbf{GB1}H_6]^{6+}$ (0.1 mM, path length = 0.1 cm) with NaCl at pH=2. b) UV-Vis. spectra recorded over the titration of an aqueous solution of $[\mathbf{GB1}H_6]^{6+}$ (0.1 mM, path length = 0.1 cm) with Na_2SO_4 at pH=2. Solid and dashed lines: initial and final spectra, respectively.
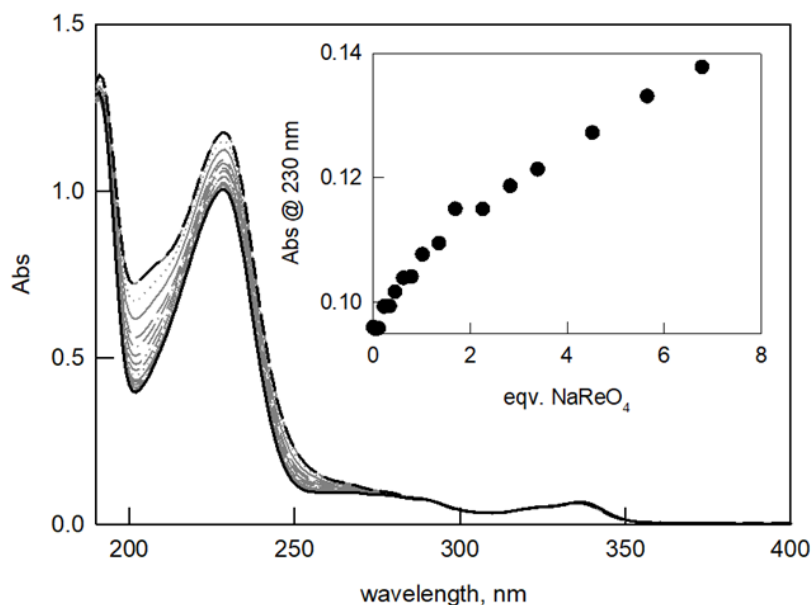
Figure 2.10 UV-Vis. spectra recorded over the titration of an aqueous solution of $[\mathbf{GB1}H_6]^{6+}$ (0.1 mM, path length = 0.1 cm) with NaReO$_4$ at pH=2. Solid and dashed lines: initial and final spectra, respectively.

2.3.5 CD Titrations

CD titrations were instead much more revealing. The CD spectrum of the free receptor $[\mathbf{GB1}H_6]^{6+}$ displays the typical exciton couplet of the binaphthyl systems centred at 230 nm ($\Delta\varepsilon_{225}/\Delta\varepsilon_{235} = +49/-55$ M^{-1} cm^{-1}), and a lower energy band around 320 nm (+7 M^{-1} cm^{-1}), also typical of the chiral chromophore. The exciton couplet is strongly affected by the added anion: in particular, ReO$_4^-$ promotes a slight blue-shift of the component at higher energy, and a remarkable increase of the intensity at both 222 and 235 nm (Figures 2.11 and 2.12).
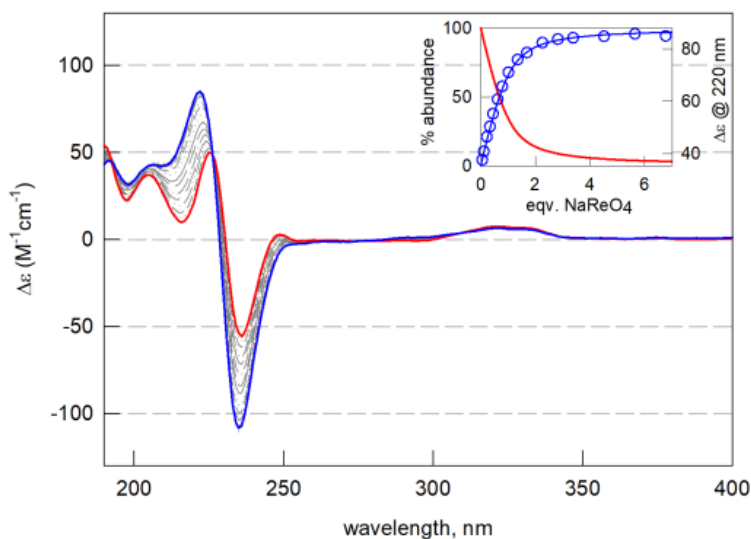
Figure 2.11 CD titration of [**GB1**H$_6$]$^{6+}$ (0.1 mM in 0.05M CF$_3$SO$_3$Na, pH 2) with NaReO$_4$ (red and blue lines: initial and final spectra, respectively). Inset: distribution diagram of the species (red line: % free [**GB1**H$_6$]$^{6+}$; blue line: % [**GB1**H$_6$(ReO$_4$)]$^{5+}$), superimposed to the experimental profile (circles).
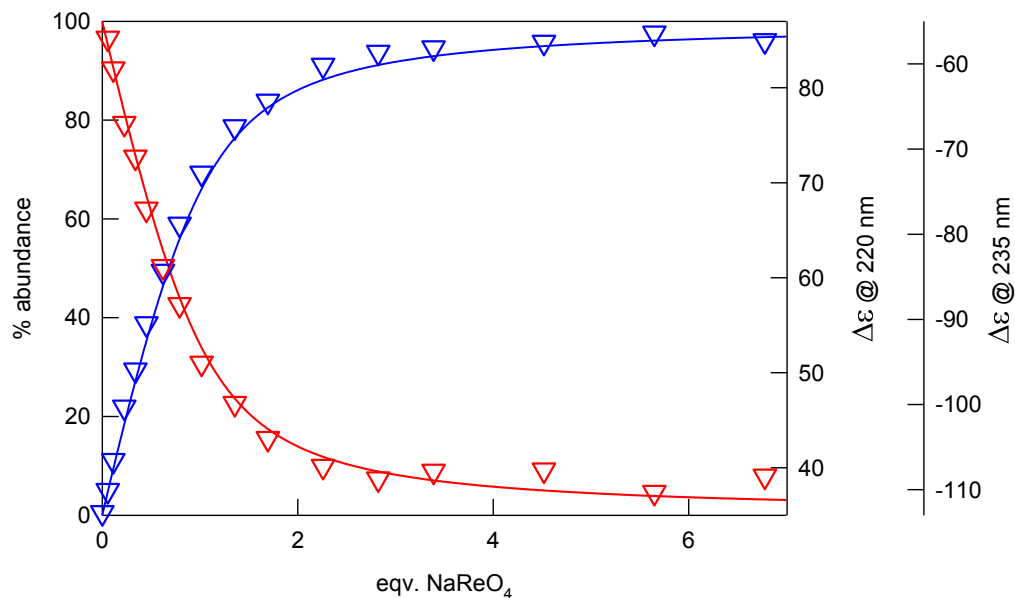

Figure 2.12 CD titration of [**GB1**H$_6$]$^{6+}$ with NaReO$_4$ in aqueous solution at pH 2. Distribution diagram of the species (red line: % free [**GB1**H$_6$]$^{6+}$; blue line: % [**GB1**H$_6$(ReO$_4$)]$^{5+}$), superimposed to the experimental profiles of $\Delta\varepsilon$ (M^{-1} cm^{-1}) *vs.* equivalents of NaReO$_4$. Blue and red symbols: experimental profiles of $\Delta\varepsilon$, taken at 220 and 235 nm, respectively.

The CD band around 320 nm is also affected by perrhenate addition, but the intensity variations are lower than those observed around 230 nm (Figure 2.13).
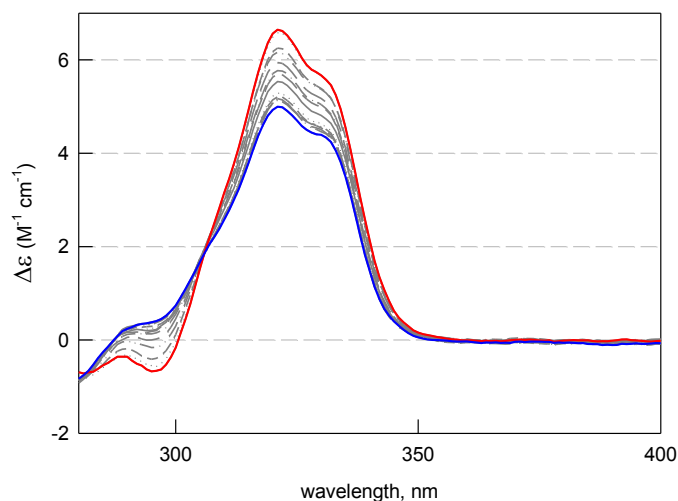

Figure 2.13 Partial CD spectra (recorded between 280 and 400 nm) taken over titration of $[\textbf{GB1}H_6]^{6+}$ (0.1 mM) with NaReO$_4$ in aqueous solution at pH 2 (path length = 1 cm); red and blue lines correspond to the initial and final spectra, respectively.

Changes in intensity of the principal binaphthyl band were also found with the other investigated anions (Figures 2.14 - 2.17). In these cases, the variations were similar but lower in magnitude, pointing out a selectivity trend that increases towards ReO$_4^-$.
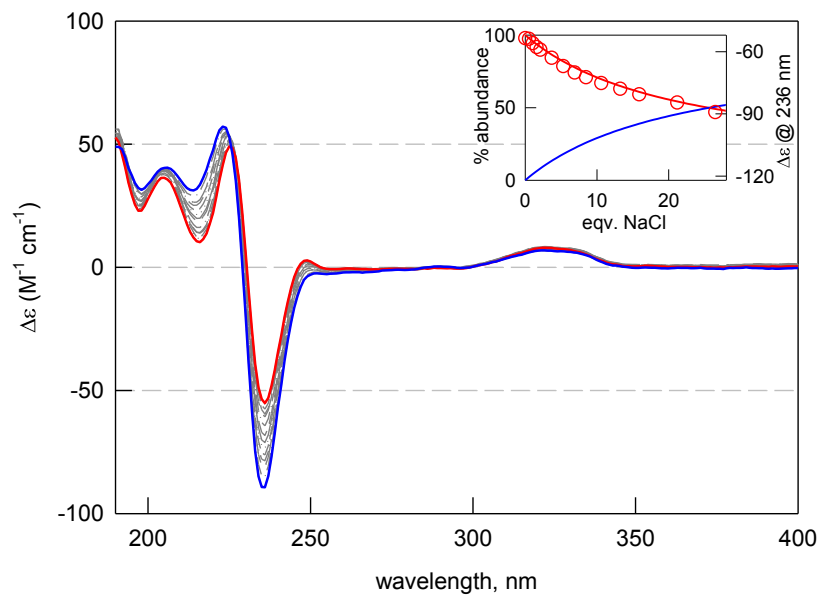
Figure 2.14 CD spectra taken over the titration of [**GB1**H$_6$]$^{6+}$ (0.1 mM) with NaCl in aqueous solution at pH 2; red and blue lines correspond to the initial and final spectra, respectively. Inset: distribution diagram of the species (red line: % free of [**GB1**H$_6$]$^{6+}$; blue line: % of [**GB1**H$_6$(Cl)]$^{5+}$), superimposed to the experimental profile of $\Delta\varepsilon$ (M^{-1} cm^{-1}) at 236 nm *vs.* equivalents of NaCl.

Figure 2.15 CD spectra taken over the titration of [**GB1**H$_6$]$^{6+}$ (0.1 mM) with Na$_2$SO$_4$ in aqueous solution at pH 2; red and blue lines correspond to the initial and final spectra, respectively. Inset: distribution diagram of the species (red line: % free [**GB1**H$_6$]$^{6+}$; blue line: % [**GB1**H$_6$(SO$_4$)]$^{4+}$), superimposed to the experimental profile of $\Delta\varepsilon$ (M^{-1} cm^{-1}) at 236 nm *vs.* equivalents of Na$_2$SO$_4$.
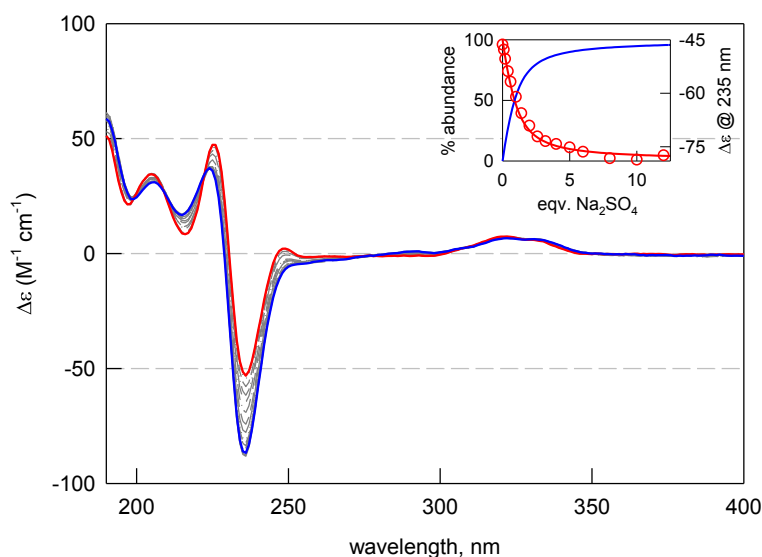
Figure 2.16 CD spectra taken over the titration of [**GB1**H$_6$]$^{6+}$ (0.1 mM) with NaNO$_3$ in aqueous solution at pH 2; red and blue lines correspond to the initial and final spectra, respectively. Inset: distribution diagram of the species (red line: % free [**GB1**H$_6$]$^{6+}$; blue line: % [**GB1**H$_6$(NO$_3$)]$^{5+}$), superimposed to the experimental profile of Δε (M^{-1} cm^{-1}) at 226 nm *vs.* equivalents of NaNO$_3$.
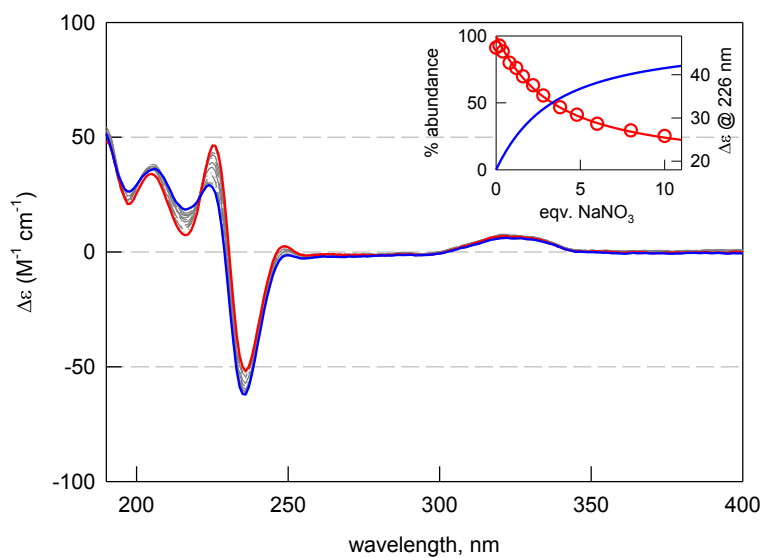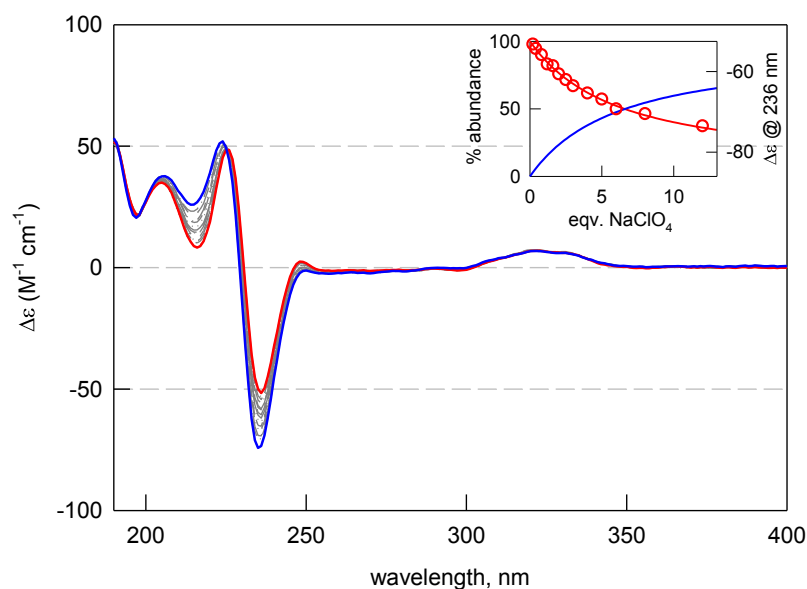

Figure 2.17 CD spectra taken over the titration of [**GB1**H$_6$]$^{6+}$ (0.1 mM) with NaClO$_4$ in aqueous solution at pH 2; red and blue lines correspond to the initial and final spectra, respectively. Inset: distribution diagram of the species (red line: % free [**GB1**H$_6$]$^{6+}$; blue line: % [**GB1**H$_6$(ClO$_4$)]$^{5+}$), superimposed to the experimental profile of Δε (M^{-1} cm^{-1}) at 236 nm *vs.* equivalents of NaClO$_4$.

The selectivity of $[\mathbf{GB1}H_6]^{6+}$ for ReO_4^- can be easily seen from the comparison of the intensity changes at 223 and 235 nm upon titration with different anions (Figure 2.18). A remarkable enhancement (+240%) of the component at 223 nm was observed along with a decrease (−200%) of the component at 235 nm. The logarithmic binding constants calculated by CD titrations are reported in table 2.4.
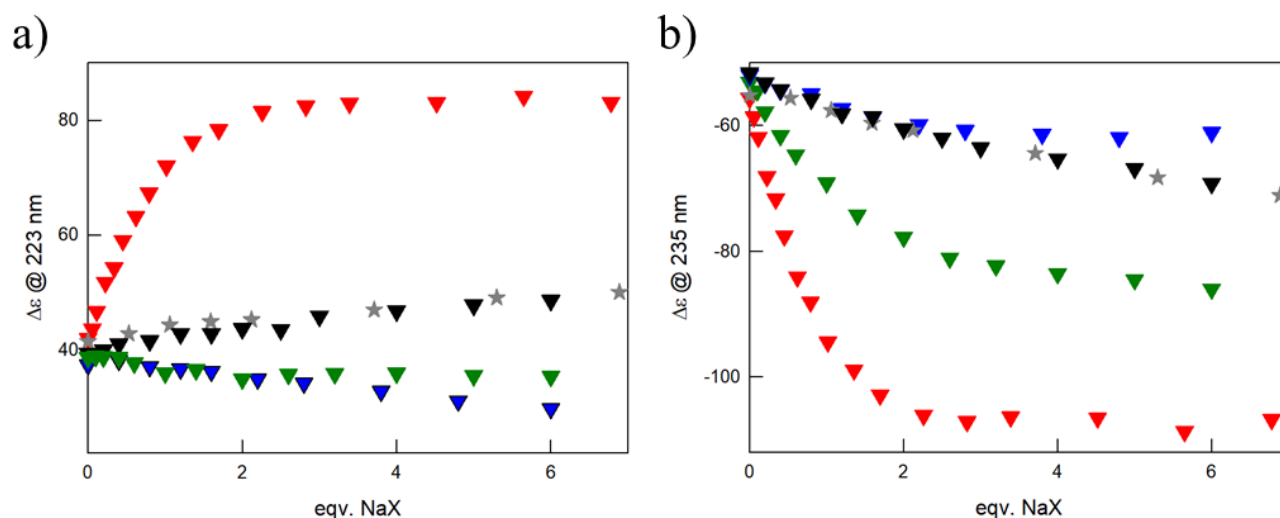

Figure 2.18 Experimental titration profiles of $\Delta\varepsilon$ (M^{-1} cm^{-1}) at a) 223 and b) 235 nm *vs.* equivalents of the added NaX. The profiles were obtained from the CD titrations of $[\mathbf{GB1}H_6]^{6+}$ (0.1 mM) with solutions of different sodium salts (symbols: red, $NaReO_4$; blue, $NaNO_3$; green, Na_2SO_4; black triangles, $NaClO_4$; grey stars, NaCl).

Table 2.4 Anion binding constants ($LogK_{11}$) determined for $[\mathbf{GB1}H_6]^{6+}$ in aqueous solution, 0.05M CF_3SO_3Na at pH 2 (by addition of CF_3SO_3H), using CD titrations. Uncertainty on the last figure is represented in parenthesis.

NaX	$LogK_{11}^{CD}$
$NaReO_4$	4.74(2)
Na_2SO_4	4.10(1)
$NaClO_4$	3.20(3)
$NaNO_3$	3.55(2)
NaCl	2.61(2)

The large enhancement of the exciton couplet can be explained with i) a subtle change of the dihedral angle θ between the naphthyl planes of the binaphthyl chromophore following anion binding (see chapter 2.3.2), and ii) the H-bonding interactions established between the OH groups of BINOL and ReO_4^- [20,28].

The decisive role of the hydroxyl groups was confirmed by comparing the anion binding capabilities of [**GB1**H_6]$^{6+}$ with those of the methylated analogue, [**GB2**H_6]$^{6+}$. For this latter, the anion-induced changes during the CD titrations are considerably smaller. In particular, the CD spectra recorded in the presence of 10 eqv. NaX are almost superimposable to the spectrum of the free cage [**GB2**H_6]$^{6+}$ (Figure 2.19), thus testifying the negligible effect of the anions on the binaphthyl moiety.
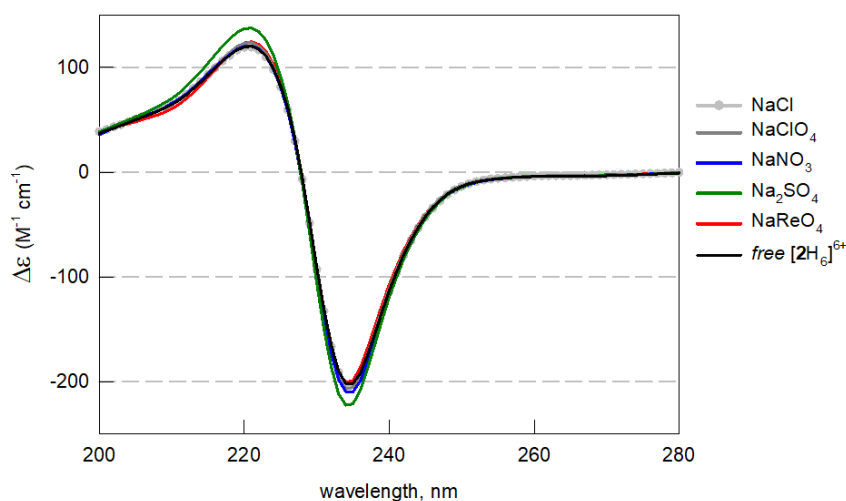

Figure 2.19 CD spectra taken on [**GB2**H_6]$^{6+}$ in aqueous solution at pH 2 (0.1 mM) alone (black line) and in presence of 10 eqv. sodium salts.

2.3.6 Fluorimetric Titrations

Emission spectroscopy was employed in the anion binding studies. Under excitation at 284 nm, the aqueous solution of $[\mathbf{GB1}H_6]^{6+}$ at pH 2 shows a fluorescence emission around 370 nm. ReO_4^- and SO_4^{2-} anions were found to promote a partial quenching of the emission, with 30% intensity reduction, while other anions showed a significantly lower effect (Figures 2.20 - 2.22). The logarithmic binding constants obtained from spectrofluorimetric titrations were therefore calculated for ReO_4^- and SO_4^{2-} only (Table 2.5).
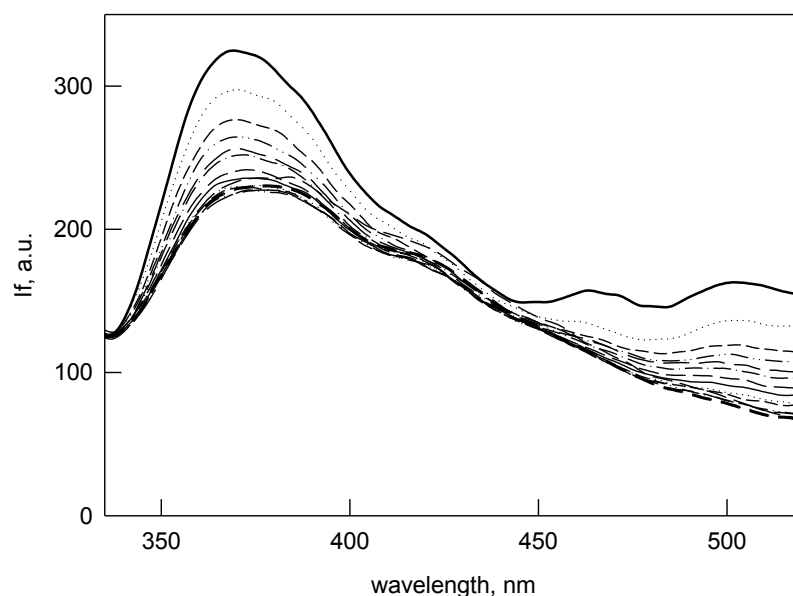

Figure 2.20 Emission spectra (Intensity in arbitrary units *vs.* wavelength) recorded over the spectrofluorimetric titration of an aqueous solution of $[\mathbf{GB1}H_6]^{6+}$ (5 μM, λ_{exc} = 284 nm) with NaReO$_4$ at pH=2. Solid and dashed lines: initial and final spectra, respectively.
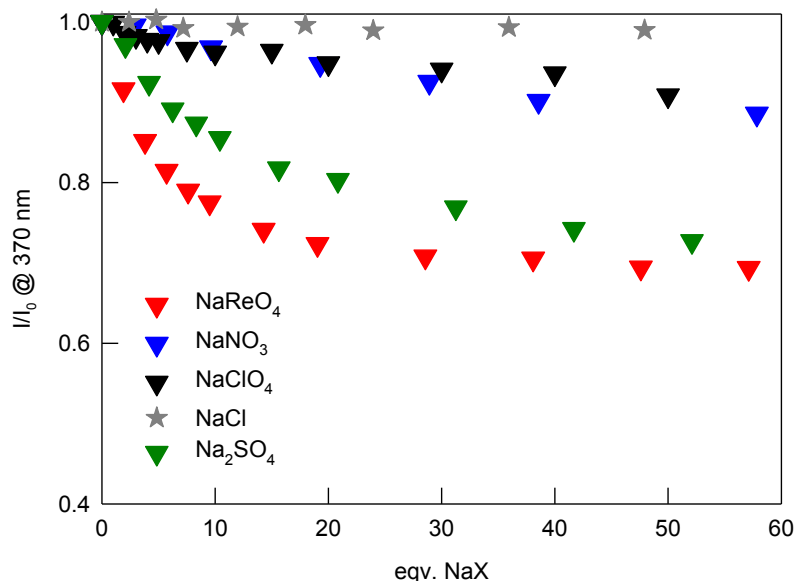
Figure 2.21 Profiles of the normalized intensity (I/I_0) at 370 nm *vs.* equivalents of the added NaX. The experimental profiles are relative to spectrofluorimetric titrations on $[\mathbf{GB1}H_6]^{6+}$ (5 µM in 0.05M CF_3SO_3Na, pH 2, λ_{exc} = 284 nm) with various sodium salts. The titrant solutions were prepared in the same solvent medium as that used for the receptor.

Figure 2.22 Profiles of the normalized intensity (I/I_0 at 370 nm) *vs.* equivalents of the added NaX, obtained from the spectrofluorimetric titrations of the $[\mathbf{GB1}H_6]^{6+}$ receptor (5 µM in 0.05M CF_3SO_3Na, λ_{exc} = 284 nm) with a) $NaReO_4$ and b) Na_2SO_4. Experimental profiles are superimposed to the distribution diagrams calculated for a) $\log K_{11}$ = 4.70 and b) 4.21.

Table 2.5 Anion binding constants ($LogK_{11}$) determined for $[\mathbf{GB1}H_6]^{6+}$ in aqueous solution, 0.05M CF_3SO_3Na at pH 2 (by addition of CF_3SO_3H), using spectrofluorimetric titrations. Uncertainty on the last figure is represented in parenthesis. *n.a.*: not available

NaX	$LogK_{11}^{CD}$
NaReO$_4$	4.70(1)
Na$_2$SO$_4$	4.21(4)
NaClO$_4$	*n.a.*
NaNO$_3$	*n.a.*
NaCl	*n.a.*

Under excitation of $[\mathbf{GB2}H_6]^{6+}$ at 284 nm, an intense emission band (λ_{max} = 360 nm), sensitive to ReO_4^- and SO_4^{2-} anions, was observed. The obtained binding constants (4.19(3) and 3.72(2) log units, for ReO_4^- and SO_4^{2-}, respectively; see Figures 2.23 - 2.26) indicate a lower anion affinity compared to the non-methylated system $[\mathbf{GB1}H_6]^{6+}$. Such reduced affinities, combined with the reduced CD responses to anions, confirm the active cooperation of the BINOL-OH groups in $[\mathbf{GB1}H_6]^{6+}$ in the anion binding.
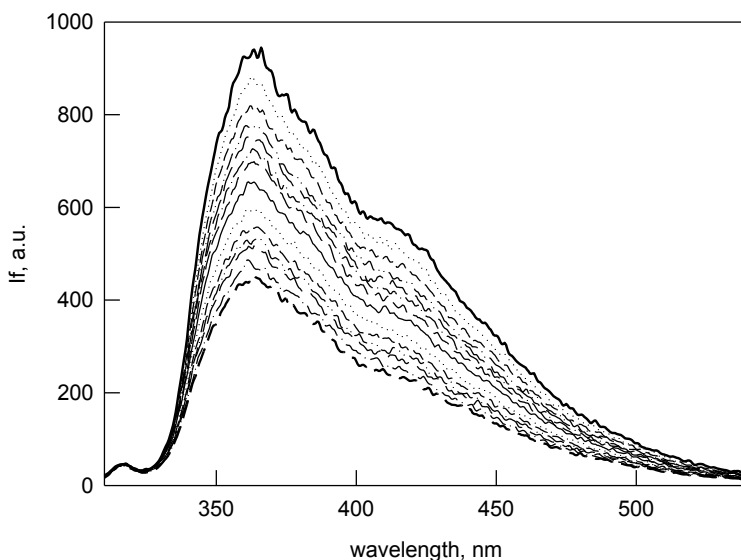
Figure 2.23 Emission spectra (Intensity in arbitrary units *vs.* wavelength) recorded over the spectrofluorimetric titration of an aqueous solution of $[\mathbf{GB2}H_6]^{6+}$ (5 μM, λ_{exc} = 284 nm) with NaReO$_4$ at pH = 2. Solid and dashed lines: initial and final spectra, respectively.
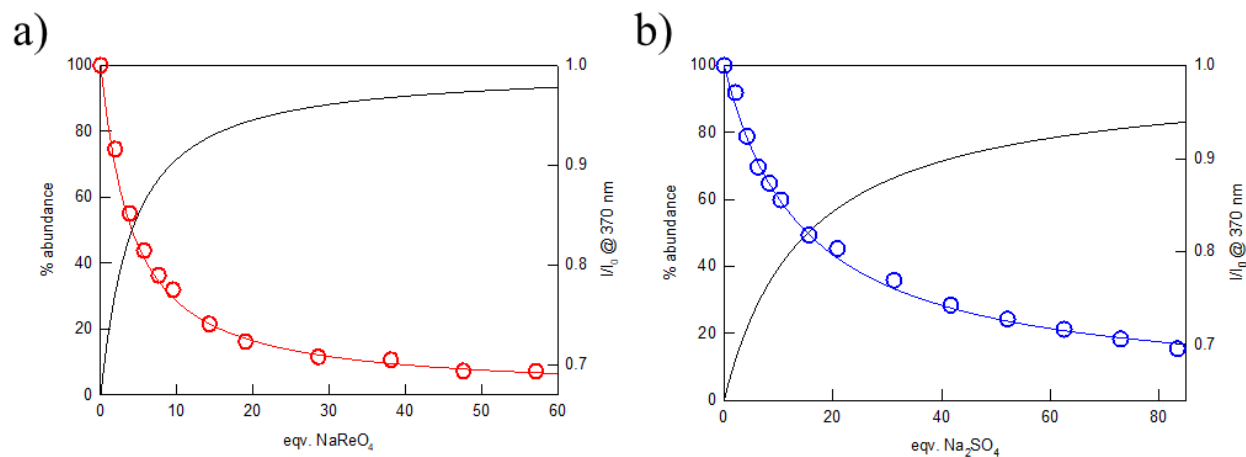
Figure 2.24 Profile of the normalized intensity (I/I_0 at 364 nm) *vs.* equivalents of the added NaX, obtained from the spectrofluorimetric titrations of $[\mathbf{GB2}H_6]^{6+}$ (5 μM, pH 2, λ_{exc} = 284 nm) with NaReO$_4$. The experimental profile is superimposed to the distribution diagram of the species, calculated for logK$_{11}$ = 4.19.

Figure 2.25 Profile of the normalized intensity (I/I_0 at 364 nm) *vs.* equivalents of the added NaX, obtained from the spectrofluorimetric titrations of $[\mathbf{GB2}H_6]^{6+}$ (5 μM, pH 2, λ_{exc} = 284 nm) with Na$_2$SO$_4$. The experimental profile is superimposed to the distribution diagram of the species, calculated for logK$_{11}$ = 3.72.

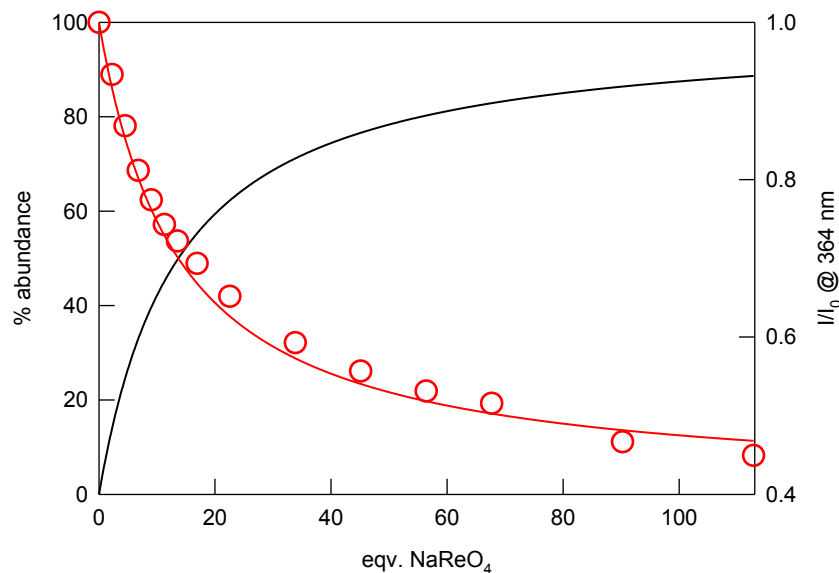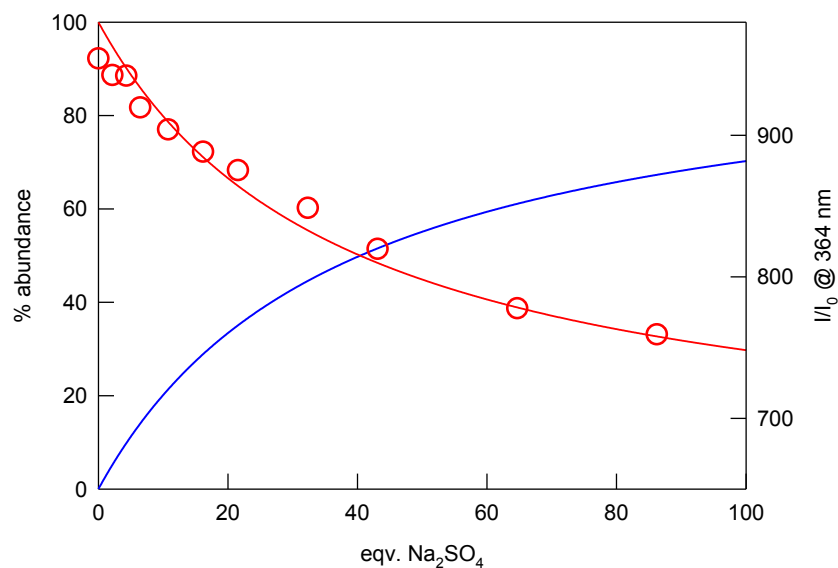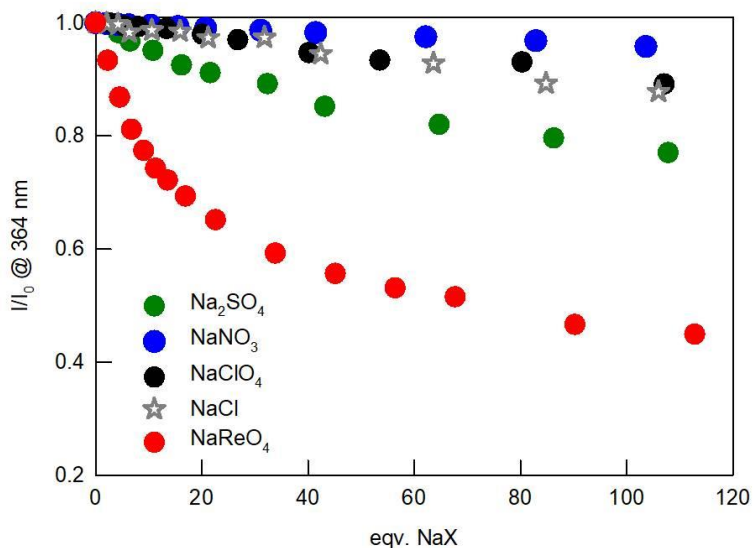**Figure 2.26** Profiles of the normalized intensity (I/I_0) at 364 nm *vs.* equivalents of the added NaX. The experimental profiles are relative to spectrofluorimetric titrations on $[\mathbf{GB2}H_6]^{6+}$ (5 μM in 0.05M CF$_3$SO$_3$Na, pH 2, λ_{exc} = 284 nm) with various sodium salts. The titrant solutions were prepared in the same solvent medium as that used for the receptor.

2.3.7 ^{1}H-NMR Titrations

The ^{1}H-NMR spectra of $[\mathbf{GB1}H_6]^{6+}$, recorded in the presence of excess anions (Figure 2.27) in D$_2$O, revealed small (Δppm < 0.1) but detectable shifts. The most pronounced shifts belonged to the proton resonances of the binaphthyl moiety. These can be actually affected by the electronic perturbations induced by the changes of dihedral angle and H-bonding interactions. For the two most representative anions, ReO$_4^-$ and SO$_4^{2-}$, full titrations were performed which allowed the calculation of the corresponding binding constants (Figures 2.28 and 2.29).

The logarithmic binding constants obtained from ^{1}H-NMR titrations were 4.77(6) for ReO$_4^-$ and 3.91(3) for SO$_4^{2-}$. These results are in close agreement with those obtained by CD and fluorimetric titrations.
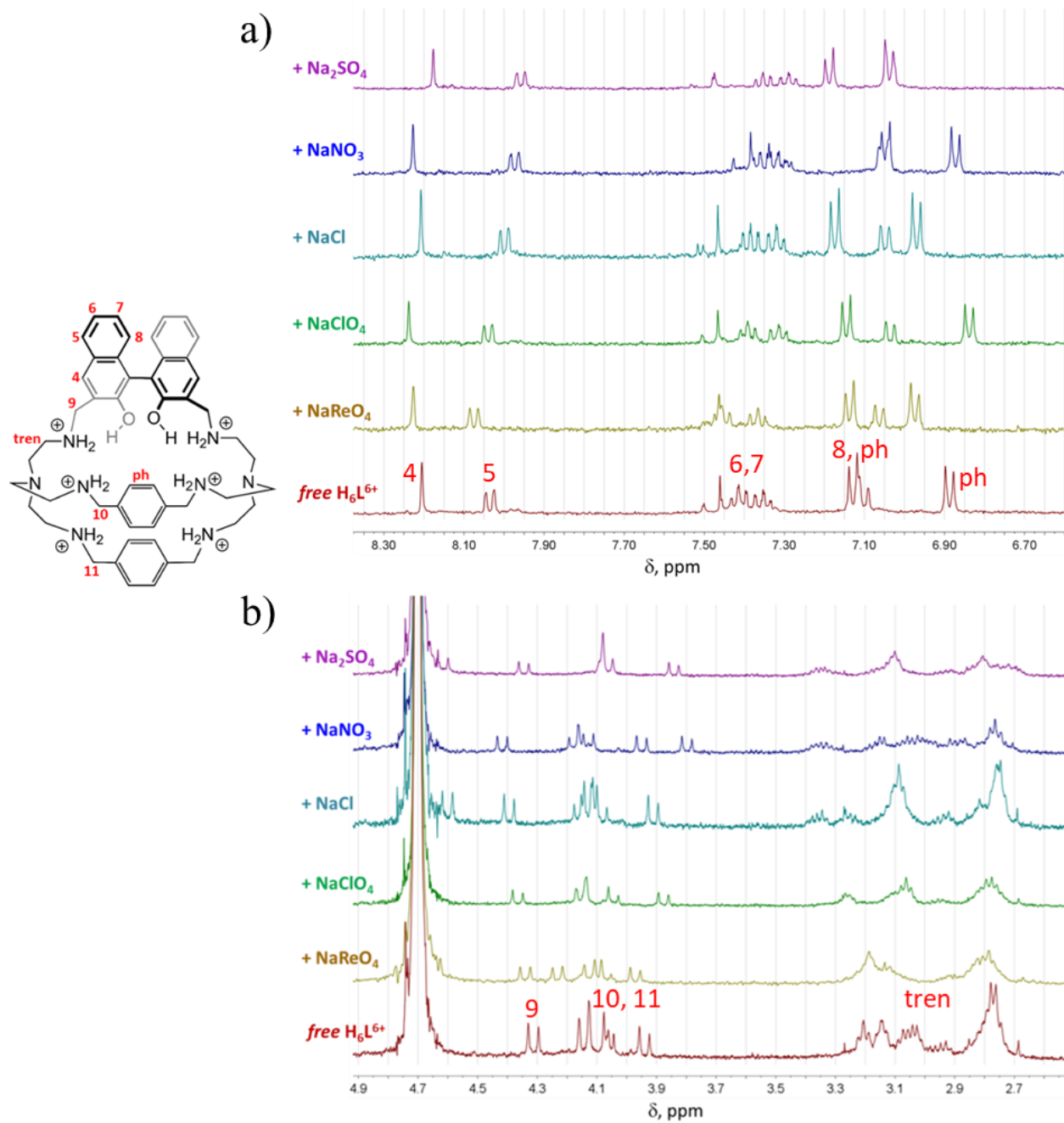
Figure 2.27 ^{1}H-NMR spectra of [**GB1**H$_6$]$^{6+}$ (0.6 mM) in D$_2$O (CF$_3$SO$_3$Na 0.05M, pD = 2), before (red line) and after the addition of excess anions (~80 eqv.) as sodium salts. a) Details of the aromatic region. b) Details of the aliphatic region.
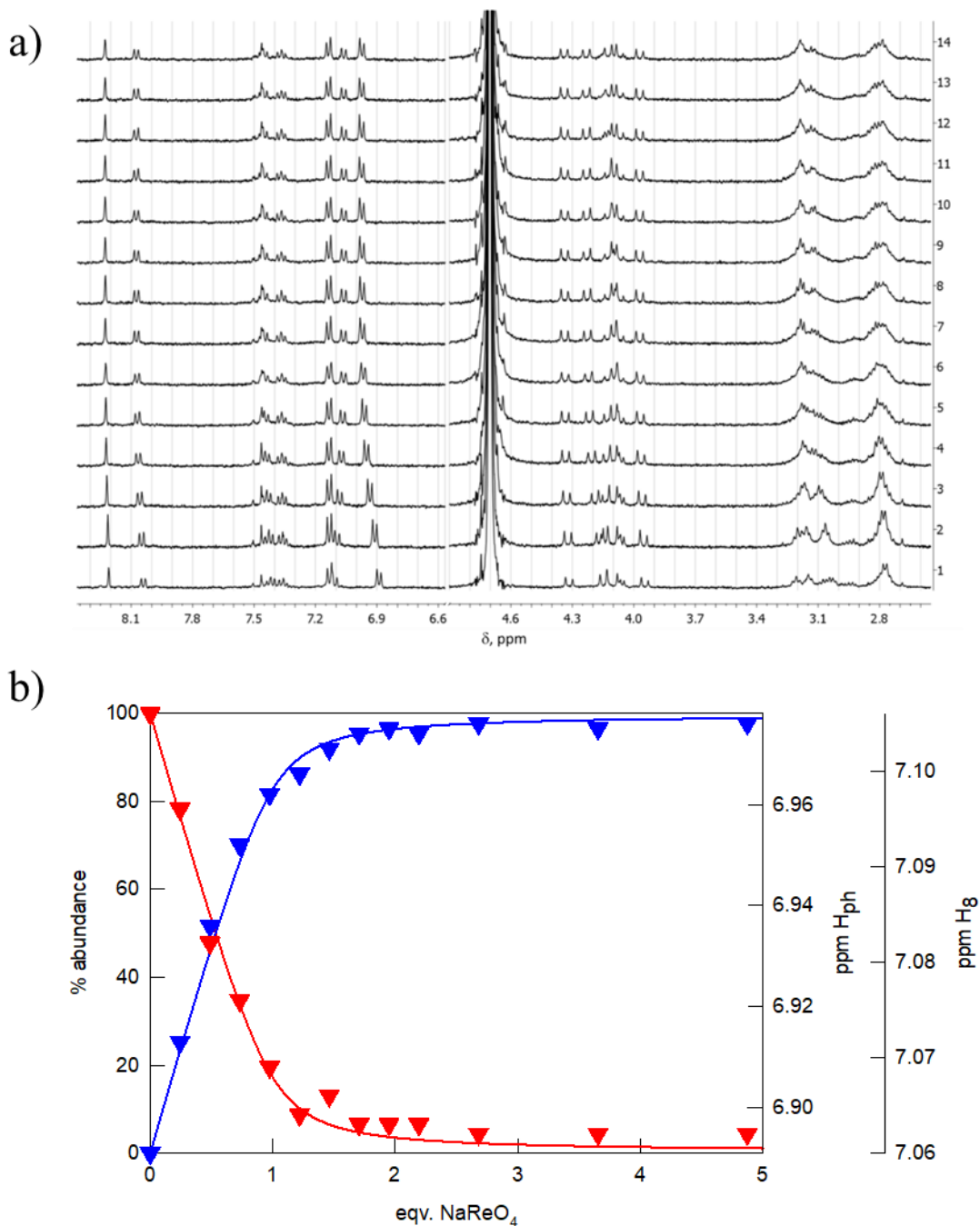
Figure 2.28 a) Family of ^{1}H-NMR spectra taken over the course of the titration of [**GB1**H$_6$]$^{6+}$ (0.6 mM in D$_2$O (pH = 2, CF$_3$SO$_3$Na 0.05M) with a standard solution of NaReO$_4$, spectrum 1 corresponds to the free receptor. b) Experimental profiles (chemical shifts of H$_{ph}$ and H$_8$: blue and red symbols, respectively) superimposed to the distribution diagram of the species *vs.* equivalents of the added sodium salt (LogK$_{11}$ = 4.77). Red line = % free [**GB1**H$_6$]$^{6+}$, blue line = % [**GB1**H$_6$(ReO$_4$)]$^{5+}$
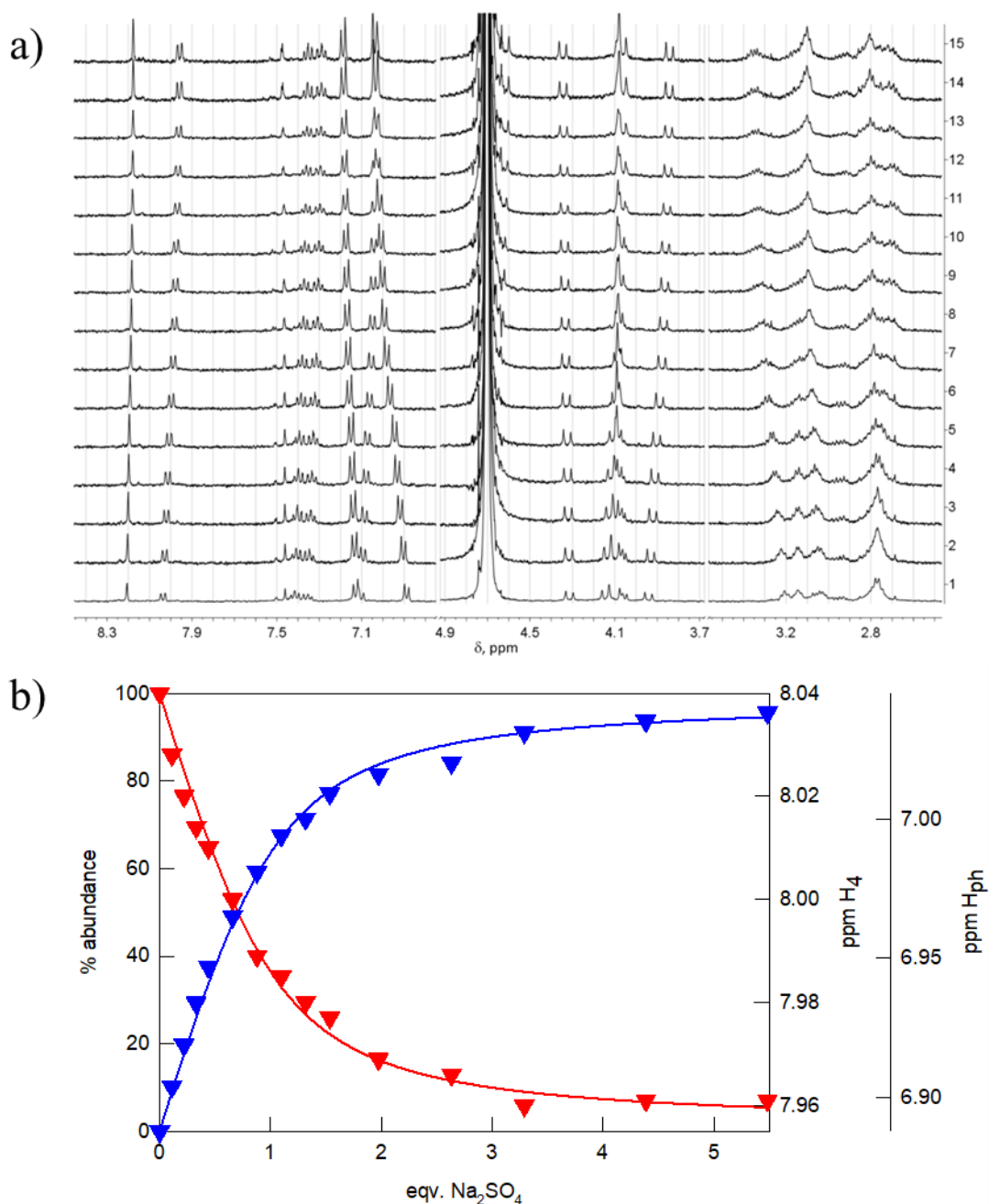
Figure 2.29 a) Family of ^{1}H-NMR spectra taken over the course of the titration of $[\textbf{GB1}H_6]^{6+}$ (0.6 mM) in D_2O (adjusted at pH = 2 with CF_3SO_3H) with a standard solution of Na_2SO_4, spectrum 1 corresponds to the free receptor. b) Experimental profiles (chemical shifts of H_{ph} and H_4: blue and red symbols, respectively) superimposed to the distribution diagram of the species *vs.* equivalents of the added sodium salt ($LogK_{11}$ = 3.91). Red line = % free $[\textbf{GB1}H_6]^{6+}$, blue line = % $[\textbf{GB1}H_6(SO_4)]^{4+}$.

2.3.8 Complex Matrices

The obtained results, and the selectivity window clearly emerging from the CD titrations with ReO$_4^-$, encouraged us to verify the possible application of [**GB1**H$_6$]$^{6+}$ as a chiroptical probe in complex aqueous media, such as beverages or biological fluids. For these studies, either artificial urine medium (AUM) or fruit juice was properly diluted and brought to pH 2 with aqueous CF$_3$SO$_3$H, and then employed as solvent medium in the preparation of both receptor and guest solutions. Commercial pineapple-lime juice contains biological ingredients and sweeteners (steviol glycosides) absorbing in the UV-Vis region of interest (Figure 2.30). Hence, it was chosen as an example of a real matrix containing possible masking components. On the other hand, AUM is an example of synthetic matrix that, besides mimicking human urine as ingredients, contains a large excess of mixed potential competitors for the receptor binding (Figure 2.31 and Table 2.2).
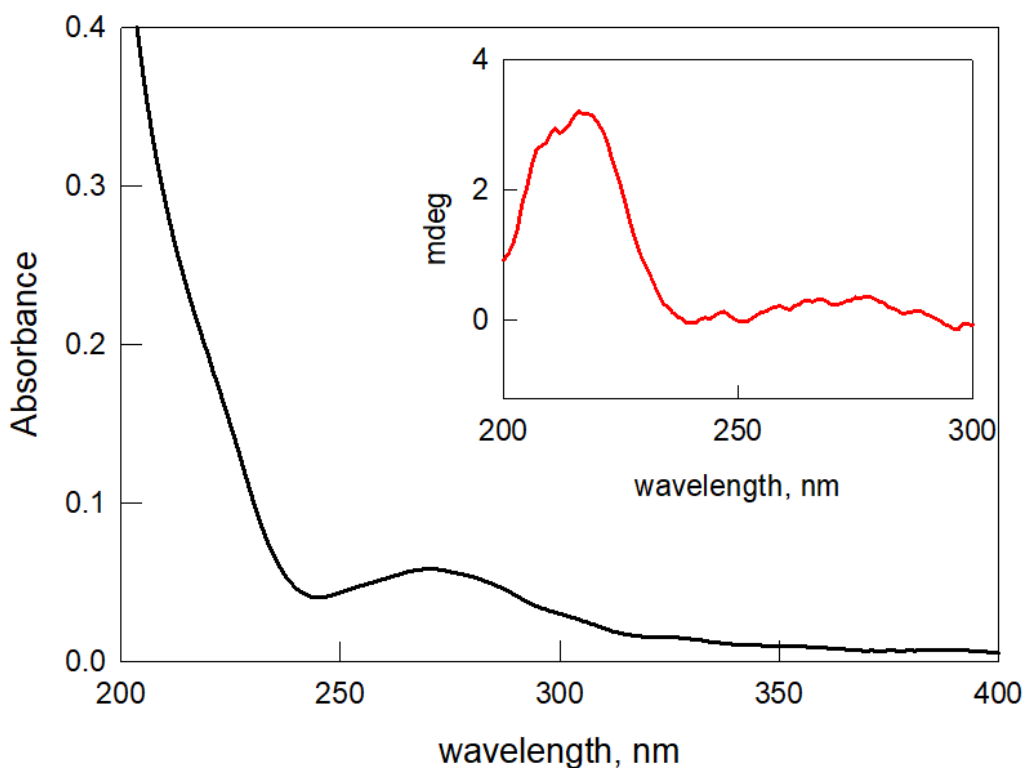
Figure 2.30 UV-Vis and CD spectra (black line and red lines, respectively) of commercial pineapple-lime juice after 10× dilution with demineralized water. The solution pH was brought to 2 by addition of aqueous CF$_3$SO$_3$H.
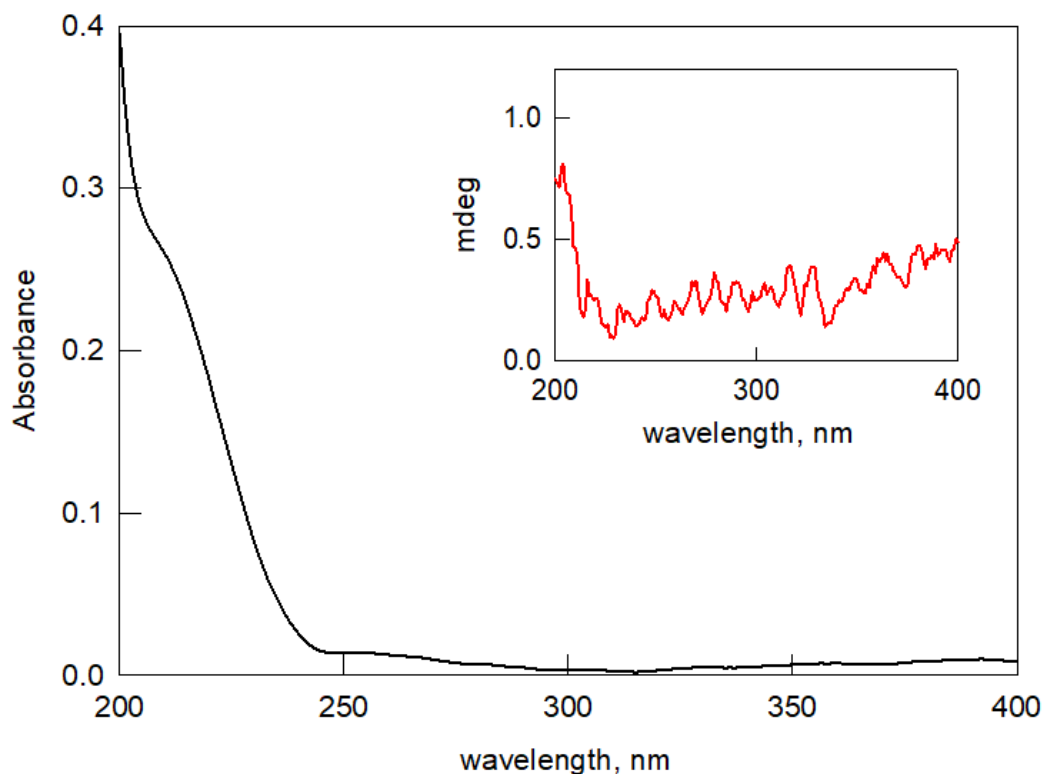
Figure 2.31 UV-Vis and CD spectra (line and red lines, respectively) of AUM after 30× dilution with demineralized water. The solution pH was brought to 2 by addition of aqueous CF_3SO_3H.

Despite potential obstacles, CD titrations on $[\mathbf{GB1}H_6]^{6+}$ with ReO_4^- were successful in both matrices. The logarithmic binding constants were found to be 4.53(1) and 3.93(2) in juice and AUM, respectively (Figures 2.32 - 2.34). These results are in close agreement with those obtained in aqueous solution with CF_3SO_3Na as supporting electrolyte (Table 2.4). No reliable values were instead obtained by UV-Vis titrations (Figures 2.35 and 2.36), further strengthening the orthogonality and the practical utility of the chiroptical sensing approach.
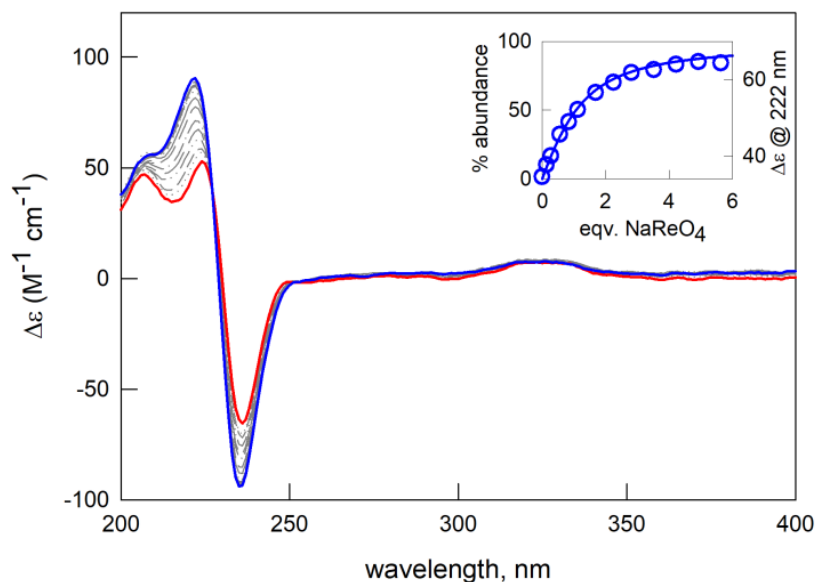
Figure 2.32 CD titration of $[\mathbf{GB1}H_6]^{6+}$ (0.05 mM) with NaReO$_4$ in diluted (10×) fruit juice at pH 2. Red and blue lines correspond to the initial and final spectra, respectively. Inset: % of $[\mathbf{GB1}H_6(ReO_4)]^{5+}$ *vs.* equivalents of NaReO$_4$ (blue line) calculated for logK$_{11}$ = 4.53, superimposed to the experimental profile (blue circles).
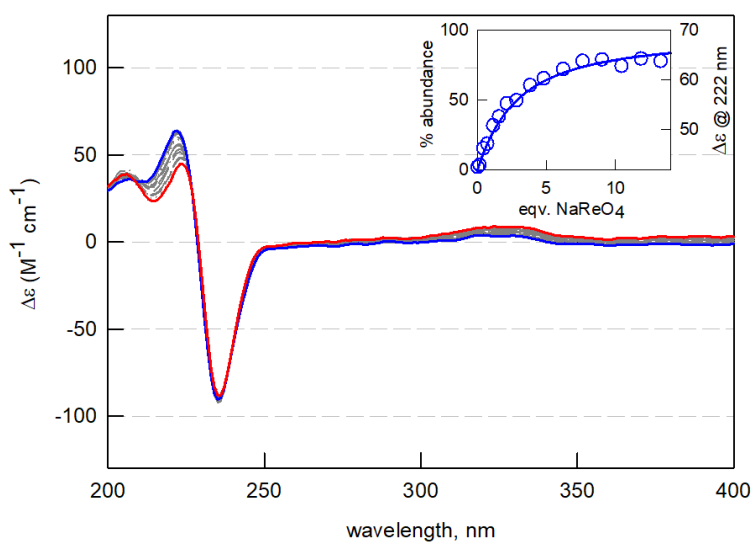
Figure 2.33 CD spectra taken over titration of $[\mathbf{GB1}H_6]^{6+}$ (0.05 mM) with NaReO$_4$ in diluted (30×) AUM at pH 2. Red and blue lines correspond to the initial and final spectra, respectively. Inset: % of $[\mathbf{GB1}H_6(ReO_4)]^{5+}$ *vs.* equivalents of NaReO$_4$ (blue line), calculated for logK$_{11}$ = 3.93, superimposed to the experimental profile (blue circles).

41
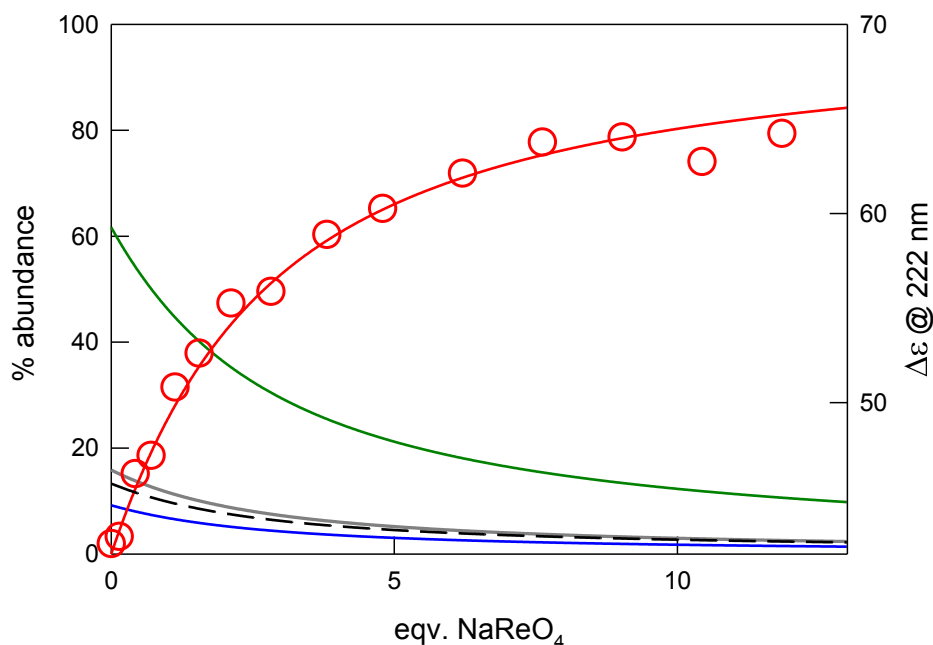
Figure 2.34 Distribution diagram of the species in solution over the course of the CD titration of [**GB1**H$_6$]$^{6+}$ (50 μM) with NaReO$_4$ in diluted AUM; red line: % [**GB1**H$_6$(ReO$_4$)]$^{5+}$; green line: % [**GB1**H$_6$(SO$_4$)]$^{4+}$; grey line: % [**GB1**H$_6$(Cl)]$^{5+}$; black dashed line: % *free* [**GB1**H$_6$]$^{6+}$, blue line: % [**GB1**H$_6$(NO$_3$)]$^{5+}$, red symbols: experimental titration profile of Δε at 222 nm *vs.* equivalents NaReO$_4$. The diagram was built using the Hyss software (Hyperquad package) [23]. In particular, knowing the concentration of the potential interfering anions and the binding constants in aqueous solution at pH 2, we could estimate that [**GB1**H$_6$]$^{6+}$ is initially distributed in AUM among the following forms: 62%,[**GB1**H$_6$(SO$_4$)]$^{4+}$; 16%, [**GB1**H$_6$(Cl)]$^{5+}$; 13%, *free* [**GB1**H$_6$]$^{6+}$; 9%, [**GB1**H$_6$(NO$_3$)]$^{5+}$ (where % corresponds to the molar fraction × 100).
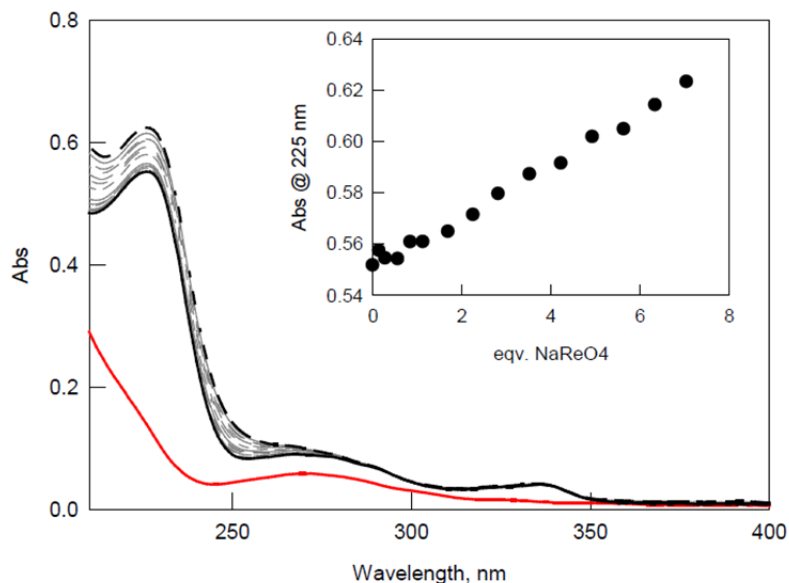
Figure 2.35 UV-Vis. spectra taken over titration of $[\textbf{GB1}H_6]^{6+}$ (0.05 mM) with NaReO$_4$ in diluted (10×) fruit juice at pH 2 (solid and dashed black lines: initial and final spectra, respectively); red line: spectrum of the diluted juice. Inset graph: profile of absorbance at 225 nm *vs.* equivalents of the added NaReO$_4$.
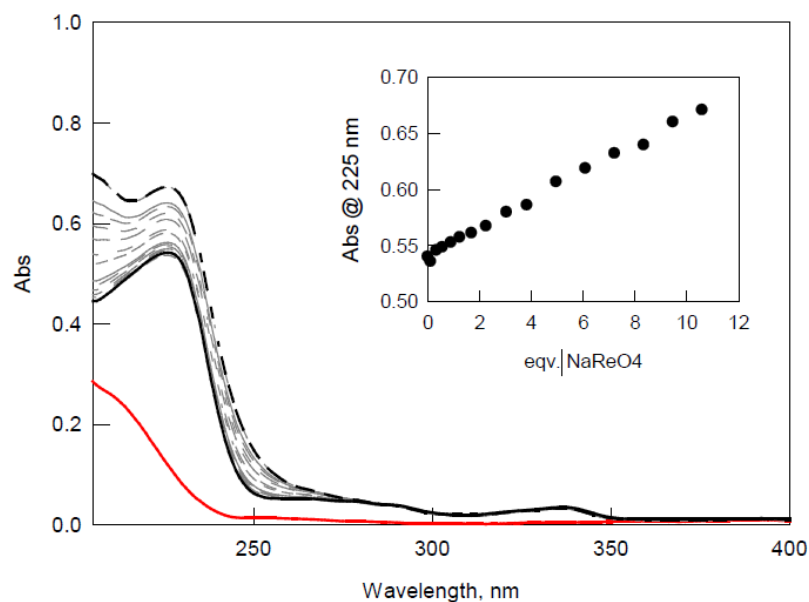
Figure 2.36 UV-Vis. spectra taken over titration of $[\textbf{GB1}H_6]^{6+}$ (0.05 mM) with NaReO$_4$ in diluted (30×) AUM at pH 2 (solid and dashed black lines: initial and final spectra, respectively); red line: spectrum of diluted AUM. Inset graph: profile of absorbance at 225 nm *vs.* equivalents of the added NaReO$_4$.

2.4 CONCLUSIONS

In conclusion, the chiral molecular cage $[\mathbf{GB1}H_6]^{6+}$ is characterized by significant chiroptical and fluorescent responses to ReO_4^- in aqueous acidic solution. The chiroptical response is the consequence of the interaction with the atropoisomerically-chiral π-extended BINOL group, promoting a strong CD response upon substrate binding. Association constants with anions were determined and compared using various spectroscopic techniques (Table 2.6): the obtained values are remarkably consistent, and point to the formation of a 1:1 receptor-anion complex for all the investigated guests. The binding constants trend shows a marked selectivity for ReO_4^-. Even if the obtained values are lower than those reported for other symmetrical cryptands, and determined in otherwise identical conditions the affinity for the perrhenate anion is still very high, also considering that the binding studies were carried out in concentrated triflate medium [13,29].

Table 2.6 Anion binding constants ($LogK_{11}$) determined for $[\mathbf{GB1}H_6]^{6+}$ in aqueous solution, 0.05M CF_3SO_3Na at pH 2, using various spectroscopic techniques: CD, spectrofluorimetry, ^{1}H-NMR. The uncertainty on the last figure is represented in parenthesis. *n.a.*: not available

NaX	$LogK_{11}^{CD}$	$LogK_{11}^{fluo}$	$LogK_{11}^{NMR}$
NaReO$_4$	4.74(2)	4.70(1)	4.77(6)
Na$_2$SO$_4$	4.10(1)	4.21(4)	3.91(3)
NaClO$_4$	3.20(3)	*n.a.*	*n.a.*
NaNO$_3$	3.55(2)	*n.a.*	*n.a.*
NaCl	2.61(2)	*n.a.*	*n.a.*

The enhanced sensing response and anion binding capability of $[\mathbf{GB1}H_6]^{6+}$, compared to the methylated analogue system $[\mathbf{GB2}H_6]^{6+}$, are attributable to the contribution of the OH donors on the BINOL moiety, as suggested by CD titrations and computational studies. This is the first example of chiroptical receptor in which the participation of BINOL OH groups in anion binding is effective in pure water [30,31]. The CD response was also proven to be effective when operating in complex matrices, where interferences are caused by either the competition for the receptor or matrix masking effects. Due to the strong similarity between ReO_4^- and $^{99}TcO_4^-$, the chiral molecular cage $[\mathbf{GB1}H_6]^{6+}$ can be proposed as a chemical probe for the sensing of ^{99}Tc in water.

2.5 CHARACTERIZATION OF GB1 and GB2
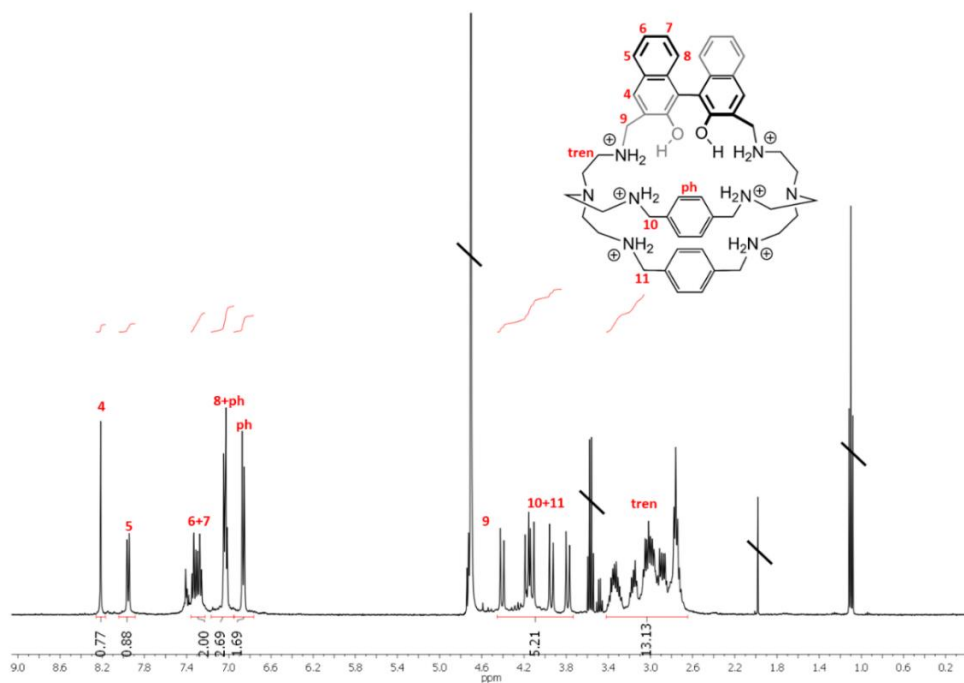
Figure 2.37 ^{1}H-NMR spectrum of **GB1** (400 MHz) in D$_2$O (+ excess CF$_3$SO$_3$H).
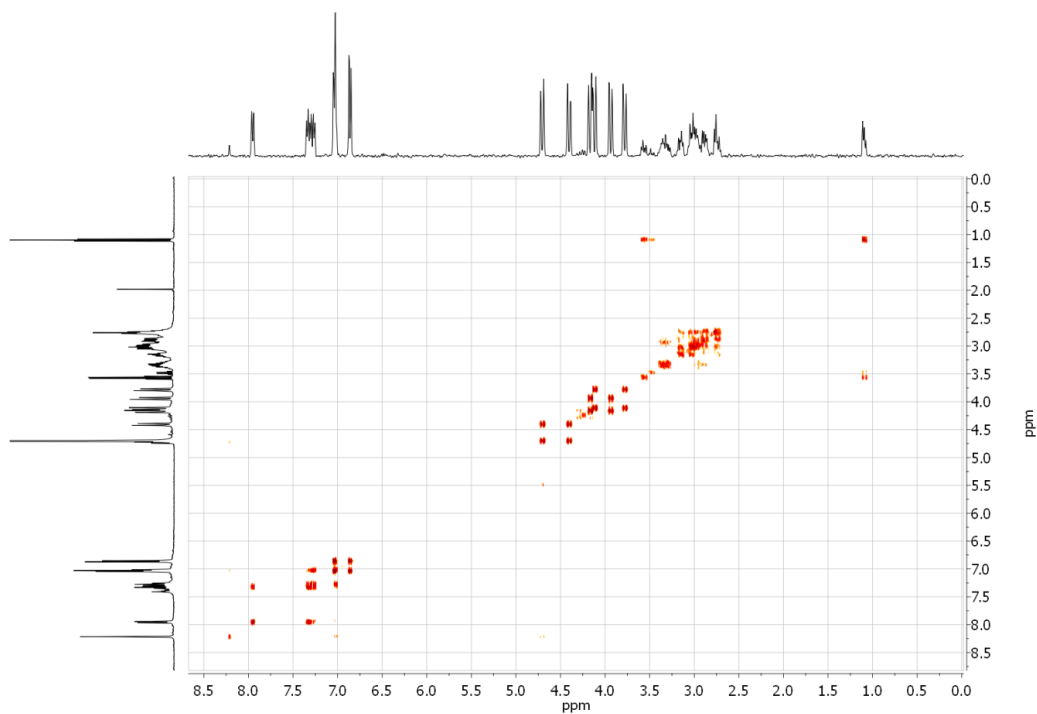
Figure 2.38 COSY spectrum of **GB1** (400 MHz) in D$_2$O (+ excess CF$_3$SO$_3$H).
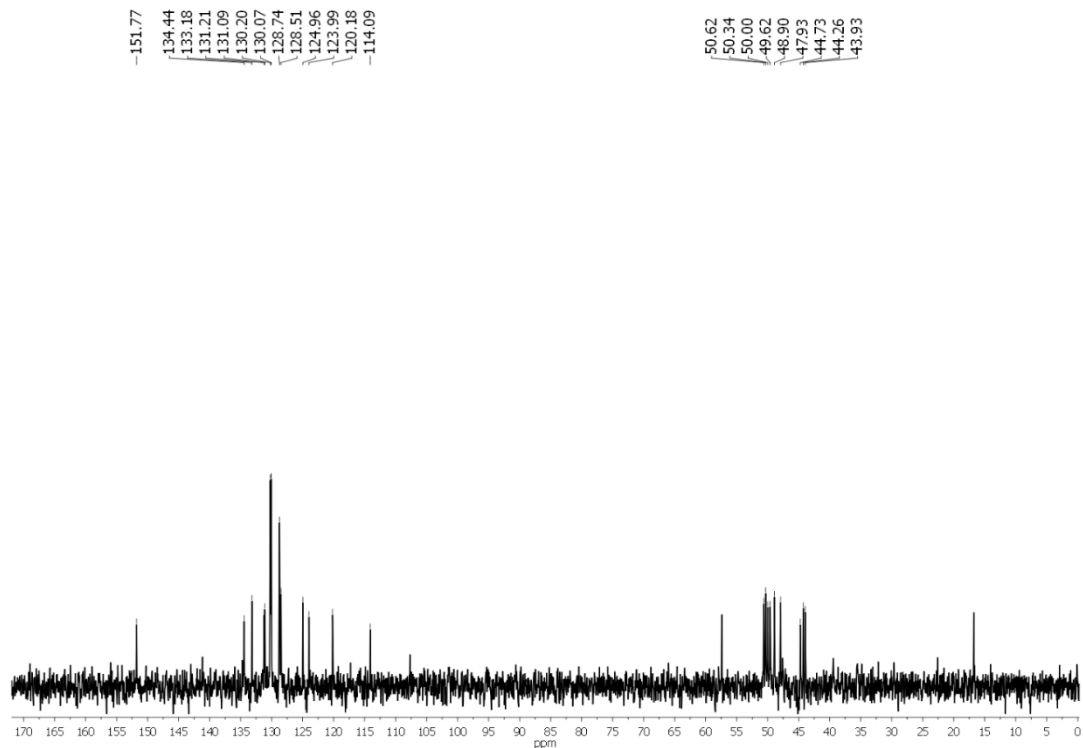
Figure 2.39 ^{13}C-NMR spectrum of **GB1** (100 MHz) in D$_2$O (+ excess CF$_3$SO$_3$H).
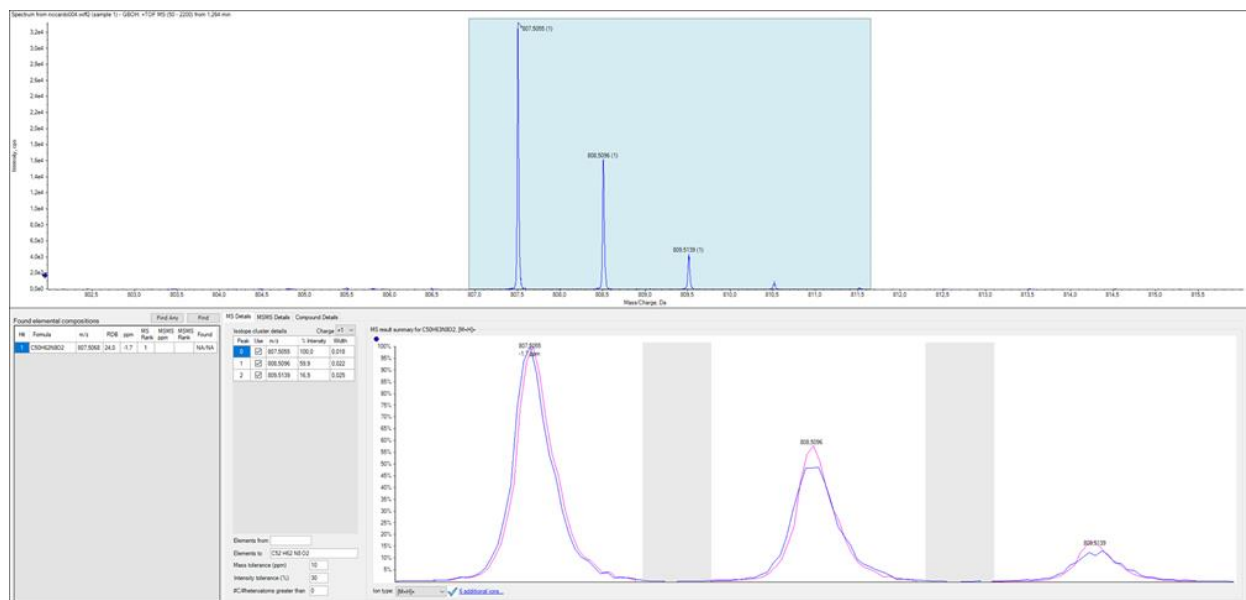
Figure 2.40 HRMS-ESI of [**GB1**+H$^+$]$^+$ in CH$_3$CN. Up: zoom scan of the peak at 807.5055 m/z obtained from the experimental HRMS-ESI spectrum. Bottom: calculated spectrum of the adduct [**GB1**+H$^+$]$^+$ superimposed to the experimental one.
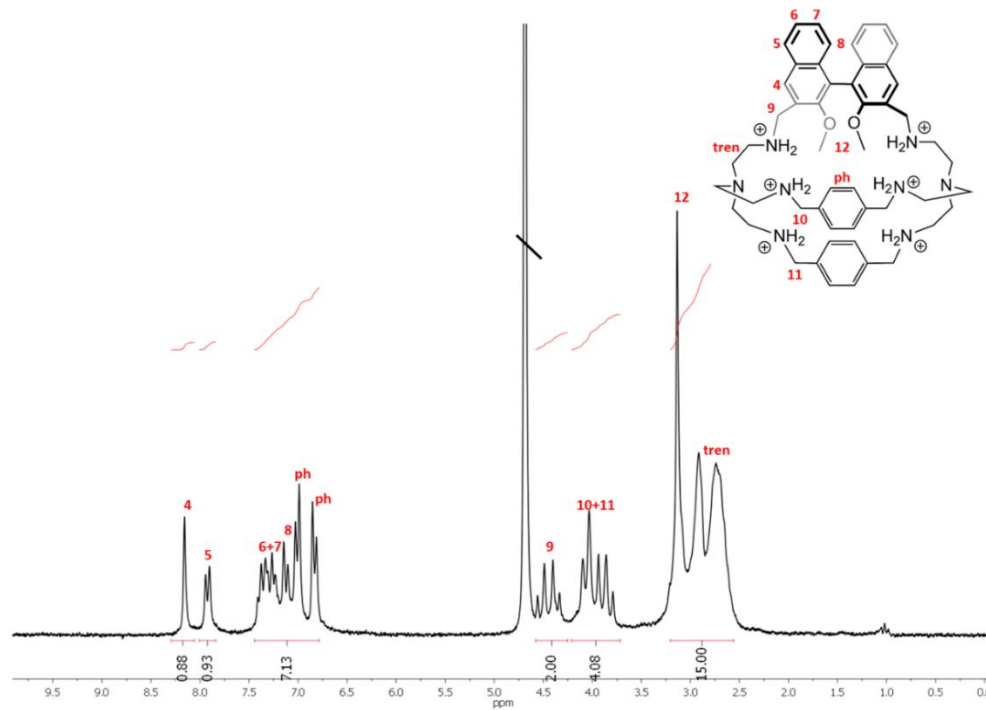
Figure 2.41 ^{1}H-NMR spectrum of **GB2** (300 MHz) in D_2O (+ excess CF_3SO_3H).
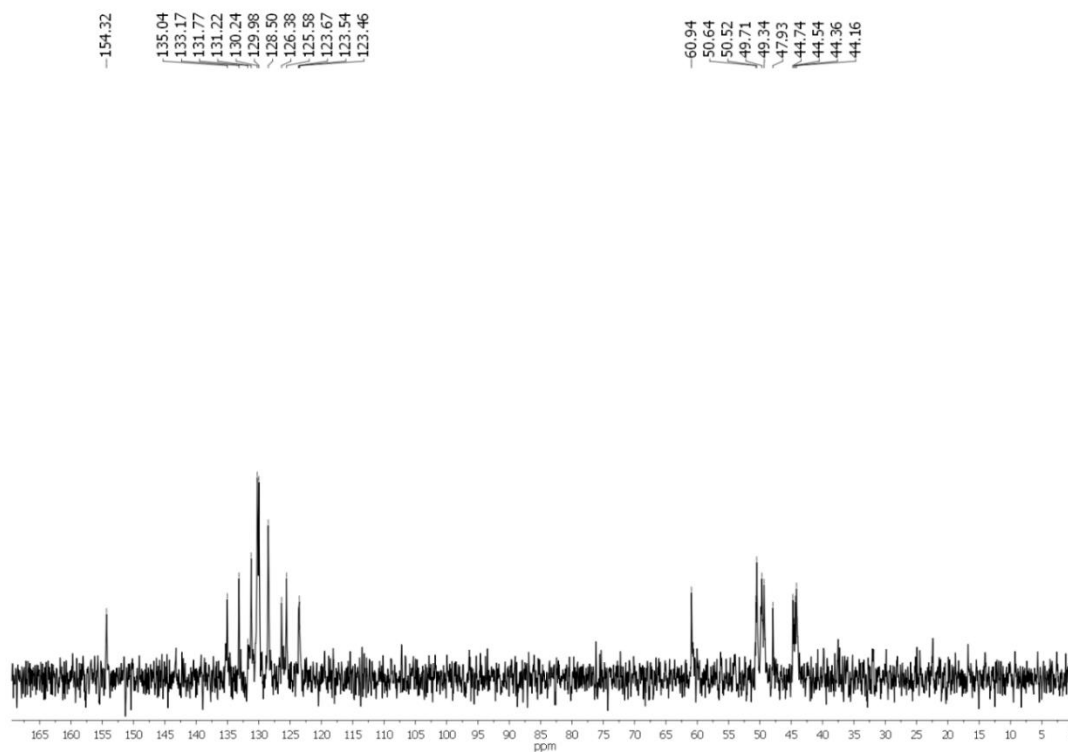
Figure 2.42 ^{13}C-NMR spectrum of **GB2** (100 MHz) in D_2O (+ excess CF_3SO_3H).
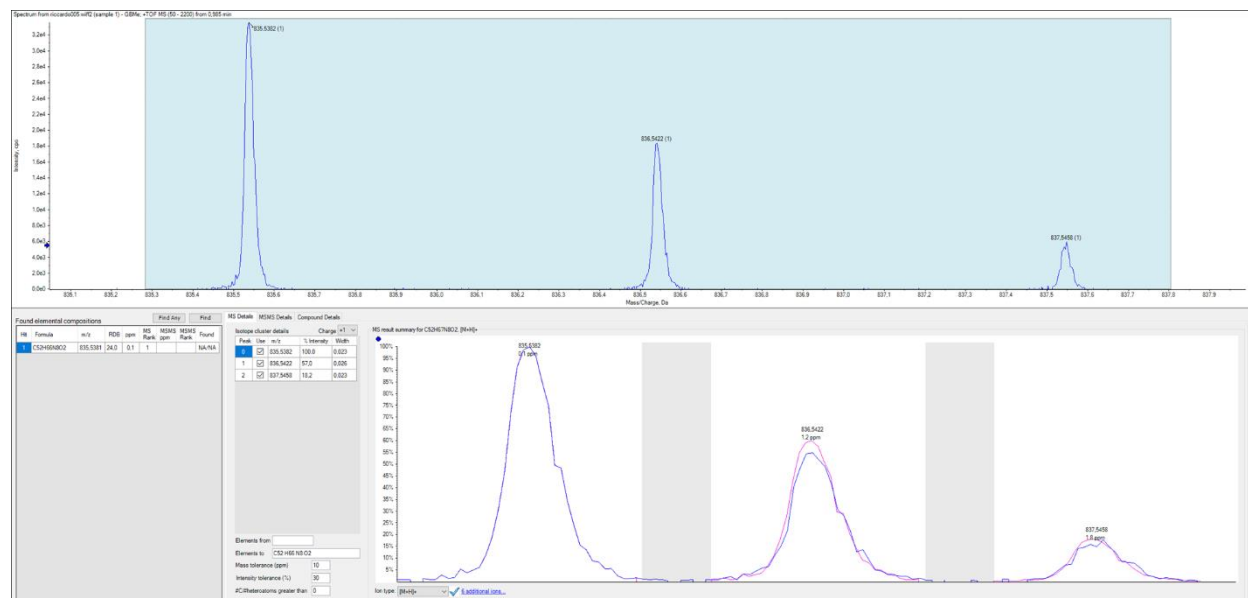
Figure 2.43 HRMS-ESI of [**GB2**+H$^+$]$^+$ in CH$_3$CN. Up: zoom scan of the peak at 835.5382 m/z obtained from the experimental HRMS-ESI spectrum. Bottom: calculated spectrum of the adduct [**GB2**+H$^+$]$^+$ superimposed to the experimental one.

2.6 REFERENCES

[1] D. Sheng, L. Zhu, C. Xu, C. Xiao, Y. Wang, Y. Wang, L. Chen, J. Diwu, J. Chen, Z. Chai, T.E. Albrecht-Schmitt, S. Wang, *Environ. Sci. Technol.*, **2017**, 51, 3471.

[2] B. Wakoff, K.L. Nagy, *Environ. Sci. Technol.*, **2004**, 38, 1765.

[3] a) R. Colton, *"The Chemistry of Rhenium and Technetium"*, John Wiley and sons Ltd, Interscience Publishers, New York, 1st ed., **1965**; b) *"Handbook of Chemistry and Physics"*, ed. D.R. Lide, H.P.R. Frederikse, CRC Press, **1997.**

[4] E.A. Katayev, G.V. Kolesnikov, J.L. Sessler, *Chem. Soc. Rev.*, **2009**, *38*, 1572.

[5] a) W.A. Volkert, T.J. Hoffman, *Chem.Rev.*, **1999**, *99,* 2269; b) F.F. Knapp, R.H. Spencer, J. Kropp, *Nucl. Med.*, **2001**, 42, 1384; c) J. Kotzerke, H. Hanke, M. Hoher, *Eur. J. Nucl. Med.*, **2000**, *27*, 223; c) S. Chattopadhyay, M.K. Das, S.K. Sarkar, P. Saraswathy, N. Ramamoorthy, *Appl.Radiat.Isot.*, **2002**, 57, 7.

[6] a) J.L. Atwood, K.T. Holman, J.W. Steed, *Chem. Commun.,* **1996**, 1401; b) H. Stephan, H. Spies, B. Johannsen, L. Klien, F. Vögtle, *Chem. Commun.,* **1999**, 1875; c) K. Rambo, J.L. Sessler, *Chem. Eur. J.*, **2011**, *17*, 4946.

[7] a) A.E.V. Gorden, J. Davis, J.L. Sessler, V. Kràl, D.W. Keogh, N.L. Schroeder, *Supramol. Chem.*, **2004**, 16, 91; b) E.A. Katayev, N.V. Boev, V.N. Khrustalev, Y.A. Ustynyuck, I.G. Tananaev, J.L. Sessler, *J. Org. Chem.*, **2007**, 72, 2886.

[8] a) E.A. Katayev, G.V. Kolesnikov, V.N. Khrustalev. M. Yu. Antipin, R.K. Askerov, A.M. Maharramov, K.E. German, G.A. Kirakosyan, I.G. Tananaev, T.V. Timofeeva, *J. Radioanal. Nucl. Chem.*, **2009**, 282, 385; b) G.V. Kolesnikov, K.E. German, G. Kirakosyan, I.G. Tananaev, Y.A. Ustynyuck, V.N. Khrustalev, E.A. Katayev, *Org. Biomol. Chem.*, **2011**, 9, 7358.

[9] a) S.O. Kang, J.M. Llinares, V.W. Day, K. Bowman-James, *Chem. Soc. Rev.*, **2010**, 39, 3980; b) S. Ghosh, B. Roehm, R.A. Begum, J. Kut, M.A. Hossain, V.W. Day, K. Bowman-James, *Inorg. Chem.,* **2007**, 46, 23, 9519; c) V. Amendola, M. Bonizzoni, D. Esteban-Gomez, L. Fabbrizzi, M. Licchelli, F. Sancenon, A. Taglietti, *Coord. Chem. Rev.*, **2006**, 250, 1451.

[10] a) M.J. Hynes, B. Maubert, V. McKee, R.M. Town*,* J. Nelson, *Dalton Trans.*, **2000**, 2853; b) D. Farrell, K. Gloe, G. Goretzki, V. McKee, J. Nelson, M. Nieuwenhuyzen, I. Pál, H. Stephan, R.M. Town, K. Wichmann, *Dalton Trans.*, **2003**, 1961; c) J. Nelson, M. Nieuwenhuyzen, I. Pál, H. Stephan, R.M. Town, *Dalton Trans.*, **2004**, 2303.

[11] a) P. Mateus, N. Bernier, R. Delgado, *Coord. Chem. Rev.*, **2010**, 254, 1726; b) L.-Z. Yang, Y. Li, L. Jiang, X.L. Fenga, T.B. Lu, *Cryst. Eng. Comm.*, **2009**, 11, 2375.

[12] H. Stephan, K. Gloe, W. Kraus, H. Spies, B. Johannsen, K. Wichmann, G. Reck, D. K. Chand, P.K. Bharadwaj, U. Müller, W.M. Müller, F. Vögtle in "*Fundamentals and Applications of Anion Separations*", ed. B.A. Moyer and R.P. Singh, Kluwer, New York, **2004**.

[13] V. Amendola, R. Alberto, G. Bergamaschi, H. Braband, T. Fox, *Angew. Chem. Int. Ed.,* **2012**, 51, 9772.

[14] V. Amendola, G. Bergamaschi, M. Boiocchi, R. Alberto, H. Braband, *Chem. Sci.*, **2014**, 5, 1820.

[15] A.M. Desai and P.K. Singh, *Chem. Eur. J.*, **2019**, 25, 2035.

[16] a) L. Xu, M. Sun, W. Ma, H. Kuang, C. Xu, *Mater. Today*, **2016**, 19, 595; b) W. Ma, H. Kuang, L. Xu, L. Ding, C. Xu, L. Wang, N.A. Kotov, *Nat. Commun.*, **2013**, 4, 2689.

[17] a) A. Ozcelik, R. Pereira-Cameselle, N. Poklar Ulrih, A.G. Petrovic, J.L. Alonso-Gomez, *Sensors*, **2020**, 20, 974; b) C. Bravin, G. Mason, G. Licini, C. Zonta, *J. Am. Chem. Soc.*, **2019**, 141, 11963; c) L. You, D. Zha, E.V. Anslyn, *Chem. Rev.*, **2015**, 115, 7840; d) G. Pescitelli, L. Di Bari, N. Berova, *Chem. Soc. Rev.*, **2011**, 40, 4603; e) K.W. Bentley, C. Wolf, *J. Am. Chem. Soc.*, **2013**, 135, 12200.

[18] D. Pasini, A. Nitti, *Chirality*, **2016**, 28, 116.

[19] M. Quan, X.Y. Pang, W. Jiang, *Angew. Chem. Int. Ed.,* **2022**, 61, e202201258.

[20] a) M. Caricato, C. Coluccini, D. Dondi, D.A. Vander Griend, D. Pasini, *Org. Biomol. Chem.*, **2010**, 8, 3272; b) M. Caricato, A. Olmo, C. Gargiulli, G. Gattuso, D. Pasini, *Tetrahedron*, **2012**, 68, 7861; c) M. Caricato, N. J. Leza, K. Roy, D. Dondi, G. Gattuso, L. S. Shimizu, D. A. Vander Griend, D. Pasini, *Eur. J. Org. Chem.*, **2013**, 6078; d) M. Agnes, A. Nitti, D.A. Vander Griend, D. Dondi, D. Merli, D. Pasini, *Chem. Commun.*, **2016**, 52, 11492.

[21] A. Thevenet, A. Miljkovic, S. La Cognata, C. Marie, C. Tamain, N. Boubals, C. Mangano, V. Amendola, P. Guilbaud, *Dalton Trans.*, **2021**, 50, 1620.

[22] Y. Zhou, D. Zhang, Y. Zhang, Y. Tang, D. Zhu, *J. Org. Chem.*, **2005**, 70, 6164.

[23] P. Gans, A. Sabatini, A. Vacca, *Talanta*, **1996**, 43, 1739.

[24] M.J Frisch, G.W. Trucks, H.B. Schlegel, G.E. Scuseria, M.A. Robb, J.R. Cheeseman, G. Scalmani, V. Barone, B. Mennucci, G.A. Petersson, H. Nakatsuji, M. Caricato, X. Li, H.P. Hratchian, A.F. Izmaylov, J. Bloino, G. Zheng, J.L. Sonnenberg, M. Hada, M. Ehara, K. Toyota,

R. Fukuda, J. Hasegawa, M. Ishida, T. Nakajima, Y. Honda, O. Kitao, H. Nakai, T. Vreven, J.A. Montgomery, J.E. Peralta, F. Ogliaro, M. Bearpark, J.J. Heyd, E. Brothers, K.N. Kudin, V.N. Staroverov, T. Keith, R. Kobayashi, J. Normand, K. Raghavachari, A. Rendell, J.C. Burant, S.S. Iyengar, J. Tomasi, M. Cossi, N. Rega, J.M. Millam, M. Klene, J.E. Knox, J.B. Cross, V. Bakken, C. Adamo, J. Jaramillo, R. Gomperts, R.E. Stratmann, O. Yazyev, A.J. Austin, R. Cammi, C. Pomelli, J.W. Ochterski, R.L. Martin, K. Morokuma, V.G. Zakrzewski, G.A. Voth, P. Salvador, J.J. Dannenberg, S. Dapprich, A.D. Daniels, O. Farkas, J.B. Foresman, J.V. Ortiz, J. Cioslowski, D.J. Fox, Gaussian 09, Revision B.01; Gaussian, Inc., Wallingford, CT, **2010**.

[25] T. Brooks, C.W. Keevil, *Lett. Appl. Microbiol.*, **1997**, 24, 3, 203.

[26] a) D. Zhang, J.C. Mulatier, J.R. Cochrane, L. Guy, G. Gao, J.P. Dutasta, A. Martinezet, *Chem. Eur. J.*, **2016**, 22, 8038; b) A.U. Malik, F. Gan, C. Shen, N. Yu, R. Wang, J. Crassous, M. Shu, H. Qiu, *J. Am. Chem. Soc.*, **2018**, 140, 2769; c) Y.Q. Zou, D. Zhang, T.K. Ronson, A. Tarzia, Z. Lu, K.E. Jelfs, J.R. Nitschke, *J. Am. Chem. Soc.*, **2021**, 143, 9009; d) G. Wu, Y. Chen, S. Fang, L. Tong, L. Shen, C. Ge, Y. Pan, X. Shi, H. Li, *Angew. Chem., Int. Ed.*, **2021**, 60, 16594; e) S. Míguez-Lago, B.D. Gliemann, M. Kivala, M. Magdalena Cid, *Chem. Eur. J.*, **2021**, 27, 13352.

[27] S. La Cognata, R. Mobili, F. Merlo, A. Speltini, M. Boiocchi, T. Recca, L.J. Maher III, V. Amendola, *ACS Omega*, **2020**, 5, 26573.

[28] C. Rosini, S. Superchi, H.W.I. Peerlings, E.W. Meijer, *Eur. J. Org. Chem.*, **2000**, 61.

[29] S. Khan, S.K. Mandal, *ACS Appl. Mater. Interfaces*, **2021**, 13, 45465.

[30] a) T.D. James, K.R.A. Samankumara Sandanayake, S. Shinkai, *Nature*, **1995**, 374, 345; b) R. Jiang, Y. Li, Z. Qin, L. Xu, D. Zhua, Y. Li, *RSC Adv.*, **2014**, 4, 2023; c) H.L. Liu, Q. Peng, Y.D. Wu, D. Chen, X.L. Hou, M. Sabat, L. Pu, *Angew. Chem., Int. Ed.*, **2010**, 49, 602.

[31] R.J. Goodwin, M.T. Blyth, A.K.K. Fung, L. M. Smith, P.L. Norcott, S. Tanovic, M.L. Coote, N.G. White, *Org. Biomol. Chem.*, **2021**, 19, 2794.

3 PEEK-WC-BASED MIXED MATRIX MEMBRANES CONTAINING POLYIMINE CAGES FOR GAS SEPARATION

3.1 INTRODUCTION

Membrane-based processes are taking a more and more prominent position in the search for sustainable and energy-efficient gas separation applications. It is known that separation performances of pure polymers may significantly be improved by the dispersion of suitable filler materials in the polymer matrix. In this work four different imine-based organic cages were dispersed in the poly(ether ether ketone) with cardo group (*i.e.* PEEK-WC) to produce mixed matrix membranes (MMMs). The H_2, He, O_2, N_2, CH_4, and CO_2 pure gas permeability of the neat polymer and the MMMs were measured and compared to understand the effect of fillers on the gas separation properties of the final membranes.

3.1.1 Membranes for Gas Separation

Membrane-based gas separation is a fast-growing technology that promises lower operating costs compared to traditional processes such as cryogenic distillation or adsorption on solid substrates. According to the International Union of Pure and Applied Chemistry (IUPAC), a membrane is defined as "a structure that has lateral dimensions much greater than its thickness, through which transfer may occur under a variety of driving forces" [1]. In other words, a membrane can be seen as a selective barrier (liquid or solid) that can separate fluids (liquids, gases or vapours) allowing only specific species to move across (permeate) while retaining the others (retentate). Membranes can be of either biological (*e.g.* cell membranes) or synthetic nature; in the latter case, they can be constituted either by organic components (*e.g.* polymers) or inorganic materials (*e.g.* metal oxides, ceramics). To be industrially relevant, an ideal membrane should meet specific requirements such as chemical and thermal stabilities, high processability and good mechanical properties even at low thicknesses. For these reasons, most of commercial membranes are based on polymers [2]. The late 1970s saw the development of the first industrial processes based on polymeric membranes, including reverse osmosis applications in water treatment (*e.g.* desalination and ultrafiltration).

Later on, between 1980 and 1990, membrane technology was successfully applied in gas separation industrial processes, especially for the separation of hydrogen from N_2, CH_4 and Ar in ammonia plant purge gas [3]. The other applications include the N_2/O_2 separation in nitrogen production, the purification of methane from CO_2, H_2S and H_2 in natural gas treatment, and the recovery of light hydrocarbons from air [4].

The transport of gas, vapour, liquid and ions across dense polymeric membranes is efficiently described by the solution–diffusion model [5]. According to this model, there are no permanent pores into the selective layer, hence the separation of chemical species is based on their different solubility and diffusivity across the membrane material. The permeation process occurs in three steps: i) the penetrating gas molecules dissolve into the membrane on the feed side; ii) the gas molecules diffuse across the matrix from the feed side to the opposite side; iii) the gas molecules desorb from the permeate side of the membrane, entering the permeate reservoir. The diffusion process, which is the rate-determining step (being slower than the other two), depends on the size of the penetrating gas, on the space available between the polymer chains (free volume) and on their rigidity. According to the solution–diffusion model, the permeability (P) of a gas through a membrane is expressed as the product between the diffusivity (D) and solubility (S) (equation 1):

$$P = D \times S$$

(eq. 1)

Permeability is a fundamental parameter that expresses the ability of the membrane material to be permeated by a specific gas. This value represents the flux of permeate generated by a pressure difference between the two sides of the membrane, normalized for the surface area and the thickness of the membrane, and it is commonly given in Barrer (1 Barrer = 10^{-10} cm$^3_{STP}$ cm cm^{-2} s^{-1} cmHg^{-1}). For a pair of gases, a and b, the separating ability of a membrane is determined by the selectivity, $\alpha_{a,b}$, defined by the ratio of the two permeabilities, P_a and P_b (equation 2):

$$\alpha_{a,b} = \frac{P_a}{P_b} = \left(\frac{D_a}{D_b}\right)\left(\frac{S_a}{S_b}\right)$$

(eq. 2)

An optimal separation efficiency requires membranes that combine high permeability with high selectivity. However, it is recognized that the selectivity generally decreases upon increasing the

permeability for the more permeable gas component, resulting in the so-called trade-off relationship. For example, common rubbery polymers exhibit high permeability and low selectivity, on the contrary of glassy ones that show high selectivity and low permeability value. This inverse relationship was first recognized in 1991 by Robeson, that plotted the log of CO_2/CH_4 selectivity *vs.* the log of the higher permeable gas in the mixture (CO_2) for all polymers reported in the open literature till then, developing the Robeson trade-off plots (Figure 3.1) [6].
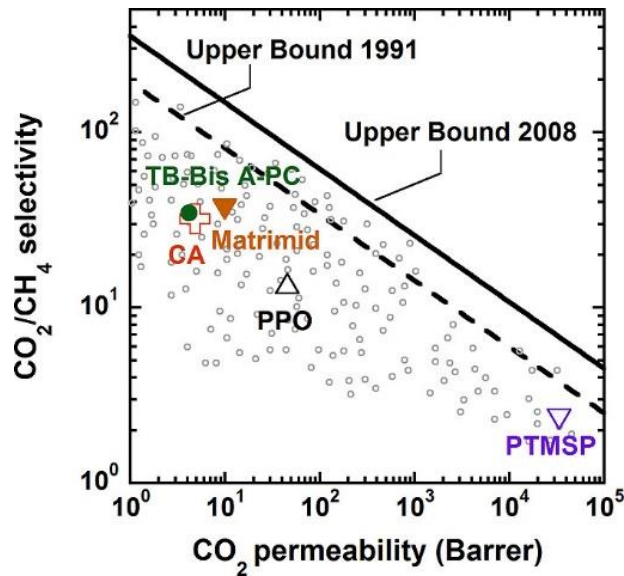
Figure 3.1 CO_2/CH_4 Robeson plot for conventional glassy polymers. Gray circles correspond to the performance of various membranes reported in the literature. The other symbols refer to specific polymers: PTMSP (poly-(trimethylsilylpropyne)); PPO (poly(phenylene oxide)); CA (cellulose acetate); TB-Bis A-PC (tetrabromobisphenol A poly(carbonate)). Continuous line represents the 2008 upper bound, and dashed line represents the 1991 upper bound. From ref. [4].

The trade-off relationship was shown to be related to an upper bound (lines in Figure 3.1) that indicates the best performance limit for known polymeric membranes. This type of plot results to be extremely convenient to easily compare the relative performance of new membrane materials. The goal of the research community is to find polymers exceeding the upper bound line: as it can be seen in figure 3.1, the original upper bound drown in 1991 shifted toward the upper-right corner in 2008, thanks to the achievements of the researchers working in the material chemistry field. The upper bound relationship was shown to be valid for almost every industrially relevant gas pair,

including O_2/N_2, CO_2/CH_4, H_2/N_2, He/N_2, H_2/CH_4, He/CH_4, He/H_2, H_2/CO_2 and He/CO_2, with each gas mixture presenting its own upper bound line [7].

3.1.2 Mixed Matrix Membranes

The excellent processability and high mechanical strength make polymeric materials very attractive for the development of gas separation membranes on an industrial scale. Unfortunately, these optimal features are generally compromised by the permeability *vs.* selectivity trade-off. This limitation has been recently overcome with the introduction of mixed matrix membranes (MMMs), which efficiently combine the processability of organic polymers with the selectivity of an embedded filler. The fillers can improve the properties of the membranes by improving i) diffusivity and selectivity features, if the porous filler acts as molecular sieves, ii) solubility and selectivity features, if the filler can interact with the target gas through its chemical functionalities *i.e.* acting as a selective adsorbent [4].

In mixed matrix membranes, the filler deeply influences the transport properties of the pure polymer. Several models have been proposed to describe this effect but one of the simplest and most applied is the Maxwell model [8,9], which is valid when spherical fillers are present in the membrane at low concentration *i.e.* up to 30 vol %. The permeability of a MMM, P_{MMM}, is given by the equation 3:

$$P_{MMM} = P_C \left[\frac{P_d + 2P_c - 2\Phi_d(P_c - P_d)}{P_d + 2P_c - \Phi_d(P_c - P_d)} \right]$$

(eq. 3)

where P_c and P_d are the permeabilities of the continuous and dispersed phase, respectively, while Φ_d is the volume fraction of the dispersed phase.

Hence, if the dispersed phase is more permeable than the continuous phase, the overall permeability increases, with a maximum theoretical limit given by $P_d = \infty$ (equation 4):

$$P_{MMM,max} = P_C \left[\frac{1 + 2\Phi_d}{1 - \Phi_d} \right]$$

(eq. 4)

The overall permeability decreases if the permeability of the dispersed phase is lower than that of the bulk polymer, with a minimum limit for $P_d = 0$ (equation 5):

$$P_{MMM,min} = P_C \left[\frac{1 - \Phi_d}{1 + 0.5\Phi_d} \right]$$

(eq. 5)

However, more complex situations occur for non-spherical particles or when the filler/polymer fraction increases due to interfacial defects that affect the properties of the bulk, and creates a stiffer interface, or an interface with a higher free volume.

Some of the most studied inorganic fillers are based on Zeolites, [10] Graphene Oxide (GO), [11] carbon nanotubes [12] and metal oxides [13]. These materials possess unique molecular sieving features, but poor interfacial compatibility with the polymer matrix. This usually results in the formation of non-selective interfacial voids, which can affect the performances and mechanical properties of the final MMM. The "sieve-in-a-cage" scenario (central picture in Figure 3.2) can be due to either high filler-loading or aggregation of the filler particles in the polymer matrix, resulting in a significant reduction of selectivity. Another unfortunate situation is described by the "plugged sieves" scenario (right picture in Figure 3.2). In this case, smaller molecules or polymer chains or the structure of the filler itself can block the filler pores, preventing the gas molecules from passing and leading to an overall decrease of permeability [14].
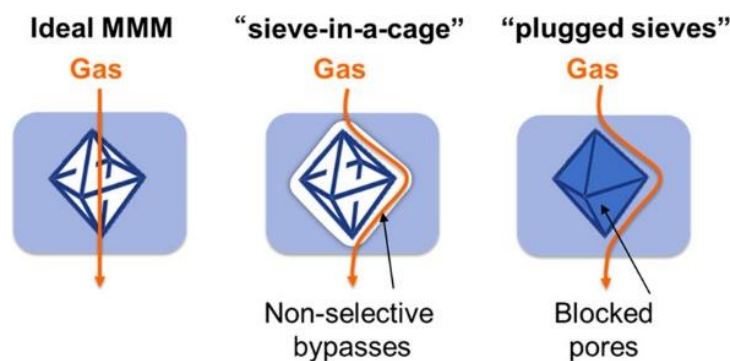
Figure 3.2 Ideal and non-ideal MMM architectures. From ref. [14].

The incompatibilities between purely inorganic fillers and the polymer matrix can be overcome by using metal-organic fillers, in which the presence of an organic component improves the adhesion of the filler to the membrane. In this regard, Porous Organic Frameworks (POFs) as well as Metal Organic Frameworks (MOFs) have attracted particular interest for membrane-based separation applications [2,15]. MOFs are defined as extended structures based on metals and organic bridging ligands, differing from classic coordination polymers by the high porosity and crystallinity. Thanks to the variety of metals and ligands that could be applied in the preparations of MOFs, various structures with unique chemical and physical properties can be formed, with exceptionally high porosity, surface areas up to 10'000 m^2/g and tuneable pore chemistry [16]. Since the first report of a MOF-based MMM, applied in the improved separation of methane, published in 2004 [17], a large number of different MOFs have been investigated as potential fillers in mixed matrix membranes. Some of the most applied in gas separations are ZIF-8, HKUST-1, MIL-53, MIL-101, MOF-74, and UiO-66 [18]. Recent studies revealed that the design of MOFs with exposed functional groups (*e.g.* -NH_2, -COOH, -SO_3H) can further improve the polymer-filler compatibility thanks to beneficial secondary interactions, such as hydrogen bonding or π-π stacking. Extensive studies have demonstrated that UiO-66-NH_2, prepared with amine functionalized dicarboxylates linkers, outperforms the pristine UiO-66 MOF thanks to the large number of H-bonding interactions between the -NH_2 groups of the MOF framework and the polymer matrix [19].

Figure 3.3. MMMs prepared from corona-MOFs and a PDMS matrix. The corona is covalently connected to both the surface of the UiO-66-allyl particles and the PDMS polymer matrix via hydrosilylation From ref. [14].

A further step in the optimization of polymer-filler interactions is taken by covalent grafting the polymers on the surface of MOFs. In this case, the external functional groups of the MOF particles can be used as an anchor for the polymer chains, thus further increasing the contacts between the filler and the polymer matrix (via Van der Waals interactions) [20], or as cross-linking agents to generate a covalently bound MOF-Polymer MMM (Figure 3.3) [14].

Examples of fully organic fillers are represented by POFs, a class of porous materials based on covalently bound pure organic building blocks and characterized by a rigid structure, high surface areas, various chemical functionality, adjustable pore structures, and good chemical and thermal stability. Compared to the semi-organic nature of MOFs, the fully organic structure of POFs can further improve the affinity with the polymer matrix. POFs can be divided in two sub-classes according to the degree of crystallinity: i) highly crystalline materials, such as Covalent Organic Frameworks (COFs); ii) amorphous materials, such as Polymers of Intrinsic Microporosity (PIMs), Hyper-Cross-linked Polymers (HCPs), Conjugated Microporous Polymers (CMPs) and Porous Aromatic Frameworks (PAFs) [21]. Among them, COFs are certainly the most widely employed as fillers in MMMs. COFs are defined as crystalline and porous covalent organic materials made by the combination of organic building units, covalently linked into extended structures. The backbone of covalent organic frameworks is composed entirely of light elements (B, C, N, O, Si) [22]. The first example of a COF-based MMM was reported in 2016. The membrane was fabricated by coating a supporting polysulfone membrane with a 10 wt% solution of a 2D imine-based COF in poly(vinylamine)(PVAm). The resulting MMM was then studied for hydrogen purification applications (*e.g.* CO_2/H_2 separation) [23]. Another good example of COF-based MMMs is from

Biswal *et al*., where two isoreticular COFs with different pore sizes were dispersed into the *tert*-butylpolybenzimidazole (PBI–BuI) matrix to fabricate MMMs with excellent mechanical strength and good separation performance. Favourable interactions between the H-bonded benzimidazole groups of PBI-BuI and the COFs made possible to enhance the filler loading up to 50% in weight (Figure 3.4) [24].
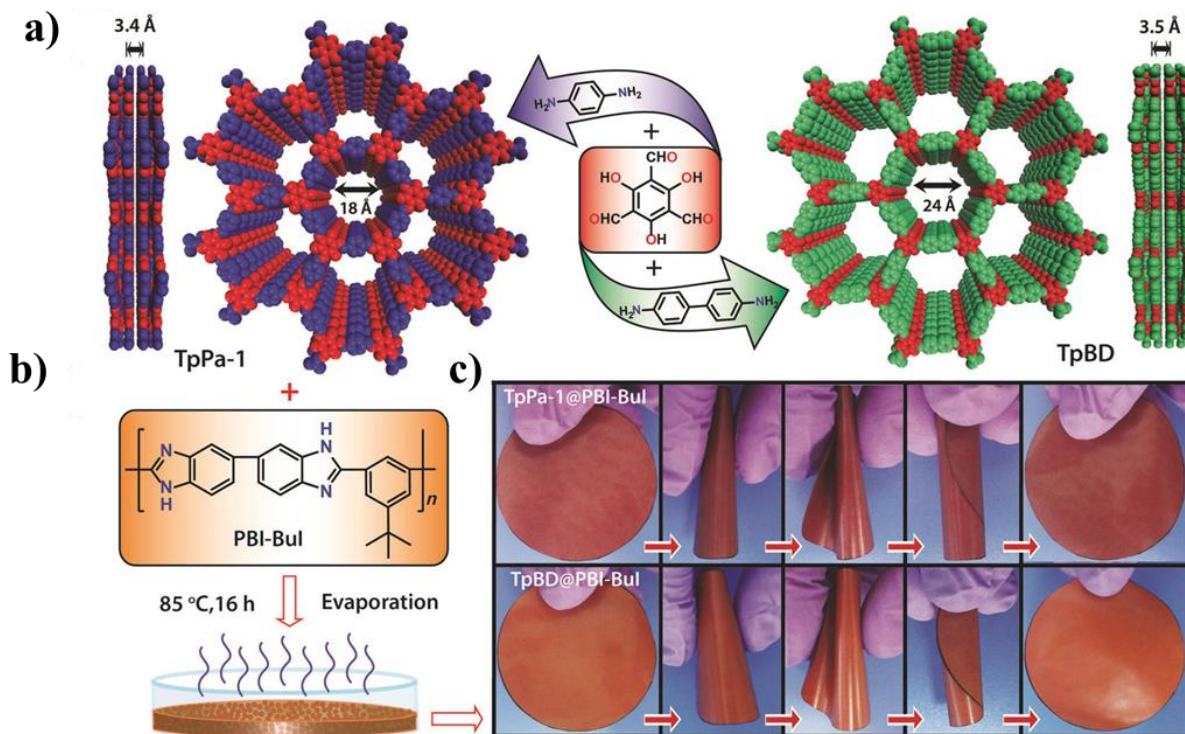

Figure 3.4 a) Schematic representations of the synthesis of COFs TpPa-1 and TpBD and their packing models indicating the pore aperture and stacking distances. b) Overview of the solution-casting method for COF@PBI-BuI hybrid membrane fabrication. c) Digital photographs showing the flexibility of TpPa-1@PBI-BuI and TpBD@PBI-BuI mixed matrix membranes. From ref. [24].

3.2.3 Organic Cages as Filler in MMMs

Extended frameworks like MOFs and POFs offer high surface areas and a wide range of chemical functionalities, but usually exhibit a low solubility in common solvents employed for polymers. This last issue may result in a poor dispersion of the filler, thus leading to defective mixed-matrix membranes. As an alternative to MOFs and POFs, Porous Organic Cages (POCs) recently attracted significant attention due to their better solubility and processability in organic solvents, as well as for the intrinsic porosity (*i.e.* the internal cavity of the cage). Moreover, the organic nature of these materials favours the establishment of polymer-filler interactions at a molecular level, resulting in a uniform distribution of the filler in the membrane.

The first example of a porous organic cage, employed as filler in MMM for gas separation applications, was reported by Bushell *et al.* in 2013 [25]. In the cited work, an imine-based porous organic cage (named **CC3**), formed by Schiff condensation of 1,3,5-triformylbenzene with (R,R)-1,2-diaminocyclohexane, was dissolved in chloroform and added to a solution of PIM-1, an amorphous glassy polymer with intrinsic microporosity and good performance in the separation of gases [26]. By slow evaporation of the mixture, a dense polymeric mixed-matrix membrane was obtained, containing crystals of the cage embedded in the PIM-1 polymer (Figure 3.5). Notably, the MMM showed better permeability and resistance towards physical aging than the plain PIM-1 membrane.
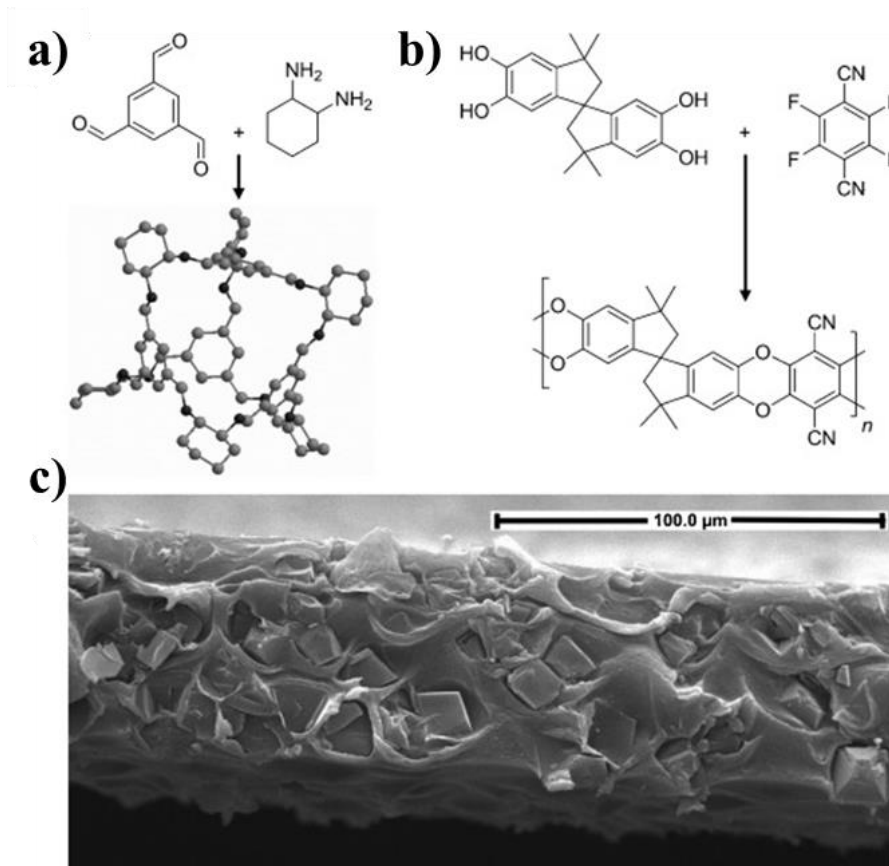
Figure 3.5 a) Synthesis of the porous **CC3** cage from 1,3,5-triformylbenzene and (*R,R*)-1,2-diaminocyclohexane. b) Synthesis of PIM-1 from 5,5′,6,6′-tetrahydroxy-3,3,3′,3′-tetramethyl-1,1′-spirobisindane and 1,4-dicyanotetrafluorobenzene by double aromatic nucleophilic substitution polymerization. c) SEM image of the cross-section of PIM-1/**CC3** composite membrane (weight ratio 10:2). From ref. [25].

These achievements were also compared by the Authors to those obtained with the MMM containing PIM-1 and the reduced form of **CC3**. Nonetheless, with respect to **CC3**, the corresponding polyamine-based molecular material is poorly porous in the solid state. As a result of the low porosity of this filler, the corresponding MMM was characterized by a lower permeability compared to the neat polymer membrane.

This study was followed by a computational work by Evans *et al.*, focused on a series of POCs as potential fillers for MMMs to be applied in the separation of industrially relevant gas mixtures (H_2/N_2, H_2/CO_2, CO_2/N_2 and CO_2/CH_4) [27]. In particular, the Authors investigated the tetrahedral imine cages (**CC1**, **CC2**, **CC3**) by Cooper and co-workers, [26] an adamantoid cage from the group

of Mastalerz, [28] and an elongated, all-carbon-bonded, triangular dipyramidal cage [29]. The results of these theoretical investigations on POC-based MMMs were compared to the experimental results, showing that the considered molecular fillers could effectively enhance both the selectivity and permeability of polymer membranes, especially for the H_2/N_2 and H_2/CO_2 separations.

In 2017, Mao and Zhang studied another family of porous organic cages (*i.e.* Noria and its derivatives) as potential fillers in MMMs [30]. Noria is a porous organic cage with high adsorption selectivity for CO_2 over H_2 and N_2 [31]. The hydroxyl groups on the molecular framework make the cage highly soluble in polar solvents, and also favour the post-functionalization of the cage with sterically demanding groups such as *tert*-butyloxycarbonyls (*i.e.* Noria-Boc) or *t*-butyl esters (*i.e.* Noria-CO^{t}Bu) (Figure 3.6). Noria-based MMMs were prepared by dissolving the cages and the polymer (6FDA-DAM: 6FDA: 4,4'-(hexafluoroisopropylidene)diphthalic anhydride and DAM: 2,4,6-trimethyl-1,3-diaminobenzene) in dimethylacetamide. The mixture was casted into glass plates, then dried for 12 h at 80 °C, and finally dried under vacuum for 24 h at 200 °C (annealing). The study showed that the presence of bulky groups on the cage framework improved the filler dispersion into the matrix, compared to pristine Noria. However, in some cases (*e.g.* Noria-Boc) a lower thermal stability was found, due to the loss of the bulky substituents during the final thermal treatment.
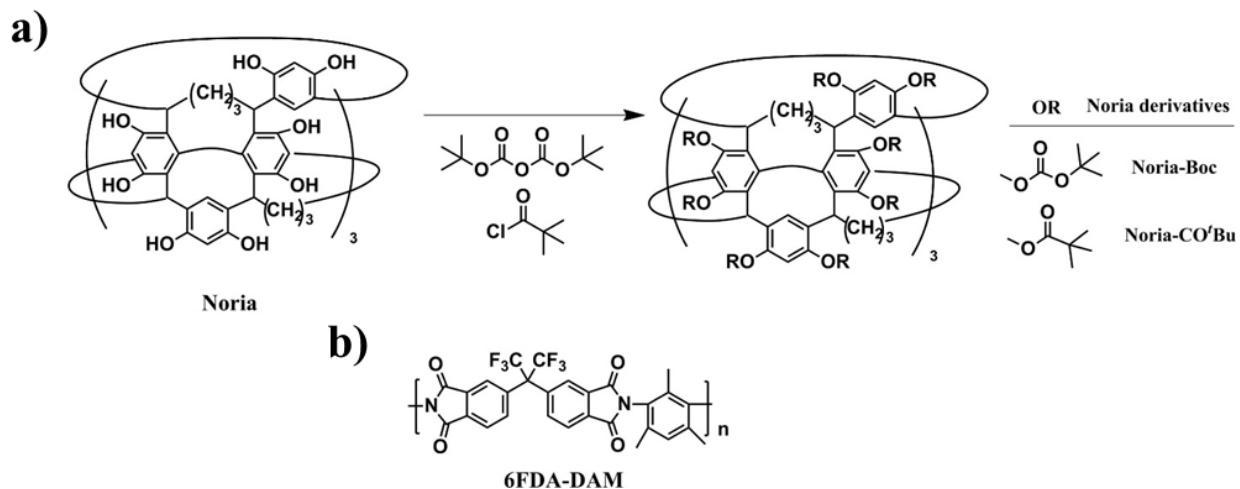
Figure 3.6 a) Noria and its derivates. b) The polyimide 6FDA-DAM. From ref. [30].

The separation performances of the resulting MMMs strongly depend on the chemical structure of the fillers. In particular, the Noria cage could increase the rigidity of polymer chains, hence decreasing the permeability but improving the selectivity. On the contrary larger pores and higher surface area in the Noria-CO^{t}Bu system improved the gas permeability at the expense of selectivity. POCs as fillers in MMMs are also interesting for C_3H_6/C_3H_8 separation processes. The purification of propylene (C_3H_6) from propane (C_3H_8), for instance, is essential in the production of many industrial chemicals. The two gases have similar sizes and boiling points and the current separation is based on a very energy-expensive cryogenic distillation. Membrane-based purification processes are considered as an effective alternative in this crucial industrial step [32]. In the work by Duan and co-workers, a defect-free mixed matrix membrane composed by 6FDA-DAM polyimide and 20 wt% **CC3** showed a very high C_3H_6 permeability and good C_3H_6/C_3H_8 selectivity, exceeding the Robeson upper bound. As in the previous study by Bushell *et al.*, [25] the cage crystallized into the polymer matrix, thus forming a hierarchical transport channel that improved the olefin permeation. Moreover, the performances of the prepared MMM proved to be stable over long term permeation tests, showing promising perspectives for industrial propylene purification through membranes [33].

3.2 EXPERIMENTAL

### 3.2.1 Chemicals and Methods

Solvents and chemicals used for synthesis were HPLC grade. Acetonitrile, diethylether, tris(2-ethylamino) amine 96%, 2,5-furandicarbaldehyde 97%, isophthalaldehyde 97%, terephthalaldehyde reagent Plus 99% and deuterated solvents used for NMR analysis ($CDCl_3$) were purchased from Sigma-Aldrich, Merck Italia (Milano, Italy). Diphenyl-4,4′-dicarboxyaldehyde was synthesized based on a procedure already described [34]. PEEK-WC was supplied by the Institute of Applied Chemistry, Changchun, China. PDMS resin ELASTOSIL® M 4601 A/B was provided by Wacker Chemie AG. (Munich, Germany). Chloroform AnalaR NORMAPUR®, was supplied by VWR International srl, Milano, Italy. Pure gases H_2, He N_2, O_2, CH_4, CO_2 (99.99+%) used for permeation tests were purchased from SAPIO. ^{1}H-NMR spectra were recorded on a Bruker ADVANCE 400 spectrometer (operating at 9.37 T, 400 MHz). Chemical shifts are reported in ppm with the residual solvent as internal reference. NMR spectra were recorded at 25.0 °C. X-ray powder diffraction (XRPD) measurements were performed at room temperature on the powders of the four cage samples after manual grinding in an agate mortar using a Bruker D5005 diffractometer (Bruker Corporation, Billerica, MA, USA) with CuKa radiation, graphite monochromator, and scintillation detector. The measurements were performed from 3° to 70° with step scan mode: scan step 0.02°, counting time 10 s per step; X-ray tube working conditions: 40 kV and 40 mA. For the Fourier Transform Infrared analysis (FTIR), a Nicolet FTIR iS10 spectrometer (Nicolet, Madison, WI, USA) equipped with attenuated total reflectance (ATR) sampling accessory (Smart iTR with diamond plate) was used. Thirty-two scans in the 4000–600 cm^{-1} range at 4 cm^{-1} resolution were coadded. Well-ground powder samples were used and spectra were obtained after pressing the sample onto the ATR diamond crystal at room temperature (20 °C). Peak wavenumbers were attributed by using the "Find peaks" function of the OMNIC™ Spectra Software. Thermogravimetric analysis (TGA) was performed by a Q5000 apparatus (TA Instruments, New Castle, DE, USA) interfaced with a TA5000 data station under nitrogen flux (10 mL min^{-1}) in a platinum pan by heating about 3 mg of sample from room temperature up to 500 °C (heating rate 5 K min^{-1}). Differential scanning calorimetry (DSC) was performed by a Q2000 apparatus (TA Instruments, New Castle, DE, USA) interfaced with a TA5000 data station by

heating about 3 mg of powder in an open aluminum crucible from −50 °C to 350 °C (heating rate 5 K min^{-1}) under nitrogen flux (50 mL min^{-1}). Three independent measurements on three different samples were performed for each cage. The temperature accuracy of the instrument is ±0.1 °C, the precision is ±0.01 °C, and the calorimetric reproducibility is ±0.05%. TGA and DSC data were analyzed by the Universal Analysis software by TA Instruments. Scanning electron microscopy (SEM) analysis of the powder was performed by Phenom Pro X desktop SEM, Phenom-World. The images were acquired with an accelerating voltage of 10 kV at different magnification: 1000×, 5000×, and 20,000×. Scanning electron microscopy (SEM) analysis of the membranes was performed by a Phenom Pro X desktop SEM, Phenom-World. The images were acquired with an accelerating voltage of 15 kV at different magnifications: 1000×, 5000×, and 20,000×.

3.2.2 Synthesis of Cages GI1-4

Cages (**GI1**–**4**) have been previously reported [35-38] and were obtained following a modified procedure recently described by Lehn *et al* [35].

The solubility of cages **GI1**–**4** was tested in various solvents (MeOH, EtOH, CHCl$_3$, CH$_2$Cl$_2$, and THF at T = 25 °C): about 2 mg of each cage was weighted in a test tube and solvent was added in small portions until complete dissolution of the powder at room temperature (under sonication). The trial was repeated for each solvent. The obtained results are shown in table 3.1.
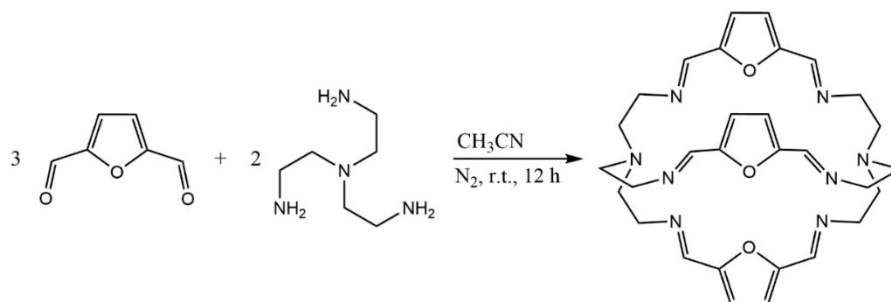
GI1. A solution of 420 µL of tren (tris(2-aminoethyl)amine) (2.67 mmol, 2 eqv) in 150 mL of acetonitrile was slowly added 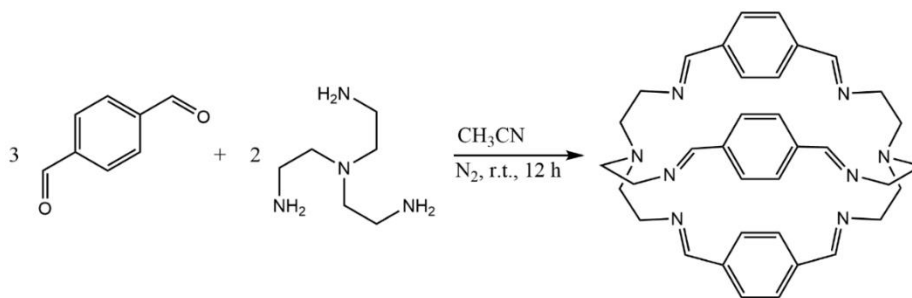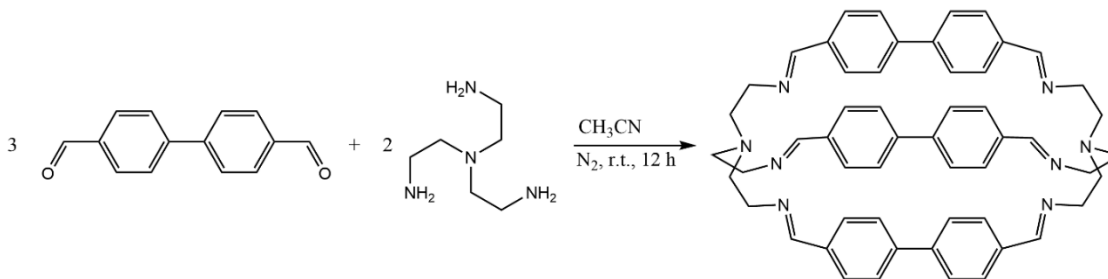to a solution of 500 mg of 2,5-furandicarbaldehyde (4 mmol, 3 eqv) in 200 mL of acetonitrile, placed into a round bottom flask, under N_2 and under vigorous magnetic stirring at room temperature. After 12 hours, the formed precipitate was collected on a Buchner funnel and washed with 50 mL of acetonitrile. The cage was dried under vacuum for two days to obtain 530 mg of brownish microcrystals, which were characterized and employed in the preparation of MMMs without further purification. Yield:72%; ^{1}H-NMR (400 MHz, CDCl$_3$) δ: 7.72 (s, 6H, CH_{imine}), 7.08 (s, 6H, CH_{fura}), 3.54 (br, 12H, CH$_2$), 2.74 (br, 12H, CH$_2$); FTIR-ATR (cm^{-1}): 1629.03 (C=N stretching).
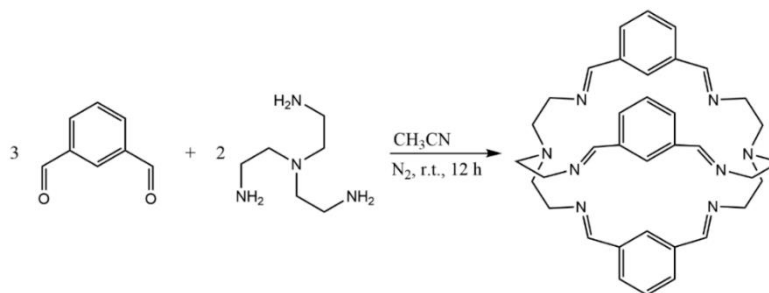
GI2. A solution of 420 µL of tren (tris(2-aminoethyl)amine) (2.67 mmol, 2 eqv) dissolved in 150 mL of acetonitrile was slowly added to a solution of 536 mg of isophthalaldehyde (4 mmol, 3 eqv) in 200 mL of acetonitrile, placed into a round bottom flask, under N_2 and vigorous magnetic stirring at room temperature. After 12 hours, the formed precipitate was collected on a Buchner funnel and washed with 50 mL of acetonitrile. The cage was dried under vacuum for two days to obtain 590 mg of a white microcrystalline powder and then characterized and employed in the preparation of MMMs without further purification. Yield:76%; ^{1}H-NMR (400 MHz, CDCl$_3$) δ: 8.19 (d, 6H, CH), 7.59 (s, 6H, CH_{imine}), 7.53 (t, 3H, CH), 5.34 (s, 3H, CH), 3.77 (br, 6H, CH_2), 3.30 (br, 6H, CH$_2$), 2.91 (br, 6H, CH_2), 2.71 (br, 6H, CH$_2$); FTIR-ATR (cm^{-1}): 1641.37 (C=N stretching).

GI3. A solution of 420 µL of tren (tris(2-aminoethyl)amine) (2.67 mmol, 2 eqv) dissolved in 150 mL of acetonitrile was slowly added to a solution of 536 mg of terephthalaldehyde (4 mmol, 3 eqv) dissolved in 200 mL of acetonitrile in a round bottom flask under N_2 and vigorous magnetic stirring at room temperature. After 12 hours, the formed precipitate was collected on a Buchner funnel and then washed with 50 mL of acetonitrile. The cage was dried under vacuum for two days to obtain 605 mg of a white powder and then characterized and employed in the preparation of MMMs without further purification. Yield:78%; ^{1}H-NMR (400 MHz, CDCl$_3$) δ: 8.17 (s, 6H, CH_{imine}), 7.17 (s, 12H, CH), 7.53 (t, 3H, CH), 3.77 (br, 12H, CH_2), 2.77 (br, 12H, CH$_2$); FTIR-ATR (cm^{-1}): 1638.62 (C=N stretching).

GI4. A solution of 210 µL of tren (tris(2-aminoethyl)amine) (1.33 mmol, 2 eqv), dissolved in 75 mL of acetonitrile, was slowly added to a solution of 421 mg of terephthalaldehyde (2 mmol, 3 eqv) in 200 mL of acetonitrile, placed into a round bottom flask, under N_2 and vigorous magnetic stirring at room temperature. After 12 hours, the formed precipitate was collected on a Buchner funnel and washed with 50 mL of acetonitrile. The cage was dried under vacuum for two days to obtain 386 mg of a white powder and then characterized and employed in the preparation of MMMs without further purification. Yield:71%; ^{1}H-NMR (400 MHz, CDCl$_3$) δ: 8.28 (s, 6H, CH_{imine}), 7.23 (d, 12H, CH), 7.10 (d, 12H, CH), 3.83 (br, 12H, CH_2), 2.83 (br, 12H, CH$_2$); FTIR-ATR (cm^{-1}): 1638.44 (C=N stretching).

3.2.3 Membranes Preparation

Mixed matrix membranes were prepared using the PEEK-WC polymer, with a loading of 20 wt % of each cage based on polymer mass. PEEK-WC was dissolved in chloroform at 3 wt % under magnetic stirring for 24 h at room temperature. Then, the obtained solution was filtered through a glass syringe filter of 3.1 μm. The cages were dispersed in chloroform and sonicated for 30 min before their addition to the PEEK-WC solution. The PEEK-WC/Cage suspension was sonicated for 5 h at room temperature, in order to obtain a homogeneous dispersion. The solutions were casted in a Teflon petri dish and the self-standing dense membranes were obtained by solvent evaporation at 35 °C. Finally, the obtained membranes were coated with PDMS Elastosil M 4601 to perform the defect healing process. The two-component PDMS, A and B, were mixed in a 9:1weight ratio, according to the instructions of the supplier, without the use of a solvent. A film of ca. 25 μm of the resin was applied on the surface of the membrane by a casting knife. The coated membranes were kept at room temperature to complete the crosslinking in 24 h.

3.2.4 Membranes Characterization

Single gas permeation measurements were performed on circular membranes (exposed area 13.84 cm^2) at 25 °C and at a feed pressure of 1 bar by a fixed volume/pressure increase instrument designed by HZG and constructed by EESR (Geesthacht, Germany).[39] Before each measurement, the membranes were evacuated in the testing cell by a turbo-molecular pump until complete desorption of all previously adsorbed gases and humidity. For the same reason, between two consecutive tests, the membranes were evacuated for a time equal to 10 times the time lag of the previous gas. The time lag method was used for the determination of the permeability (P), diffusion (D), and solubility coefficients (S), which can be obtained from the increase of the permeate pressure, p_t, as a function of time, t, after exposure of the membrane to the gas (equation 6) [40]:

$$p_t = p_0 + \left(\frac{dp}{dt}\right)_0 \cdot t + \frac{RT}{V_p \cdot V_m} \cdot A \cdot l \cdot p_f \cdot S \cdot \left(\frac{Dt}{l^2} - \frac{1}{6} - \frac{2}{\pi^2} \sum_{n=1}^{\infty} \frac{(-1)^n}{n^2} exp\left(\frac{Dn^2\pi^2 t}{l^2}\right)\right)$$

(eq. 6)

where p_0 and $(dp/dt)_0$ are the starting pressure and baseline slope, respectively, which should be negligible in a well-evacuated and leak free membrane and permeability instrument. R is the universal gas constant, T the absolute temperature, V_p the permeate volume, V_m the molar volume of a gas at standard temperature and pressure [22.41×10^{-3} m^{3}STP mol^{-1} at 0 °C and 1 atm], A the exposed membrane area, l its thickness, p_f the feed pressure, S the gas solubility and D the diffusion coefficient. The permeability P was obtained from the permeation curve in the pseudo steady-state (equation 7):

$$p_t = p_0 + \left(\frac{dp}{dt}\right)_0 \cdot t + \frac{RTA}{V_p \cdot V_m} \cdot \frac{p_f P}{l} \cdot \left(t + \frac{l^2}{6D}\right)$$

(eq. 7)

The diffusion coefficient is inversely proportional to time lag (θ) and was calculated from equation 8:

$$\theta = \frac{l^2}{6D}$$

(eq. 8)

The solubility coefficient (S), was calculated from the solution–diffusion transport model (equation 9):

$$S = \frac{P}{D}$$

(eq. 9)

3.3 RESULTS AND DISCUSSION

3.3.1 Cages Preparation and Characterization

The polyimine bis-tren cages **GI1–GI4** (Figure 3.7) were obtained in high yields (>70%) following a modified procedure described in the literature, which consist in the slow addition of a solution of tren to a solution of the chosen dialdehyde – mixed in a 2:3 molar ratio – in acetonitrile solution [35]. The imine condensation produced pure solid products, that precipitated from the reaction mixture, while unreacted reagents and other impurities remained dissolved. Simple vacuum filtration and subsequent drying allowed to obtain the pure cages (Figure 3.7).
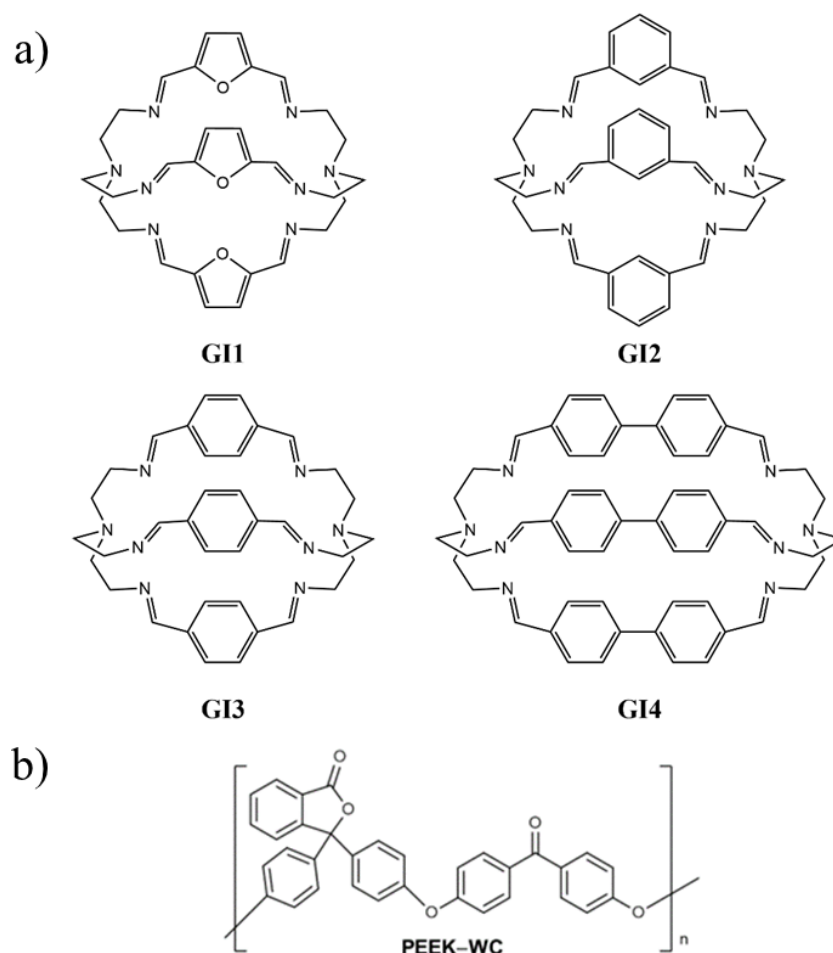

Figure 3.7 Chemical structure of the cages **GI1-4** and PEEK-WC polymer.

The ^{1}H-NMR spectra of cages **GI1–GI4** (see chapter 3.5) in CDCl$_3$ correspond to those reported in the literature [35]; FTIR-ATR spectra further confirm the presence of imine bonds as it results

from the typical peaks (between 1629 and 1641 cm^{-1}) due to the stretching of the C=N bond. Before starting the MMM preparation, solubility tests were conducted on the compounds to determine the best solvent for the dissolution of the cages. The experiment was conducted at room temperature with various solvents normally used in membrane preparation (see chapter 3.2.2). The results listed in table 3.1 showed that **GI1** and **GI2** cages are generally more soluble than **GI3** and **GI4** in all tested solvents. Halogenated solvents (*i.e.* chloroform and dichloromethane) resulted to be the best for all four cages even if the absolute value is not as high as we expected. Despite this result, we decided to use CHCl$_3$ as solvent for membrane preparation since it is a good solvent for the dissolution of the PEEK-WC polymer too.

Table 3.1 Solubilities of the cages. X = insoluble

Cage	Spacer	Solubility (wt/vol %) in the given solvent				
		MeOH	EtOH	CHCl$_3$	CH$_2$Cl$_2$	THF
GI1	furanyl	0.10	0.08	0.13	0.10	X
GI2	m-xylyl	0.13	0.10	0.40	0.40	0.20
GI3	p-xylyl	X	X	0.20	0.13	X
GI4	diphenyl	X	X	0.10	0.07	X

XRPD analyses were conducted on the dried cages to investigate their phases. **GI1** and **GI2** resulted to be in a microcrystalline phase, as indicated by the intense and sharp signals in the XRPD patterns (Figure 3.8). Notably, the experimental patterns of **GI1** and **GI2** are in very good agreement with the patterns predicted based on the single crystal X-ray diffraction data found in the literature. The orthorhombic crystals of **GI1**, reported by Nelson *et al.*, present one crystallization water molecule per cage, H-bonded to the imine nitrogen atoms of two adjacent macrobicyclic molecules (Figure 3.9) [36]. These hydrogen bonds link the cages in one-dimensional chains that extend through the structure. On the other hand, in the rhombohedral crystals of **GI2**, there is no evidence of intermolecular interactions with solvent molecules (Figure 3.10) [37]. XRPDs of **GI3** and **GI4** are completely different from those of **GI1** and **GI2**, with few peaks superimposed to a broad signal, attributable to a significant amorphous phase, in the 10-30° angular range (Figure 3.11).
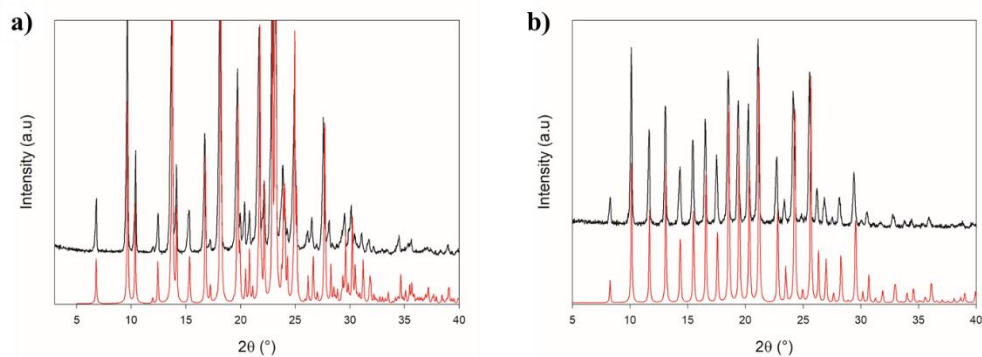
Figure 3.8 a) XRPD pattern of **GI1**. b) XRPD pattern of **GI2**. Black lines: experimental; Red lines: predicted on the basis of SCXRD data reported in ref.s [36,37].
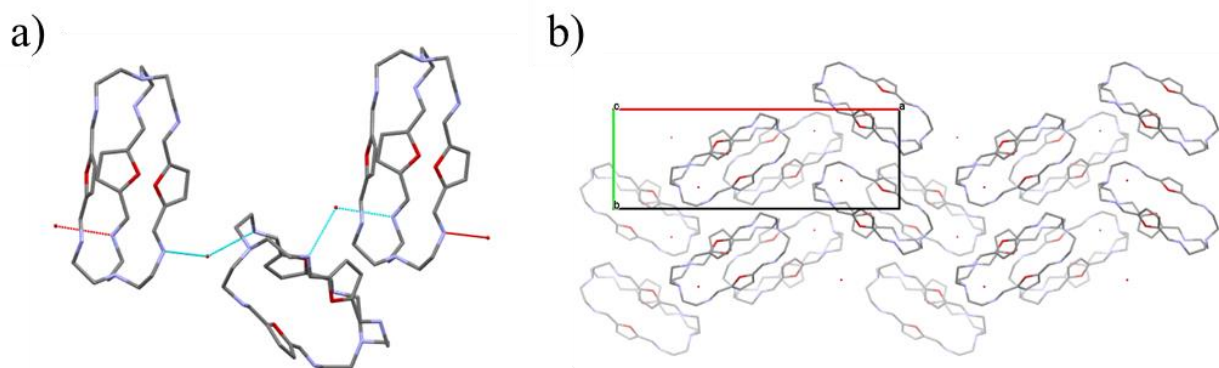

Figure 3.9 s) SCXRD of **GI1** reported in ref. [36] with highlighted H-bonds between water molecules and two adjacent cages. b) View of crystal packing along c-axis. Red: oxygen; Gray: carbon; Blue: nitrogen. Hydrogen atoms omitted for clarity.
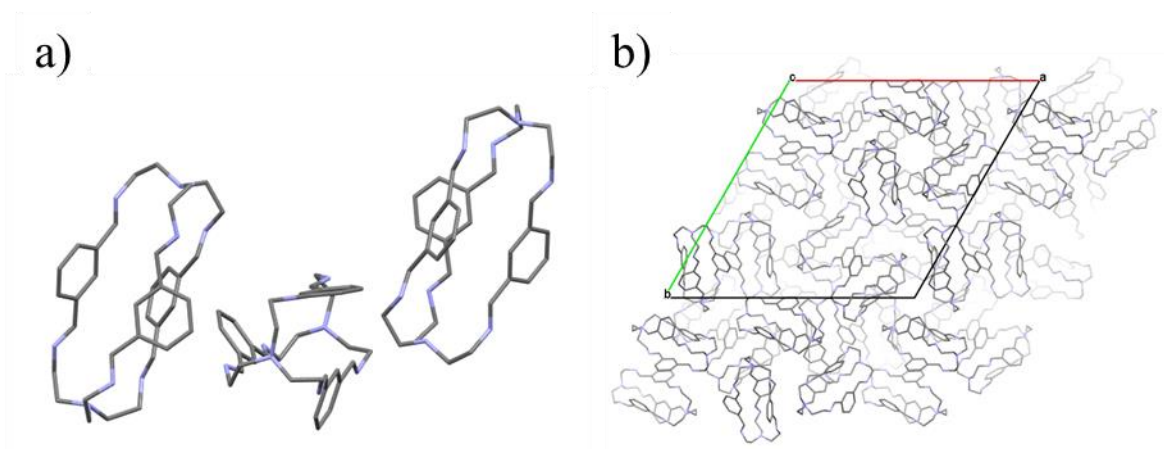
Figure 3.10 Left: SCXRD of **GI2** reported in ref. [37]. No solvent molecules are present in this case. Right: view of crystal packing along c-axis. Gray: carbon; Blue: nitrogen. Hydrogen atoms omitted for clarity.
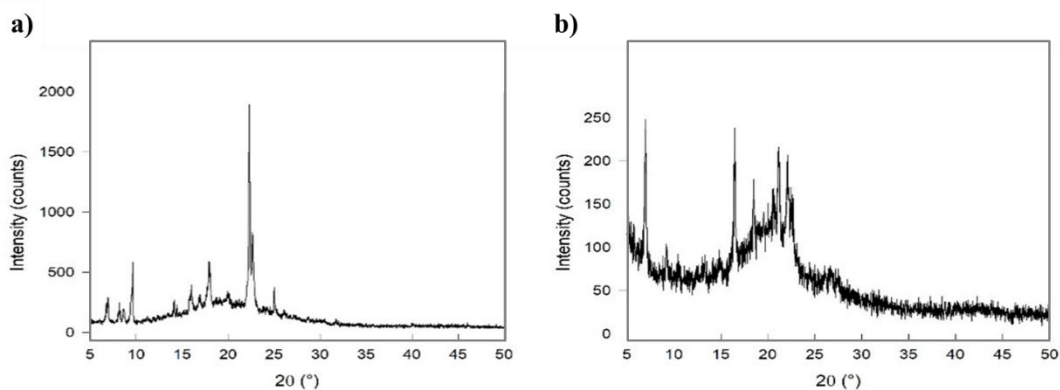

Figure 3.11 a) XRPD pattern of **GI3**. b) XRPD pattern of **GI4**.

Thermal stability was evaluated by TGA and DSC measurements (Figures 3.12-3.15). These analyses revealed that **GI2** and **GI4** are the most thermally stable compounds, with no decomposition up to 250 °C (Figures 3.13 and 3.15 respectively). On the other hand, **GI1** and **GI3** start to decompose at lower temperatures, as shown by the derivative of TGA curves (*i.e.* DTG, δm/δT) and by the events in DSC profiles (Figures 3.12 and 3.14, respectively). In the TGA curves, it was also possible to detect mass losses due to the release of adsorbed solvent (residual solvent from synthesis, humidity). In the case of **GI1**, for instance, the solvent release occurs at about 80 °C. In a similar way. the TGA curve of **GI3** shows two small mass losses between room temperature and 100 °C. On the contrary, **GI2** and **GI4** did not show any solvent loss.

The irreversible nature of these processes (release of adsorbed solvent or decomposition) is confirmed by the cooling curves in the DSC profiles, that are "flat" and do not show any relevant signal in the same temperature range.
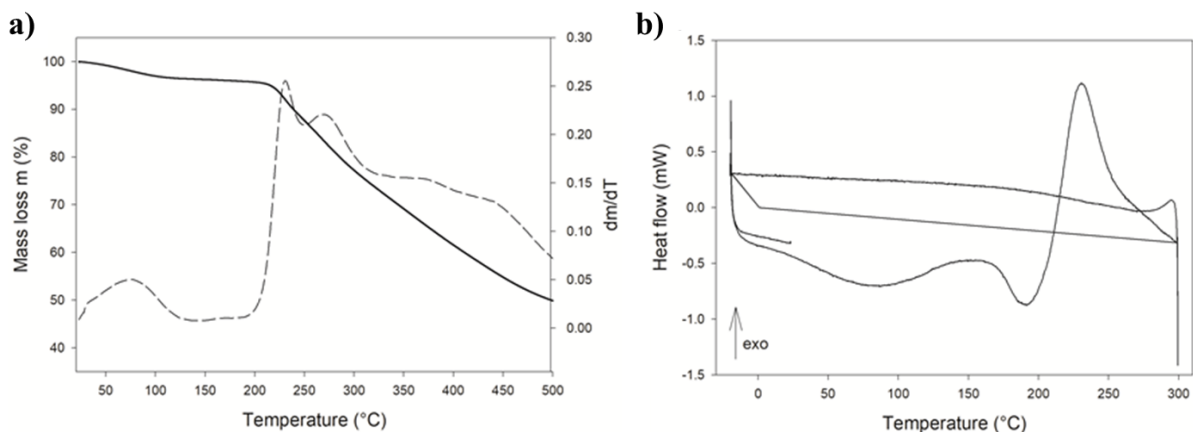

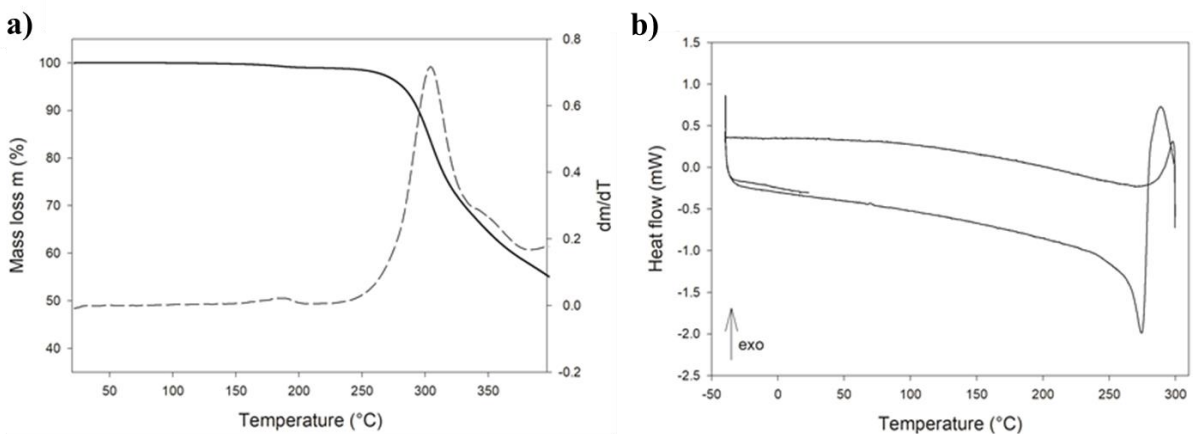**Figure 3.12** a) TGA (solid line) and DTG (dashed line) of **GI1**. b) DSC curve of **GI1**.

Figure 3.13 a) TGA (solid line) and DTG (dashed line) of **GI2**. b) DSC curve of **GI2**.
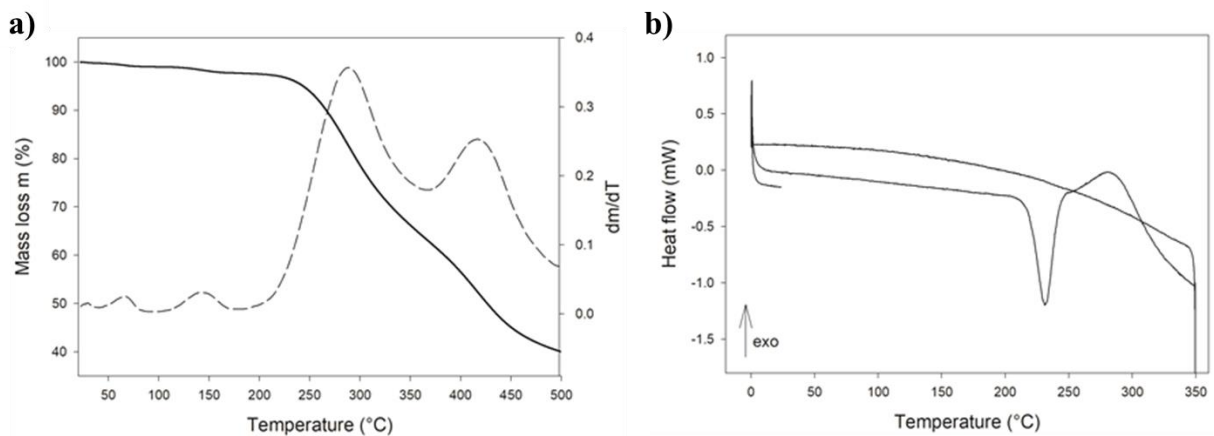
Figure 3.14 a) TGA (solid line) and DTG (dashed line) of **GI3**. b) DSC curve of **GI3**.
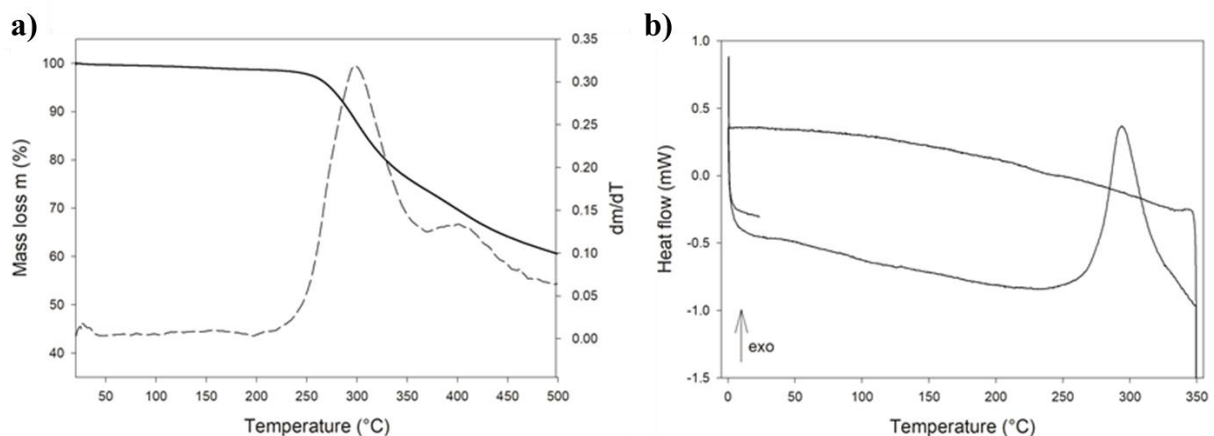

Figure 3.15 a) TGA (solid line) and DTG (dashed line) of **GI4**. b) DSC curve of **GI4**.

The morphological analysis of the cages by SEM showed that most of the powders are composed by irregular-shape particles with heterogeneous size (Figures 3.16-3.19). In the case of **GI2**, large and irregular aggregates were found with size up to 80 μm, while for **GI3** we observed aggregates of fine spherical-shaped particles, with diameter of ca. 1 μm, that could be seen at the highest magnification. The SEM images of **GI4** displayed heterogeneous agglomerates of flakes and needle-like crystals, but no specific morphology could be identified. Only in the case of **GI1**, the SEM images displayed microcrystals of various size, with length from few μm up to 50 μm, whose shape is consistent with an orthorhombic lattice. This agrees with the result obtained by comparing the experimental XRPD pattern with that predicted on the basis of published single crystal analysis (Figure 3.8) [36].
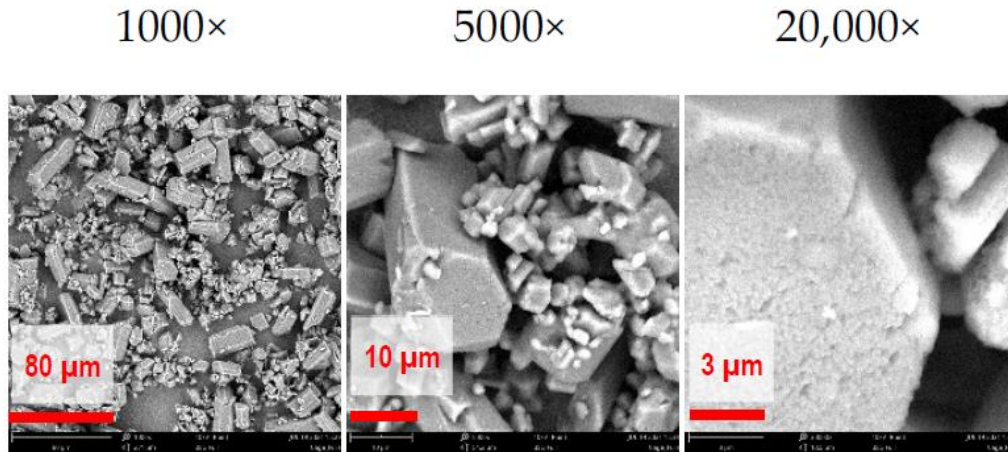
Figure 3.16 SEM images of **GI1** as collected in its powder form at different magnifications.
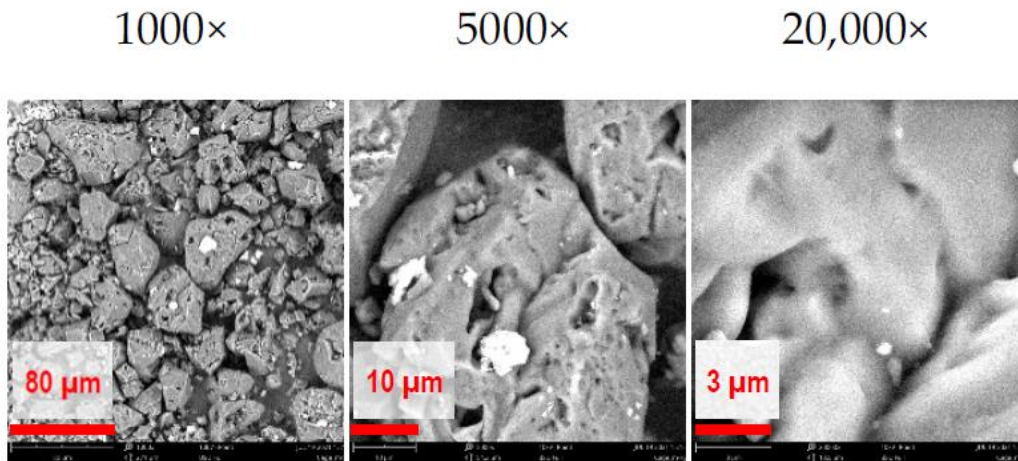
Figure 3.17 SEM images of **GI2** as collected in its powder form at different magnifications.
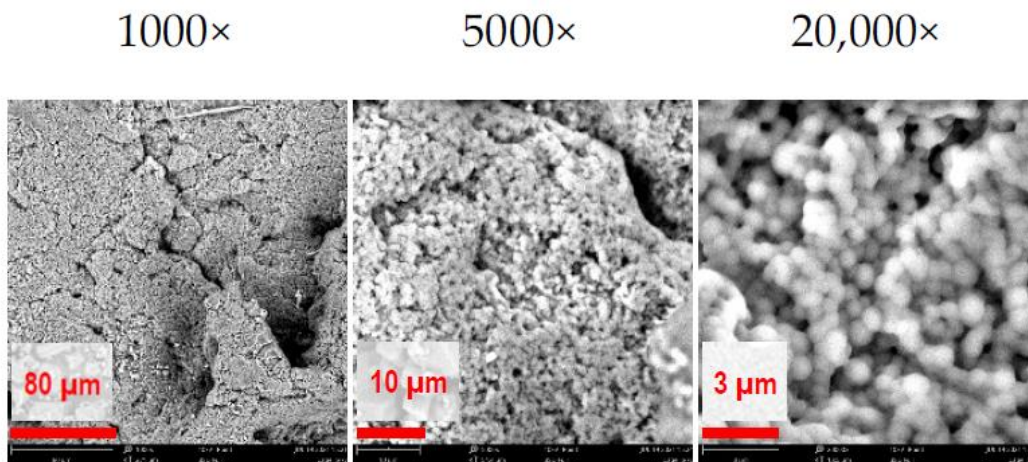
Figure 3.18 SEM images of **GI3** as collected in its powder form at different magnifications.
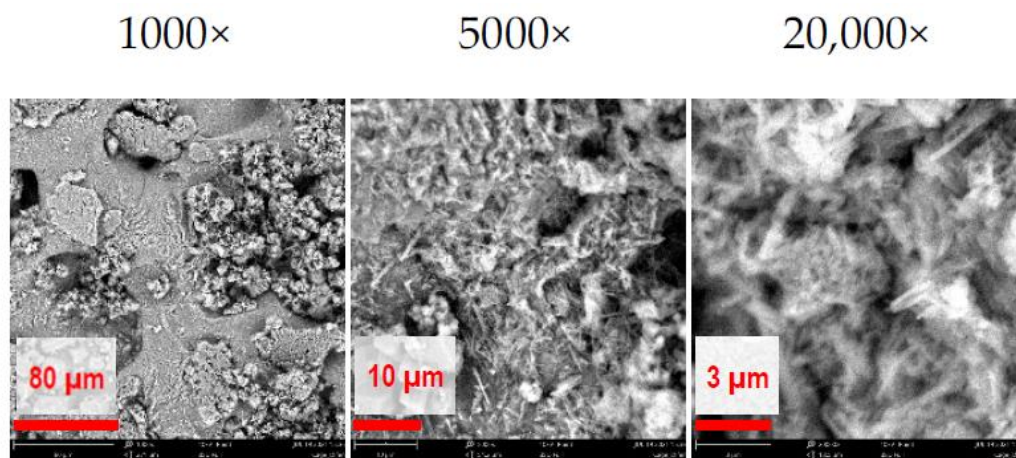
Figure 3.19 SEM images of **GI4** as collected in its powder form at different magnifications.

3.3.2 Membranes Preparation and Characterization

The cages solubility was found to be rather low in all the investigated solvents (Table 3.1). Therefore, as a route for the mixed-matrix membranes preparation, the cages were dispersed into solutions of the polymer in chloroform. This approach, however, allowed to obtain robust membranes only in the case of cages **GI1** and **GI2**. The novel MMMs, PEEK-WC/**GI1** and PEEK-WC/**GI2**, did not show any visible macroscopic defect or inhomogeneity, suggesting an even dispersion of the fillers in the polymer matrix. The membranes were only slightly opaque due to the different refractive index of the polymer and the filler materials and showed a thickness of 78

μm and 42 μm for PEEK-WC/**GI1** and PEEK-WC/**GI2**, respectively. On the other hand, **GI3** and **GI4** were not suitable for the preparation of homogeneous and stable membranes due to their poor dispersion in the polymeric solution. This is a consequence of the clustering of **GI3** and **GI4**, confirmed by the SEM images (Figures 3.18 and 3.19), that hindered the homogenous dispersion of the cages into the polymer matrix. The morphology of good MMMs was then studied by SEM analysis of the top and bottom surfaces, as well as their cross-section (Figure 3.20-3.22).

Figure 3.20 SEM images of the top surface of PEEK-WC-based membranes and the cages **GI2** (top) and **GI1** (bottom) at different magnifications.
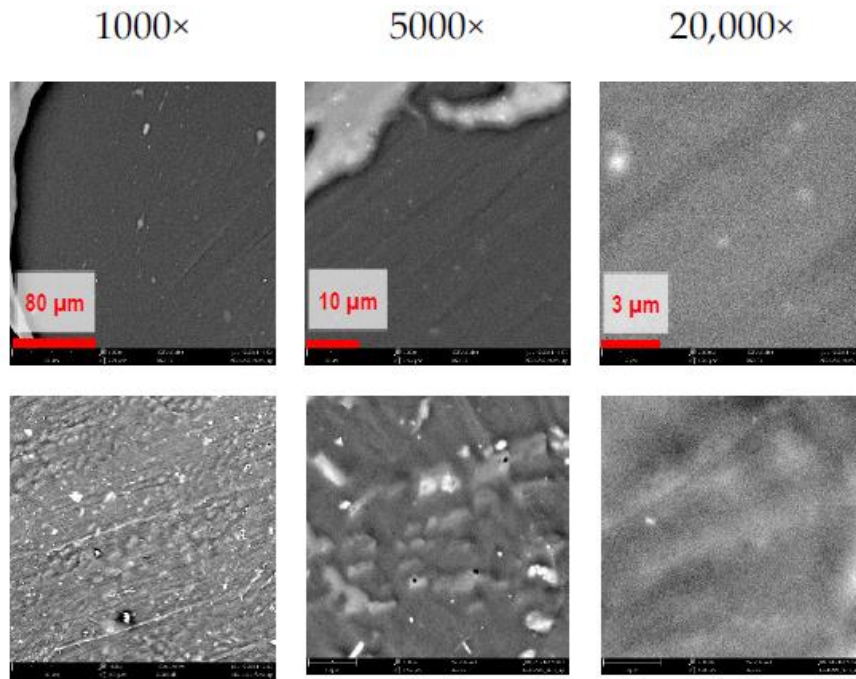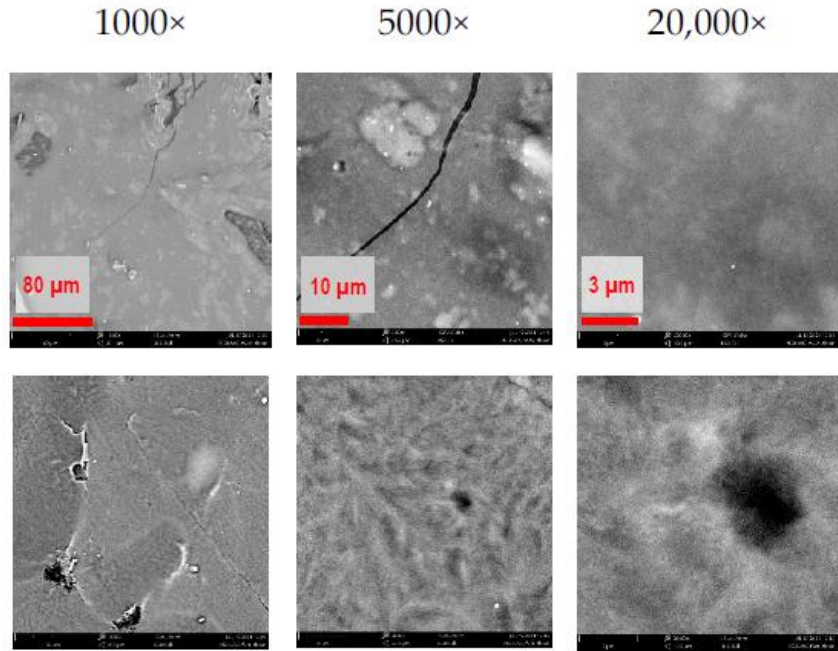
Figure 3.21 SEM images of the bottom surface of PEEK-WC-based membranes and the cages **GI2** (top) and **GI1** (bottom) at different magnifications.
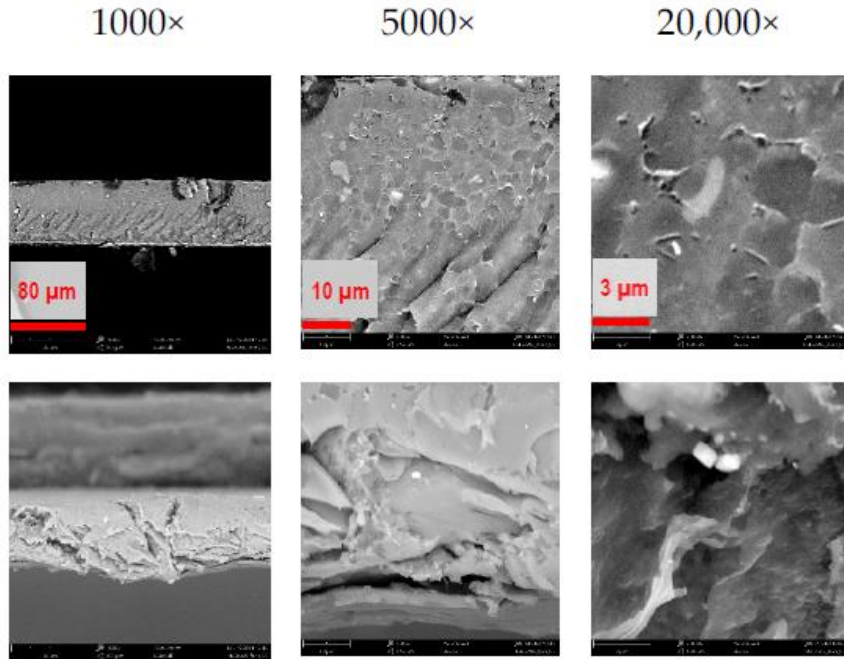

Figure 3.22 SEM images of the cross section of PEEK-WC-based membranes and the cages **GI2** (top) and **GI1** (bottom) at different magnifications.

It should be noted that the fully organic nature of both polymer and cages does not give a strong contrast in the SEM pictures, hence the cage clusters are poorly visible. The top and bottom surface images show that the PEEK-WC/**GI1** membrane has several irregularities such as pores and cracks. On the contrary, PEEK-WC/**GI2** displays smooth and homogenous surfaces with only few defects. Cross-section images confirmed this trend, showing that the PEEK-WC/**GI1** membrane is not uniform while PEEK-WC/**GI2** is characterized by a well-defined and dense layer. These pictures indicate that the dispersion of **GI2** in the membrane is quite good, while **GI1** leads to more defects in the corresponding membrane. The presence of cracks and pores usually brings about low selectivity membranes, for which the gas separation process takes place through Knudsen diffusion. The Knudsen diffusion occurs when channels of a larger diameter than the mean free path of gas species are present in the membrane. This kind of transport must be avoided as it prevails over the solution–diffusion mechanism, making gas separation less effective.

For this reason, membranes presenting these types of imperfections need to undergo a healing process. In this case, membranes were coated with a dense polydimethylsiloxane (PDMS) layer, following a widely used procedure for the correction of pinhole defects in membranes for gas separation [41-44]. It should be noted that the effect of PDMS on the diffusive transport through the dense membrane is negligible, when there is a difference of several orders of magnitude in the intrinsic permeability coefficients with the polymer, as in the case of PEEK-WC-based MMMs. In addition, PDMS completely blocks the Knudsen diffusion through the pinhole defects, hence the transport through the coated membrane is only governed by the solution–diffusion mechanism. The success of the healing process can be confirmed by comparing the pure gas permeation curves in a fixed-volume pressure-increase setup, before and after PDMS coating. For example, in figure 3.23 the permeate pressure of CO_2 in the PEEK-WC/**GI2** membrane is plotted as a function of time. From the immediate pressure increase and the very steep slope of the uncoated sample, it is evident that, in the absence of PDMS layer, gas transport is governed by the Knudsen diffusion. The estimation of the gas transport parameters of MMMs, *i.e.* the permeability and diffusion coefficients of the gases and, indirectly, the solubility, is only possible if the determination of the time lag is clear and well defined (see chapter 3.2.4). The resulting flat baseline in the PDMS-coated membrane, *i.e.* the tangent to the very initial part of the curve defined by the term $(dp/dt)_0$ in equations (6) and (7), confirms that the leak flow through remaining pinhole defects is negligible for CO_2 and it is possible to apply the solution-diffusion model.
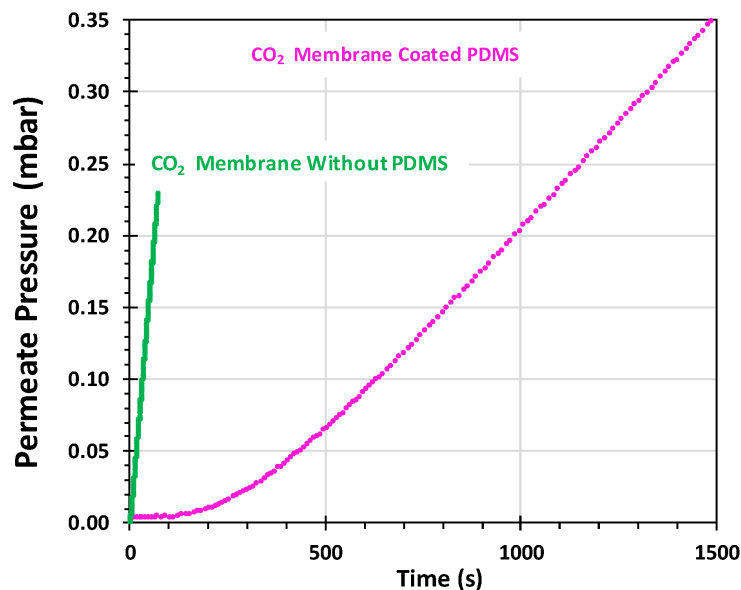
Figure 3.23 Example of CO_2 pure gas permeation curves at 25 °C and 1 bar feed pressure of PEEK-WC/**GI2** membrane with and without silicone coating, showing the effective healing of pinhole defects by the flat baseline (dashed line).

3.3.3 Pure Gas Transport Properties

Single gas permeation tests were performed as described in chapter 3.2.4. Wherever this is not the case, a baseline correction was applied via equation (6) and (7). As described previously, this procedure allows the correct calculation of the values of *P, D,* and *S* of membranes with few defects [45]. The results of the permeation tests with six pure gases at 25 °C are collected in tables 3.2-3.4. The measurements were performed in the order H_2, He, O_2, N_2, CH_4, and finally CO_2. Tests with O_2, N_2 were repeated at the end of the cycle to confirm that there was no change in the material caused by physical aging or plasticization. Physical aging is indeed a common issue in glassy polymer-based membranes. In these materials, polymer chains pack inefficiently, leaving a lot of free volume in the matrix. Over time, polymer chains gradually reorder, reducing the specific volume of the polymer membrane. The effect of improved packing is the reduction of the penetrant diffusion coefficients [46]. Another frequent issue that affect gas separation membranes is plasticization. This phenomenon is caused by the permeation of highly soluble species (*e.g.* CO_2) in the membrane, causing a significant swelling of the polymer matrix. As a result, the free volume and the mobility of polymer chains increase, resulting in a loss of the polymer size-sieving ability

[47]. Repeating gas permeation tests and comparing the obtained results, before and after the use of CO_2, is a good practice to assess the membrane condition.

In this study, the incorporation of cages into the polymer matrix induced different effects in the transport properties of the polymer membrane, which strongly depended on the cage used. In the presence of **GI1**, the permeability of all gases increased, compared to the neat polymer membrane. On the contrary, the selectivity decreased for most the investigated gas pairs, with the exception of CO_2/N_2 for which it stayed almost unvaried. The opposite behaviour occurred with **GI2**, where a decrease of permeability for all gases was observed, while a gain in selectivity was found for the CO_2/CH_4, CO_2/N_2, O_2/N_2, and He/CH_4 gas pairs. The Robeson plots derived from these results are shown in figure 3.24 to figure 3.27 where the performances of the three membranes (neat PEEK-WC, PEEK-WC/**GI1** and PEEK-WC/**GI2**) are compared to the literature data, obtained from the database of the Membrane Society of Australasia (MSA) for poly(aryl ethers) and poly(aryl ether ketones)-based membranes. The remarkable gain in selectivity in PEEK-WC/**GI2** for the O_2/N_2 gas pair leads to an overall improvement of the membrane separation performance that approaches the 1991 upper bound (Figure 3.26). The MMM with **GI2** as filler is among the best performing membranes in the class of poly(aryl ether) and poly(aryl ether ketone)-based systems in terms of selectivity, while the MMM with **GI1** are among the best ones in terms of permeability.

Table 3.2 Pure gas permeability coefficients and relative selectivity for the neat PEEK-WC, PEEK-WC/**GI1** and PEEK-WC/**GI2** membranes.

Membrane	Permeability (Barrer)						α (P_a/P_b)			
	N_2	O_2	CO_2	CH_4	H_2	He	CO_2/CH_4	CO_2/N_2	O_2/N_2	He/CH_4
PEEK-WC [48]	0.24	1.24	6.04	0.25	13.4	12.5	24.2	25.2	5.17	50.0
PEEK-WC/**GI1**	2.25	10.1	52.7	4.27	40.1	30.9	12.3	23.4	4.49	7.24
PEEK-WC/**GI2**	0.07	0.68	3.41	0.10	7.75	8.58	34.1	48.7	9.71	85.8

Table 3.3 Pure gas diffusivity coefficients and relative selectivity for the neat PEEK-WC, PEEK-WC/**GI1** and PEEK-WC/**GI2** membranes.

Membrane	Diffusivity (10^{-12} m^2 s^{-1})						α (D_a/D_b)			
	N$_2$	O$_2$	CO$_2$	CH$_4$	H$_2$	He	CO$_2$/CH$_4$	CO$_2$/N$_2$	O$_2$/N$_2$	He/CH$_4$
PEEK-WC [48]	0.45	2.02	0.58	0.14	135	529	4.14	1.29	4.49	3779
PEEK-WC/**GI1**	28.0	53.0	15.1	10.5	455	776	1.44	0.54	1.89	73.9
PEEK-WC/**GI2**	1.02	3.86	0.85	0.20	188	708	4.25	0.83	3.78	3540

Table 3.4 Pure gas solubility coefficients and relative selectivity for the neat PEEK-WC, PEEK-WC/**GI1** and PEEK-WC/**GI2** membranes.

Membrane	Solubility (cm$^3_{STP}$ cm^{-3} bar^{-1})						α (S_a/S_b)			
	N$_2$	O$_2$	CO$_2$	CH$_4$	H$_2$	He	CO$_2$/CH$_4$	CO$_2$/N$_2$	O$_2$/N$_2$	He/CH$_4$
PEEK-WC [48]	0.39	0.46	7.77	1.33	0.07	0.02	5.84	19.9	1.18	0.015
PEEK-WC/**GI1**	0.06	0.14	2.62	0.30	0.07	0.03	8.73	43.7	2.33	0.100
PEEK-WC/**GI2**	0.05	0.13	3.02	0.38	0.03	0.009	7.95	60.4	2.60	0.024

On the basis of the Maxwell equation (3), the decrease in permeability for PEEK-WC/**GI2** and the increase in permeability for PEEK-WC/**GI1,** with respect to the neat PEEK-WC membrane, suggests that the **GI2** and **GI1** fillers have a lower and higher permeability than the polymer, respectively. Assuming a density of approx. 0.5 g cm^{-3} for the cages [49] and 1.249 g cm^{-3} for the PEEK-WC [50], and considering that the MMMs were prepared with 20 wt % of filler, the volume fraction of the cages is 38.4%. Equations (4) and (5) predict that their permeability falls in the interval:

$$0.517 \, P_c < P_{MMM} < 2.87 \, P_c$$

where P_{MMM} is the permeability of the mixed matrix membrane and P_c is the permeability of the neat PEEK-WC membrane. The decrease of permeability for many gases in the **GI2**-based MMM is close to or even slightly larger than predicted by equation (5), suggesting that the cage acts as an almost impermeable filler as in the case of "plugged sieves" (see chapter 3.1.2). A decrease of the solubility coefficient for nearly all bulkier gases was observed in the PEEK-WC/**GI2** membranes. Unfortunately, since this loss in solubility is not balanced by a significant increase in diffusivity, the final permeability decreases. However, along with a loss in P there is an increase in selectivity,

indicating that the separation performance of the membrane increases, despite its lower productivity.

On the other hand, the increase in permeability with the **GI1**-based MMM is much higher than predicted by the Maxwell equation while, at the same time, there is a strong reduction in diffusion selectivity (Table 3.3). This is probably related to the presence of additional free volume and might indicate: i) the formation of non-selective diffusion paths around the cage microcrystals due to poor adhesion with the polymer; ii) the presence of voids between poorly dispersed clusters. This behaviour is typical of fillers that falls in the suboptimal structure group of "sieve-in-a-cage" (see chapter 3.1.2). Even in the case of PEEK-WC/**GI1** membrane, there is a decrease of the solubility coefficient for nearly all bulkier gases, but this time the loss in S is overcompensated by a dramatic increase in the gas diffusion coefficients, leading to an overall increase in permeability.
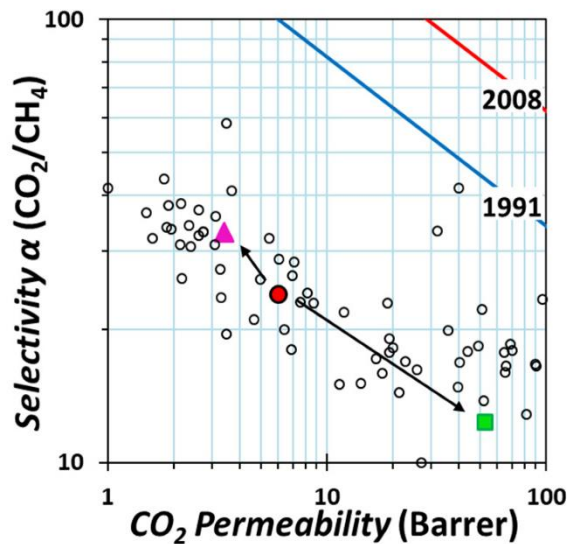

Figure 3.24 Robeson diagrams for the CO_2/CH_4, pairs with the upper bounds represented by a blue line for 1991 [6] and a red line for 2008 [7]. The gas permeability data for PEEK-WC are reported with a red circle ●, with a green square for PEEK-WC/**GI1** ■ and with a pink triangle for PEEK-WC/**GI2** ▲. Empty symbols are literature data for Poly(aryl ethers) and Poly(aryl ether ketones)-based membranes.

Figure 3.25 Robeson diagrams for the CO_2/N_2, pairs with the upper bounds represented by red lines for 2008 [52] and purple lines for 2019 [51]. The gas permeability data for PEEK-WC are reported with red circles ●, with green squares for PEEK-WC/**GI1** ■ and with pink triangles for PEEK-WC/**GI2** ▲. Empty symbols are literature data for Poly(aryl ethers) and Poly(aryl ether ketones)-based membranes.
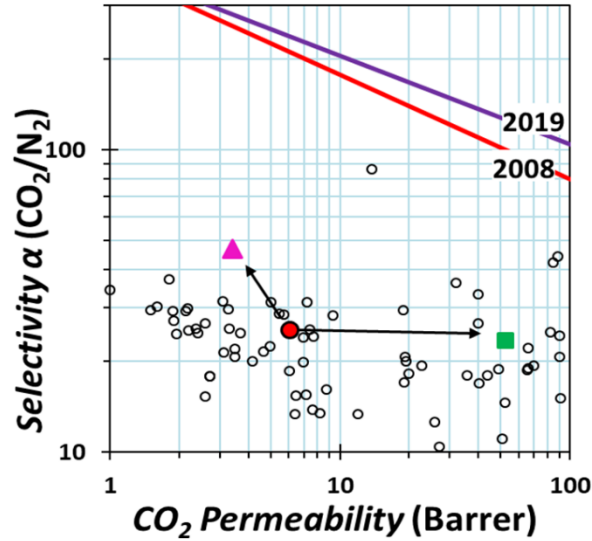

Figure 3.26 Robeson diagrams for the O_2/N_2, pairs with the upper bounds represented by blue lines for 1991 [6], red lines for 2008 [7] and yellow lines for 2015 [52]. The gas permeability data for PEEK-WC are reported with red circles ●, with green squares for PEEK-WC/**GI1** ■ and with pink triangles for PEEK-WC/**GI2** ▲. Empty symbols are literature data for Poly(aryl ethers) and Poly(aryl ether ketones)-based membranes.
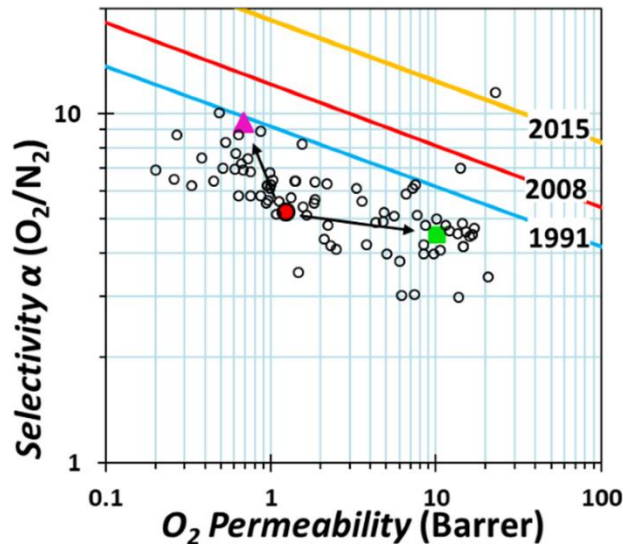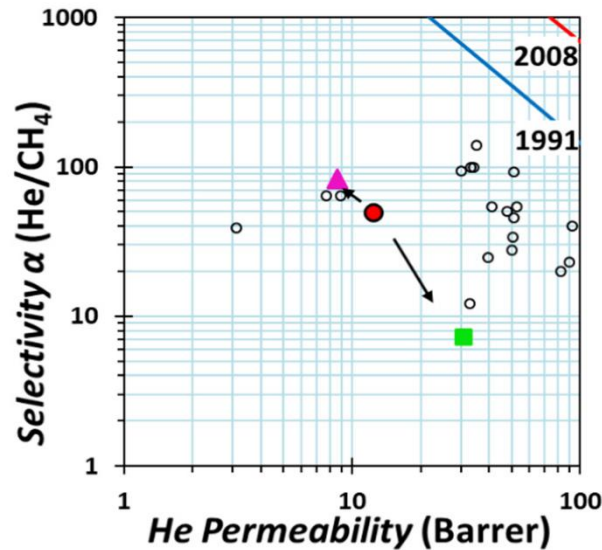
Figure 3.27 Robeson diagrams for the He/CH4, pairs with the upper bounds represented by blue lines for 1991 [6] and red lines for 2008 [7]. The gas permeability data for PEEK-WC are reported with red circles ●, with green squares for PEEK-WC/**GI1** ■ and with pink triangles for PEEK-WC/**GI2** ▲. Empty symbols are literature data for Poly(aryl ethers) and Poly(aryl ether ketones)-based membranes.

As a confirmation that the gas transport process follows the solution–diffusion model, the logarithm of the diffusion coefficient D showed a linear correlation with the square of the gas diameter, d^2_{eff}, (Figure 3.28) [53]. However, while the PEEK-WC/**GI2** MMM has a similar behaviour with respect to the neat polymer membrane, PEEK-WC/**GI1** has a much gentler slope, indicating a weaker size-sieving behaviour. This is in agreement with the hypothesis, formulated during the Maxwell analysis, that **GI1** acts as a "sieve-in-a-cage", creating nonselective free volume elements (*e.g.* diffusion paths around the cages due to poor adhesion or due to voids between poorly dispersed clusters). It should be noted that only in the neat PEEK-WC membrane, the diffusion coefficient of CO_2 is higher than that of N_2, as expected based on the effective gas diameters. On the other hand, in both MMMs, the CO_2 diffusion coefficient does not increase as much as that of N_2, and the order of the two gases is inverted. This outcome may suggest the presence of specific interactions of CO_2 with the fillers (dipole-quadrupole interaction with heteroatoms), but it can also depend on a higher solubility of the gas in the internal voids of the dispersed phase.
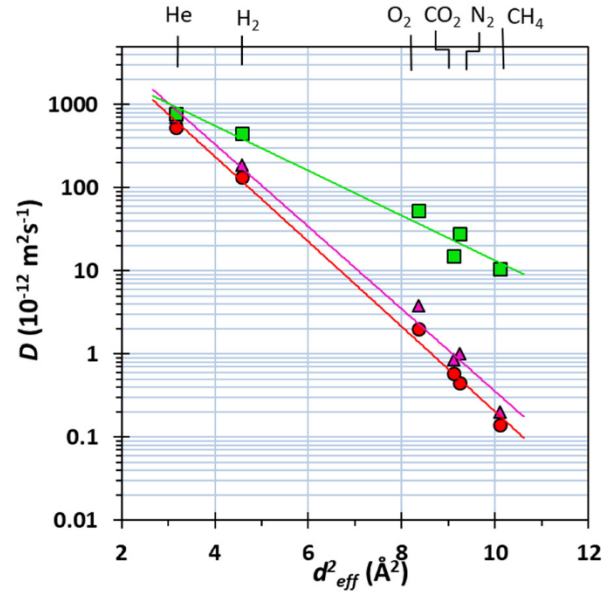
Figure 3.28 Correlation of the effective diffusion coefficient of six gases as a function of their molecular diameter, as defined by Teplyakov and Meares [54], for the PEEK-WC ●, PEEK-WC/**GI1** ■ and PEEK-WC/**GI2** ▲ membranes.

3.4 CONCLUSIONS

Four different polyimine bis-tren cages (**GI1-GI4**) were studied as fillers for the preparation of PEEK-WC-based mixed matrix membranes for gas separation. The compounds were dispersed in the polymer solution due to their poor solubility in common organic solvents. Only the two cages, *i.e.* **GI1** and **GI2**, proved to be suitable for obtaining robust dense MMMs with few enough pinhole defects to be healed by PDMS coating. On the contrary, the dispersion of the other two cages, *i.e.* **GI3** and **GI4** brought to an inhomogeneous distribution of the filler in the polymer matrix, which led to non-uniform and highly defective membranes also after the PDMS coating. PEEK-WC/**GI1** and PEEK-WC/**GI2** were then tested in single gas permeation studies and the results were compared to those of the pure polymer membrane. The permeability for all the tested gases increased with **GI1**-based MMM and decreased with the **GI2**-based one. Besides, the presence of **GI2** as filler increased the selectivity for the gas pairs CO_2/CH_4, CO_2/N_2, O_2/N_2, and He/CH_4, whereas with **GI1** cage the selectivity decreased for all gas pairs except CO_2/N_2, for which it remained steady. These results indicate that, based on the Maxwell model, the permeability of **GI2** is much lower than that of the polymer matrix whereas that of **GI1** is much higher. The exceptionally high permeability in the presence of **GI1** suggests the presence of additional permeation pathways, probably at the cage/polymer interface. However, the gas transport follows the solution–diffusion mechanism also after the dispersion of the cages in the membranes, as indicated by the linear correlation between the logarithm of the diffusion coefficient and the square of the effective gas diameter d^2_{eff}.

This is the first time that bis-tren cages are tested as fillers in mixed matrix membranes, and one of the few studies involving organic cages in gas separation applications. Further developments will point to the control of the filler particles size, down to the nanometer-scale. To achieve this goal, either top-bottom approaches (*e.g.* ball-milling) or bottom-up strategies (changes in reaction conditions) have to be explored. Small particles size is needed to produce integrally skinned or thin film composite PEEK-WC membranes, showing both a selective layer below 100 nm thick and increased gas separation properties [55].
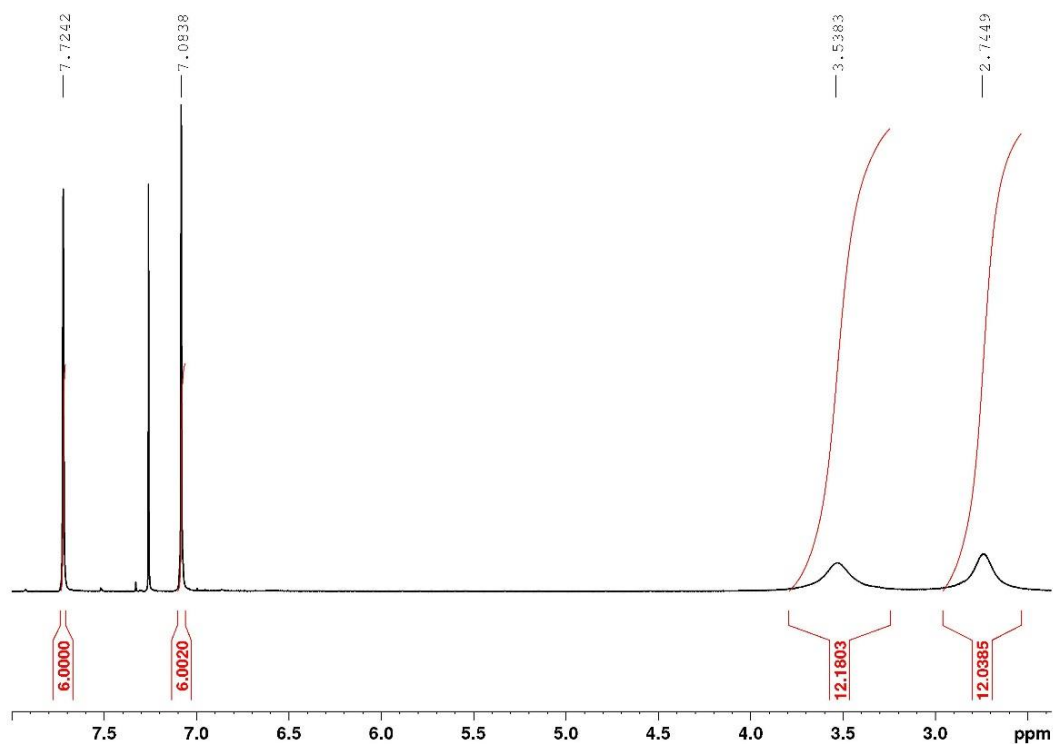
3.5 CHARACTERIZATION OF GI1-4

Figure 3.29 ^{1}H-NMR spectrum of **GI1** (400 MHz) in CDCl$_3$.
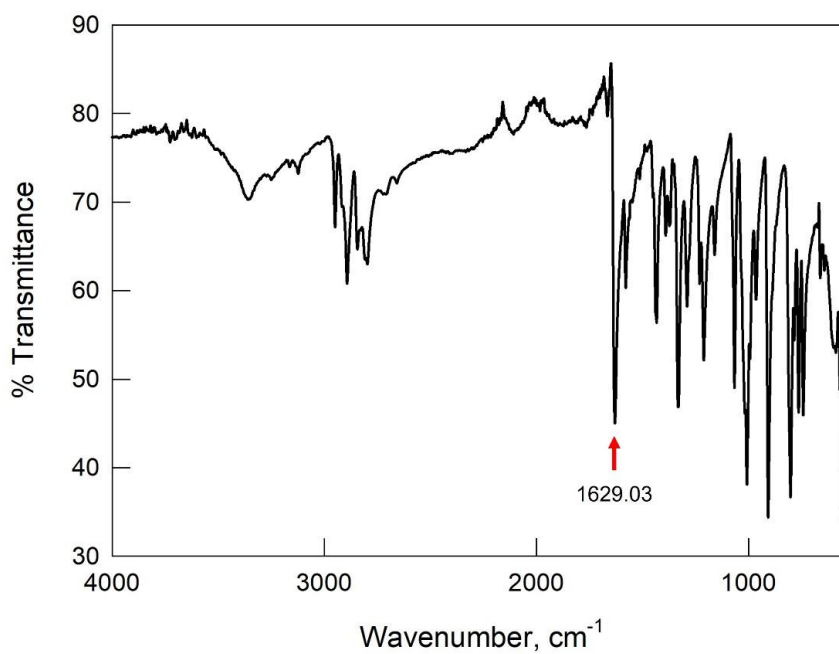
Figure 3.30 FTIR-ATR spectrum of **GI1** cage (1629.03 C=N stretching).
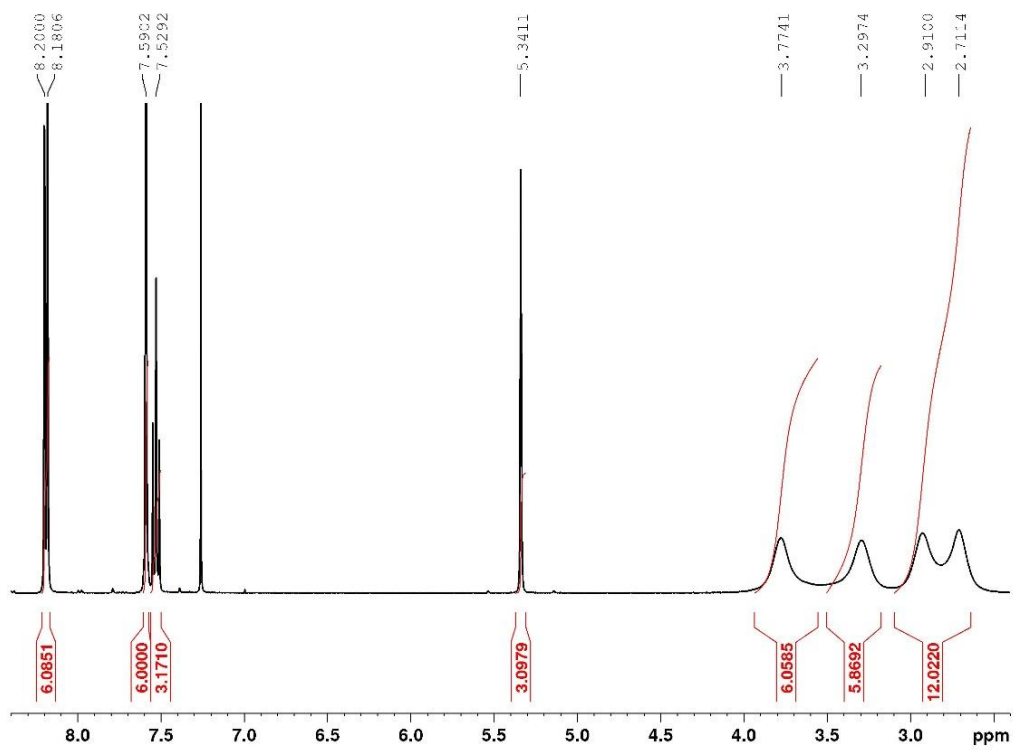
Figure 3.31 ^{1}H-NMR spectrum of **GI2** (400 MHz) in CDCl$_3$.

Figure 3.32 FTIR-ATR spectrum of **GI2** cage (1641.37 C=N stretching).

Figure 3.33 ^{1}H-NMR spectrum of **GI3** (400 MHz) in CDCl$_3$.

Figure 3.34 FTIR-ATR spectrum of **GI3** cage (1638.62 C=N stretching).
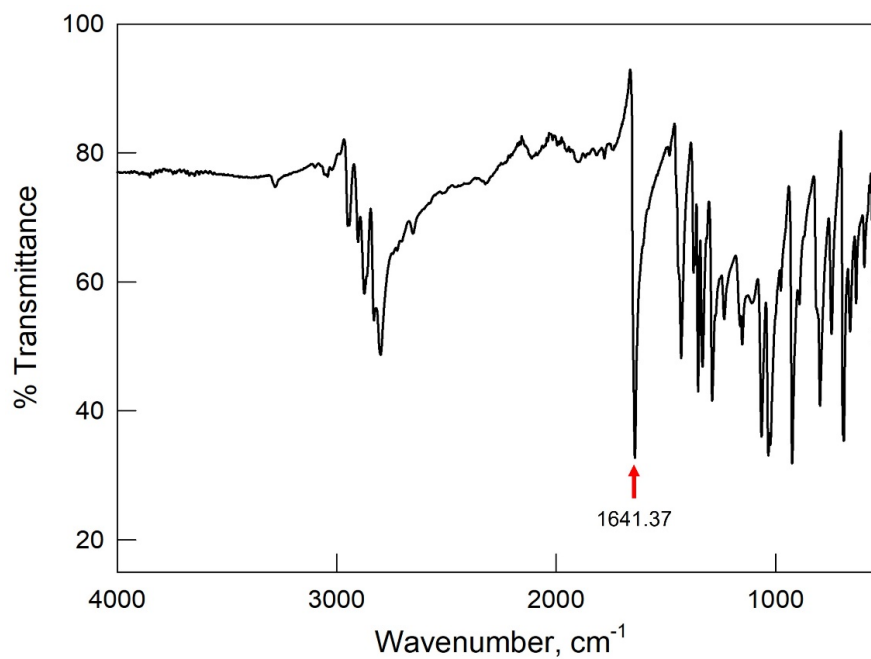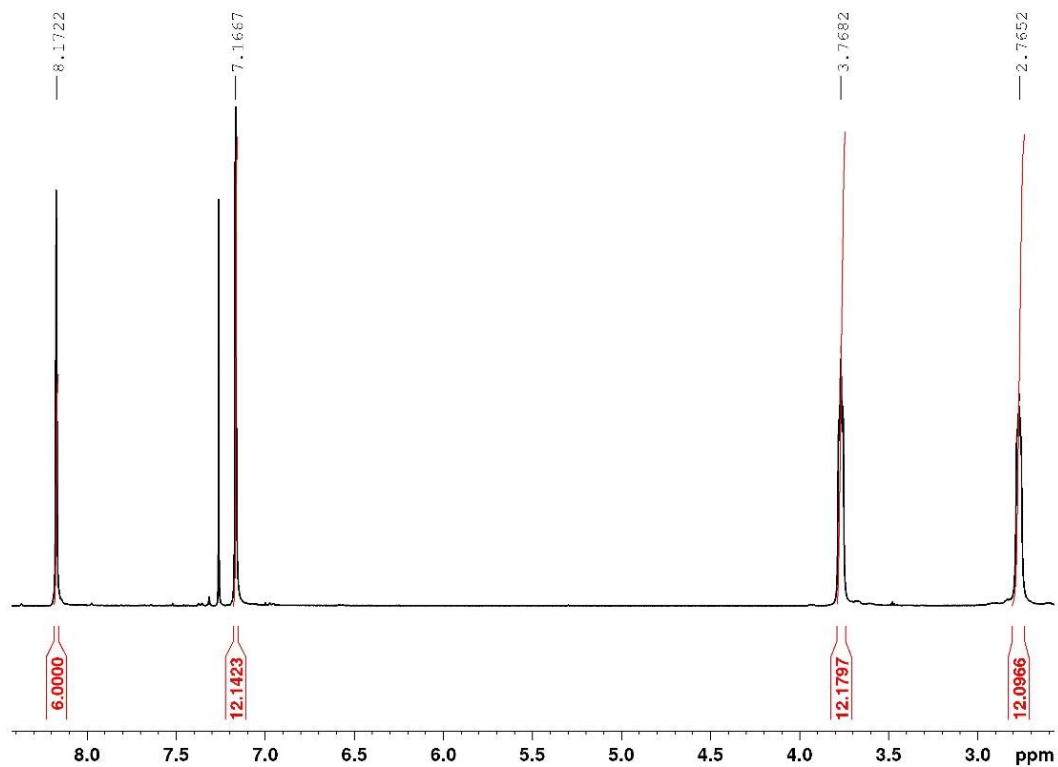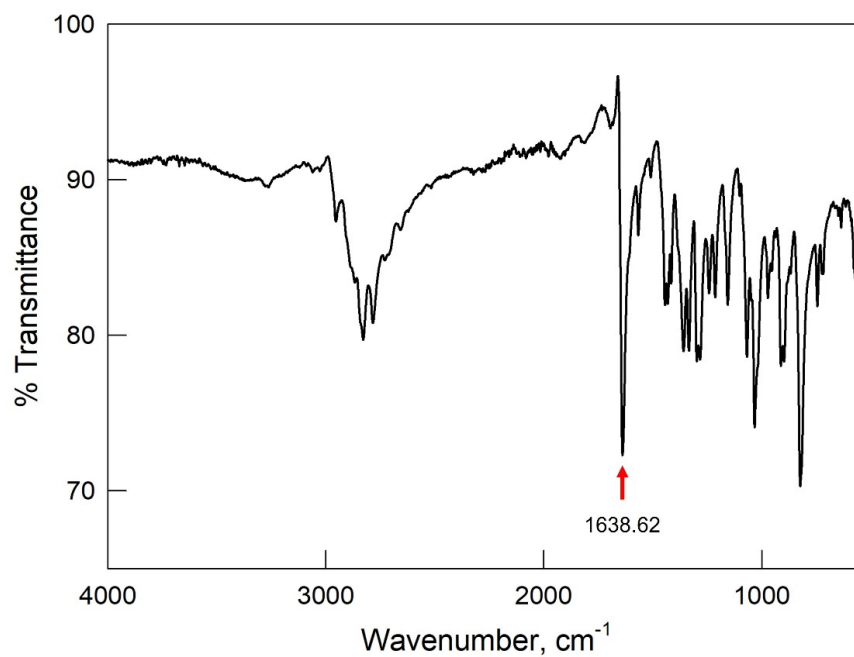
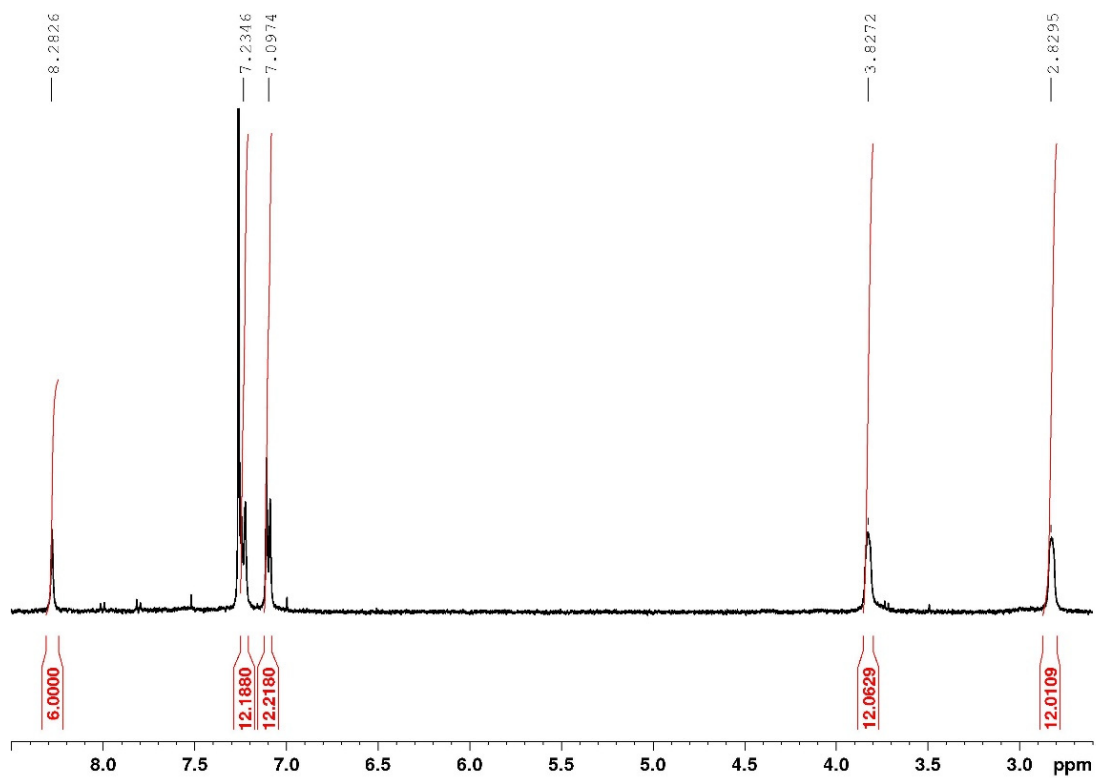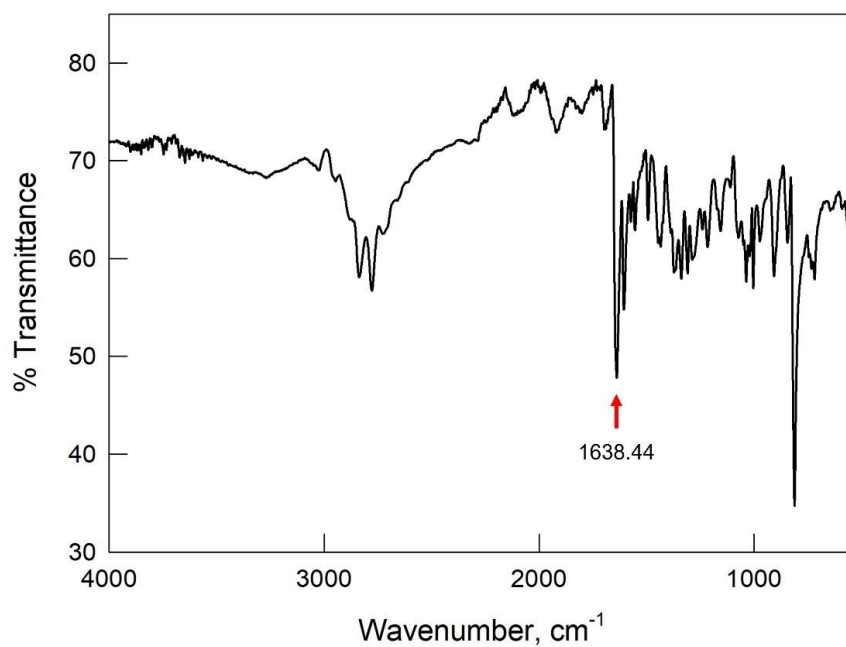**Figure 3.35** ^{1}H-NMR spectrum of **GI4** (400 MHz) in CDCl$_3$.

Figure 3.36 FTIR-ATR spectrum of **GI4** cage (1638.44 C=N stretching).

3.6 REFERENCES

[1] P. Aptel, J. Armor, R. Audinos, R.W. Baker, R. Bakish, G. Belfort, B. Bikson, R.G. Brown, M. Bryk, J.J. Burke, *J. Membr. Sci.*, **1996**, 120, 149.

[2] M. Fang, C. Montoro, M. Semsarilar, *Membranes*, **2020**, 10, 107.

[3] W. Bollinger, D. MacLean, R. Narayan, *Chem. Eng. Prog.*, **1982**, 10, 78.

[4] M. Galizia, W.S. Chi, Z.P. Smith, T.C. Merkel, R.W. Baker, B.D. Freeman, *Macromolecules*, **2017**, 50, 7809.

[5] J.G. Wijmans, R.W. Baker, *J. Membr. Sci*., **1995**, 107, 1.

[6] L.M. Robeson, *J. Membr. Sci*., **1991**, 62, 165.

[7] L.M. Robeson, *J. Membr. Sci*., **2008**, 320, 390.

[8] B. Shimekit, H. Mukhtar, T. Murugesan, *J. Membr. Sci*., **2011**, 373, 152.

[9] R. Pal, *J. Colloid Interface Sci*., **2008**, 317, 191.

[10] N. Kosinov, J. Gascon, F. Kapteijn, E.J.M. Hensen, *J. Membr. Sci*., **2016**, 499, 65.

[11] R. Balasubramanian, S. Chowdhury, *J. Mater. Chem. A*, **2015**, 3, 21968.

[12] D. Mattia, H. Leese, K.P.J. Lee, *J. Membr. Sci*., **2015**, 475, 266.

[13] N. Azizi, T. Mohammadi, R.M. Behbahani, *J. Energy Chem*., **2017**, 26, 454.

[14] Y. Katayama, K.C. Bentz, S.M. Cohen, *ACS Appl. Mater. Interfaces*, **2019**, 11, 13029.

[15] Y. Cheng, Y. Ying, S. Japip, S.D. Jiang, T.S. Chung, S. Zhang, D. Zhao, *Adv.Mater*., **2018**, 30, 1802401.

[16] S.L. James, *Chem. Soc. Rev.*, **2003**, 32, 276.

[17] H. Yehia, T.J. Pisklak, J.P. Ferraris, K.J. Balkus, I.H. Musselman, *Polym. Prepr*., **2004**, 45, 35.

[18] a) B. Seoane, J. Coronas, I. Gascon, M.E. Benavides, O. Karvan, J. Caro, F. Kapteijn, J. Gascon, *Chem. Soc. Rev.*, **2015**, 44, 2421. b) R. Lin, B. Villacorta Hernandez, L. Ge, Z. Zhu, *J. Mater. Chem. A*, **2018**, 6, 293.

[19] a) J. Shen, G. Liu, K. Huang, Q. Li, K. Guan, Y. Li, W. Jin, *J. Membr. Sci*., **2016**, 513, 155. b) Z. Wang, H. Ren, S. Zhang, F. Zhang, J. Jin, *J. Mater. Chem. A*, **2017**, 5, 10968.

[20] H. Wang, S. He, X. Qin, C. Li, T. Li, *J. Am. Chem. Soc*., **2018**, 140, 17203.

[21] X. Zou, H. Ren, G. Zhu, *Chem. Commun*., **2013**, 49, 3925.

[22] P.J. Waller, F. Gándara, O.M. Yaghi, *Acc. Chem. Res.*, **2015**, 48, 12, 3053.

[23] X. Cao, Z. Qiao, Z. Wang, S. Zhao, P. Li, J. Wang, S. Wang, *Int. J. Hydrogen Energy*, **2016**, 41, 9167.

[24] B.P. Biswal, H.D. Chaudhari, R. Banerjee, U.K. Kharul, *Chem. Eur. J.*, **2016**, 22, 4695.

[25] A.F. Bushell, P.M. Budd, M.P. Attfield, J.T.A. Jones, T. Hasell, A.I. Cooper, P. Bernardo, F. Bazzarelli, G. Clarizia, J.C. Jansen, *Angew. Chem. Int. Ed.*, **2013**, 52, 1253.

[26] T. Tozawa, J.T.A. Jones, S.I. Swamy, S. Jiang, D.J. Adams, S. Shakespeare, R. Clowes, D. Bradshaw, T. Hasell, S.Y. Chong, C. Tang, S. Thompson, J. Parker, A. Trewin, J. Bacsa, A.M.Z. Slawin, A. Steiner, A.I. Cooper, *Nat. Mater.*, **2009**, 8, 973.

[27] J.D. Evans, D.M. Huang, M.R. Hill, C.J. Sumby, A.W. Thornton, C.J. Doonan, *J. Phys. Chem. C*, **2014**, 118, 3, 1523.

[28] M.W. Schneider, I.M. Oppel, H. Ott, L.G. Lechner, H.J.S. Hauswald, R. Stoll, M. Mastalerz, *Chem. Eur. J.*, **2012**, 18, 836.

[29] A. Avellaneda, P. Valente, A. Burgun, J.D. Evans, A.W. Markwell-Heys, M.R. Hill, D.J. Nielsen, C.J. Sumby, C.J. Doonan, *Angew. Chem. Int. Ed.*, **2013**, 52, 3746.

[30] H. Mao, S. Zhang, *J. Colloid Interface Sci.*, **2017**, 490, 29.

[31] J. Tian, P.K. Thallapally, S.J. Dalgarno, P.B. McGrail, J.L. Atwood, *Angew. Chem. Int. Ed.*, **2009**, 48, 5492.

[32] D.S. Sholl, R.P. Lively, *Nature*, **2016**, 532, 435.

[33] Q. Zhang, H. Li, S. Chen, J. Duan, W. Jin, *J. Membr. Sci.*, **2020**, 611, 118288.

[34] A. Miljkovic, S. La Cognata, G. Bergamaschi, M. Freccero, A. Poggi, V. Amendola, *Molecules*, **2020**, 25, 1733.

[35] M. Kołodziejski, A.R. Stefankiewicz, J.M. Lehn, *Chem. Sci.*, **2019**, 10, 1836.

[36] D. McDowell, J. Nelson, V. McKee, *Polyhedron*, **1989**, 8, 1143.

[37] V. McKee, W.T. Robinson, D. McDowell, J. Nelson, *Tetrahedron Lett.*, **1989**, 30, 7453.

[38] Z. Yang, J.M. Lehn, *J. Am. Chem. Soc.*, **2020**, 142, 15137.

[39] S.C. Fraga, M. Monteleone, M. Lanč, E. Esposito, A. Fuoco, L. Giorno, K. Pilnáček, K. Friess, M. Carta, N.B. McKeown, P. Izák, Z. Petrusová, J.G. Crespo, C.Brazinha, J.C. Jansen, *J. Membr. Sci.*, **2018**, 561, 39.

[40] J.G. Wijmans, R.W. Baker, Chapter: The Solution–Diffusion Model: A Unified Approach to Membrane Permeation. In: Materials Science of Membranes for Gas and Vapor Separation, Eds. B. Freeman, Y. Yampolskii, I. Pinnau, JohnWiley & Sons, Ltd.: Hoboken, NJ, USA, **2006**.

[41] M.S. Suleman, K.K. Lau, Y.F. Yeong, *Procedia Eng.*, **2016**, 148, 176.

[42] B. Haider, M.R. Dilshad, M. Atiq Ur Rehman, J. Vargas Schmitz, M. Kaspereit, *Sep. Purif. Technol.*, **2020**, 248, 116899.

[43] S.S. Madaeni, M.M.S. Badieh, V. Vatanpour, N. Ghaemi, *Polym. Eng. Sci.*, **2012**, 52, 2664.

[44] S.S. Madaeni, M.M.S. Badieh, V. Vatanpour, *Polym. Eng. Sci.*, **2013**, 53, 1878.

[45] J.C. Jansen, K. Friess, E. Drioli, *J. Membr. Sci.*, **2011**, 367, 141.

[46] B.W. Rowe, B.D. Freeman, D.R. Paul, *Polymer*, **2009**, 50, 5565.

[47] J.S. Chiou, J.W. Barlow, D.R. Paul, *J. Appl. Polym. Sci.*, **1985**, 30, 2633.

[48] E. Esposito, R. Bruno, M. Monteleone, A. Fuoco, J. Ferrando Soria, E. Pardo, D. Armentano, J.C. Jansen, *Appl. Sci.*, **2020**, 10, 1310.

[49] R.K. Gajula, R. Kishor, M.J. Prakash, *Chemistry Select*, **2019**, 4, 12547.

[50] J. Jansen, M. Macchione, E. Drioli, *J. Membr. Sci.*, **2005**, 255, 167.

[51] B. Comesaña-Gándara, J. Chen, C.G. Bezzu, M. Carta, I. Rose, M.C. Ferrari, E. Esposito, A. Fuoco, J.C. Jansen, N.B. McKeown, *Energy Environ. Sci.*, **2019**, 12, 2733.

[52] R. Swaidan, B. Ghanem, I. Pinnau, *ACS Macro Lett.*, **2015**, 4, 947.

[53] A. Fuoco, C. Rizzuto, E. Tocci, M. Monteleone, E. Esposito, P.M. Budd, M. Carta, B. Comesaña-Gándara, N.B. McKeown, J.C. Jansen, *J. Mater. Chem. A*, **2019**, 7, 20121.

[54] V. Teplyakov, P. Meares, *Gas Sep. Purif.*, **1990**, 4, 66.

[55] J.C. Jansen, M.G. Buonomenna, A. Figoli, E. Drioli, *J. Membr. Sci.*, **2006**, 272, 188.

4. CO$_2$ SEPARATION BY IMIDE/IMINE ORGANIC CAGES

4.1 INTRODUCTION

Two novel imide-containing organic cages have been designed and synthesized with imine condensation reaction. Gas adsorption studies on the new compounds showed selectivity for carbon dioxide over nitrogen and methane. The cages were also tested as fillers in mixed-matrix membranes for gas separation. Dense and robust membranes were obtained by loading the cages in either Matrimid® or PEEK-WC polymers. Improved gas-transport properties and selectivity for CO$_2$ were achieved compared to the neat polymer membranes for CO$_2$/N$_2$ and CO$_2$/CH$_4$ binary mixtures.

4.1.1 The CO$_2$ issue

Since the industrial revolution in the 1750s, the atmospheric carbon dioxide concentration continuously raised from 290 ppm to more than 410 ppm in our days [1]. Such a large increase is attributable to anthropogenic emission of CO$_2$, mainly due to electricity and heat generation sectors, and it is strictly correlated to the global demographic and economic developments. According to the United Nation's prospects, the world population is estimated to reach up to 9.7 billion by 2050 [2]. This rapid growth is expected to tremendously increase the energy demand from 600 quadrillion of Btu (British Thermal Unit) today to approximately 900 quadrillion Btu in 2050. At the same time, the energy production deriving from renewable sources was only 15% in 2020, leaving the remaining energy demand to be satisfied by fossil fuels and nuclear power plants. Nowadays, the burning of natural gas, coal, and oil accounts for about 81% of the total energy production (24%, 27% and 30%, respectively) and it should decrease only to 70% by 2050 [3]. Fossil fuels combustion releases more than 32 Gt of CO$_2$ every year, a tremendous amount when compared to the 6 Gt emitted in 1950 [4]. According to the International Energy Agency's (IEA) 2019 report, non-renewable-based energy and heat production is the main source of anthropogenic carbon dioxide emissions, with 41% of the total CO$_2$ emitted every year, whereas both transportation and industrial sectors account for 24% of the emissions each. The building sector contributes to approximately 8% [5]. This accumulation of carbon dioxide in the atmosphere

caused a 0.8-1.2 °C increase in the global temperatures compared to pre-industrial levels. According to the Intergovernmental Panel on Climate Change (IPCC), the warming of the Earth is increasing by 0.2 °C per decade, and it is expected to reach 1.5 °C by 2040 (Figure 4.1) [6]. Global warming has been associated with a large number of different natural calamities, such as rise of sea levels, acidification of the oceans and extreme weather events (droughts, floods, heatwaves and storms), contributing to threat environment and human health, thus endangering both current and future generations. The rise of the average global temperatures is directly correlated to the presence of greenhouse gases (GHGs) in the atmosphere, that adsorb outgoing longwave radiation producing the so-called greenhouse effect. The main GHGs are CO_2, methane, nitrous oxide, and fluorinated gases (hydrofluorocarbons, chlorofluorocarbons and SF_6) but carbon dioxide is the major contributor, accounting for three quarter of the total GHGs emissions [7]. Therefore, the development and implementation of new technologies for efficient management of carbon dioxide emissions and Carbon Capture and Sequestration (CCS) systems are imperative tasks to limit warming under 2 °C.
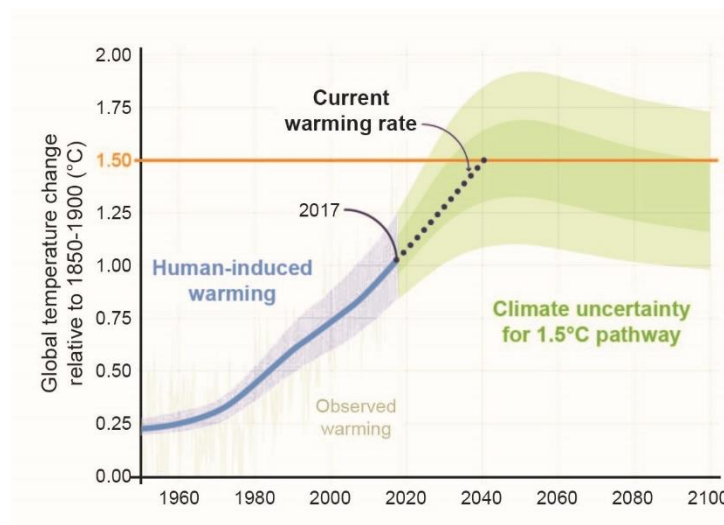

Figure 4.1 Human-induced warming registered until 2017 and projections for future temperature increase at the present rate (global temperatures would reach 1.5°C around 2040). The green range around 1.5°C shows temperature variation if CO_2 emission reductions started immediately, reaching emissions zero by 2055. From ref. [6].

In carbon capture and sequestration processes the CO_2 is selectively captured and then stored for example underground in deep geological formations. The removal of carbon dioxide can be done at point sources, such as coal-fired power plants and several manufacturing industries, or by Direct Air Capture (DAC) in order to reduce the existing CO_2 concentration in the atmosphere. Although the development of efficient DAC systems is necessary to mitigate the atmospheric CO_2 levels, some difficulties have limited the widespread application of this separation process. One critical point is that the removal of carbon dioxide from a diluted source (400 ppm in air) is less attractive than the other CCS methods where the concentration range is from few percent up to 50%. Moreover, current commercial DAC plants extract CO_2 by using solutions of alkali hydroxide, that need to be regenerated in a high energy and water consuming step [8]. Figure 4.2 describes the three main types of CCS: i) pre-combustion capture; ii) oxy-fuel combustion and iii) post-combustion capture.

In pre-combustion capture systems, fuel is converted into syngas (*i.e.* a mixture of CO and H_2) through the reaction with steam (called steam reforming) or oxygen (called partial oxidation or gasification, when applied to solid fuels).

$$C_xH_y + xH_2O \rightleftarrows xCO + (x+y/2)H_2$$
$$C_xH_y + (x/2)O_2 \rightleftarrows xCO + (y/2)H_2$$
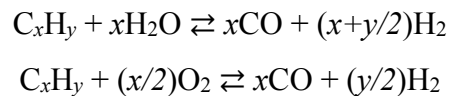
The syngas is then further converted to more hydrogen through the water-gas shift (WGS) reaction, resulting in a mixture of CO_2 and H_2.

$$CO + H_2O \rightleftarrows CO_2 + H_2$$
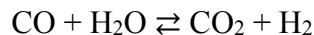
Separation of these two components allows for the sequestration of CO_2, while H_2 can be used in several processes, such as power generation in fuel cells [9].

In oxy-fuel combustion systems, pure oxygen is used to burn fuel instead of air. The resulting flue gas contains only CO_2 and water, that is easily condensed leaving pure carbon dioxide [10].

In post-combustion capture, carbon dioxide is separated from the flue gas, mainly composed by N_2, before it is released into the atmosphere. The concentration of CO_2 is relatively high and depends on the fuel used and the combustion process. For example, a typical coal-fired power plant emits a flue gas stream at ambient pressure that contains 13-15% CO_2, while that of natural gas power plants contains only 3-9% of CO_2 [4]. This technology is the most studied, as it can be retrofitted to most existing fossil fuel power plants and industries, and does not require the expensive production of high-purity O_2 or fuel pre-treatment.

Another process, in which the selective removal of carbon dioxide can be applied, is the production of biomethane, a renewable natural gas equivalent derived from biogas. Biogas is a mixture of CH_4 (40-75%), CO_2 (15-60%) and small amounts of several gases, such as oxygen (0-1%), nitrogen (0-2%), ammonia (<1%), hydrogen sulfide (0.005-2%), carbon monoxide (<0.6%), volatile organic compounds (<0.6%) and water (5-10%), produced by anaerobic digestion of plant or animal waste. Transforming biogas to biomethane requires two steps: i) cleaning harmful trace components such as H_2S, NH_3, CO, etc.; ii) biogas upgrading by separation of CO_2 from CH_4. The upgraded and purified biogas contains 95-97% of methane with a very low amount of CO_2 (<2%), and it represents a valid alternative to natural gas [11].
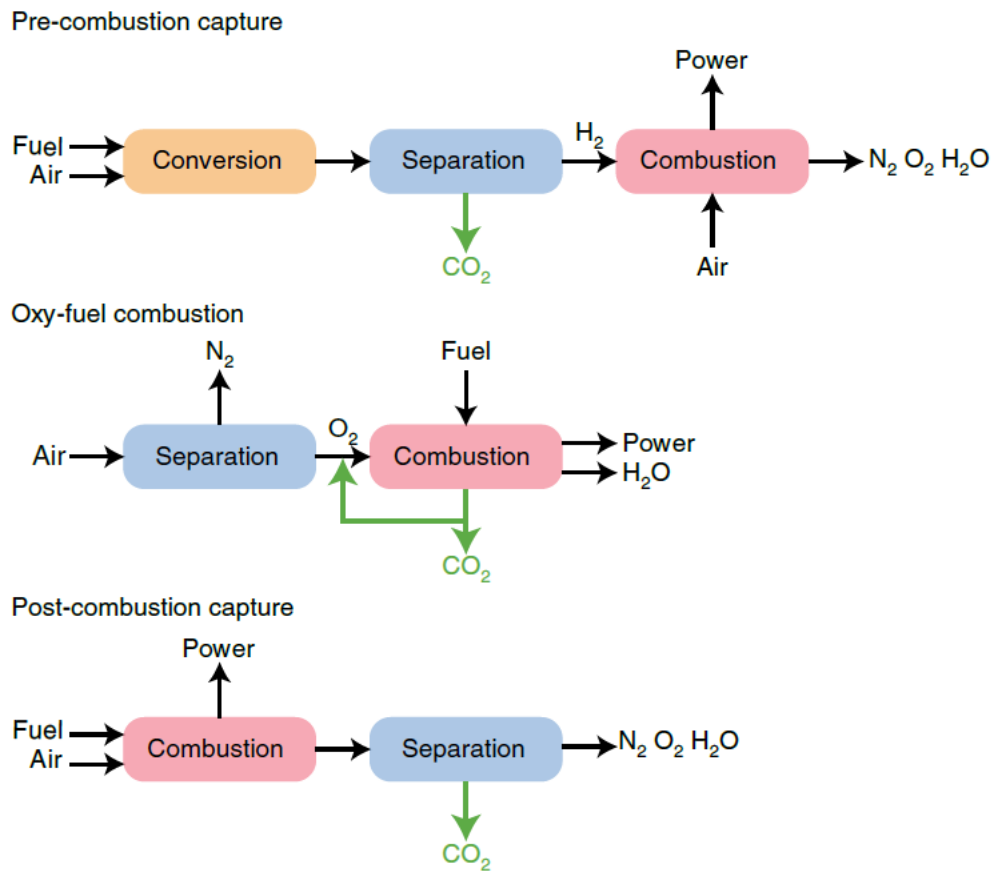

Figure 4.2 Carbon capture configurations. Strategies for carbon capture in the power sector include pre-combustion, oxy-fuel combustion and post-combustion capture from fossil fuel-fired power plants. From ref. [4].

Even though the compositions of flue gas and biogas are different (Table 4.1), the common goal is to remove anthropogenic CO_2 from both mixtures. For this reason, the applied gas separation technologies are similar and can be resumed as: i) adsorption; ii) cryogenic separation; iii) absorption; iv) membrane separation [12].

Adsorption-based techniques rely on the use of solid sorbents that can selectively interact with a gas species through physical interaction (*e.g.* zeolites, molecular sieves, COFs, MOFs, POCs, ecc…). The regeneration of the adsorbent with the subsequent release of the trapped gas can be done by rising the temperature (Temperature Swing Adsorption, TSA), reducing the pressure (Pressure Swing Adsorption, PSA) or applying vacuum (Vacuum Swing Adsorption, VSA). In all three cases the recovery of the sorbent is the energy-demanding step [12]. Cryogenic separation is based on the differences in boiling points of the flue gas components and is commonly found in natural gas purification. Carbon dioxide is obtained in a very high purity grade but the massive energy costs due to cooling limit the application of this process [13]. Chemical absorption of acidic CO_2 into basic solutions of alkali hydroxides or organic amines (*e.g.* monoethanolamine, MEA) is a mature and commercialized technology as well. The selectivity toward carbon dioxide is high, but the uptake capacities are generally low and the regeneration step is quite expensive. Moreover, amine solutions pose additional problems such as equipment corrosion and environmental and human health risks [14].

Table 4.1 Comparison of flue gas and biogas compositions. From ref. [11].

	Flue Gas		Biogas	
Molecules	Natural Gas	Coal	Molecules	Amount
N_2	70-76%	73-77%	CH_4	40-75%
CO_2	3-9%	13-15%	CO_2	15-60%
H_2O	7-18%	5-7%	H_2O	5-10%
O_2	2-15%	3-4%	N_2	0-2%
SO_2	/	800 ppm	O_2	0-1%
SO_3	/	10 ppm	NH_3	<1%
HCl	/	100 ppm	H_2S	0.005-2%
CO	200-300 ppm	20-50 ppm	CO	<0.6%
NO_x	10-300 ppm	500 ppm	VOC	<0.6%

To overcome the limitations of these separation processes, membrane technologies have been reported for CCS in recent years [12,15]. Compared with adsorption, absorption and cryogenic distillation, membrane-based gas separations have smaller footprint, higher energy efficiency, and are more environmentally sustainable. Numerous membrane technologies are currently commercialized for carbon dioxide separation, like in natural gas sweetening, where they cover 10% of the market (amine absorption has the rest). Cellulose acetate (CA) membranes are normally employed but, due to their poor performances, a two-stage energy-intensive process is required. However, the final cost is comparable to amine absorption, but the biggest drawback is the 4% loss of feed methane (with the CO_2 permeate stream) compared to the 1% loss of CH_4 in amine absorption upgrading. To overcome this issue and thus making CO_2/CH_4 membrane separation really competitive, future membranes should double the CO_2 permeance with respect to CA (from 100 to ca. 200 GPU) as well as the selectivity (from 12 to ca. 24) [16].

In the case of post-combustion systems, carbon dioxide should be separated from mostly N_2 with feed stream at atmospheric pressure and 0.2-0.3 bar in the permeate side (Figure 4.3). In this condition the membranes should have very high CO_2 permeances (>2000 GPU) and CO_2/N_2 selectivity of 20-30 [16]. For these reasons there is a huge research activity to find suitable polymers or good fillers for MMMs, that are able to reach the optimal performances for CCS.
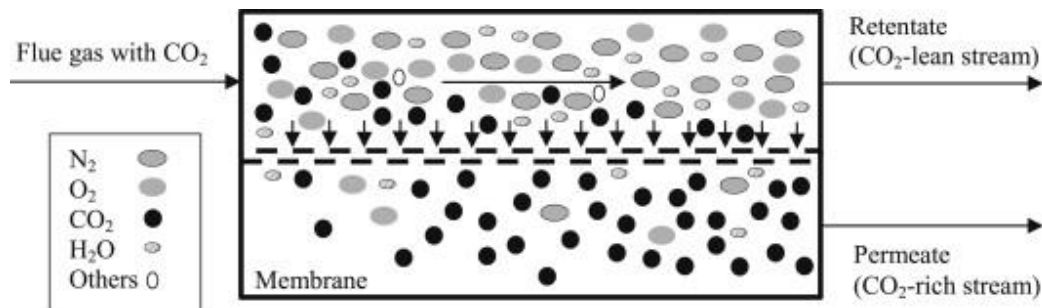

Figure 4.3 Schematic diagram of post-combustion membrane-based CO_2 separation. From ref. [15].

4.1.2 Porous Organic Molecular Materials

As defined by IUPAC, a porous solid is "a solid with pores, *i.e.* cavities, channels, or interstices, which are deeper than they are wide", and the pores can be either "open" or "closed" [17].

Porous materials are applied in a wide range of processes, including catalysis [18], energy storage [19], separations [20] and sensing [21]. Depending on the pore size, materials are classified as macro-porous (> 50 nm), meso-porous (between 2 and 50 nm) and micro-porous (< 2 nm) [22]. According to the long-range order degree, porous materials can also be classified into crystalline or amorphous: the first class is preferable because of an easier structural characterization.

Porous materials can be generated through the self-organization or polymerization of rigid precursors to give polymers, (supra)molecular assemblies or networks. Polymers of intrinsic microporosity and conjugated microporous polymers (named PIMs and CMPs, respectively) are typically based on strong covalent bonds while dynamic covalent chemistry approach is widely applied in the synthesis of organic materials like covalent organic frameworks (COFs) and organic cages [23-25]. However, porous materials can also be based on metal-to-ligand interactions (*e.g.* metal organic frameworks, MOFs, and coordination cages, MOCs) and secondary interactions [26]. For example, porous frameworks based on supramolecular interactions such as hydrogen and halogen bonding, have also been reported in the recent literature (H-bonded organic frameworks, HOFs, and halogen bonded organic frameworks, XOFs) [27,28].

Each type of material has both advantages and disadvantages; some of that are summarized in figure 4.4 where major classes of porous materials reported in the literature are compared with commercial zeolites (first column) [30]. The selection of porous materials for target applications is often challenging because of the large number of physico-chemical characteristics that should be considered. Beside a high superficial area, the porous material should also meet other requirements such as high stability (*e.g.*, thermal, mechanical, hydrolytic, chemical, or photolytic), processability, ease of handling, adsorption/desorption kinetics and thermal transport properties. Moreover, the use of expensive, rare, or toxic elements or reagents as building blocks or in the synthesis should be avoided [29].
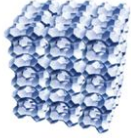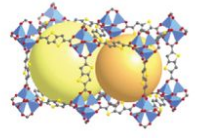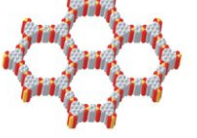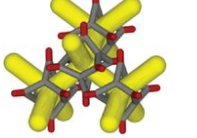
	Zeolites	Metal-organic frameworks	Covalent-organic frameworks	Porous organic polymers	Porous molecular solids
Porosity	Microporous or mesoporous ; narrow pore size distributions	Can be ultraporous[i]/ mesoporous; narrow pore size distributions	Can be ultraporous/ mesoporous; narrow pore size distributions	Can be ultraporous/ mostly microporous; broader pore sizes	Can be ultraporous/ mesoporous, but this is rare so far
Crystallinity	Typically high; can also be amorphous	Typically high	Modest to high	Amorphous	High, but amorphous examples, too
Stability	Thermal stability generally excellent; can be acid/base sensitive	Poor to good; growing number of water-stable MOFs	Boronates generally poor; imines generally good	Good to excellent, especially hydrothermal	Generally poor, though isolated examples of hydrothermal stability
Modularity/ diversity	High; new structures can be based on known zeotypes[ii]	Very high even for single-linker MOFs; also multivariate MOFs[iii]	In principle high; less developed than MOFs	Very high; multiple linkers and linker functions possible[iv]	Cocrystals possible[v]; not widely exemplified yet
Processing	Insoluble, but technologies for films, composites and pellets are well developed	Insoluble, though many recent examples of composite and films	Insoluble, but examples of surface growth	Modest processability, with exception of soluble PIMs	Soluble, as for PIMs could be advantage or disadvantage, depending on function

Figure 4.4 Comparative table of some classes of porous solids. Notes: (i) "Ultraporous" refers here to a material with high pore volume and surface area, whether comprising micropores or mesopores. (ii) A zeotype is a framework that is based on a known zeolite topology. (iii) "Multivariate" MOFs comprise more than one organic linker in a single framework. (iv) For example, the combination of three different aromatic linkers allowed band gap tuning over a wide range for porous polymeric water-splitting catalysts. (v) A co-crystal is a molecular crystal containing more than one molecular building unit. From ref. [29].

Porous molecular materials are a class of porous solids with a molecular structure that can pack in the solid state to produce pores. The molecular nature of these materials promotes their solubility in common organic solvents and processability, *e.g.* as fillers in MMMs. Among porous molecular materials, Porous Organic Cages (POCs) display an internal three-dimensional cavity acting as an intrinsic pore, able to selectively recognize and trap target guests.

Beside the intrinsic porosity, these materials can display extrinsic pores or channels, which originate from the non-efficient packing of the molecules in the solid state. The connection between intrinsic and extrinsic pores is paramount to the development of porous molecular materials, while isolated intrinsic cavities can only form zero-dimensional hardly porous solids [31]. When intrinsic and extrinsic voids are connected, either 1D, 2D or 3D extended pore networks can form, resulting in materials that can be extremely porous [32]. Noteworthy, only shape-persistent cages, whose

rigid structure and porosity are maintained in the solid state after desolvation, can be classified as effective POCs [33]. Most POCs are synthesized by DCC reactions, such as imine condensation, boronate ester formation, and alkyne metathesis, that promote the formation of closed three-dimensional structures instead of open networks. The application of irreversible reactions is rare, but examples of cages obtained by nucleophilic aromatic substitution or metal catalysed cross-coupling are known [34,35]. The spatial arrangement of the functional groups in the building blocks is essential for the convergent assembling into a closed molecular structure. If the precursors have a symmetry axis not higher than twofold, the resulting products can be at most linear polymers or macrocycles. On the other hand, convex molecules with more than two reactive sites and appropriate bite angles are suitable precursors for cage-like molecules. Most cages so far are a combination of two- and three-way linkers in [2+3], [4+6], or [8+12] arrangements, depending on the geometry of the synthons. On the contrary, building blocks with multiple reactive sites and planar or three-dimensional geometry are more prone to form 2D or 3D infinite frameworks, respectively (Figure 4.5) [25].
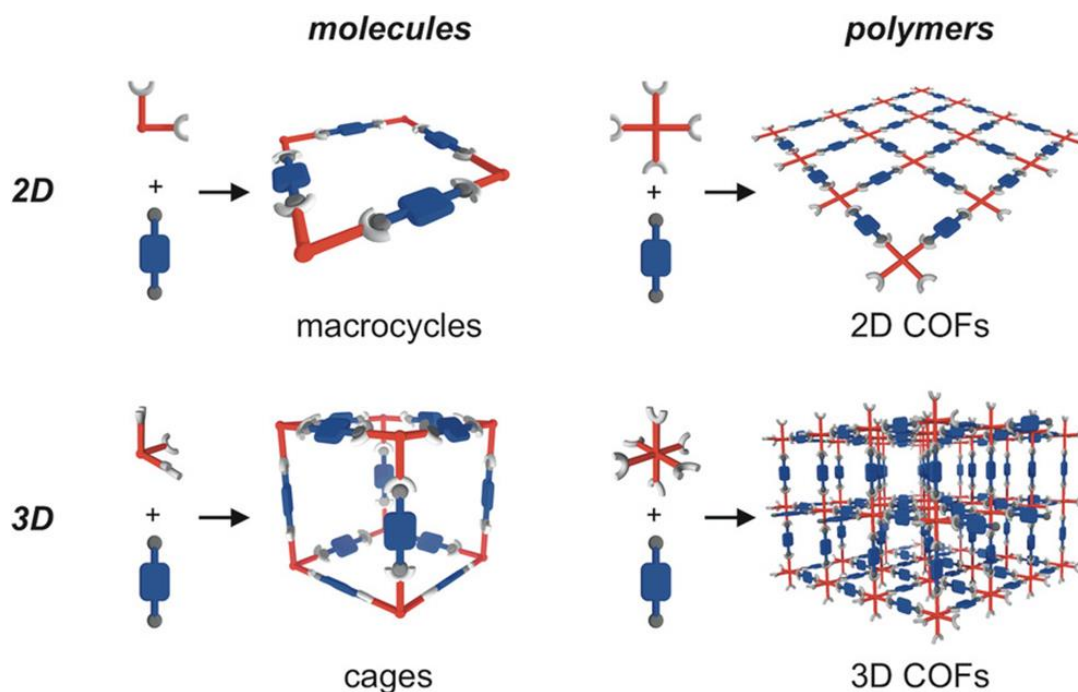

Figure 4.5 Dynamic covalent self-assembly of organic subcomponents into 2D and 3D molecular and polymeric nanostructures. From ref. [25].

One of the first examples of an organic cage studied for its gas adsorption properties was reported by Atwood and colleagues in 2009 [36]. The molecule named "Noria" has a paddle-wheel shape and can form porous structures in the amorphous state. The adsorption of N_2 at 77 K resulted to be very low, with a surface area of just 40 m^2/g. On the contrary, the uptake of CO_2 at ambient temperature was significantly greater, with approx. 4 mole of carbon dioxide adsorbed per mole of cage at 30 bar (Figure 4.6).

In the same year, Cooper and co-workers published their seminal paper on crystalline microporous materials based on imine-linked organic cages [37]. The condensation between 1,3,5-triformylbenzene with 1,2-ethylenediamine, 1,2-propylenediamine and (R,R)-1,2-diaminocyclohexane resulted in the formation of [4+6] tetrahedral cages named **CC1**, **CC2** and **CC3**, respectively.
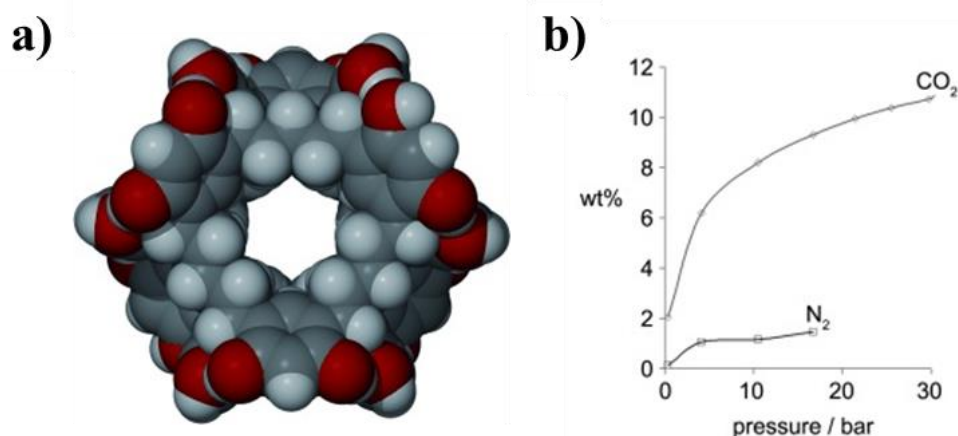

Figure 4.6 a) Space-filling representation of the Noria molecule. b) Gravimetric CO_2 and N_2 capacity for amorphous Noria material at 298 K. From ref. [36].

The desolvated crystals of these compounds showed a permanent porosity that resulted from both intrinsic and extrinsic voids. Notably, the interconnection between the inside and outside of the cages was strongly directed by functional groups attached to the vertices. In particular, **CC1** packed in a window-to-arene fashion, resulting in isolated void volume. On the other hand, **CC2** formed similar window-to-arene stacks, but the methyl groups frustrated the packing thus producing inter-stack 1D pore channels. On the contrary, the cyclohexyl groups in **CC3** directed the packing to a window-to-window motif, thus generating an interconnected 3D pore network (Figure 4.7). Gas uptakes are directly correlated to the interconnection of the voids, with **CC2** and **CC3** showing

higher surface areas with respect to **CC1** (*i.e.* 533 and 624 m^2/g against 23 m^2/g, respectively). The highly porous crystals of **CC2** and **CC3** also adsorbed large amounts of carbon dioxide (*i.e.* 3.0 and 2.47 mmol/g at 275 K and 1 bar, respectively) and methane (*i.e.* 0.95 and 1.15 mmol/g at 289 K and 1 bar, respectively). This work demonstrated how the proper design of the building units is fundamental to the formation of organic cages that retain porosity in the solid state.
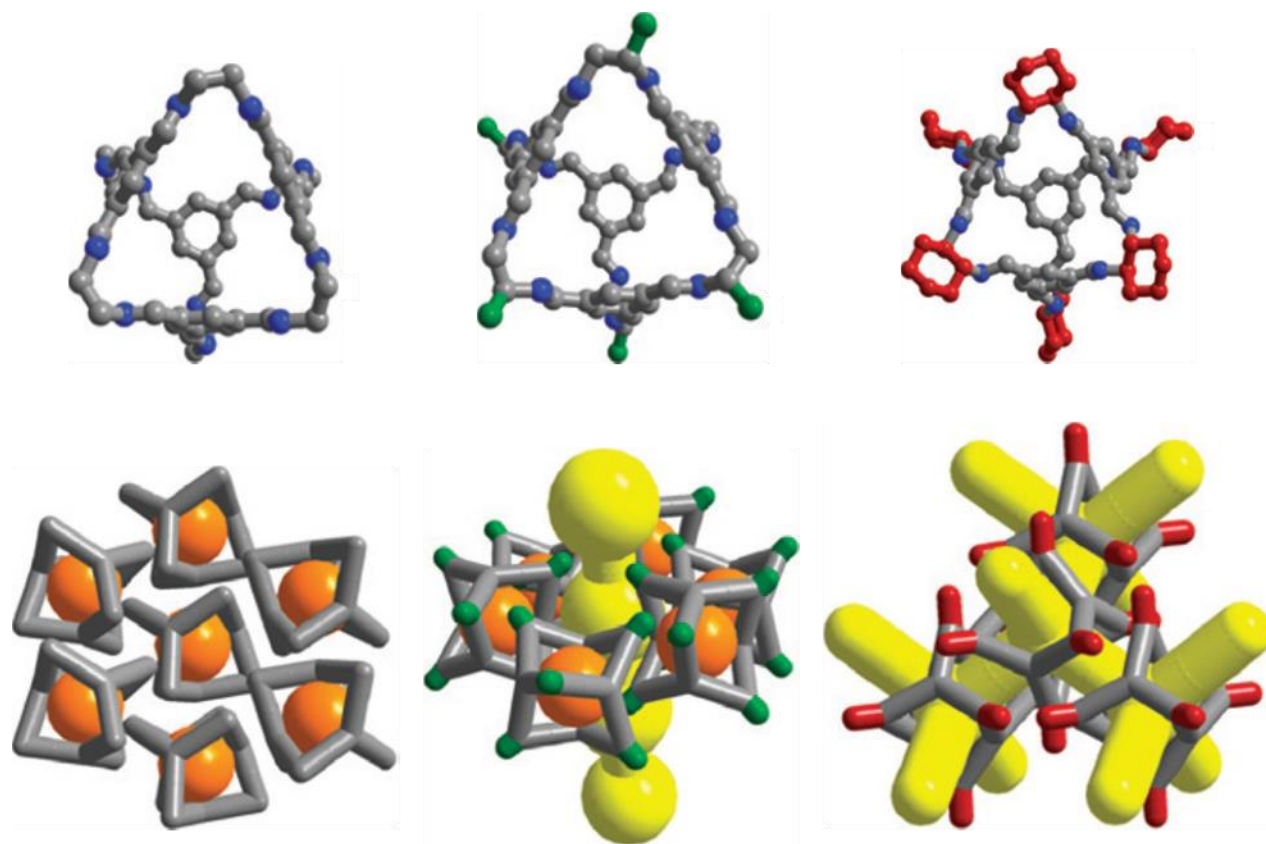

Figure 4.7 From left to right up, structures for cages **CC1**, **CC2** and **CC3** determined by single crystal X-ray diffraction for desolvated cages. Hydrogen atoms are omitted for clarity. Carbon and nitrogen atoms are coloured grey and blue, respectively. The methyl and cyclohexyl groups on the vertices of cages **CC2** and **CC3** are shown in green and red, respectively. From left to right bottom, the cage-to-cage packing in the crystal structures is schematized. Isolated void volume is shown in orange, while 1D and 3D pore channels in yellow. From ref. [37].

Soon after, the group of Mastalerz reported a [4+6] salicylbisimine cage compound with a very large internal pore volume [38]. In this case, π-π stacking interactions of the building blocks directed the packing of the cages to form an interconnected pore network (Figure 4.8). Even if the calculated surface area was more than double with respect to **CC2** and **CC3** (*i.e.* 1375 m^2/g), the adsorption of carbon dioxide and methane in the same conditions was found to be smaller, with values of 2.1 and 0.61 mmol/g, respectively, but with an ideal CO_2/CH_4 selectivity of 10/1. The authors referred this high selectivity to the presence of polar hydroxyl groups, inside the cavity, that could give more favourable interactions with carbon dioxide than with methane. The reduction of the imine linkers to form the correspondent amines resulted in a non-porous material with a surface area minor than 1 m^2/g. This confirms that a shape-persistent rigid structure is advantageous for gas adsorption, since the more flexible amine cages usually collapse in the solid state thus impeding gas penetration.
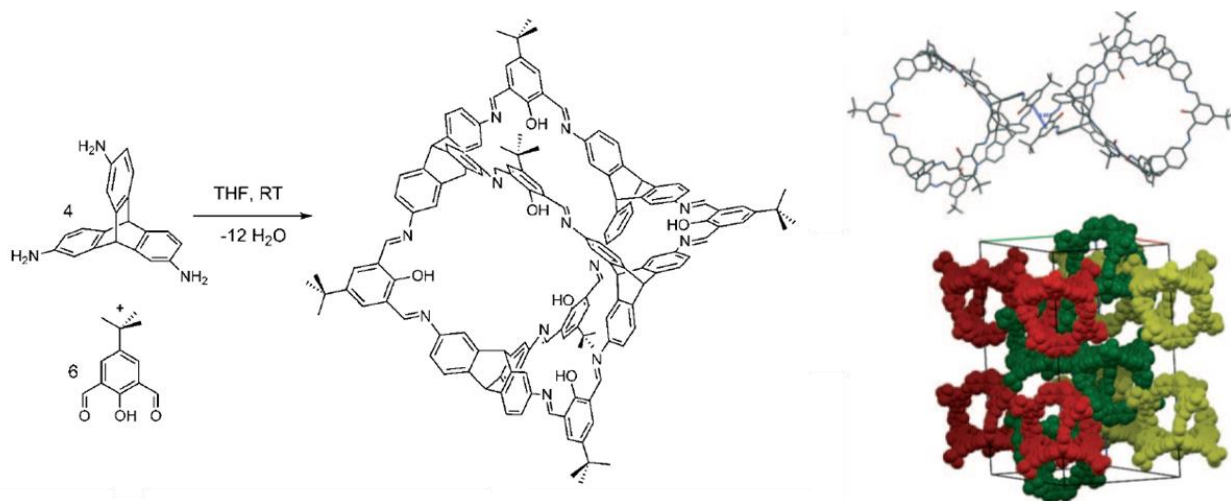

Figure 4.8 Synthesis of the salicylbisimine cage and crystal structure of cage compound with the arrangement of two adjacent molecules interacting by π-π stacking and packing in the unit cell. Hydrogen atoms are omitted for clarity. From ref. [38].

These seminal papers showed the great potential of POCs in gas adsorption and carbon capture applications. The separation of gas mixtures by porous materials is essentially based on size sieving and thermodynamic equilibrium effects. The first one is related with the different size of the gas molecules that lead to different steric hindrance during the separation. The second one is instead based on the chemical or physical interactions between the gas molecules and the material's

scaffold. As for the kinetic diameter (that is the average distance between two subsequent collisions of the gas particles), carbon dioxide molecule is smaller than nitrogen and methane (*i.e.* 3.3 Å against 3.64 and 3.82 Å, respectively). Moreover, CO_2 shows higher polarizability and quadrupole moment, and this feature can be exploited to establish favourable interactions with the porous material [39]. In 2011, Zhang and co-workers studied a series of porous organic cages in order to understand which parameters could promote a high selectivity for CO_2 [40]. This study showed that the adsorption selectivity for carbon dioxide over nitrogen is generally correlated to both a high density of amine (or imine) groups in the material and a small cage cavity size. N-rich materials actually promote the adsorption of the acidic CO_2 gas, while small pores limit the adsorption of nitrogen. The optimal balance of these two properties is therefore essential to produce performing porous molecular materials for carbon capture technologies.

Over the last ten years, the series of porous organic cages greatly expanded, approaching conventional porous materials in terms of surface areas [41]. Moreover, besides CO_2 adsorption and separation, POCs have also been exploited for other applications, such as catalysis, transport, sensing, isotopes or isomers separation [42]. Future developments should focus on further improving the stability and solubility of this class of compounds, as well as on further increasing their porosity and selectivity.

4.2 EXPERIMENTAL

4.2.1 Chemicals and Methods

All commercially available starting materials and solvents were purchased from Sigma-Aldrich and VWR, and used without further purification. 4-aminobenzaldehyde was obtained using a modified known procedure (see below). For the synthesis of 1,3,5-tris(methylamino)-2,4,6-triethylbenzene was used a reported procedure [43]. All reactions were performed under nitrogen. All the samples were homogenized by ball-milling for 30 min (first cycle of 20 min + 10 min pause + second cycle of 10 min) at a milling speed of 350 rpm using a ball-milling Planetary mill (Pulverisette 7, Premium line, Fritsch, Germany) in tungsten carbide bowls (Fritsch) with WC balls (Fritsch) in a ball to powder ratio of ca. 5:1 (ball diameter 0.5 cm, ball mass ca. 1g). ^{1}H- and ^{13}C-NMR spectra were recorded on a Bruker AVANCEIII 400 MHz (operating at 9.37 T, 400 MHz), equipped with a 5 mm BBO probe head with Z-gradient (Bruker BioSpin). The data were processed with Topspin 3.6 (Bruker Biospin). Deuterated solvents for NMR analysis (CDCl$_3$, CD$_3$CN) were purchased and used as received. Chemical shifts are reported in ppm with the residual solvent as internal reference, while 2D spectra were graphically referenced. The HSQC and ^{13}C-NMR spectra for **GI6** were recorded at 298 K on a Bruker Avance NEO 700 MHz spectrometer, equipped with a triple resonance helium cooled cryoprobe. The data were processed with Topspin 4.1 (Bruker Biospin). Elemental analyses were conducted on a Perkin Elmer CHN 2400SERIES II ELEMENTAL ANALYZER at the Department of Chemistry of the University of Milano (Italy).

4.2.2 Synthesis of Bisaldehyde 7 and Cages GI5-6

Synthesis of 4-aminobenzaldehyde
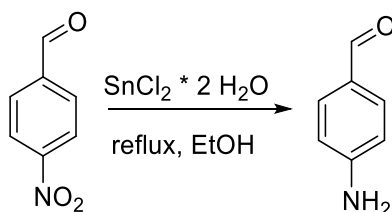
1 g of 4-nitrobenzaldehyde (6.6 mmol; 1 eqv) and 7.5 g of $SnCl_2 \cdot 2\ H_2O$ (33 mmol; 5 eqv) were added to 30 mL of EtOH and refluxed under N_2. The reaction was monitored by TLC (Silica gel, *n*-hexane:AcOEt = 1:1) until the complete disappearance of the reactant (about 2 hours). The red-brown mixture was then cooled to r.t. and poured in 120 g ice. pH was adjusted to 10-12 by the addition of aqueous NaOH. The yellow aqueous mixture was then extracted with AcOEt (5 x 100 mL). The organic phases where collected, washed with brine (2 x 200 mL), dried on Na_2SO_4, filtered and the solvent was removed under vacuum to obtain 730 mg of an orange solid. The final product was used without further purification. Yield: 91.3 %. ^{1}H-NMR (400 MHz; CDCl$_3$) δ: 9.68 (s, 1H, C*H*O), 7.63-7.61 (d, 2H, C*H*$_{ph}$), 7.64-7.62 (d, 2H, C*H*$_{ph}$), 4.17 (broad, 2H, N*H*$_2$).

Synthesis of 7
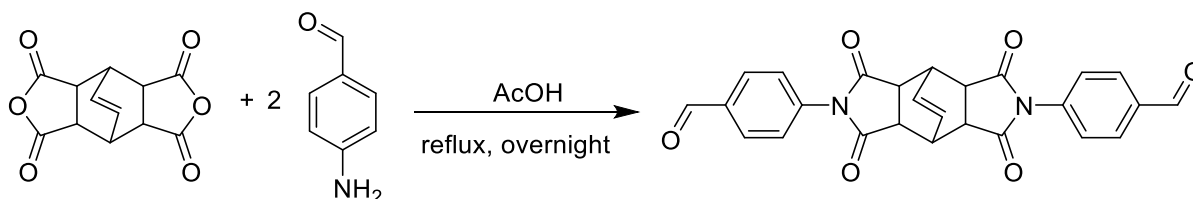
270 mg of bicyclo[2.2.2]oct-7-ene-2,3,5,6-tetracarboxylic dianhydride (1.09 mmol; 1 eqv) and 330 mg of 4-aminobenzaldehyde (2.72 mmol; 2.5 eqv) were added in a round-bottom flask to 20 mL of acetic acid (AcOH). The reaction mixture was refluxed overnight under vigorous stirring. The mixture was then cooled to r.t. and the precipitate (a light brown solid) was collected on a Buchner funnel. The solid was washed with AcOH (20 mL), H_2O (20 mL), MeOH (20 mL), Et_2O (20 mL)

and dried under vacuum. The final product (340 mg, light brown powder) was used without further purification. Yield: 68.8 %. ATR-FTIR, cm^{-1}: 1699 (str. C=O), 1707 (sym. str. C=O), 1779 (asym. str. C=O). ^{1}H-NMR (400 MHz; DMSO-d6) δ: 10.04 (s, 1H, CHO), 8.03 (d, 2H, CH_{ph}), 7.44 (d, 2H, CH_{ph}), 6.35 (m, 1H, CH_{olef}), 3.57 (s, 1H, CH), 3.49 (s, 2H, CH). ^{13}C-NMR (100 MHz; DMSO-d6) δ: 192.88, 176.83, 137.47, 136.10, 131.63, 130.51, 127.79, 43.04, 34.52. $C_{26}H_{18}N_2O_6 + H_2O$: calc. C 66.10%, H 4.27%, N 5.93%; exp. C 66.08%, H 4.40%, N 5.89%.

Synthesis of GI5
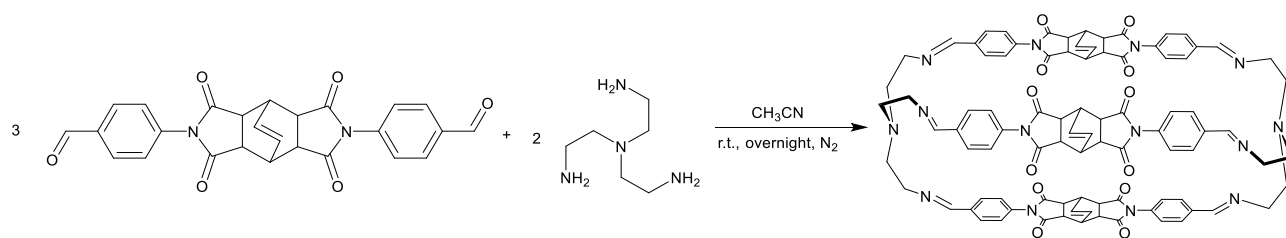
100 mg of **7** (0.22 mmol; 3 eqv) were dissolved in 100 mL of MeCN in a 3-necked round-bottom flask under N_2 and vigorous stirring. A solution of 23 μL of tris(2-aminoethyl)amine (96%; d=0.978; 0.15 mmol; 2 eqv) in 50 mL of MeCN was then added from a dropping funnel over 3 hours. The reaction mixture was stirred overnight at r.t. under N_2. The mixture was then concentrated under vacuum and the precipitate was filtered on a Buchner funnel. The solid product was washed with MeCN (10 mL) and dried under vacuum to yield 100 mg of an off-white powder. Yield: 86.2 %. ATR-FTIR, cm^{-1}: 1644 (str. C=N), 1704 (sym. str. C=O), 1744 (asym. str. C=O). ^{1}H-NMR (400 MHz; DMSO-d6; 80 °C) δ, ppm: 7.57 (s, 1H, CHN), 7.12 (d, 2H, CH_{ph}), 6.94 (d, 2H, CH_{ph}), 6.29 (m, 1H, CH_{olef}), 3.63 (s br, 1H, CH), 3.49 (s, 4H, CH + CH_{2tren}), 2.75 (m, 2H, CH_{2tren}). ^{13}C-NMR (100 MHz; DMSO-d6; 80 °C) δ, ppm: 177.28, 160.15, 136.72, 134.59, 131.24, 129.18, 129.01, 59.53, 55.48, 43.19, 34.50. $C_{90}H_{78}N_{14}O_{12} \cdot 4H_2O$: calc. C 66.20%, H 5.41%, N 12.07%; exp. C 66.74%, H 5.35%, N 12.11%.

Synthesis of GI6
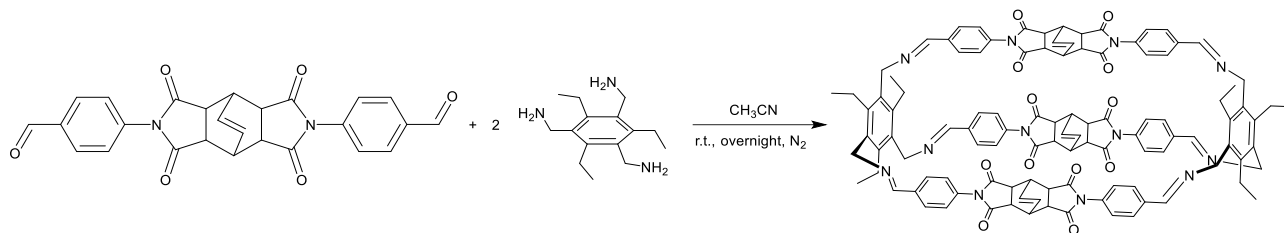
100 mg of dialdehyde **7** (0.22 mmol; 3 eqv) were dissolved in 100 mL of MeCN in a 3-necked round-bottom flask under N$_2$ and vigorous stirring. A solution of 36.6 mg of 1,3,5-tris(methylamino)-2,4,6-triethylbenzene (0.15 mmol; 2 eqv) in 5 ml of dichloromethane was added to 50 mL of MeCN and the resulting solution was added to the dialdehyde solution with a dropping funnel in 3 hours. The reaction was stirred overnight at r.t. under N$_2$. After a night a precipitate was formed. The mixture was filtered on a Buchner funnel and the solid was washed with MeCN (10 mL) and dried under vacuum to obtain 72 mg of an off-white powder. Yield: 54.7 %. ATR-FTIR, cm^{-1}: 1636 (str. C=N), 1709 (sym. str. C=O), 1749 (asym. str. C=O). ^{1}H-NMR (400 MHz; DMSO-d6) δ: 8.47 (s, 1H, C*H*N), 7.77 (d, 2H, C*H*$_{ph}$), 7.19 (d, 2H, C*H*$_{ph}$), 6.24 (t, 1H, C*H*$_{olef}$), 4.89 (s, 1H, C*H*$_2$N), 3.55 (s, 1H, C*H*), 3.40 (s, 2H, C*H*), 2.77 (q, 2H, C*H*$_2$), 1.20 (t, 3H, C*H*$_3$). ^{13}C-NMR (700 MHz, DMSO-d6) δ: 176.91, 160.74, 143.16, 136.42, 134.28, 132.98, 131.47, 128.81, 127.25, 58.10, 43.02, 34.20, 22.51, 13.12. C$_{108}$H$_{96}$N$_{12}$O$_{12}$ 2H$_2$O: calc. C 72.46%, H 5.63%, N 9.39%; exp. C 72.43%, H 5.69%, N 9.27%.

4.2.3 Solid-State Characterization of GI5 and GI6

For the Fourier Transform-Infrared analysis (FT-IR), a Nicolet FT-IR iS10 spectrometer (Nicolet, Madison, WI, USA) equipped with attenuated total reflectance (ATR) sampling accessory (Smart iTR with diamond plate) was used. Thirty-two scans in the 4000-600 cm^{-1} range at 4 cm^{-1} resolution were co-added. Well-ground powder samples were used, and spectra were obtained after pressing the sample onto an ATR diamond crystal at room temperature (20 °C). Peak wavenumbers were attributed by using the "Find peaks" function of the OMNIC™ Spectra Software.

Powder X-ray diffraction (PXRD) measurements were performed at room temperature on powders of the cage samples after manual grinding in an agate mortar using a Bruker D5005 diffractometer (Bruker Corporation, Billerica, MA, USA) with Cu-Kα radiation, graphite monochromator, and a scintillation detector. The measurements were performed from 5° to 50° in 2θ with step scan mode: scan step 0.02°, counting time 10 s per step; X-ray tube working conditions: 40 kV and 40 mA. Thermogravimetric analysis (TGA) was performed by a Q5000 apparatus (TA Instruments, New Castle, DE, USA) interfaced with a TA5000 data station under nitrogen flux (10 mL min^{-1}) in a platinum pan by heating about 3 mg of sample from room temperature up to 1000 °C (heating rate 5 K min^{-1}). TGA data were analyzed by the Universal Analysis software by TA Instruments.

A Zeiss EVO MA10 (Carl Zeiss, Oberkochen, Germany) Scanning Electron Microscope (SEM) was used for the morphological study on gold sputtered samples (Secondary Electrons detector). The measurements were performed at 20 kV with a working distance of 8.5 mm.

4.2.4 SCXRD Analysis

Diffraction data for **GI5**-α crystal (colourless, prismatic, 0.18 x 0.25 x 0.37 mm^3) have been collected at ambient temperature by means of a Bruker-Axs three circle diffractometer equipped with the SMART-APEX CCD area detector and working with graphite-monochromated Mo-Kα X-radiation ($\lambda = 0.7107$ Å). Data reduction was performed with the SAINT software and intensities were corrected for Lorentz and polarization effects [44].

Crystals of **GI6**-β were selected and mounted on a MITIGEN holder in Paratone oil, then quickly placed in a nitrogen stream to extract the best data set avoiding the possible degradation upon desolvation or exposure to air. Diffraction data for **GI6**-β crystal (colourless, prismatic, 0.12 x 0.28 x 0.35 mm^3) have been collected at 190 K by means of a Bruker-Nonius X8 four-circle diffractometer equipped with the APEX-II CCD area detector and working with graphite-monochromated Mo-Kα X-radiation ($\lambda = 0.7107$ Å). Data reduction, including intensity integrations and corrections for Lorentz and polarization effects, was performed with the APEX2 software [45]. Absorption effects for the diffraction data of both studied crystals were empirically evaluated by the SADABS software and absorption corrections were applied to the data [46]. The **GI5**-α crystal structure was solved by direct methods (SIR 2019), whereas the **GI6**-β crystal structure was solved by dual-space iteration starting from Patterson superposition (SHELXT)

[47,48]. Both crystal structures were refined by full-matrix least-square procedures on F^2 using all reflections (SHELXL 2018/3) and crystal data are reported in table 4.2 [49]. Positions of hydrogens, belonging to a water solvent molecule in **GI5**-α, were located in the final ΔF maps; these positions were refined in the final least-square refinement cycles, restraining the O-H distances to be 0.9 ± 0.01 Å. Unresolved positional disorder probably affected one of the two acetonitrile solvent molecules in the **GI5**-α crystal, which resulted with large and elongated thermal ellipsoids. These atom sites were refined with soft restraints on the atom displacement parameters (ISOR and DELU) and on the molecular geometry (SAME). Positions of hydrogens belonging to water solvent molecules in the **GI6**-β crystal remained undetermined and extensive positional disorder affected 5 of the 11 DMSO solvent molecules. Disorder resulted in apical S atoms occurring over two alternative positions, mutually exclusive and with the same statistical probability, which correspond to the two opposite vertexes of the trigonal pyramid having as a common base the two C and the O atoms. Atom belonging to DMSO solvent molecules were refined with soft restraints on the molecular geometries (SAME) and on the atom displacement parameters (ISOR, DELU and RIGU).

Crystals of **GI6**-δ (~100 μm) were picked out of the liquor and immediately covered with immersion oil (Cargille, NVH) to avoid disintegration outside of the solvent. Single crystal data were collected, at room temperature, on the XRD2 beamline at the Elettra synchrotron light-source (Trieste, Italy) at a wavelength of 0.6199 Å [50]. The light source obtained from the superconducting wiggler was monochromatized using a Si-crystal double monochromator. The diffraction setup consisted of an Arinax MD2S high throughput diffractometer and Pilatus 6M detector. A standard 360° φ-scan was used, with 1° step size. Data reduction, including intensity integrations and corrections for Lorentz and polarization effects, was performed using XDS [51]. The structure of **GI6**-δ was solved using ShelXT and refined using ShelXL as implemented in the OLEX2 package [52]. Hydrogen atoms belonging to the organic moieties were placed at calculated positions with the appropriate AFIX instructions and refined using a riding model.

Considering the crystal structure without guest molecules, the free volume accessible to CO_2 were calculated (per unit cell) as solvent accessible surface for a spherical molecular probe of 1.72 Å radius and an approximate grid space of 0.7 Å. Calculations were carried out by the Mercury software [53]. Deposition Numbers 2172063, 2172064 and 2172328 (**GI5**-α, **GI6**-β and **GI6**-δ, respectively) contain the supplementary crystallographic data.

Table 4.2 Single crystal data for the studied compounds.

	GI5-α	GI6-β	GI6-δ
Formula	$C_{94}H_{86}N_{16}O_{13}$	$C_{130}H_{172}N_{12}O_{28}S_{11}$	$C_{72}H_{64}N_8O_8$
M	1647.79	2703.45	1169.31
crystal system	monoclinic	monoclinic	Triclinic
space group	$P2_1$ (no. 4)	$P2_1/n$ (no. 14)	$P\bar{1}$ (no. 2)
a (Å)	19.1383(13)	24.354(3)	14.423(3)
b (Å)	11.6804(8)	20.120(2)	25.413(5)
c (Å)	19.3415(14)	31.705(3)	32.957(7)
α (°)	90	90	85.77(3)
β (°)	92.2030(10)	109.434(5)	78.52(3)
γ (°)	90	90	78.30(3)
V (Å³)	4320.5(5)	14650(3)	11585(4)
Z	2	4	6
ρ_{calcd} (g cm^{-3})	1.267	1.226	1.006
Wavelength, λ (Å)	Mo-Kα	Mo-Kα	0.6199
μ at λ (mm^{-1})	0.087	0.235	0.050
min/max transmission	0.876/0.985	0.896/0.978	
θ range (°)	2.04-25.06	2.52-25.00	1.43-64.26
measured reflections	43404	238616	270908
unique reflections	15199	25747	80293
R_{int}	0.041	0.119	0.2606
strong data [$I_O > 2\sigma(I_O)$]	9750	12991	14895
refined parameters	1116	1680	2390
$R1$, w$R2$ strong data	0.0464, 0.1056	0.1364, 0.3732	0.1070, 0.2863
$R1$ w$R2$ all data	0.0840, 0.1243	0.2180, 0.4198	0.2932, 0.3913
max/min residual (eÅ^{-3})	0.28/-0.20	1.23/-0.91	0.35/-0.28

Table 4.3 Geometrical features of the weak intermolecular C-H⋯O hydrogen bonds connecting adjacent molecular cages in the crystals of **GI5**-α and **GI6**-β.

GI5-α				
Donor group	**D⋯A (Å)**	**H⋯A (Å)**	**D-H⋯A (°)**	Acceptor atom
$C_{sp3}(1)$-H(1B)	3.33(1)	2.66(1)	126.2(3)	O(8)[1]
$C_{sp3}(11)$-H(11)	3.53(1)	2.68(1)	145.8(3)	O(7)[2]
$C_{sp3}(18)$-H(18)	3.09(1)	2.54(1)	115.5(3)	O(2)[2]
$C_{sp3}(42)$-H(42)	3.06(1)	2.46(1)	119.1(3)	O(9)[3]
$C_{sp3}(43)$-H(43)	3.18(1)	2.64(1)	114.7(3)	O(9)[6]
$C_{sp3}(72)$-H(72)	3.46(1)	2.54(1)	156.5(3)	O(6)[4]
$C_{sp3}(73)$-H(73)	3.31(1)	2.63(1)	127.1(3)	O(11)[5]
$C_{sp3}(76)$-H(76)	3.12(1)	2.60(1)	113.3(3)	O(6)[5]
$C_{aryl}(83)$-H(83)	3.08(1)	2.46(1)	123.9(3)	O(9)[6]
GI6-β				
Donor group	D⋯A (Å)	H⋯A (Å)	D-H⋯A (°)	Acceptor atom
$C_{sp2}(8)$-H(8)	3.43(1)	2.63(1)	142.1(4)	O(7)[7]
$C_{sp3}(17)$-H(17)	3.54(1)	2.54(1)	171.0(4)	O(8)[8]
$C_{sp2}(33)$-H(33)	3.28(1)	2.61(1)	128.1(4)	O(9)[9]
$C_{sp3}(37)$-H(37B)	3.31(1)	2.67(1)	122.9(4)	O(12)[10]
$C_{aryl}(43)$-H(43)	3.33(1)	2.42(1)	158.9(5)	O(2)[11]
$C_{sp3}(53)$-H(53)	3.36(1)	2.72(1)	122.0(4)	O(1)[11]
$C_{sp3}(64)$-H(64A)	3.15(1)	2.55(1)	118.7(4)	O(11)[12]
$C_{sp3}(76)$-H(76)	3.32(1)	2.57(1)	131.1(4)	O(3)[13]
$C_{sp3}(78)$-H(78)	3.25(1)	2.49(1)	132.4(4)	O(3)[13]
$C_{sp3}(106)$-H(06C)	3.65(1)	2.68(1)	171.1(6)	O(11)[12]

Symmetry code: ([1]) = −x+1, y−^{1}/$_2$, −z+2; ([2]) = −x+1, y−^{1}/$_2$, −z+1; ([3]) = x, y+1, z; ([4]) = x, y−1, z; ([5]) = −x, y−^{1}/$_2$, −z+1; ([6]) = −x, y+^{1}/$_2$, −z+1; ([7]) = x−^{1}/$_2$, −y+^{1}/$_2$, z−1/2; ([8]) = −x+^{3}/$_2$, y−^{1}/$_2$, −z+^{3}/$_2$; ([9]) = x+^{1}/$_2$, −y+^{1}/$_2$, z+^{1}/$_2$; ([10]) = −x+1, −y+1, −z+1; ([11]) = −x+^{3}/$_2$, y+^{1}/$_2$, −z+^{3}/$_2$; ([12]) = −x+1, −y+1, −z+2; ([13]) = −x+^{1}/$_2$, y+^{1}/$_2$, −z+^{3}/$_2$.

4.2.5 Gas Adsorption Analysis

The fine powder samples were weighed in a Quantachrome adsorption cell and outgassed under vacuum for 15 hours at 350 K.

Low-temperature N_2 (77 K and 298 K), CO_2 (273 K and 298 K) and CH_4 (298 K) adsorption/desorption measurements of cage powders were made using a Quantachrome Nova-e. Samples were degassed for 800 min at 100 °C under high vacuum prior to analysis. The gases were supplied by BOC and used without any further purification (N_2 purity > 99.999, CO_2 purity > 99.995%, CH_4 purity > 99.995%). The specimen was measured twice after outgas in two different cells to minimize the error, providing the same results. The data were analysed with the software provided with the instrument. The BET was calculated at a relative pressure P/P_0 < 0.1. Non-local density functional theory (NLDFT) was performed to calculate the pore size distribution and volume, considering a carbon equilibrium transition kernel at 273 K based on a slit-pore model; the kernel is based on a common, one centre, Lennard-Jones model. P_0 always refers to 1 bar, which is the maximum pressure reached by the instrument, not the saturation pressure of the probe gas. To assess the potential chemisorption, heats of adsorption were calculated from the CO_2 curves measured at 237 K and 298 K. The data were analysed with the QuadraWin software and fitted with the Langmuir-Freundlich equation and calculated via the Clausius-Clapeyron equation.

4.2.6 Preparation of the Mixed Matrix Membranes

The two cages **GI5** and **GI6** were loaded in the polymer matrix at 20 wt % on the basis of the total mass of the membranes. The polymers Matrimid® 9725 and PEEK-WC were dissolved at 2 wt.% and 3 wt.% respectively, in chloroform for 24h, and filtered by glass syringe filter of 3.1µm. Cages (15 mg each for PEEK-WC membranes and 30 mg for Matrimid® 9725 based) were first dispersed in chloroform (1 g) by sonication for 30 min at 25 °C and then the required amount of polymeric solution was added to this dispersion. The resulting mixture was further sonicated for 3 hrs. to obtain a homogenous dispersion of the cages. Finally, the dispersion was poured into a Teflon petri dish and dense membranes were obtained by slow evaporation of the solvent at 25 °C for 24 hrs. The resulting mixed matrix membranes were removed from the Petri dish and their top surface was then coated with a diluted PDMS Elastosil M 4601 (prepolymer+cross-linker) solution in *n*-hexane

to cover possible pinhole defects. The coated membranes were kept at room temperature to complete the crosslinking in 24 hrs. Further details of the coating procedure were reported previously [54].

4.2.7 Membranes Characterization

Single gas permeation studies were performed on circular membranes (exposed area 13.84 cm^2) at 25 °C and at a feed pressure of 1 bar by a fixed volume/pressure increase instrument designed by HZG and constructed by EESR (Geesthacht, Germany) [55]. Before each measurement, the membranes were evacuated in the testing cell by a turbo-molecular pump until complete desorption of all previously adsorbed gases and humidity. For the same reason, between two consecutive tests, the membranes were evacuated for a time equal to 10 times the time lag of the previous gas.

The time lag method was used for the determination of the permeability (P), diffusion (D), and solubility coefficients (S). See previous chapters for details.

4.3 RESULTS AND DISCUSSION

4.3.1 Design, Synthesis and Characterization of the Cages

GI5 and **GI6** are two novel imide/imine organic cages (Figure 4.9) prepared by [2+3] imine condensation of two different polyamines with a novel dialdehyde compound (**7**), containing the rigid bicyclo[2.2.2]oct-7-ene-2,3,5,6-tetracarboxydiimide core. This spacer was chosen for two main reasons: i) the large number of heteroatoms and polar groups that brings on itself can increase the selectivity for CO_2 with respect to N_2 and CH_4; ii) its bent structure can have a positive effect on the formation of a cage, disfavouring the formation of oligomers/polymeric species.
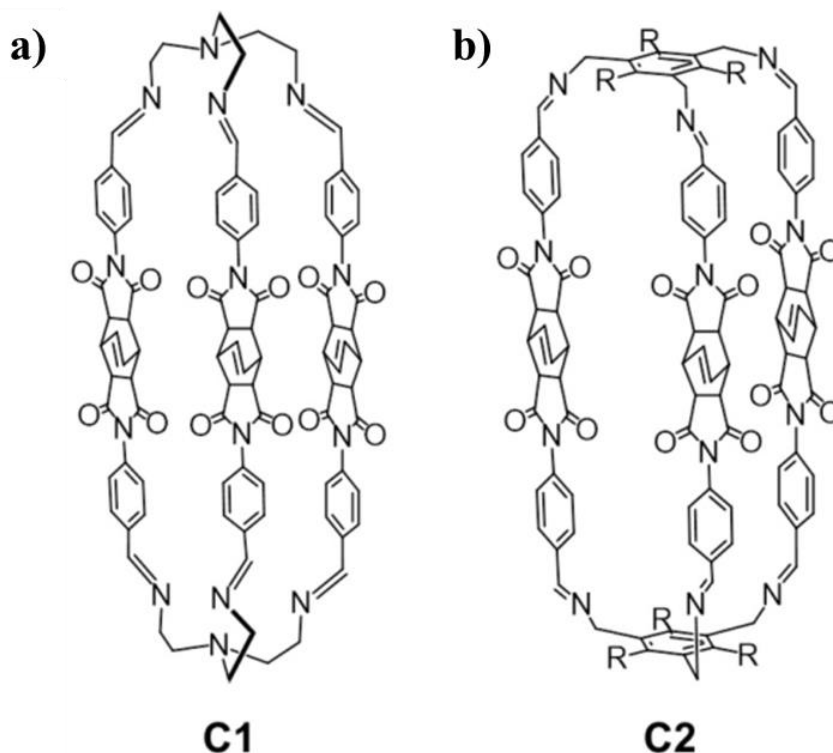
Figure 4.9 a) Structure of **GI5**. b) Structure of **GI6**. (R = CH_2CH_3).

The chosen polyamines were *N,N*-bis(2-aminoethyl)ethylenediamine (tren) and the 1,3,5-tris(aminomethyl)-2,4,6-triethylbenzene for **GI5** and **GI6**, respectively. The first amine is very flexible while the latter is more rigid and preorganized. Both **GI5** and **GI6** cages precipitated as

pure solids from the reaction mixture in acetonitrile (MeCN) as solvent, and the structures were confirmed by ^{1}H and ^{13}C-NMR spectroscopies as well as CHN elemental analysis (see chapters 4.2.2 and 4.5). Scanning electron microscopy (SEM) images on precipitated **GI5** showed a mixture of an aggregated material in nanometric form and larger prismatic microcrystals (Figure 4.10).
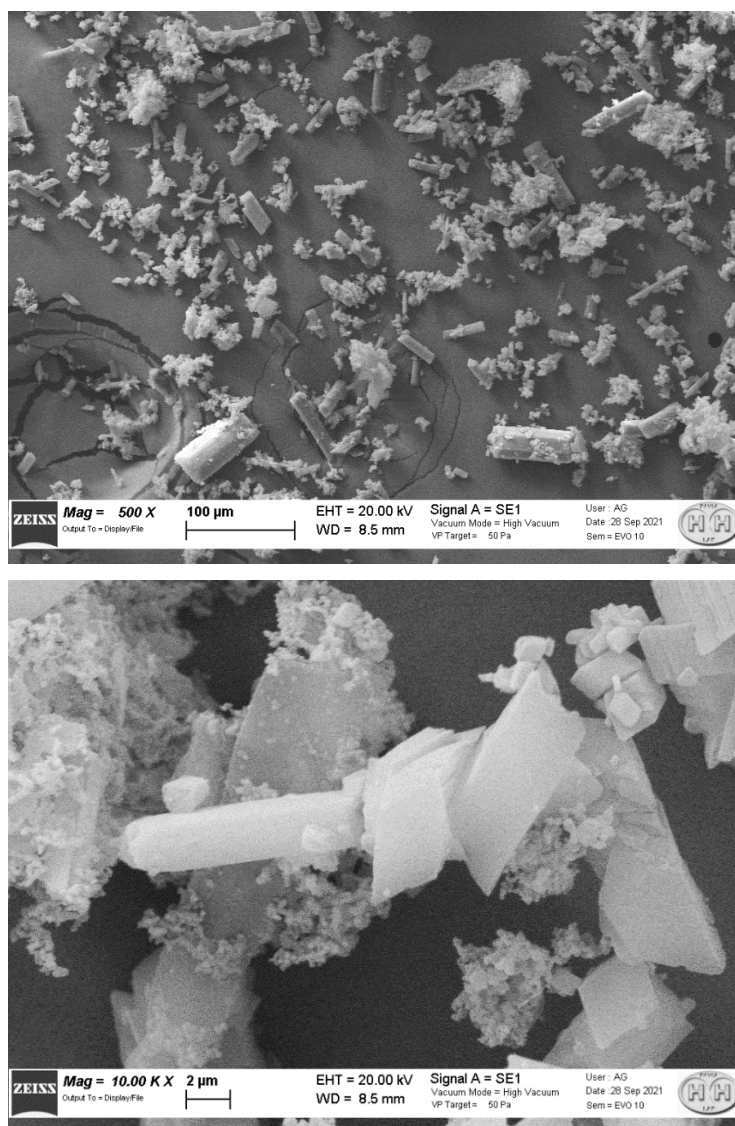
Figure 4.10 SEM images of **GI5** as precipitated from reaction mixture at different magnifications.

On the other hand, SEM images of **GI6** showed a crystalline prismatic and well-defined morphology (Figure 4.11).
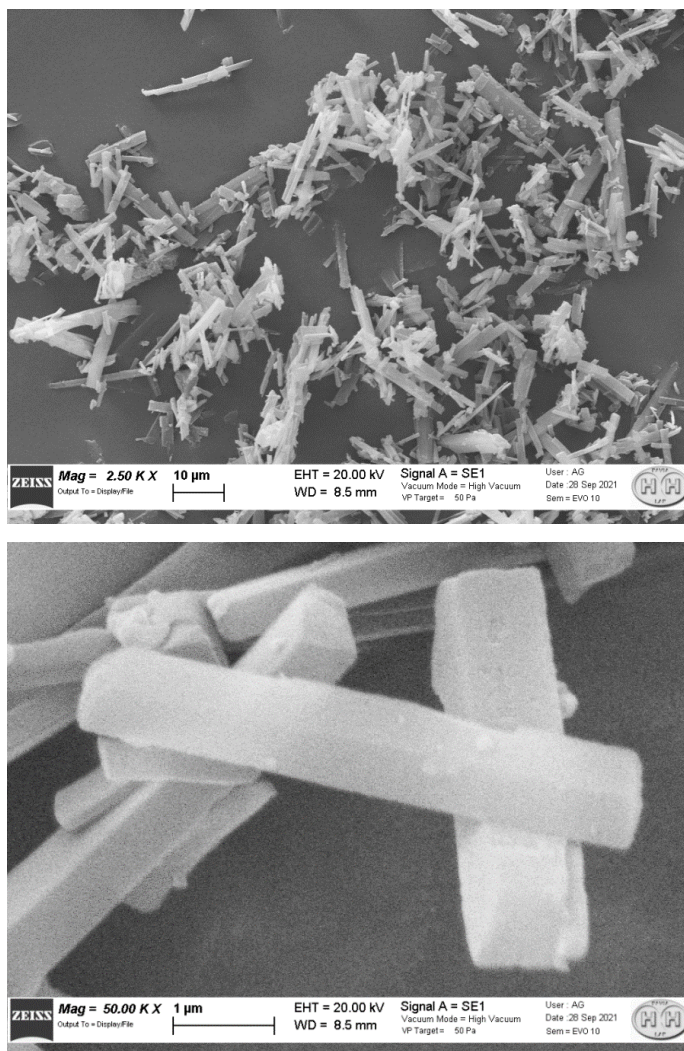
Figure 4.11 SEM images of **GI6** as precipitated from reaction mixture at different magnifications.

The higher crystallinity of **GI6** compared to **GI5** was confirmed by powder X-ray diffraction analysis (Figures 4.12 and 4.13). The PXRD pattern of **GI5** is dominated by the "halo" of an amorphous component superimposed to some intense peaks, corresponding to the calculated diffraction pattern of the **GI5**-α phase (see chapter 4.3.2). On the other hand, PXRD analysis on **GI6** showed sharper peaks with a hardly visible amorphous "halo", in agreement with the morphological analysis made by SEM. Unfortunately, none of the phases resolved by SCXRD (*i.e.* **GI6**-β and **GI6**-δ) correspond to the experimental pattern of the cage material (see chapter 4.3.2).
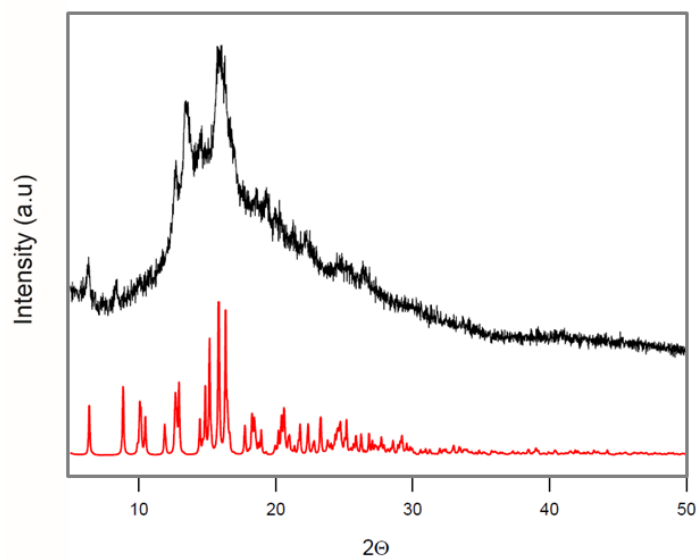
Figure 4.12 Experimental PXRD pattern (black line) for **GI5**, recorded on the bulk solid precipitated from the reaction mixture (MeCN solvent); simulated PXRD pattern (red line) produced using the SCXRD data collected on crystals of **GI5-α**, obtained by slow evaporation of an MeCN solution of the cage.
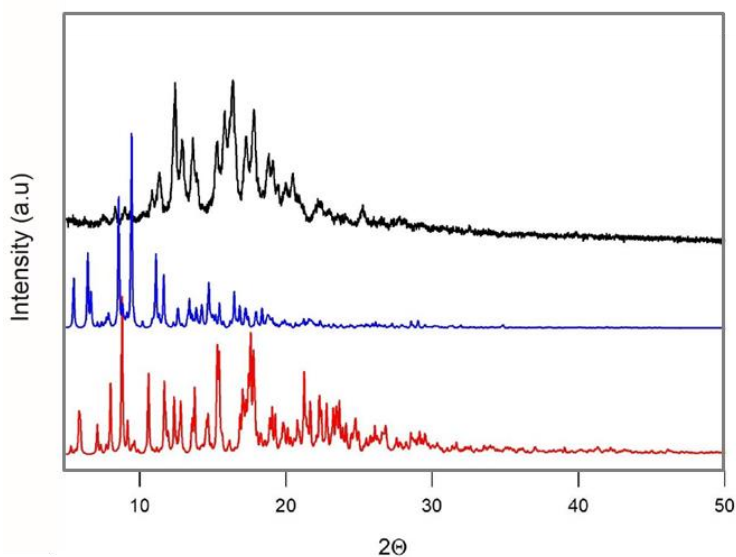
Figure 4.13 Experimental PXRD pattern (black line) for **GI6**, recorded on the bulk solid precipitated from the reaction mixture (MeCN solvent); simulated PXRD patterns produced using the SCXRD data collected on crystals of **GI6-β** (red line) and **GI6-δ** (blue line).

The cages were also characterized by Fourier transform infrared spectroscopy-attenuated total reflectance (FTIR-ATR) analysis. The spectra of the two compounds showed the typical imine C=N stretching features at 1644 and 1636 cm^{-1} for **GI5** and **GI6**, respectively. Peaks assigned to the diimide groups (*i.e.* symmetric and asymmetric stretching of C=O) were also visible at 1704 and 1774 cm^{-1} for **GI5**, 1709 and 1779 cm^{-1} for **GI6** (Figures 4.14 and 4.15).
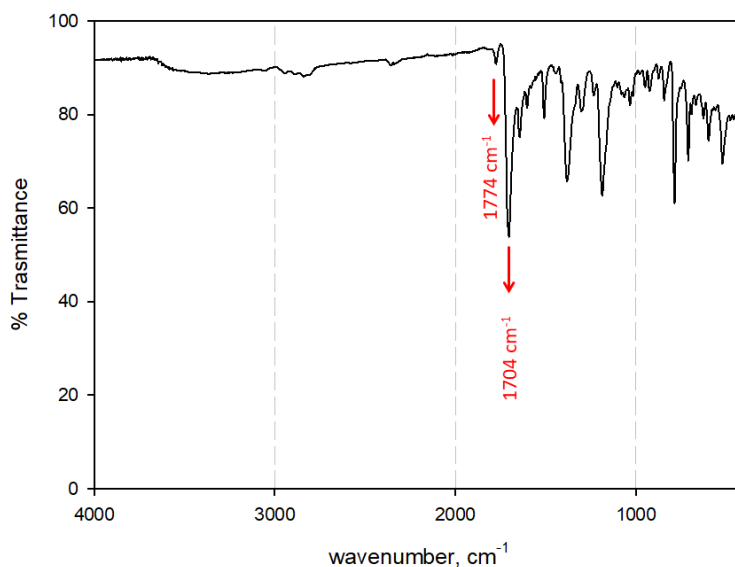
Figure 4.14 FTIR-ATR spectrum of **GI5**.
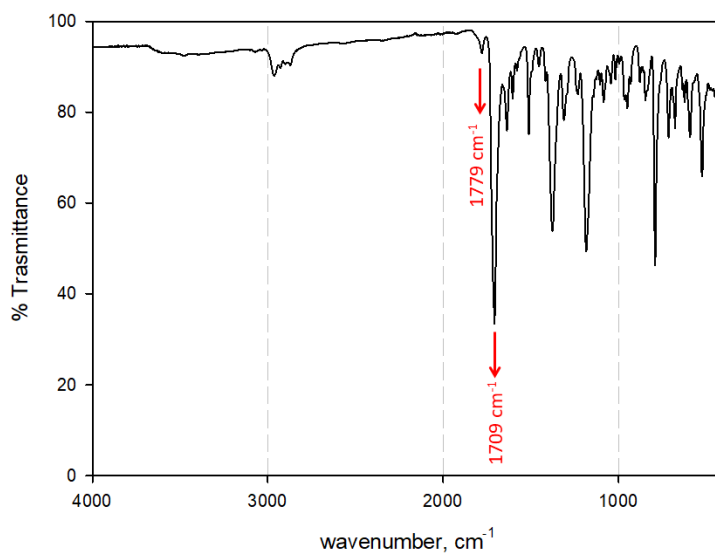
Figure 4.15 FTIR-ATR spectrum of **GI6**.

The thermal stability of **GI5** and **GI6** was assessed through thermogravimetric analysis (TGA). Apart from a small weight loss for the first sample, very likely from humidity, both cages showed decomposition only starting from around 220 and 330 °C, respectively (Figures 4.16 and 4.17).
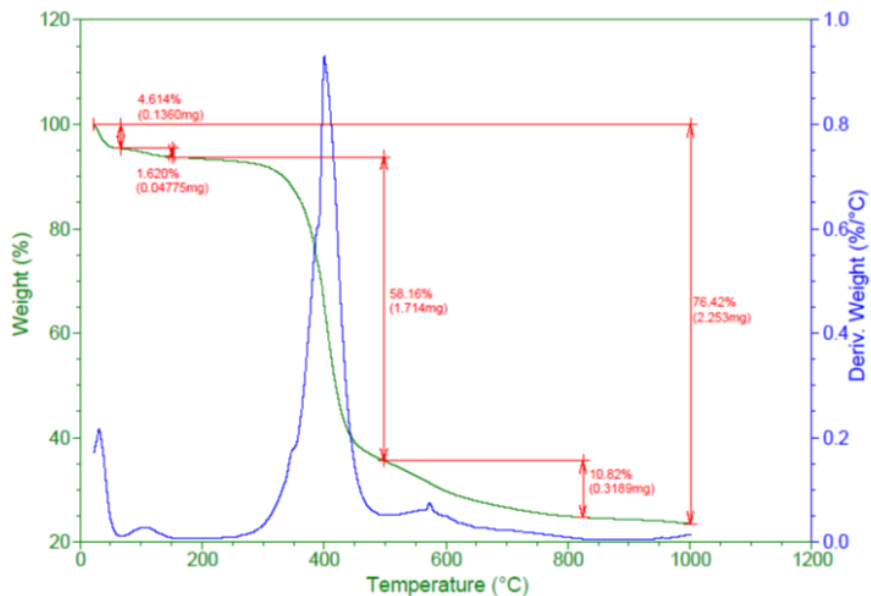
Figure 4.16 TGA (green) and DTG (blue) curves for **GI5**.
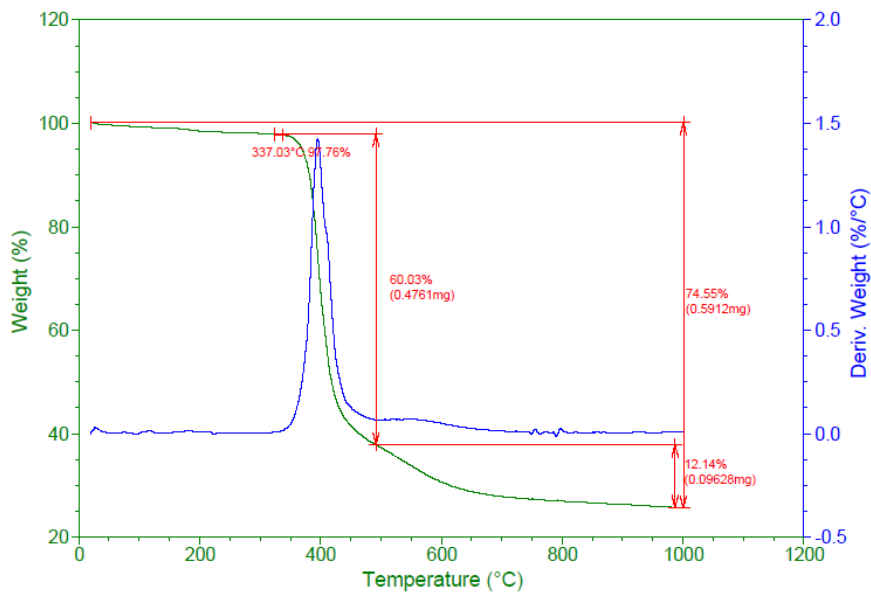
Figure 4.17 TGA (green) and DTG (blue) curves for **GI6**.

4.3.2 SCXRD Studies

Single crystals suitable for XRD study were obtained for both **GI5** and **GI6**.

Crystals of the **GI5** cage of formula $C_{90}H_{78}N_{14}O_{12} \cdot 2MeCN \cdot H_2O$ crystallize in the monoclinic system (**GI5**-α, P21; a=19.1383(13) Å, b=11.6804(8) Å, c=19.3415(14) Å, β=92.2030(10)°, V=4320.5(5) Å^3) and were formed by slow evaporation of a solution of the compound in MeCN. As revealed by the SCXRD analysis of this crystalline phase, each molecular cage assumes an elongated conformation with collapsed cavity. The distance between the apical tertiary amines measures approximately 22 Å, and the bicyclo[2.2.2]oct-7-ene containing groups are oriented towards the cavity centre. The average shortest intramolecular separation between the olefin hydrogens of the three cage-arms is about 3.0 Å (Figure 4.18).
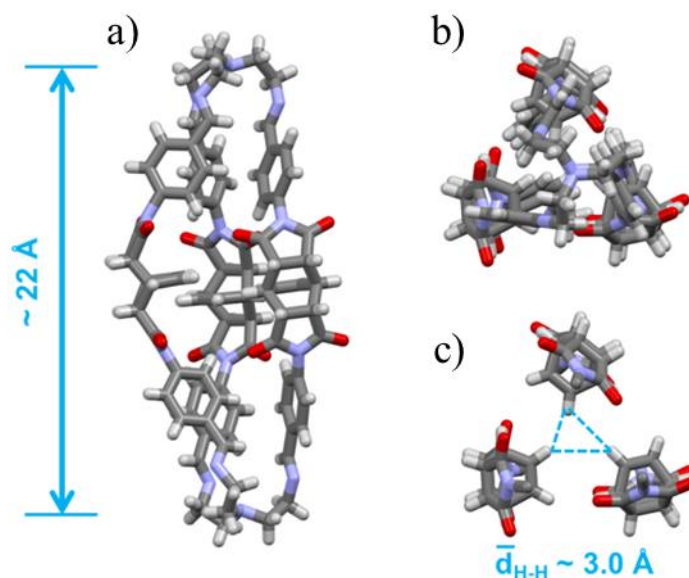
Figure 4.18 a) Front and b) top views of the crystal structure of **GI5** in **GI5**-α crystals; MeCN and water molecules are omitted for clarity. c) Focus on the central portion of the cage cavity (top view), dashed cyan lines show minimum distances between HC=CH hydrogens.

This closed conformation is stabilized by intramolecular H-bonding interactions between carbonyl oxygen atoms and hydrogen atoms of different arms of the cage (Figure 4.19).

The asymmetric unit contains three crystallization solvent molecules (two acetonitrile and one water), as shown by the formula, that occupy extrinsic voids. The cages are tightly packed,

generating a thick network of intermolecular H-bonds (Figure 4.20). These involve the carbonyl oxygen atoms as H-acceptors, and the C_{aryl}-H and C_{sp3}-H bonds of bicyclo[2.2.2]oct-7-ene-based spacers as H-donors. Geometrical features of these weak C-H···O interaction are reported in table 4.3. Considering the crystal structure without guest molecules, the calculated voids accessible to a molecular probe of 1.72 Å radius (generally used for CO_2) correspond only to 0.1% of unit cell volume (Figure 4.20) [56]. From the comparison of the calculated PXRD pattern for **GI5-α** with the experimental pattern acquired on the powder precipitated from the reaction mixture, and used in the studies with gases (Figure 4.12), it was possible to observe some similarities. In particular, a few diffraction peaks calculated for **GI5-α** can be also found under the "halo" of the amorphous component in the experimental pattern. It is therefore possible to speculate that the microcrystalline part of the bulk solid corresponds to the **GI5-α** phase obtained by SCXRD.
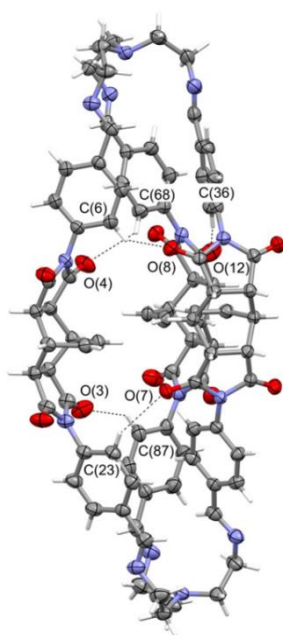
Figure 4.19 Plot showing thermal ellipsoids (at the 30% probability level) for the **GI5-α** phase (additional water and MeCN solvent molecules are omitted for clarity). The central cavity of **GI5** is collapsed and this conformation is stabilized by weak intramolecular C_{aryl}-H···O H-bonds (dashed lines)
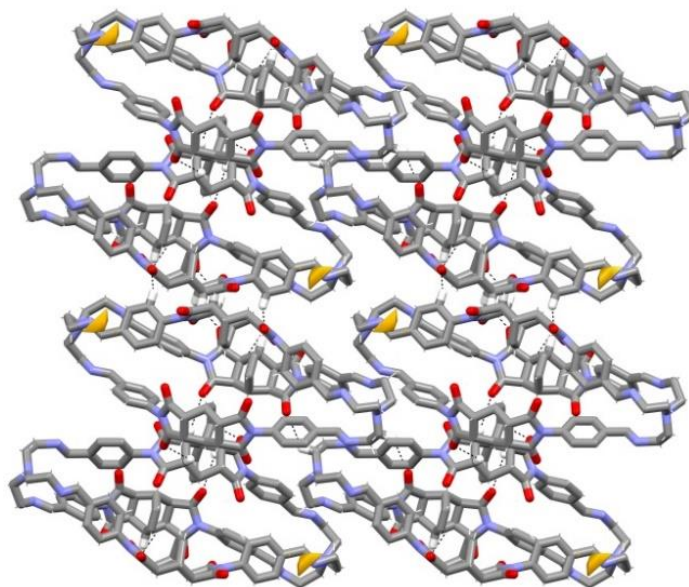
Figure 4.20 A view of the packing along the *b*-axis, for the **GI5**-α phase (MeCN and crystallization water molecules have been omitted for clarity). Free volume is reported in yellow. H-bonding interactions are highlighted as dashed lines. H-atoms are drawn as small sticks, except for the ones involved in C-H···O hydrogen bonds.

In the case of **GI6**, the slow cooling of a saturated solution of the cage in dimethyl sulfoxide (DMSO) led to crystals of formula $C_{108}H_{96}N_{12}O_{12} \cdot 11DMSO \cdot 5H_2O$, belonging to the monoclinic system (**GI6**-β, P21/*n*; *a*= 24.354(3) Å, *b*=20.120(2) Å, *c*=31.705(3) Å, *β*=109.434(5), *V*= 14650(3) $Å^3$). The crystals proved to be very fragile and unstable outside of the mother liquor, especially at room temperature. For this reason, the SCXRD data were collected at 190 K. Any attempt to measure them at lower temperatures (in the range 90–170 K) failed due to the collapse of the crystalline lattice, probably caused by the very large amount of lattice DMSO molecules. The cavity of **GI6** is open, large, and filled with solvent crystallization molecules (Figure 4.21). The rigidity of the polyamine building block used in this case probably prevented the cavity from collapsing, as instead observed for **GI5** with the tren polyamine. The molecule has a prolate spheroid shape with a separation between the triethylaryl platforms of about 20 Å (calculated by the centroid-centroid distance). Even in this case the HC=CH bonds of the bicyclo[2.2.2]oct-7-ene containing spacers point towards the cage cavity, and the average separation between the close olefin hydrogens measures 7.1 Å. Now, intramolecular H-bonding interactions between carbonyl

oxygen atoms and hydrogen atoms of different aromatics are not present due to the higher distance between the arms.

In the **GI6**-β phase, adjacent cages are involved in weak C-H⋯O interactions having the carbonyl oxygen atoms as H-acceptors, and C_{aryl}-H, C_{sp2}-H, and C_{sp3}-H as H-donors (Table 4.3). However, the cage packing is less dense compared to **GI5**-α and many additional guest solvent molecules co-crystallized within the pores. The unit cell totally contains 11 DMSO and 5 H_2O crystallization solvent molecules. For the crystal structure without guest molecules, the calculated voids correspond to 9.8% of unit cell volume (Figure 4.22). As said in the chapter 4.3.1, the calculated PXRD pattern for the **GI6**-β phase is different from the experimental one recorded on the microcrystalline precipitate (Figure 4.13). From now on, this microcrystalline phase will be called **GI6**-γ.
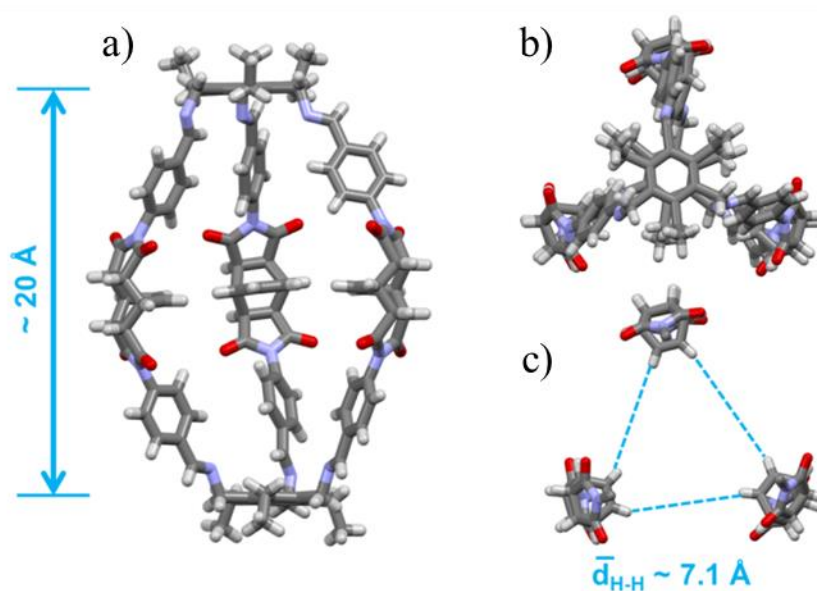
Figure 4.21 a) Front and b) top views of the crystal structure of **GI6** in **GI6**-β; DMSO and water molecules are omitted for clarity. c) Focus on the central portion of the cage cavity (top view), dashed cyan lines: minimum distances between HC=CH hydrogens.
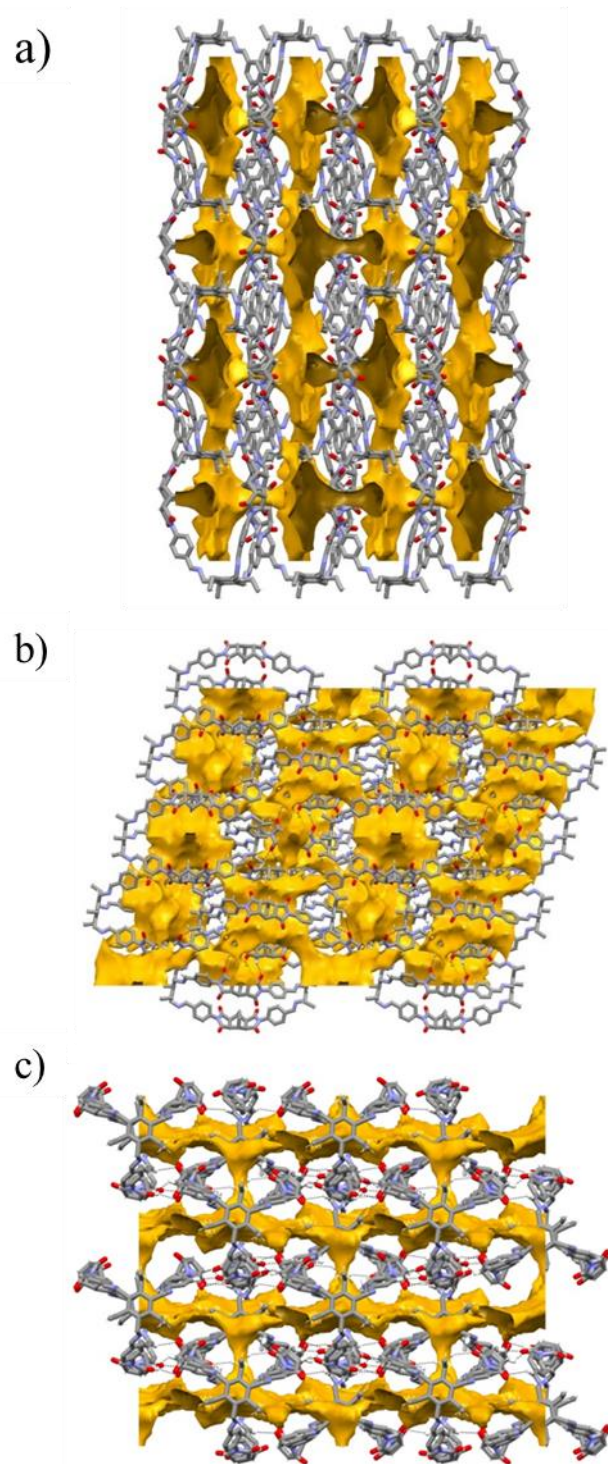
Figure 4.22 Views of the packing for the **GI6**-β phase along the: a) *a*-axis; b) *b*-axis; c) c-axis. DMSO and water crystallization molecules are omitted. Free volume is reported in yellow, while H-bonding interactions are highlighted by dashed lines. H-atoms are drawn as small sticks, except for the ones involved in C-H···O hydrogen bonds.

Crystals suitable for SCXRD were also obtained from a saturated solution of **GI6** in MeCN. Single-crystal data were collected at 300 K on the XRD2 beamline at the Elettra synchrotron light-source (Trieste, Italy) at a wavelength of 0.6199 Å. In this case, **GI6** crystallizes in a triclinic phase containing two molecules as asymmetric unit (**GI6**-δ, Z=6; s.g. $P\bar{1}$; a=14.423(3) Å, b=25.413(5) Å, c=32.957(7) Å, α=85.77(3)°, β=78.52(3)°, γ=78.30(3)°; V=11585(4) Å^3). At 300 K, the solvent trapped in the **GI6**-δ cavities is in a disordered form. For this reason, a solvent mask was calculated, and 768 electrons were found in a volume of 3648 Å^3 in two voids per unit cell. This is consistent with the presence of about 5.8 MeCN molecules per asymmetric unit (which account for 770 electrons per unit cell), or approx. 3 solvent molecules per cage. The molecule structure is similar but slightly smaller than in **GI6**-β, with an average separation between the HC=CH hydrogens of 6.1 Å. However, **GI6** molecules in this phase form partly entangled dimers and the effective inner void results smaller than that expected for a single molecule (Figure 4.23). Another difference is that one cage molecule (yellow in Figure 4.23) exhibit one of the external CH$_3$ groups oriented facing toward the inner void, while the structure of the second molecule (blue in Figure 4.23) is comparable to that of **GI6**-β.
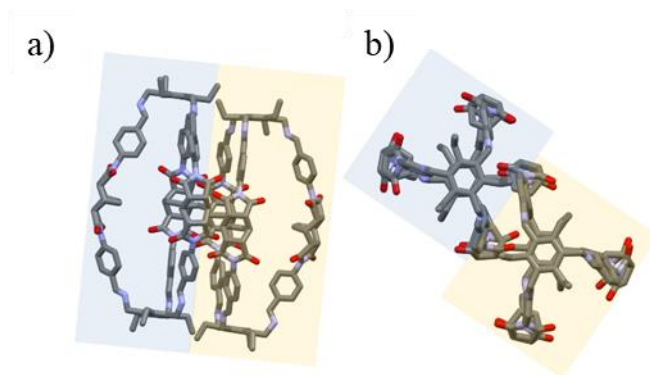

Figure 4.23 a) Front and b) top views of the two cage molecules (highlighted in blue and yellow) per asymmetric unit of the **GI6**-δ phase. Hydrogens and solvent molecules are omitted for clarity.

In this phase, the cage molecules are more densely packed than in the **GI6**-β phase, and the calculated voids potentially accessible to CO_2 are reduced to 1.9% of unit cell volume (Figure 4.24). Unfortunately, even in this case, the calculated PXRD pattern is different from the experimental one recorded on the precipitated cage (Figure 4.13).
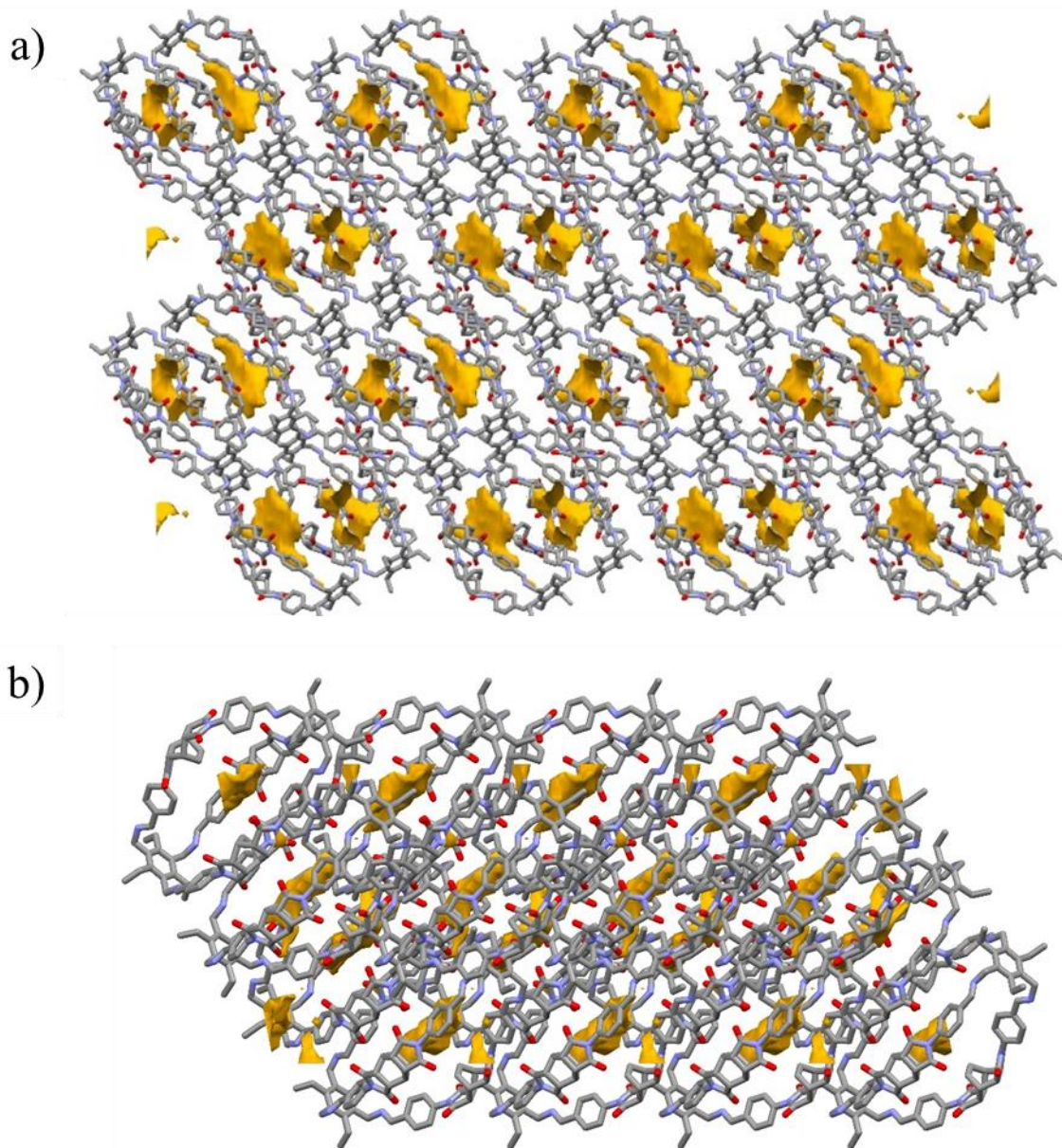

Figure 4.24 Views of the packing for the **GI6**-δ cage along: a) *a*-axis; b) *c*-axis. MeCN crystallization molecules and H atoms are omitted for clarity. Free volume is reported in yellow.

4.3.3 Gas-Adsorption Studies on GI5 and GI6

To confirm the assumed porosity of the two new molecules, gas-adsorption studies were performed on the precipitated cages (*i.e.* amorphous **GI5** and microcrystalline **GI6**-γ) using CO_2, N_2, and CH_4 as probe gases. **GI5** and **GI6** samples were firstly homogenized in a ball-mill, and then activated by heating overnight at 373 K under vacuum to remove traces of humidity. Brunauer-Emmett-Teller surface areas (SA_{BET}) were initially determined using N_2 as the probe gas. The isotherm curves showed a very poor adsorption of nitrogen at 77 K (Figures 4.25 and 4.26). The BET surface areas, calculated at a relative pressure $P/P_0 < 0.1$, showed an apparent surface area of ~44 m^2g^{-1} and a pore volume of 3.4×10^{-2} cm^3g^{-1} for **GI5** and an apparent surface area of ~35 m^2g^{-1} and a pore volume of 8.2×10^{-2} cm^3g^{-1} for **GI6**. Usually, similar results are given by either nonporous samples or materials where the pores are not readily accessible, especially at cryogenic temperatures where the adsorption kinetic is very slow. In this case, the pronounced hysteresis of both isotherms supports the second option [57,58]. The N_2 adsorption was also measured at room temperature (298 K) but, as expected, the quantity adsorbed at this temperature is much lower than that at 77 K, with very low values up to 1 bar (Figure 4.27). This analysis is anyway important to calculate the separation selectivity of the cages for CO_2/N_2 in post-combustion carbon capture conditions.
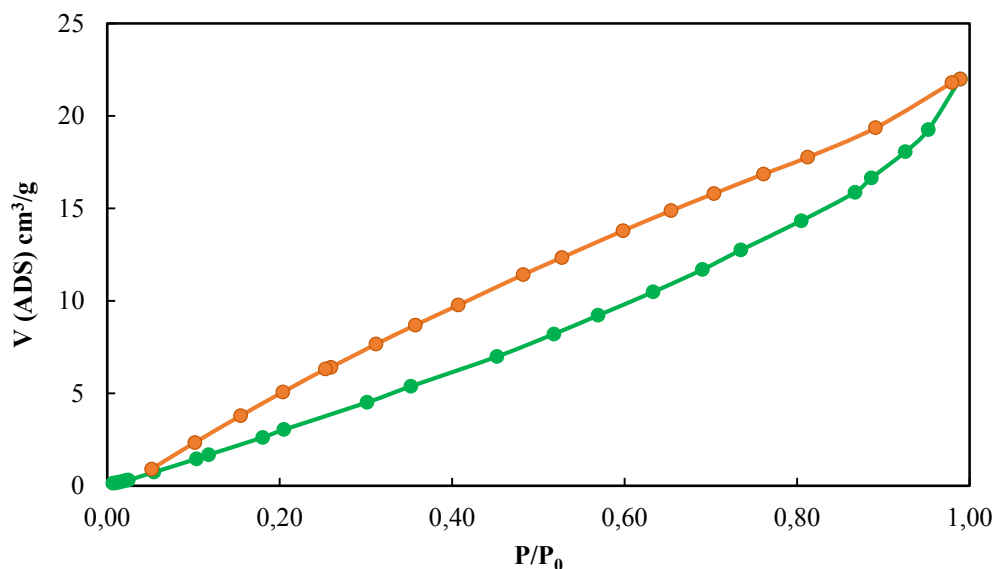
Figure 4.25 N$_2$ isotherm measured for **GI5** at 77 K (green line: adsorption; orange line: desorption; dots: experimental data).
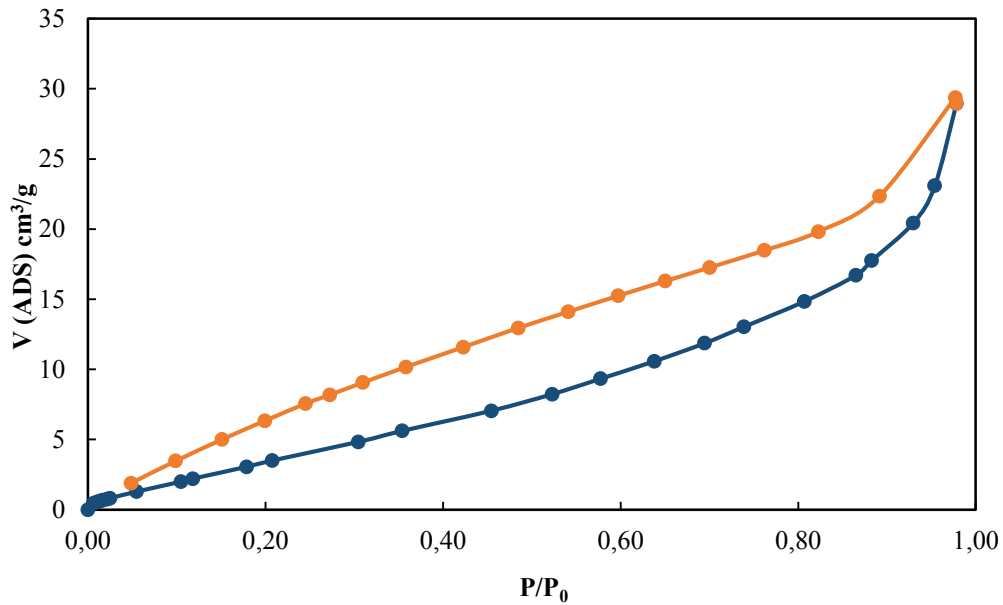

Figure 4.26 N$_2$ isotherm measured for **GI6** at 77 K (blue line: adsorption; orange line: desorption; dots: experimental data).
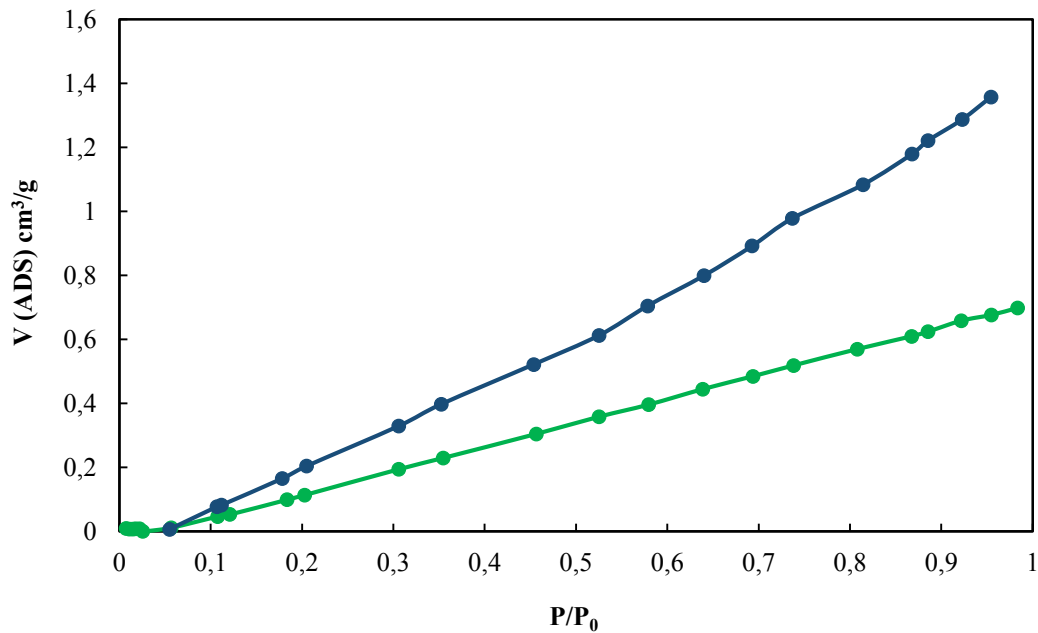

Figure 4.27 Overlay of N$_2$ adsorption isotherms, measured for **GI5** (blue) and **GI6** (green) at 298 K (dots: experimental data).

After nitrogen adsorption studies, CO_2 uptake was measured at both 273 and 298 K. The lower temperature is crucial to assess the superficial area, the pore size distribution (PSD) and the heats of adsorption (Q_{st}) [58,59]. At 273 K, **GI5** and **GI6** samples exhibited a carbon dioxide uptake of ~17.9 cm^3g^{-1} (0.799 $mmolg^{-1}$) and ~26 cm^3g^{-1} (1.161 $mmolg^{-1}$), respectively. In this case, the CO_2 isotherms (Figures 4.28 and 4.29) showed a less pronounced hysteresis than the N_2 curves. This may depend on two factors: i) the cages are porous, but the pores are too poorly accessible to be measured with N_2; ii) the higher temperature (*i.e.* 273 K for CO_2 *vs.* 77 K for N_2) produces some swelling of the flexible parts of the cages, which permits a higher and faster kinetic adsorption of carbon dioxide compared to nitrogen [60,61]. The latter reason may also account for the relatively good CO_2 adsorption for **GI5**, beside the poorly accessible free volume in the crystal structure. The calculation of the BET surface area from the CO_2 curve is more unusual, than from N_2, but it is however feasible and reliable [60]. Values of 224 m^2g^{-1} and 325 m^2g^{-1} were obtained for **GI5** and **GI6**, respectively.
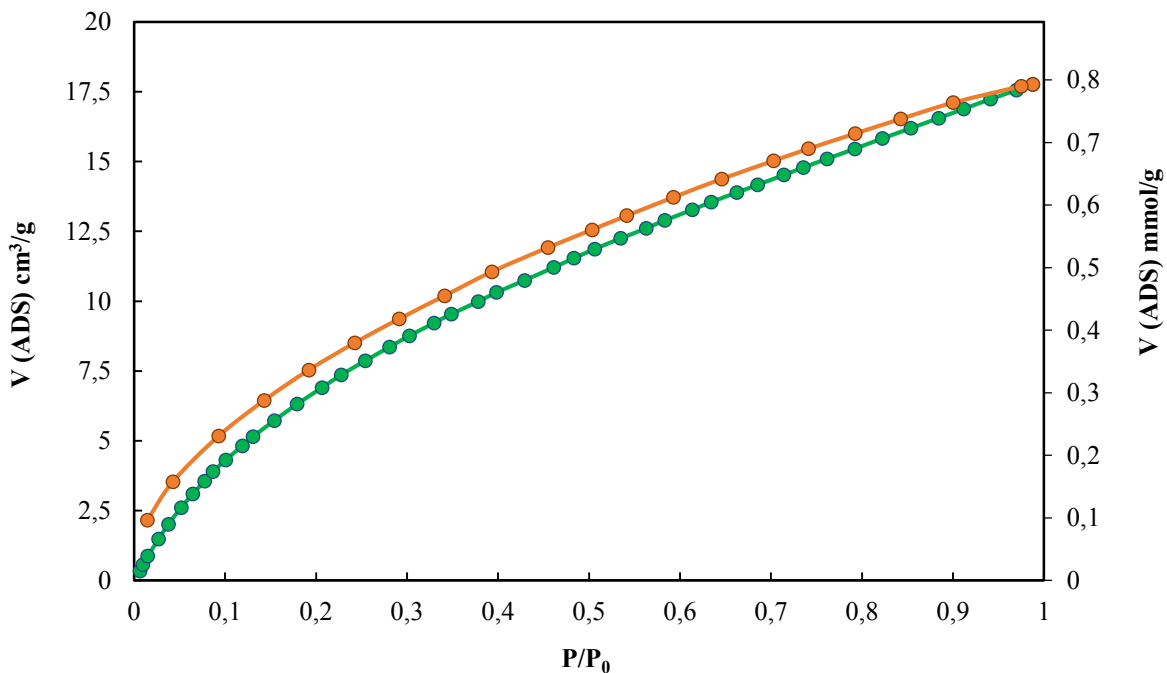

Figure 4.28 CO_2 isotherm measured for **GI5** at 273 K (green line: adsorption; orange line: desorption; dots: experimental data).
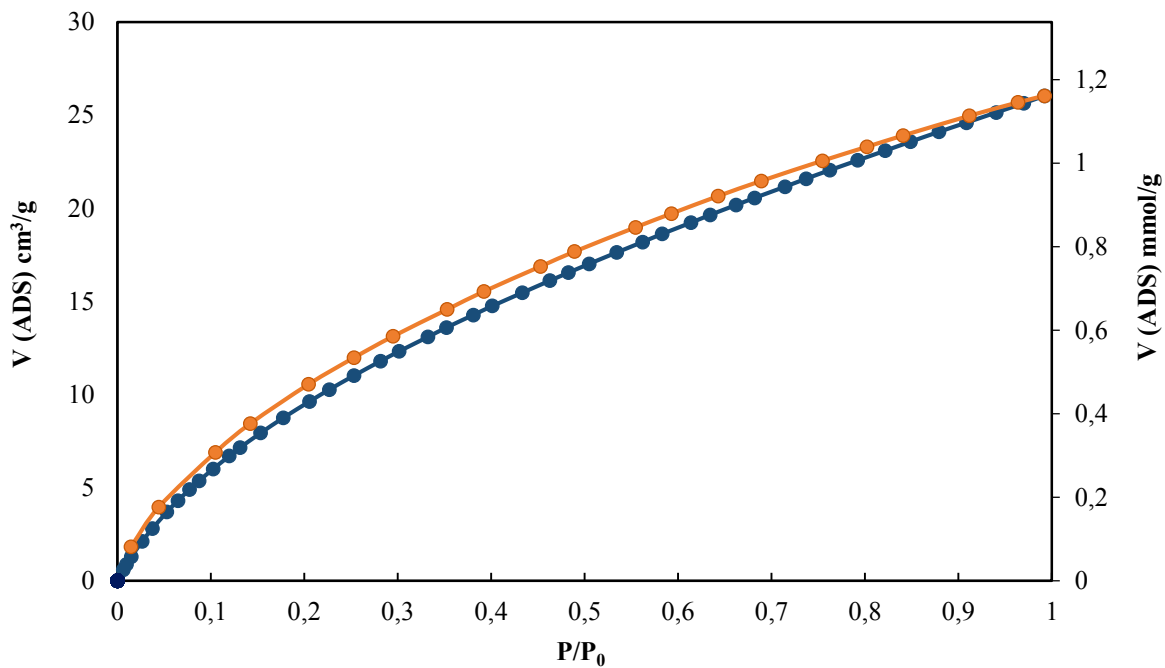
Figure 4.29 CO$_2$ isotherm measured for **GI6** at 273 K (blue line: adsorption; orange line: desorption; dots: experimental data).

PSD was preferably assessed from CO_2 adsorption at 273 K compared to N_2 at 77 K, because nitrogen cannot penetrate pores smaller than 5 Å while carbon dioxide allows the evaluation of pores ~3.5 Å. NLDFT is one of the most reliable methods to evaluate PSD, also providing information about the contribution of different pore sizes. The calculation of the pore size distribution by NLDFT from CO_2 at 273 K revealed that both cages present pores centred at 3.5, 5.0 and 8.2 Å (Figures 4.30 and 4.31). In the case of **GI5**, the contribution of ultra-microporosity (pores of ~3.5 Å) is very small, with a low overall pore volume centred in that region (<0.1 $cm^3nm^{-1}g^{-1}$). On the other hand, in **GI6** the peak at ~3.5 Å is more pronounced, suggesting a slightly higher ultra-microporosity contribution. Pore size distribution is considered as a merely qualitative analysis, but the scattered distribution of peaks and the low amount of ultra-micropores confirm previous speculations: both materials have a low porosity and the accessibility for the gases seems to be hindered.
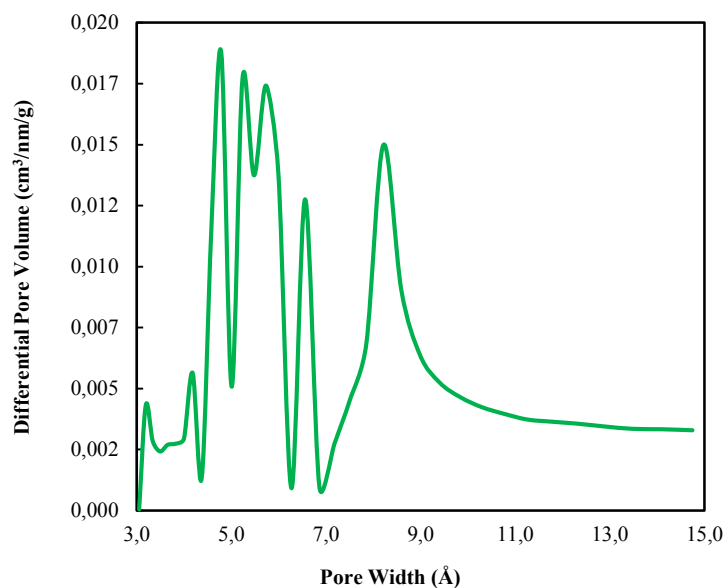

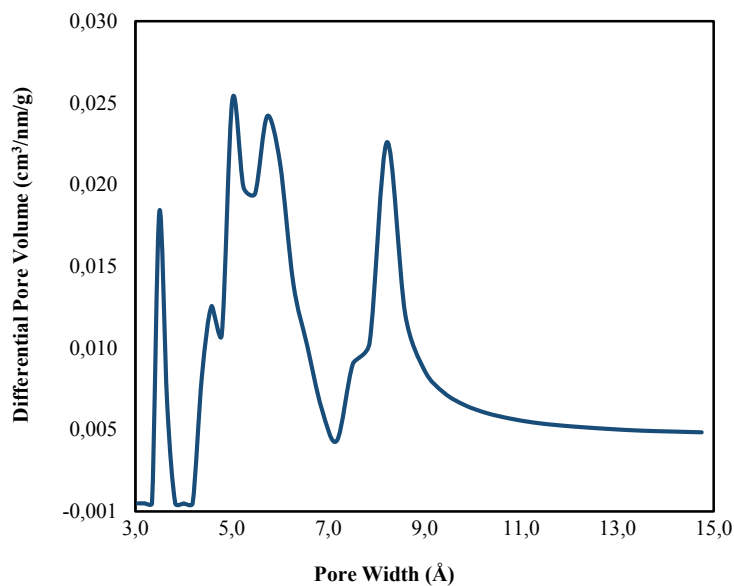**Figure 4.30** NLDFT pore size distribution for **GI5** from CO_2 at 273 K.

Figure 4.31 NLDFT pore size distribution for **GI6** from CO_2 at 273 K.

Heats of adsorption (Q_{st}) were calculated from the CO_2 isotherms measured at 273 and 298 K. The curves were fitted with the Langmuir-Freundlich equation and the Q_{st} calculated using the Clausius-Clapeyron equation at zero coverage [62]. The analysis resulted in approx. values of 35 KJ mol^{-1} for **GI5** and 39 KJ mol^{-1} for **GI6** (Figures 4.32 and 4.33). These data suggest that the main adsorption mechanism is driven by physisorption, but a little contribution from chemisorption cannot be excluded since is considered for values of $Q_{st}>30$ KJ mol^{-1}. Notably, these heats of adsorption are indicative of a high affinity of the cages for CO_2. The quantity of carbon dioxide adsorbed at 298 K is lower than that adsorbed at 273 K (*i.e.* 13.6 cm^3g^{-1}, 0.607 $mmolg^{-1}$ for **GI5** and 15.5 cm^3g^{-1}, 0.692 $mmolg^{-1}$ for **GI6**), but the decrease is not much. This fact, added to the relatively high value of Q_{st} that includes a contribution from chemisorption, may validate the choice of the bicyclo[2.2.2]oct-7-ene-2,3,5,6-tetracarboxydiimide core: the presence of heteroatoms, polar and H-bonding groups in the cages structure can effectively enhance the affinity for CO_2.
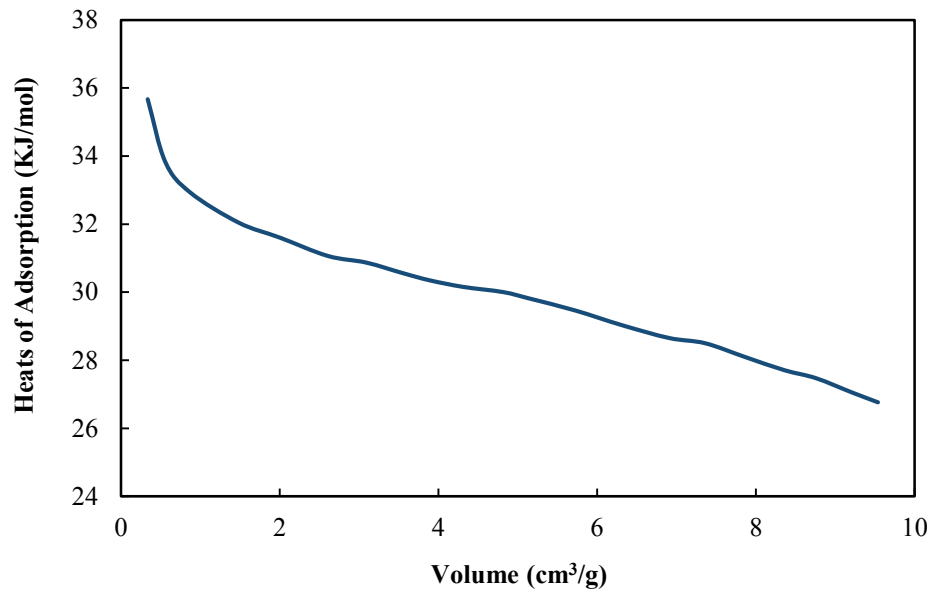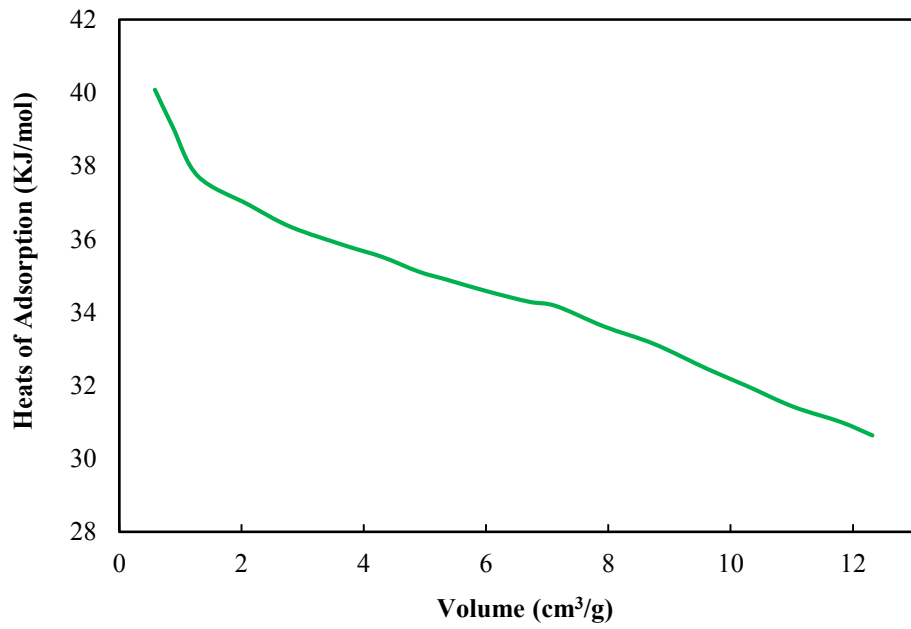
Figure 4.32 Heats of adsorption for **GI5**.

Figure 4.33 Heats of adsorption for **GI6**.

To evaluate these cages for biogas upgrading, CH_4 uptake was measured at 298 K also. As expected, the quantity adsorbed is very low, with values of 7.1 cm^3g^{-1} and 7.7 cm^3g^{-1} for **GI5** and **GI6**, respectively. In figure 4.34 its shown the comparison of the curves deriving from the isothermal gas adsorption measurements at 298 K for CO_2, N_2 and CH_4. It is easy to see that the amount of adsorbed CO_2 largely exceeds that of nitrogen and methane for both cages, thus provide interesting insight into the potential use of these materials for post-combustion carbon capture and biogas upgrading in VSA systems [63].
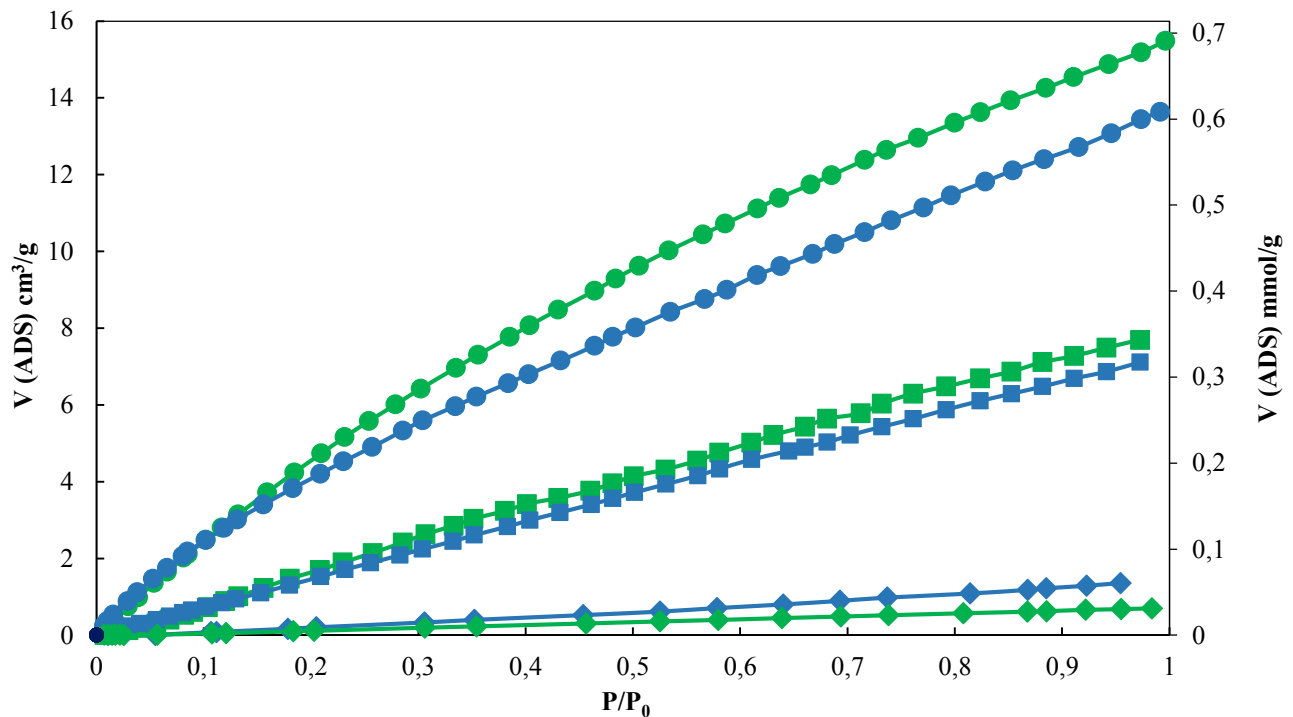

Figure 4.34 Overlay of CO_2 (circles), CH_4 (squares), and N_2 (diamonds) adsorption isotherms, measured for **GI5** (blue) and **GI6** (green) at 298 K.

The calculation of the gas adsorption selectivity can be done by fitting the curves with the Ideal Adsorption Solution Theory (IAST) method [64]. The IAST method, reported for the first time by Myers and Prausnitz, was created to predict the selectivity of binary gas mixtures from the analysis of single gas adsorption isotherms. IAST is currently considered as a reliable method to predict the selectivity for porous materials [65]. For post-combustion carbon capture applications, the selectivity must be calculated for a hypothetical CO_2/N_2 mixture. The curves obtained from CO_2 and N_2 adsorption measurements at 298 K are fitted with the dual site Langmuir-Freundlich

equation, using the IAST++ software, and the selectivity is calculated according to equation 1, assuming 15/85 %v composition of the CO_2/N_2 gas mixture, thus simulating the typical flue gas compostion [66,67].

$$S = \frac{Q_{CO_2}}{Q_{N_2}} \cdot \frac{P_{N_2}}{P_{CO_2}}$$

<div align="right">(eq. 1)</div>

P_{CO2} and P_{N2} are the partial pressures of CO_2 and N_2, while Q_{N2} and Q_{CO2} are CO_2 and N_2 uptakes, respectively.

The final selectivity is taken from the curve approaching 1 bar, as this is the typical pressure for post-combustion capture by VSA (Figures 4.35 and 4.36). The selectivity of **GI5** and **GI6** for this separation (*i.e.* 41 and 32, respectively) demonstrated to be competitive compared to similar reported Porous Organic Cages and other porous materials [68,69]. The slightly higher value of **GI5** with respect to **GI6** is most likely due to smaller pores and lower superficial area, leading to an improved molecular sieving effect.

These two cages were also tested for the potential separation of CO_2 from CH_4, simulating biogas upgrading, which can be performed by VSA at 1 bar (Figures 4.37 and 4.38) [70]. According to the operating conditions typically reported for this separation, the CO_2/CH_4 selectivity was simulated assuming a 50/50 %v composition. The calculated selectivity for this gas pair is lower than for the correspondent CO_2/N_2 separation, but it is in line with other reported POCs. Notably, **GI5** proved again more selective than **GI6** with CO_2/CH_4 IAST selectivity values of 5.3 and 3.0, respectively.
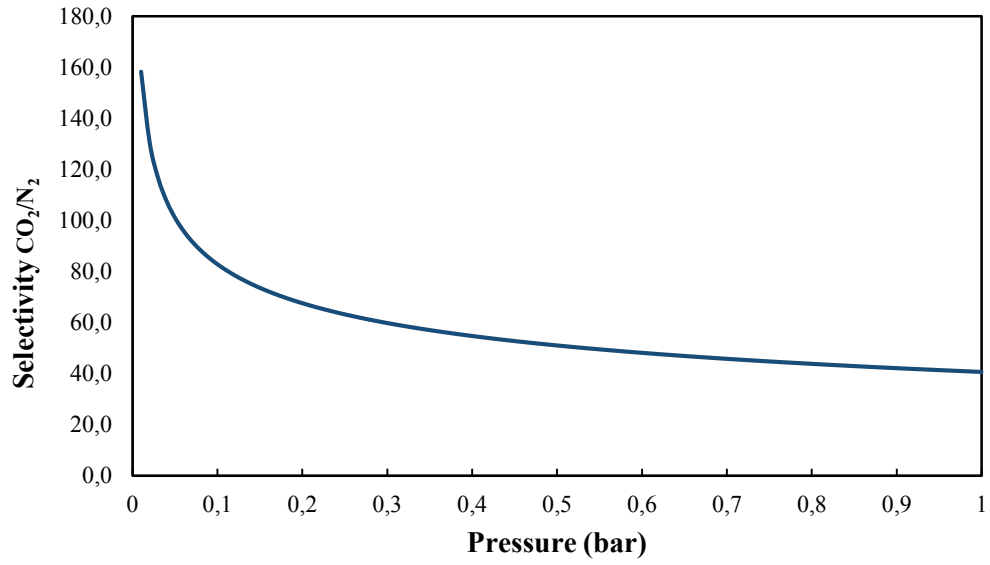
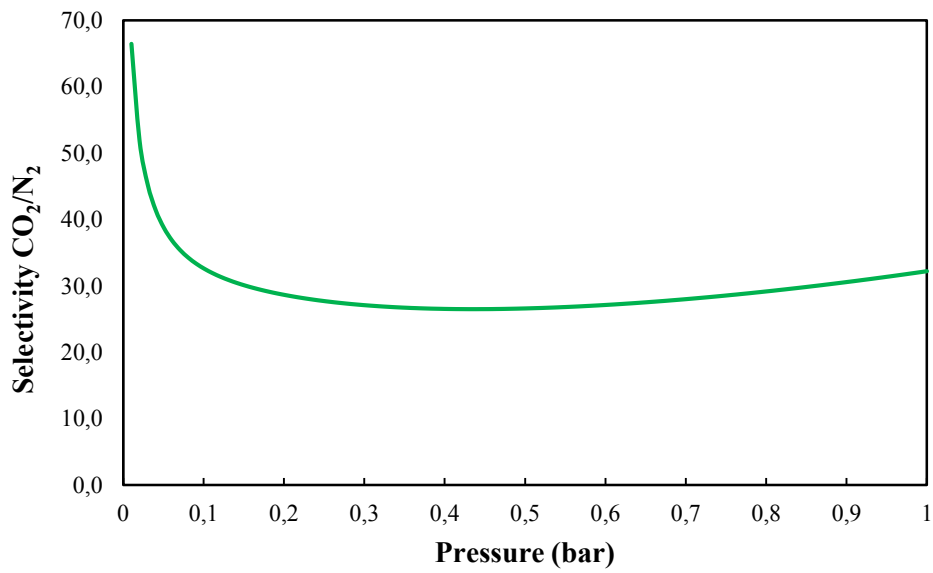**Figure 4.35** Ideal CO_2/N_2 selectivity for **GI5** for a potential 15/85 mixture.

Figure 4.36 Ideal CO_2/N_2 selectivity for **GI6** for a potential 15/85 mixture.
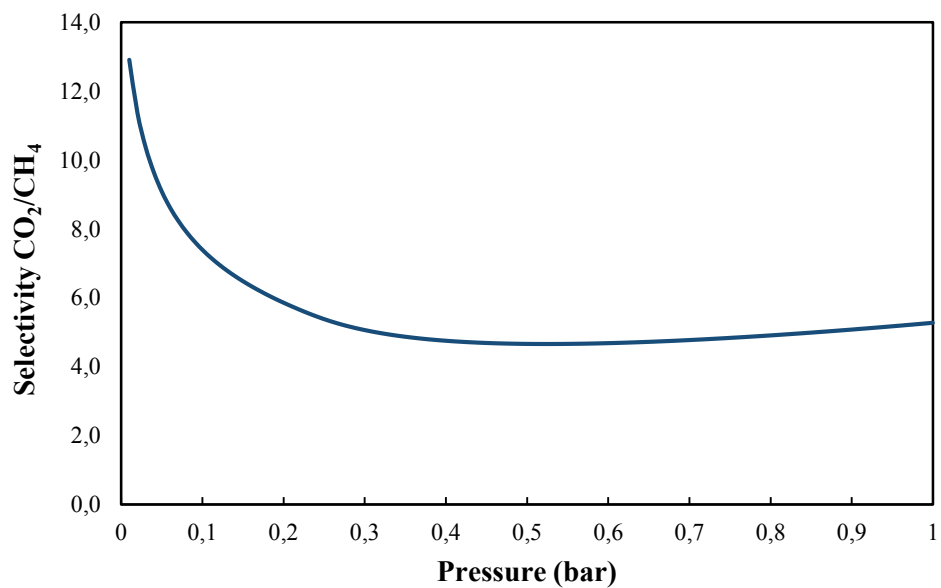
Figure 4.37 Ideal CO_2/CH_4 selectivity for **GI5** for a potential 50/50 mixture.
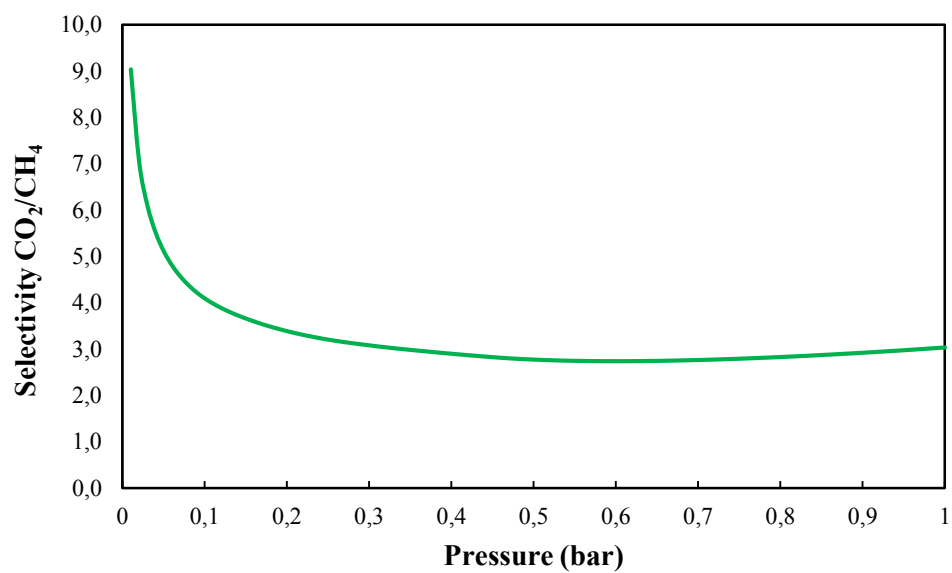

Figure 4.38 Ideal CO_2/CH_4 selectivity for **GI6** for a potential 50/50 mixture.

4.3.4 GI5 and GI6 as Fillers in MMMs

The novel cages were also tested as fillers in MMMs with polymer matrices that are commonly used for gas separation membranes. In particular, two different polymers were employed for these studies: the polyimide Matrimid® 9725 and the poly(ether-ether ketone) PEEK-WC (Figure 4.39) [71,72]. As for the studies in VSA conditions, The studies where focused on CO_2/N_2 and CO_2/CH_4 separations, which are of interest for post-combustion carbon capture and biogas upgrading.
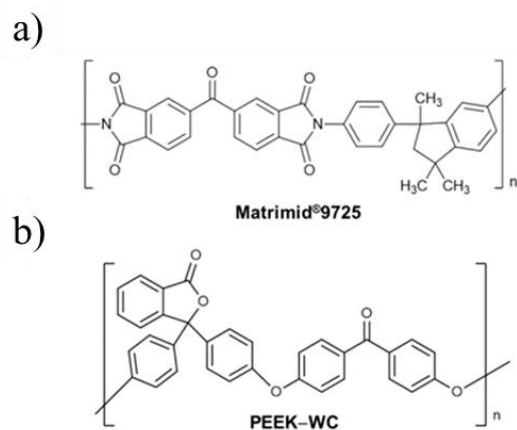

Figure 4.39 Chemical structures of: a) Matrimid®9725; b) PEEK-WC.

For the preparation of MMMs, the ball milled cages were firstly homogeneously dispersed in chloroform, then the required amount of polymer solution (2 wt.% Matrimid® 9725 or 3 wt.% PEEK-WC in $CHCl_3$) was added. **GI5** and **GI6**, were loaded in the polymer matrix at a final concentration of 20 wt.% based on the overall mass of the membranes. The resulting mixture was sonicated, and then poured into a Teflon petri dish to slowly evaporate the solvent for 24 h. Dense membranes were obtained, and their top surface was coated with PDMS Elastosil M 4601 (prepolymer+crosslinker) to cover possible pinhole defects (Figure 4.40) [54].

After the coating, pure gas permeation tests were performed at 298 K, and at a feed pressure of 1 bar in a fixed volume/pressure increase setup using the time-lag method for the determination of the permeability (P), diffusion (D), and solubility coefficients (S). The measurements were performed in the order O_2, N_2, CH_4, and finally CO_2. Tests with O_2 were done to have a better correlation of $\log(D)$ versus the squared gas diameter.
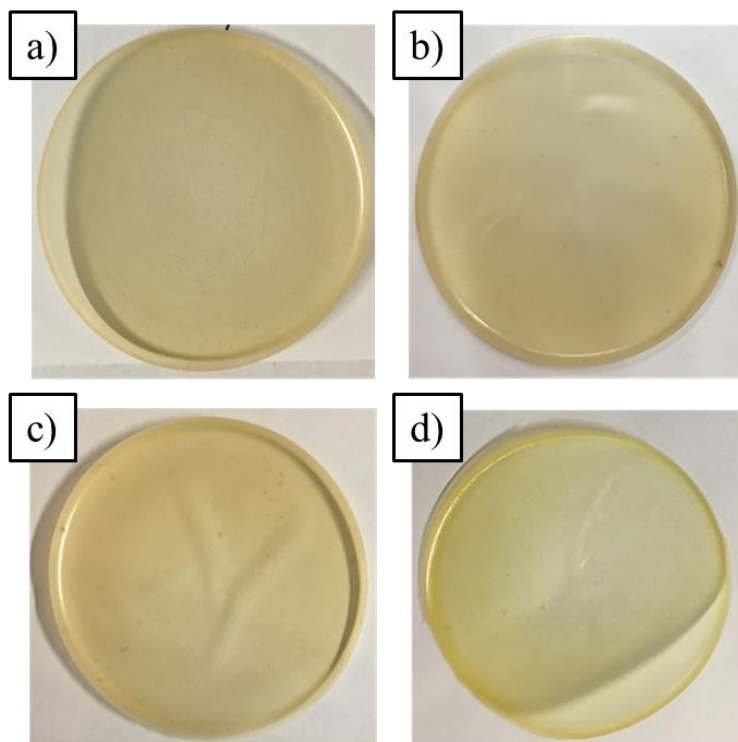
Figure 4.40 Images of the MMMs obtained with: a) PEEK-WC/**GI5**; b) PEEK-WC/**GI6**; c) Matrimid®9725/**GI5**; d) Matrimid®9725/**GI6**.

The results of the permeation tests with the three pure gases at 25 °C are collected in tables 4.4 and 4.5.

Table 4.4 Pure gas permeability and selectivity for neat and mixed matrix membranes.

Membrane	Permeability (Barrer)			Selectivity $\alpha(P_x/P_y)$	
	N_2	CH_4	CO_2	CO_2/N_2	CO_2/CH_4
PEEK-WC [73]	0.24	0.25	6.04	25.4	23.9
20% **GI5**	0.10	0.20	4.10	42.1	20.8
20% **GI6**	0.15	0.24	6.15	39.9	25.7
Matrimid®9725	0.31	0.35	10.8	35.5	31.1
20% **GI5**	0.28	0.28	10.1	35.4	36.6
20% **GI6**	0.51	0.40	16.7	32.7	41.7

Table 4.5 Diffusion coefficients and solubility for neat and mixed matrix membranes.

Membrane	Diffusivity $(10^{-12} \ m^2 \ s^{-1})$			Solubility $(cm^3_{STP} \ cm^{-3} \ bar^{-1})$		
	N_2	CH_4	CO_2	N_2	CH_4	CO_2
PEEK-WC [73]	0.45	0.14	0.58	0.39	1.33	7.77
20% **GI5**	0.68	0.15	0.59	0.11	0.95	5.19
20% **GI6**	0.91	0.14	0.74	0.13	1.24	6.22
Matrimid®9725	1.12	0.19	0.84	0.20	1.32	9.59
20% **GI5**	0.69	0.14	0.64	0.31	1.50	11.8
20% **GI6**	1.22	0.22	1.21	0.31	1.38	10.4

The Robeson plots for CO_2/N_2 and CO_2/CH_4 separations, derived from these data, are shown in figures 4.41 and 4.42, respectively. Notably, the two cages have opposite effects on the CO_2 permeability: the addition of **GI5** results in a marginal decrease of the CO_2 permeability in Matrimid® 9725 and an approximately 1/3 decrease in PEEK-WC. On the other hand, **GI6** increases the CO_2 permeability by few percent in PEEK-WC and about 50% in Matrimid® 9725. Based on the Maxwell equation (see chapter 3.1.2), the decrease in permeability for **GI5** and the increase for **GI6** suggest that the fillers have a lower and higher permeability than the polymers, respectively. This result is also in line with the lower porosity of **GI5** compared to **GI6** resulting from the gas adsorption studies on the two materials. In terms of selectivity, both cages significantly increase the CO_2/N_2 selectivity in PEEK-WC and the CO_2/CH_4 selectivity in Matrimid® 9725. Little improvement of CO_2/CH_4 selectivity was also found for the PEEK-WC/**GI6** membrane, while **GI5** slightly decreased it. Finally, the CO_2/N_2 selectivity for MMMs with Matrimid® 9725 was not affected by the addition of **GI5** or slightly decreases with the addition of **GI6**. These changes in the selectivity are associated with a general increase of the effective diffusion coefficient by **GI6** in both polymers (Table 4.5), especially for gases with small molecular diameter. Instead, **GI5** increases the diffusion coefficient in PEEK-WC, but reduces it in Matrimid® 9725.
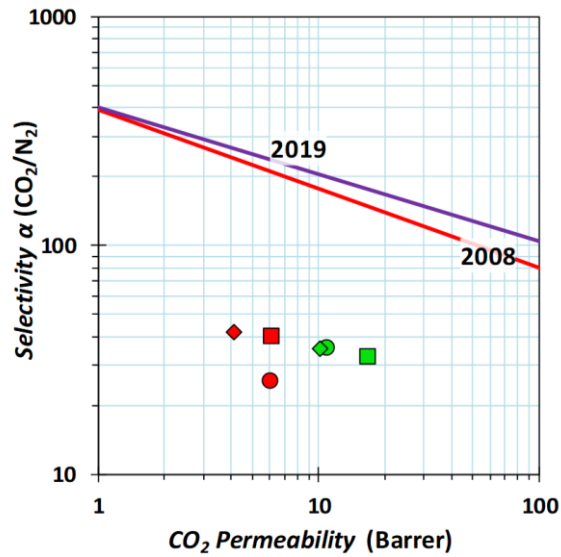
Figure 4.41 Robeson plots for the CO_2/N_2 gas pair. Red and purple lines correspond to 2008 and 2019 upper bounds, respectively [74,75]. The data are reported with the following symbols: Matrimid®9725 green circle ●, Matrimid®9725/**GI6** green square ■, Matrimid®9725/**GI5** green diamond ◆, PEEK-WC red circle ●, PEEK-WC/**GI6** red square ■ and PEEK-WC/**GI5** red diamond ◆.
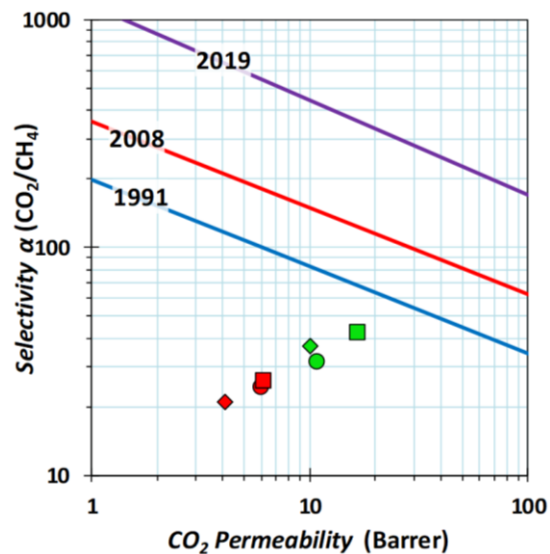

Figure 4.42 Robeson plots for the CO_2/CH_4, gas pair. Blue and red lines correspond to 1991 and 2008 upper bounds, respectively [74,75]. The purple line corresponds to 2019 upper bound [76]. The data are reported with the following symbols: Matrimid®9725 green circle ●, Matrimid®9725/**GI6** green square ■, Matrimid®9725/**GI5** green diamond ◆, PEEK-WC red circle ●, PEEK-WC/**GI6** red square ■ and PEEK-WC/**GI5** red diamond ◆.

The confirm that the gas transport process follows the solution–diffusion model is that the logarithm of the diffusion coefficient D shows a linear correlation with the square of the gas diameter, d^2_{eff}. Notably, in PEEK-WC MMMs the slope of the correlation increases with both cages, indicating that there is an increase in size-selectivity (Figure 4.43). On the other hand, the cages have negligible effect on the size-selectivity in Matrimid® 9725 (Figure 4.44). The differences between the two cages can be ascribed once again to the higher porosity of **GI6**.
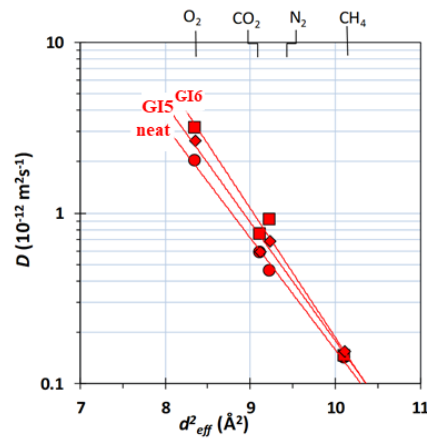

Figure 4.43 Correlation of the effective diffusion coefficient as a function of the molecular diameter [77] of four light gases in PEEK-WC. The data are reported with the following symbols: PEEK-WC red circle ●, PEEK-WC/**GI5** red diamond ♦, PEEK-WC/**GI6** red square ■.
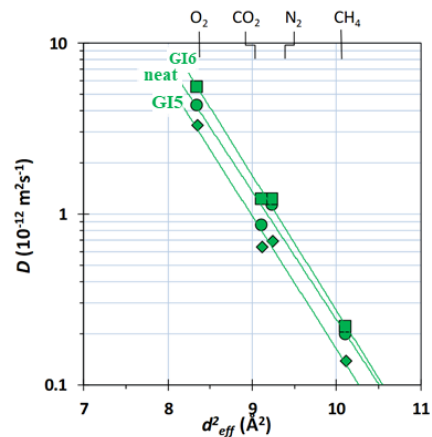

Figure 4.44 Correlation of the effective diffusion coefficient as a function of the molecular diameter [77] of four light gases in Matrimid®9725. The data are reported with the following symbols: Matrimid®9725 green circle ●, Matrimid®9725/**GI5** green diamond ♦, Matrimid®9725/**GI6** green square ■.

4.4 CONCLUSIONS

Two novel imide/imine-based organic cages were investigated as materials for gas separation processes as both pure solids and fillers in mixed matrix membranes. SCXRD analyses showed that both cages crystallize forming a thick network of intermolecular H-bonds, which principally involve the bicyclo[2.2.2]oct-7-ene-based spacers of different cage molecules. This dense packing significantly reduces the free volume potentially accessible to gases in the crystal, that is calculated to be only 0.1% and 9.8% of unit cell volume for **GI5** and **GI6**, in the **GI5**-α and **GI6**-β phases, respectively. PXRD analyses showed that **GI5** mostly precipitates from the reaction mixture as an amorphous powder, whereas **GI6** was obtained as a microcrystalline material, although in a different phase from those characterized by SCXRD. After a ball-milling step, the bulk solids were studied for their gas adsorption properties. In agreement with the crystal structures, the adsorption studies with N_2 at 77 K suggested that the pores accessibility is rather hindered in both **GI5** and **GI6**. Notably, the BET surface areas calculated with CO_2 at 273 K resulted much higher than those obtained with N_2 at cryogenic temperatures. This suggests that **GI5** and **GI6** materials are more porous than expected from the studies with N_2, probably because the cages are flexible enough to swell at higher temperatures. **GI5** and **GI6** were also successfully tested for potential CO_2/N_2 and CO_2/CH_4 separations in VSA processes. Gas adsorption studies performed with CO_2, N_2 and CH_4 at 298 K showed a preferential carbon dioxide adsorption. The good IAST selectivity for CO_2 confirms that the imide/imine groups can effectively promote the interaction with the quadrupolar CO_2 gas with respect to the other gas species. **GI5** and **GI6** also proved to be suitable as fillers for mixed matrix membranes. Dense and robust MMMs were obtained from both cages with PEEK-WC and Matrimid® 9725 polymers. Pure gas permeation tests with CO_2, N_2, and CH_4 gases showed an improvement of the gas-transport properties compared to the neat polymer membranes. An increase of CO_2/CH_4 selectivity was found with **GI5** and **GI6** in Matrimid® 9725, whereas an increase of CO_2/N_2 selectivity was achieved with both cages in PEEK-WC.
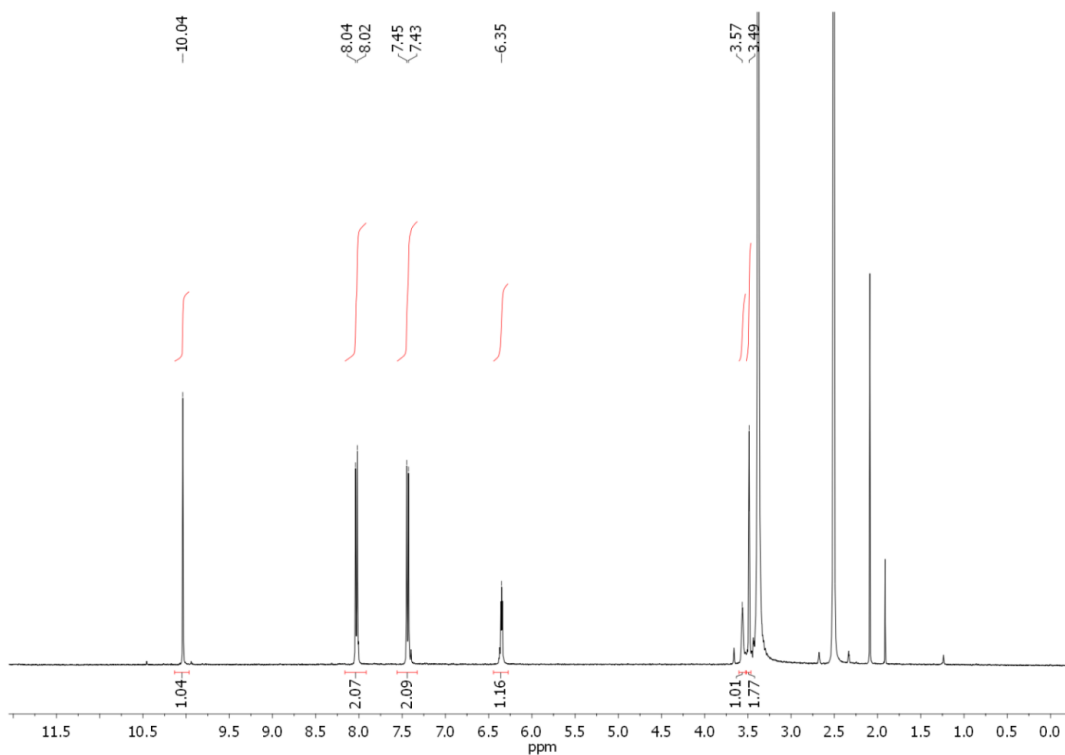
4.5 CHARACTERIZATION

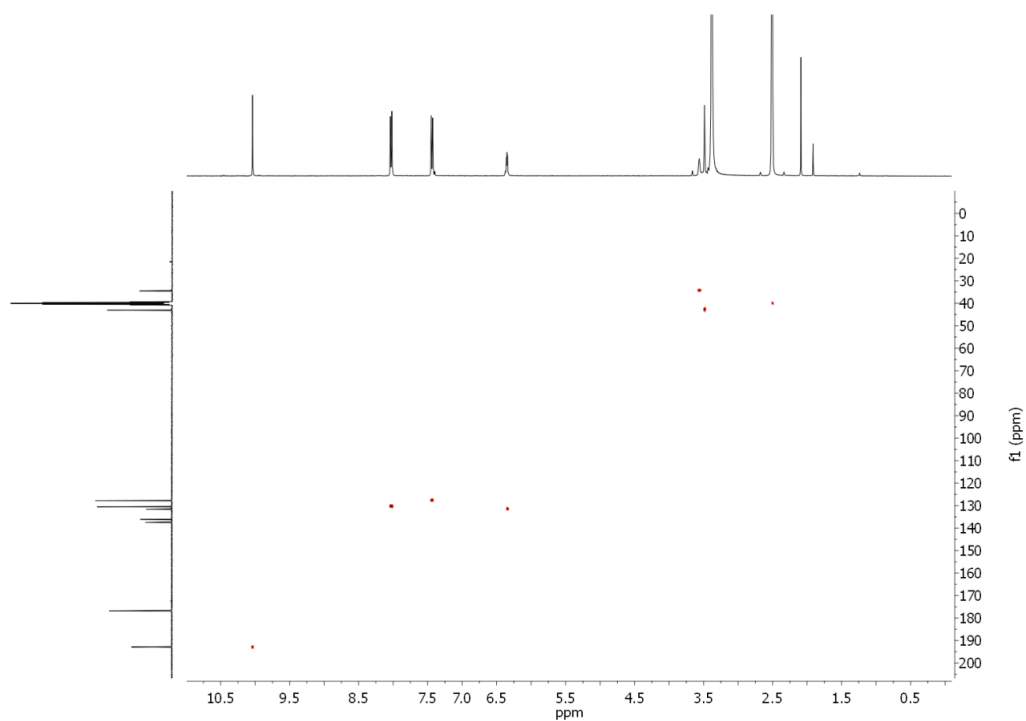**Figure 4.45** ^{1}H-NMR spectrum (400 MHz; d^{6}-DMSO) of **7**.

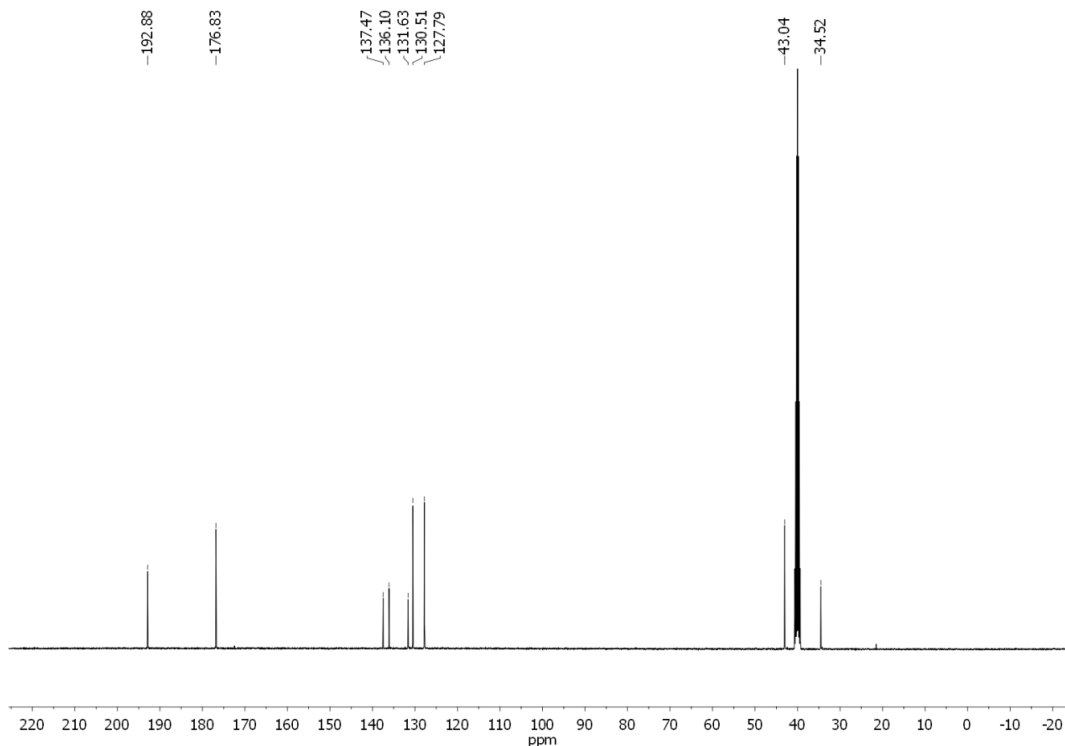**Figure 4.46** HSQC spectrum (d^{6}-DMSO) of **7**.

Figure 4.47 ^{13}C-NMR spectrum (100 MHz; d^6-DMSO) of **7**.
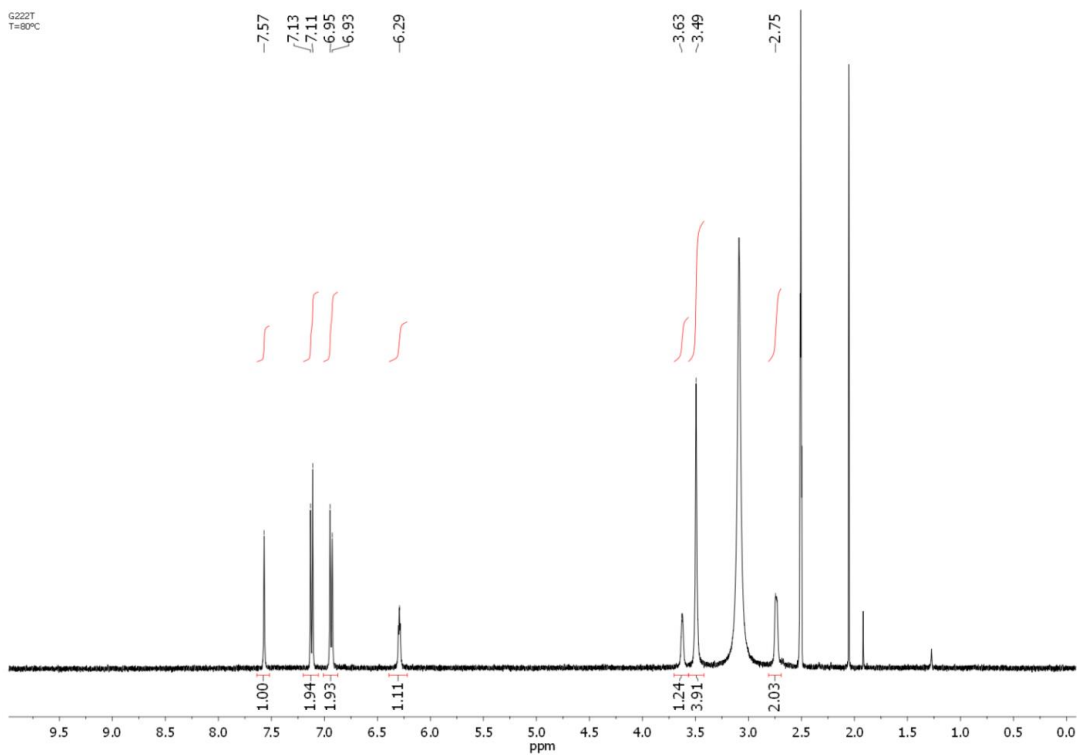

Figure 4.48 ^{1}H-NMR spectrum (400 MHz; d^6-DMSO) of **GI5** at 80°C.
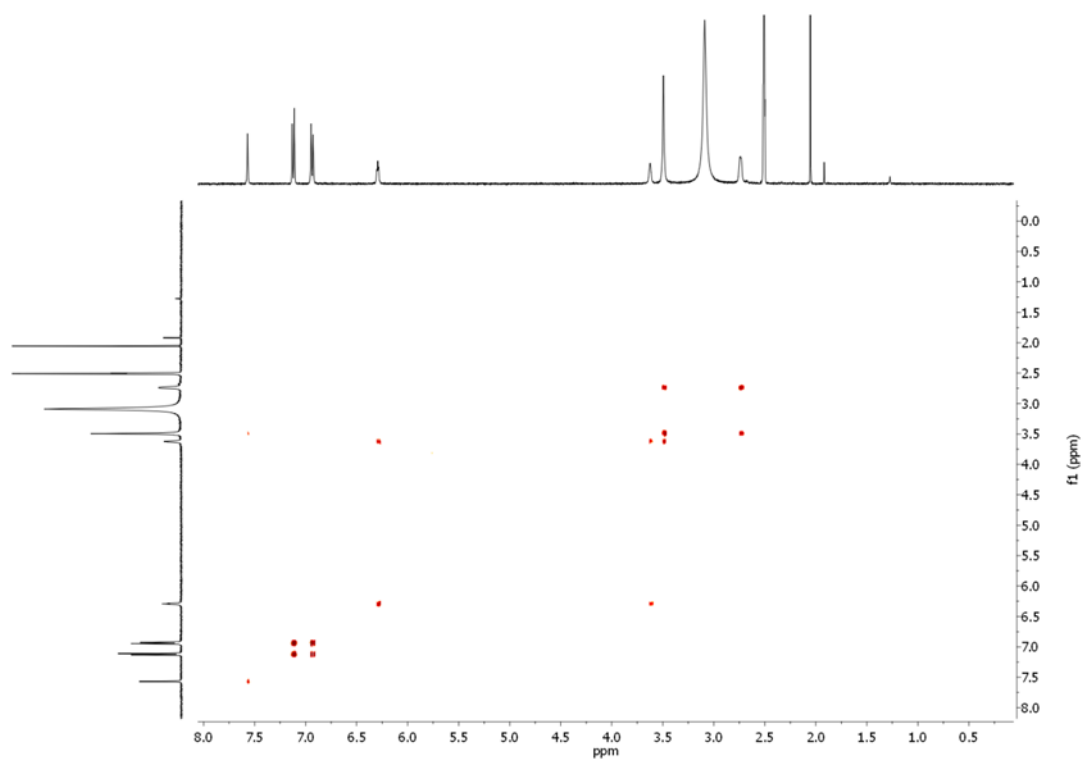
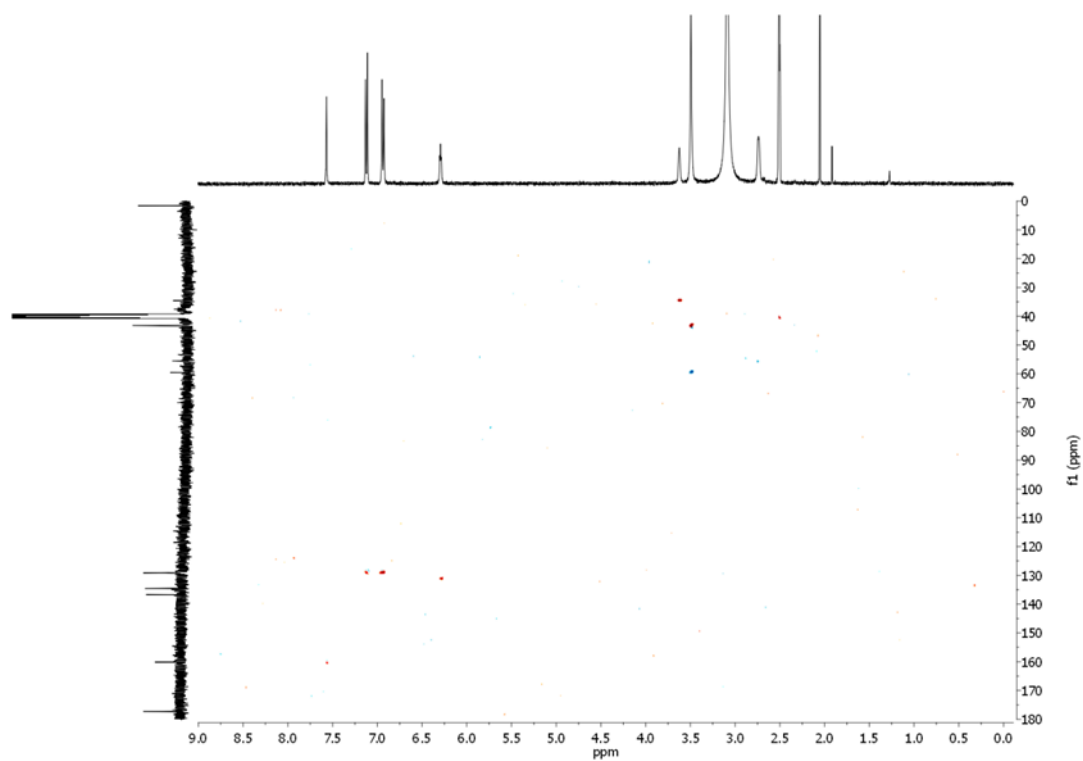**Figure 4.49** COSY spectrum (d^6-DMSO) of **GI5** at 80°C.

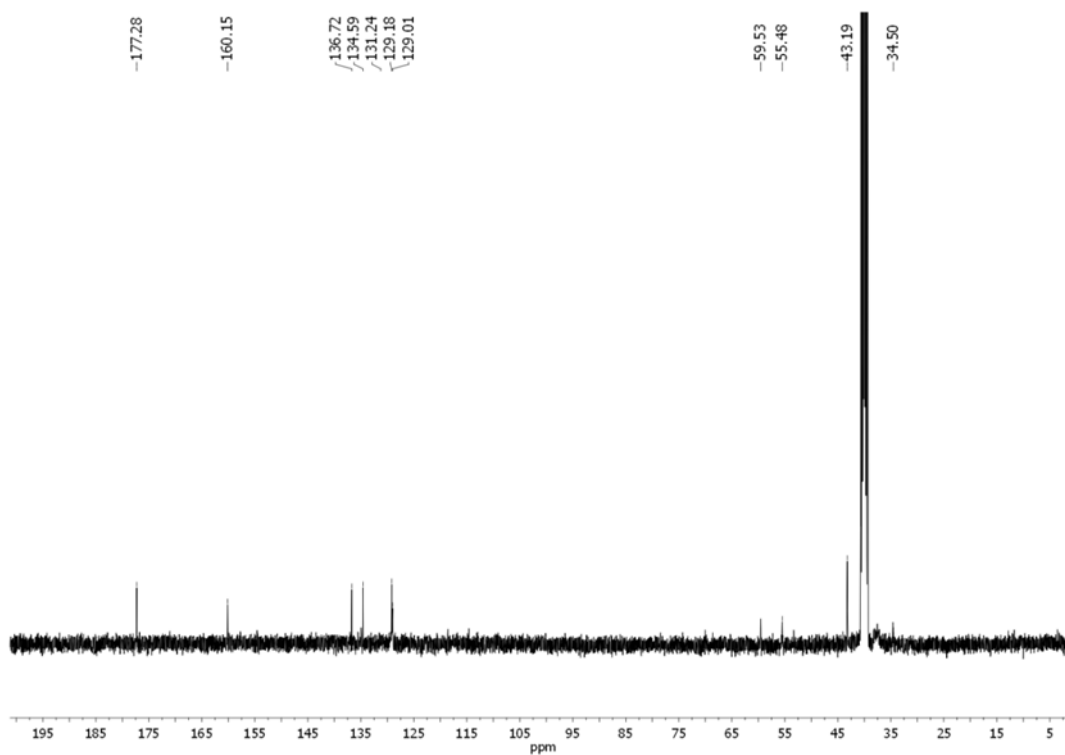**Figure 4.50** HSQC spectrum (d^6-DMSO) of **GI5** at 80°C.

Figure 4.51 ^{13}C-NMR spectrum (100 MHz; d^6-DMSO) of **GI5** at 80 °C.
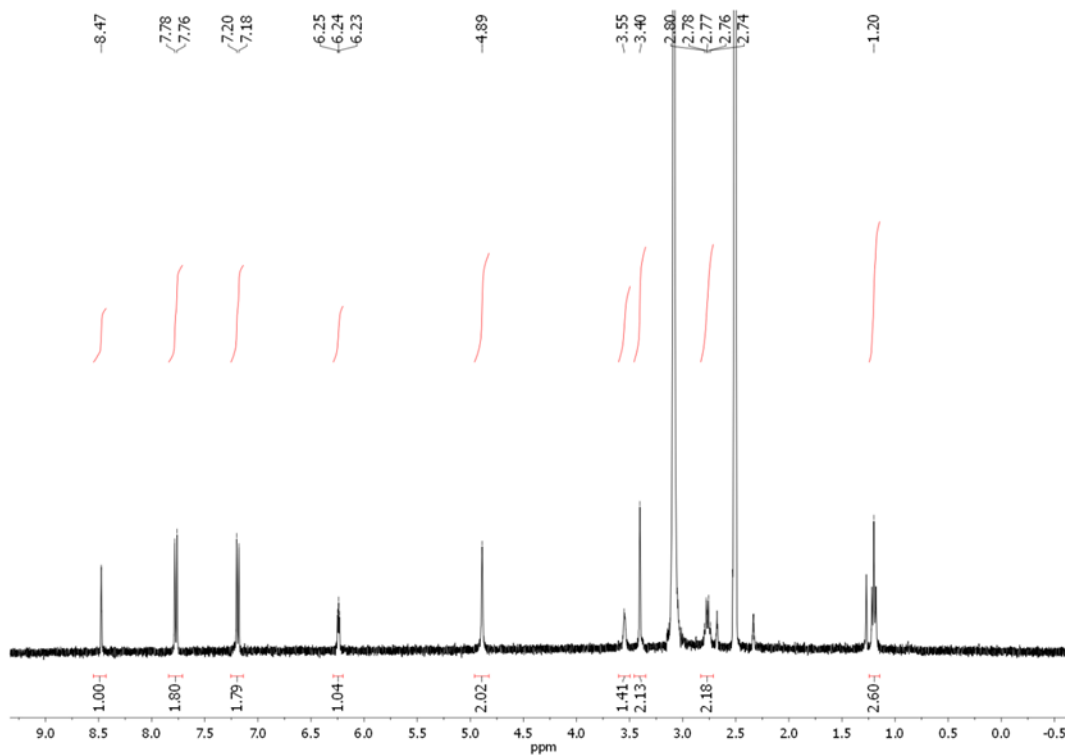

Figure 4.52 ^{1}H-NMR spectrum (400 MHz; d^6-DMSO) of **GI6** at 80°C.
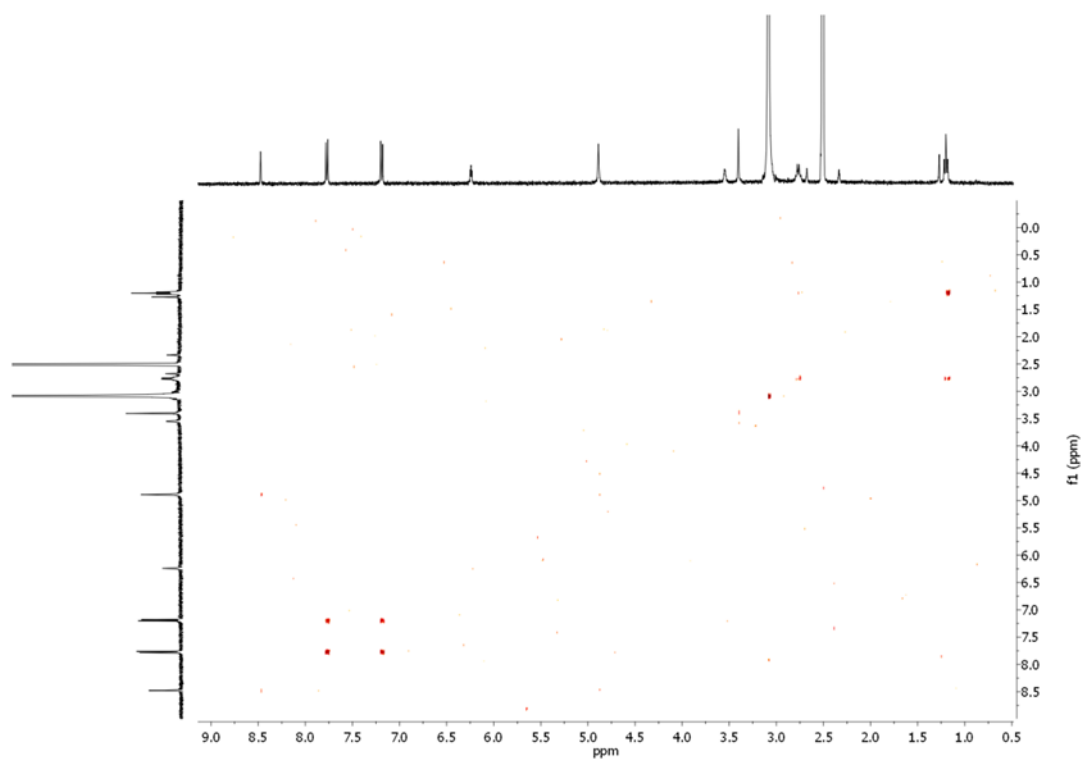
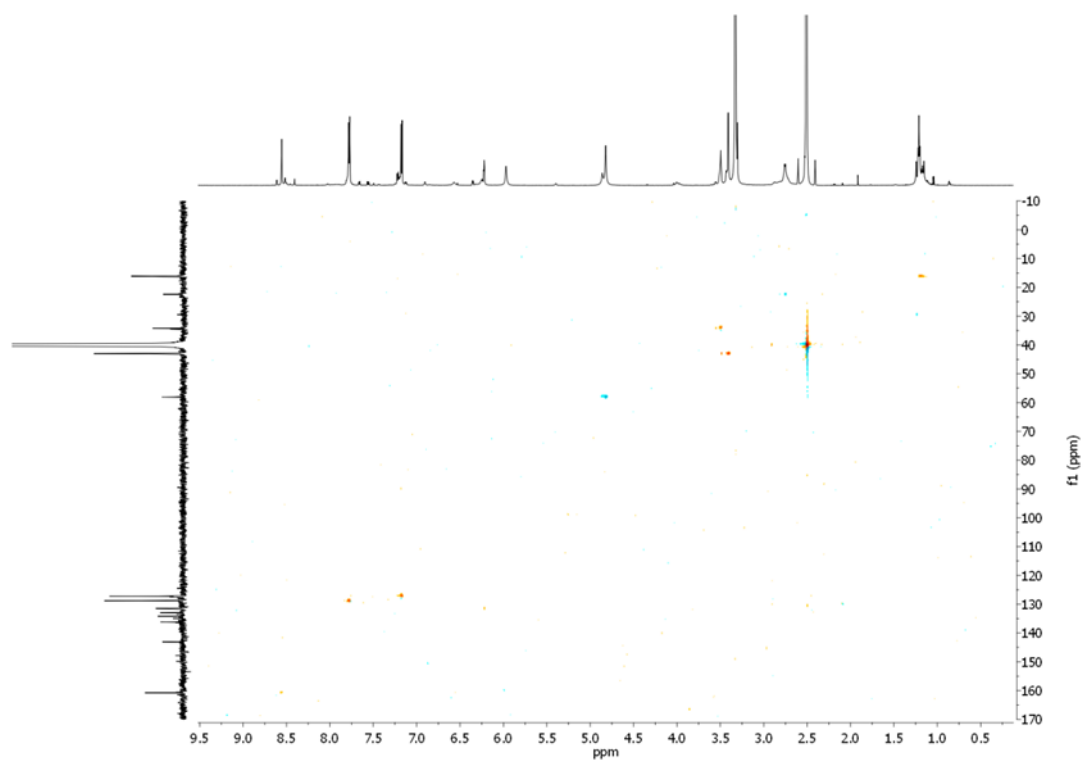**Figure 4.53** COSY spectrum (d^6-DMSO) of **GI6** at 80°C.

Figure 4.54 HSQC spectrum (d^6-DMSO) of **GI6** at 80°C.
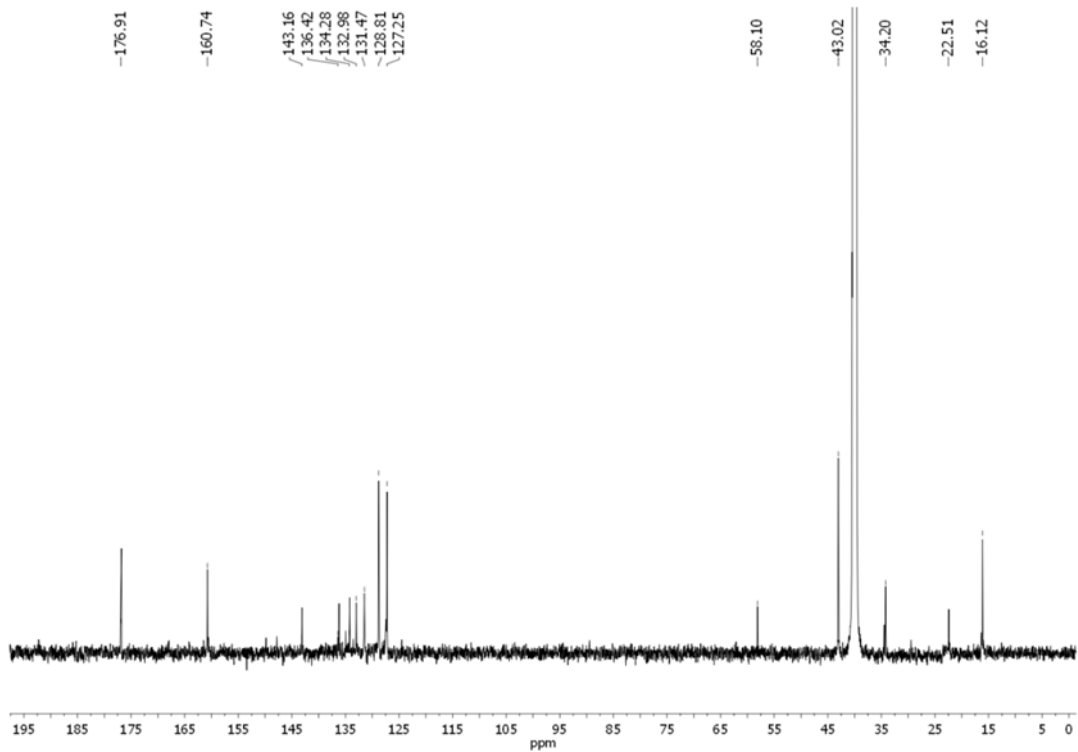
Figure 4.55 ^{13}C-NMR spectrum (175 MHz; d^6-DMSO) of **GI6.**

4.5 REFERENCES

[1] "*Trends in atmospheric Carbon Dioxide*", Earth System Research Laboratory (ESRL), **2019**. https://www.esrl.noaa.gov/gmd/ccgg/trends

[2] "*World Population Prospects 2022: Summary of Results*", United Nations DoEaSA, Population Division, **2022**. https://www.un.org/development/desa/pd/sites/www.un.org.development.desa.pd/files/wpp2022_summary_of_results.pdf

[3] "*International Energy Outlook 2021*", US EIA, **2021**. https://www.eia.gov/outlooks/ieo/pdf/IEO2021_ChartLibrary_full.pdf

[4] R.L. Siegelman, E.J. Kim, J.R. Long, *Nat. Mater.*, **2021**, *20*, 1060.

[5] "*CO_2 Emissions from Fuel Combustion*", International Energy Agency, **2019**. https://iea.blob.core.windows.net/assets/eb3b2e8d-28e0-47fd-a8ba-160f7ed42bc3/CO2_Emissions_from_Fuel_Combustion_2019_Highlights.pdf

[6] "*IPCC, 2018: Summary for Policymakers. In: Global Warming of 1.5°C. An IPCC Special Report on the impacts of global warming of 1.5°C above pre-industrial levels and related global greenhouse gas emission pathways, in the context of strengthening the global response to the threat of climate change, sustainable development, and efforts to eradicate poverty*", V. Masson-Delmotte, P. Zhai, H.-O. Pörtner, D. Roberts, J. Skea, P.R. Shukla, A. Pirani, W. Moufouma-Okia, C. Péan, R. Pidcock, S. Connors, J.B.R. Matthews, Y. Chen, X. Zhou, M.I. Gomis, E. Lonnoy, T. Maycock, M. Tignor, and T. Waterfield (eds.), Cambridge University Press, Cambridge, UK and New York, NY, USA, pp. 3-24.

[7] "*CO_2 and Greenhouse Gas Emissions*", H. Ritchie, M. Roser, P. Rosado, **2020**. https://ourworldindata.org/co2-and-other-greenhouse-gas-emissions

[8] X. Zhu, W. Xie, J. Wu, Y. Miao, C. Xiang, C. Chen, B. Ge, Z. Gan, F. Yang, M. Zhang, D. O'Hare, J. Li, T. Ge, R. Wang, *Chem. Soc. Rev.*, **2022**, 51, 6574.

[9] D. Jansen, M. Gazzani, G. Manzolini, E.V. Dijk, M. Carbo, *International Journal of Greenhouse Gas Control*, **2015**, 40, 167.

[10] R. Stanger, T. Wall, R. Spörl, M. Paneru, S. Grathwohl, M. Weidmann, G. Scheffknecht, D. McDonald, K. Myöhänen, J. Ritvanen, S. Rahiala, T. Hyppänen, J. Mletzko, A. Kather, S. Santos, *International Journal of Greenhouse Gas Control*, **2015**, 40, 55.

[11] R. Sahoo, S. Mondal, D. Mukherjee, M.C. Das*, Adv. Funct. Mater.,* **2022**, *32*, 2207197.

[12] K.K. Wong, Z.A. Jawad, *J. Polym. Res.*, **2019**, 26, 289.

[13] C. Font-Palma, D. Cann, C. Udemu, *C*, **2021**, 7, 58.

[14] B. Dutcher, M. Fan, A.G. Russell, *ACS Appl. Mater. Interfaces*, **2015**, 7, 2137.

[15] R. Khalilpour, K. Mumford, H. Zhai, A. Abbas, G. Stevens, E.S. Rubin, *J. Clean Prod.*, **2015**, 103, 286.

[16] M. Galizia, W. S. Chi, Z. P. Smith, T. C. Merkel, R. W. Baker, B. D. Freeman, *Macromolecules*, **2017**, 50, 7809.

[17] J. Rouquerou, D. Avnir, C.W. Fairbridge, D.H. Everett, J.H. Haynes, N. Pernicone, J.D.F. Ramsay, K.S.W. Sing, K.K. Unger, *Pure Appl. Chem.,* **1994**, 66, 1739.

[18] S.M. J. Rogge, A. Bavykina, J. Hajek, H. Garcia, A.I. Olivos-Suarez, A. Sepùlveda-Escribano, A. Vimont, G. Clet, P. Bazin, F. Kapteijn, M. Daturi, E.V. Ramos-Fernandez, F.X. Llabrès I. Xamena, V. Van Speybroeck, J. Gascon, *Chem. Soc. Rev.*, **2017**, 46, 3134.

[19] X. Zhan, Z. Chen, Q. Zhang, *J. Mater. Chem. A*, **2017**, 5, 14463.

[20] J.R. Li, J. Sculley, H.C. Zhou, *Chem. Rev.*, **2012**, 112, 869.

[21] D.J. Wales, J. Grand, V.P. Ting, R.D. Burke, K.J. Edler, C.R. Bowen, S. Mintova, A.D. Burrows, *Chem. Soc. Rev.*, **2015**, 44, 4290.

[22] K.S.W. Sing, D.H. Everett, R.A. Haul, W.L. Moscou, R.A. Pierotti, J. Rouquérol, T. Siemieniewska, *Pure Appl. Chem.,* **1985**, *57*, 603.

[23] P.M. Budd, B.S. Ghanem, S. Makhseed, N.B. McKeown, K.J. Msayib, C.E. Tattershall, *Chem. Commun.*, **2004**, 2, 230.

[24] J.X. Jiang, F. Su, A. Trewin, C.D. Wood, N.L. Campbell, H. Niu, C. Dickinson, A.Y. Ganin, M.J. Rosseinsky, Y.Z. Khimyak, A.I. Cooper, *Angew. Chem. Int. Ed.*, **2007**, 46, 8574.

[25] F. Beuerle, B. Gole, *Angew. Chem. Int. Ed*., **2018**, 57, 4850.

[26] T.R. Cook, Y.R. Zheng, P.J. Stang, *Chem. Rev.*, **2013**, 113, 734.

[27] a) W. Yang, A. Greenaway, X. Lin, R. Matsuda, A.J. Blake, C. Wilson, W. Lewis, P. Hubberstey, S. Kitagawa, N.R. Champness, M. Schröder, *J. Am. Chem. Soc.*, **2010**, 132, 14457. b) R.B. Lin, Y. He, P. Li, H. Wang, W. Zhou, B. Chen, *Chem. Soc. Rev.,* **2019**, 48, 1362.

[28] V.I. Nikolayenko, D.C. Castell, D.P. van Heerden, L.J. Barbour, *Angew. Chem. Int. Ed.*, **2018**, 57, 12086. b) G. Gong, S. Lv, J.Han, F. Xie, Q. Li, N. Xia, W. Zeng, Y. Chen, L. Wang, J. Wang, S. Chen, *Angew. Chem. Int. Ed.*, **2021**, 60, 14831.

[29] A.G. Slater, A.I. Cooper, *Science*, **2015**, 348, 988.

[30] K. Nishi, R.W. Thompson, "*Synthesis of Classical Zeolites*" in "*Handbook of Porous Solids*", Wiley-VCH Verlag GmbH, **2008**; pp 736-814.

[31] J.T.A. Jones, D. Holden, T. Mitra, T. Hasell, D.J. Adams, K.E. Jelfs, A. Trewin, D.J. Willock, G.M. Day, J. Bacsa, A. Steiner, A.I. Cooper, *Angew. Chem., Int. Ed.*, **2011**, 50, 749.

[32] T. Hasell, A.I. Cooper, *Nat. Rev. Mater.*, **2016**, 1, 16053.

[33] M. Mastalerz, *Angew. Chem. Int. Ed.*, **2010**, 49, 5042.

[34] C. Zhang, Z. Wang, L. Tan, T.L. Zhai, S. Wang, B. Tan, Y.S. Zheng, X.L. Yang, H.B Xu, *Angew. Chem. Int. Ed.*, **2015**, 54, 9244.

[35] A. Avellaneda, P. Valente, A. Burgun, J.D. Evans, A.W. Markwell-Heys, D. Rankine, D.J. Nielsen, M.R. Hill, C.J. Sumby, C.J. Doonan, *Angew. Chem. Int. Ed.*, **2013**, 52, 3746.

[36] J. Tian, P.K. Thallapally, S.J. Dalgarno, P.B. McGrail, J.L. Atwood, *Angew. Chem. Int. Ed.*, **2009**, 48, 5492.

[37] T. Tozawa, J.T.A. Jones, S.I. Swamy, S. Jiang, D.J. Adams, S. Shakespeare, R. Clowes, D. Bradshaw, T. Hasell, S.Y. Chong, C. Tang, S. Thompson, J. Parker, A. Trewin, J. Bacsa, A.M.Z. Slawin, A. Steiner, A.I. Cooper, *Nature Materials*, **2009**, 8, 973.

[38] M. Mastalerz, M.W. Schneider, I.M. Oppel, O Presly, *Angew. Chem. Int. Ed.*, **2011**, 50, 1046.

[39] S. Sircar, *Ind. Eng. Chem. Res.*, **2006**, 45, 16, 5435.

[40] Y. Jin, B.A. Voss, A. Jin, H. Long, R.D. Noble, W Zhang, *J. Am. Chem. Soc.*, **2011**, 133, 6650.

[41] G. Zhang, O. Presly, F. White, I.M. Oppel, M. Mastalerz, *Angew. Chem. Int. Ed.*, **2014**, 53, 1516.

[42] D. Hu, J. Zhang, M. Liu, *Chem. Commun.*, **2022**, 58, 11333.

[43] S.I. Etkind, D.A. Vander Griend, T.M. Swager, *J. Org. Chem.*, **2020**, 85, 10050.

[44] SAINT Software Reference Manual, Version 6, Bruker AXS Inc., **2003**, Madison, Wisconsin, USA.

[45] APEX 2, Bruker AXS Inc., **2012**, Madison, Wisconsin, USA.

[46] L. Krause, R. Herbst-Irmer, G.M. Sheldrick, D. Stalke, *J. Appl. Cryst.*, **2015**, 48, 3.

[47] M.C. Burla, R. Caliandro, B. Carrozzini, G.L. Cascarano, C. Cuocci, C. Giacovazzo, M. Mallamo, A. Mazzone, G. Polidori, *J. Appl. Cryst.,* **2015**, 48, 306.

[48] G.M. Sheldrick, *Acta Cryst.*, **2015**, A71, 3.

[49] G.M. Sheldrick, *Acta Cryst.*, **2015**, C71, 3.

[50] A. Lausi, M. Polentarutti, S. Onesti, J.R. Plaisier, E. Busetto, G. Bais, L. Barba, A. Cassetta, G. Campi, D. Lamba, A. Pifferi, S.C. Mande, D.D. Sarma, S.M. Sharma, G. Paolucci, *Eur. Phys. J. Plus*, **2015**, 130.

[51] W. Kabsch, *Acta Cryst.*, **2010**, D66, 125.

[52] O.V. Dolomanov, L.J. Bourhis, R.J. Gildea, J.A.K. Howard, H. Puschmann, *J. Appl. Cryst.*, **2009**, 42, 339.

[53] C.F. Macrae, I.J. Bruno, J.A. Chisholm, P.R. Edgington, P. McCabe, E. Pidcock, L. Rodriguez-

Monge, R. Taylor, J. Van De Streek, P.A. Wood, *J. Appl. Crystallogr.*, **2008**, 41, 466.

[54] M. Monteleone, R. Mobili, C. Milanese, E. Esposito, A. Fuoco, S. La Cognata, V. Amendola, J.C. Jansen, *Molecules*, **2021**, 26, 5557.

[55] S.C. Fraga, M. Monteleone, M. Lanč, E. Esposito, A. Fuoco, L. Giorno, K. Pilnáček, K. Friess, M. Carta, N.B. McKeown, P. Izák, Z. Petrusová, J.G. Crespo, C. Brazinha, J.C. Jansen, *J. Memb. Sci.*, **2018**, 561, 39.

[56] S. Jiang, J. Bacsa, X. Wu, J.T. A. Jones, R. Dawson, A. Trewin, D.J. Adams, A.I. Cooper, *Chem. Commun.*, **2011**, 47, 8919.

[57] J. Jeromenok, J. Weber, *Langmuir*, **2013**, 29, 12982.

[58] M. Thommes, K. Kaneko, A.V. Neimark, J.P. Olivier, F. Rodriguez-Reinoso, J. Rouquerol, K.S.W. Sing, *Pure Appl. Chem.*, **2015**, 87, 1051.

[59] M. Thommes, K.A. Cychosz, *Adsorption*, **2014**, 20, 233.

[60] K.C. Kim, T.U. Yoon, Y.S. Bae, *Microporous Mesoporous Mater.*, **2016**, 224, 294.

[61] M. Chen, B. Coasne, R. Guyer, D. Derome, J. Carmeliet, *Nat. Commun.*, **2018**, 9, 3507.

[62] K. Wang, S. Qiao, X. Hu, *Sep. Purif. Technol.*, **2004**, 34, 165.

[63] H. Zhou, C. Rayer, A.R. Antonangelo, N. Hawkins, M. Carta, *ACS Appl. Mater. Interfaces*, **2022**, 14, 18, 20997.

[64] A.L. Myers, J.M. Prausnitz, *AIChE J.*, **1965**, 11, 121.

[65] a) M. Kang, S. Yoon, S. Ga, D.W. Kang, S. Han, J.H. Choe, H. Kim, D.W. Kim, Y.G. Chung, C.S. Hong, *Adv. Sci.*, **2021**, 8, 2004940; b) X. Lv, L. Li, S. Tang, C. Wang, X. Zhao, *Chem. Commun.*, **2014**, 50, 6886.

[66] S. Lee, J.H. Lee, J. Kim, *Korean J. Chem. Eng.*, **2018**, 35, 214.

[67] K.T. Leperi, R.Q. Snurr, F. You, *Ind. Eng. Chem. Res.*, **2016**, 55, 3338.

[68] G. Zhang, B. Hua, A. Dey, M. Ghosh, B.A. Moosa, N.M. Khashab, *Acc. Chem. Res.*, **2021**, 54, 155.

[69] D. Lv, R. Shi, Y. Chen, Y. Chen, H. Wu, X. Zhou, H. Xi, Z. Li, Q. Xia, *Ind. Eng. Chem. Res.*, **2018**, 57, 12215.

[70] B. Aghel, S. Behaein, S. Wongwises, M.S. Shadloo, *Biomass Bioenergy*, **2022**, 160, 106422.

[71] M.J.C. Ordoñez, K.J. Balkus, J.P. Ferraris, I.H. Musselman, *J. Membr. Sci.*, **2010**, 361, 28.

[72] J.C. Jansen, E. Drioli, *Polym. Sci. Ser. A*, **2009**, 51, 1355.

[73] E. Esposito, R. Bruno, M. Monteleone, A. Fuoco, J. Ferrando Soria, E. Pardo, D. Armentano, J.C. Jansen, *Appl. Sci.*, **2020**, 10, 1310.

[74] L.M. Robeson, *J. Membr. Sci.*, **1991**, 62, 165.

[75] L.M. Robeson, *J. Membr. Sci.*, **2008**, 320, 390.

[76] B. Comesaña-Gándara, J. Chen, C.G. Bezzu, M. Carta, I. Rose, M.C. Ferrari, E. Esposito, A. Fuoco, J.C. Jansen, N.B. McKeown, *Energy Environ. Sci.*, **2019**, 12, 2733.

[77] V. Teplyakov, P. Meares, *Gas Sep. Purif.*, **1990**, 4, 66.